Cosmological models of galaxy clusters: the role of feedback processes

---

Dissertation

zur

Erlangung der naturwissenschaftlichen Doktorwürde
(Dr. sc. nat.)

vorgelegt der

Mathematisch-naturwissenschaftlichen Fakultät

der

Universität Zürich

von

Davide Martizzi

aus Italien

Promotionskomitee

Prof. Dr.	Ben Moore	(Vorsitz)
Prof. Dr.	Romain Teyssier	(Leiter)
Prof. Dr.	George Lake	
Prof. Dr.	Thomas Gehrmann	
Prof. Dr.	Uros Seljak	
Prof. Dr.	Laura Baudis	

Zürich 2013

All in all, it's just another brick in the wall.

Roger Waters

Acknowledgements

The last part I wrote for this Thesis is the acknowledgments section. I'm placing them at the beginning just because they are the most important part, the one that most people will entirely read. They also represent a sort of seal showing that the writing of this Thesis is finally over. I'm writing these lines while sitting on a really comfortable couch in my office and I'm pretty much enjoying that. From this very comfortable position, I have to say that this PhD was a great time, not only from a professional point of view, but from a general perspective. It was great to have the occasion of living in Zürich for almost four years, it was great to meet so many cool people. From a professional point of view I was introduced to the field of computational astrophysics that was almost completely new to me, and for this I have to thank Ben and Romain. More importantly, Romain has to be thanked because of his Long Island Ice Teas and Ben for not firing me after a notorious night. No more comments about this story needed. I have to thank Regina and Esther whose support was really indispensable. I have to thank Regina twice because she saved me every time I didn't want to talk about science over lunch (basically almost every day – lunch time is holy). Doug has to be mentioned too, because he's a great guy and because without his support and computer administration nobody would be able to work in our institute. During my stay at the ITP I had the opportunity to meet a lot of people that contributed making these years really enjoyable, first of all the ones that worked or still work in the "sloth office": Volker, Darren, Zvonimir, Valentina, Lea and Lucas. There are (and there were) great people also in the other offices, anyway (in random order): Rok, Donnino, Tobias, Simon, Michael, Andreu, Andreas (all of them), Davide, Thomas (all of them), Christine, George, Joachim, Prasenjit, Crescenzo, Mario, Oscar, Antoine, Lucio, Markus, Sarah, Sebastian, Pier Francesco, Fabio, Lorenzo, Alessandro, Niccolò, Elena, Marina, Ray, Dan, Tina, Jonathan, Rebekka, Simone, Irshad, Timo, Erich. I'm sure I forgot somebody, I've always had memory issues... Send me your complaints via email if it's the case (sorry). A special mention should go to Oliver that's almost an honorary member of

this institute and whose relaxed, healthy lifestyle should be taken as a model by the entire human population of this planet. My stay in Zürich wouldn't have been the same if I hadn't lived with great friends: Andrea M., Andrea P., Fabio and Lorenzo, thank you (also for enduring my weirdnesses)! Sandra, you are one of my personal icons! Fun times wouldn't have been as fun without Benoît and John Jon! I wish François could read this too... Furthermore, I really enjoyed the time spent with Chiara, Michela, Michele, Daniela, Andrea S., Beatrice, Diane and Mathieu! Great people, great time! Finally, I want to thank my family, mamma Daniela, papà Antonio and fratello Paolo, which always supported me on everything I tried to do, including this PhD. Grazie a tutti!

Zusammenfassung

Galaxienhaufen sind die grössten gravitativ gebunden Strukturen im Universum in denen einige interessante astrophysikalische Prozesse erfolgen. Sie enthalten grosse Mengen an Dunkler Materie und heissem Gas, welches Röntgen-Strahlung ausstrahlt. Zudem enthalten sie oft ausgedehnte Mikrowellen-Strahlung und Zeichen hydrodynamischer Schocks. Sie enthalten auch die grössten Galaxien im Universum, die sich meistens im Zentrum befinden. Aus diesen Gründen sind Galaxienhaufen eine einzigartige Klasse von Objekten in denen viele astrophysikalische Prozesse betrachtet werden können. Ausserdem werden Galaxienhaufen als Tracer der grossräumigen Strukturen benutzt. Ihre räumliche Verteilung und numerische Dichte können für kosmologische Studien benutzt werden. Aus diesen Gründen ist es äusserst interessant die Prozesse aus einer theoretischen Perspektive zu betrachten, mit welcher die Eigenschaften der Galaxienhaufen nachmodelliert, selektiv überprüft und untersucht werden können. In dieser Arbeit verwende ich Simulationen mit adaptiver Gitterverfeinerung (adaptive mesh refinement), um die Eigenschaften der Galaxienhaufen im Kontext des kosmologischen Modelles nachzubilden. Insbesondere konzentriere ich mich auf den Effekt der nicht-gravitativen Erhitzung von super-massereichen Schwarzen Löchern, welche sich im Zentrum der grössten Galaxien befinden. Dieser Effekt ist als "Aktiver galaktischer Kern (AGK) Rückkoppelungsprozess"bekannt. AGKs sind astrophysikalische Objekte welche die Restenergie der Masse des Gases sehr effizient umwandeln können. Das Gas wird dabei in verschiedene Arten von Energie umgewandelt. Der AGK Rückkoppelungsprozess ist das Resultat einer Verknüpfung zwischen der Energie der AGKs mit dem Gas rund um die massereichen Schwarzen Löcher. Ich werde zeigen, dass der AGK Rückkoppelungsprozess ein relevantes Verfahren zur Bildung der zentralen Galaxien und für die Bestimmung der Massenverteilung innerhalb der Galaxienhaufen ist. Ich werde auch zeigen, dass der AGK Rückkoppelungsprozess einen Einfluss auf die Bestimmung der Gesamtmasse in simulierten Galaxienhaufen hat. Dieser Effekt ist es wert betrachtet zu werden, weil er sehr wichtig für die Bestimmung der dunklen Halo Massenfunktion ist.

Summary

Clusters of galaxies are the largest gravitationally bound structures in the Universe. Several interesting astrophysical processes take place in clusters. They host hot X-ray emitting gas and large quantities of dark matter. They frequently show extended radio emission and signature of hydrodynamical shocks. They also host the most massive galaxies in the Universe, which usually sit at their centres. For these reasons, clusters of galaxies represent a unique class of objects where a large number of astrophysical processes can be studied. Furthermore, galaxy clusters are frequently used as tracers of the large scale structure and their spatial distribution and abundance can be used for cosmological studies. Given the importance of these objects, it is extremely interesting to study the processes that shape the properties of clusters from a theoretical perspective. In this Thesis, I use adaptive mesh refinement (AMR) simulations aimed at reproducing the properties of galaxy clusters in the context of the concordance cosmological model. In particular, I focus on the effect of non-gravitational heating from supermassive black holes present at the centres of massive galaxies, an effect known as active galactic nucleus (AGN) feedback. AGNs are astrophysical objects that are very efficient in converting a fraction of the rest mass energy of the gas they accrete into different kinds of energy. AGN feedback is the result of the coupling between the energy emitted from AGNs with the gas surrounding the supermassive black holes. I will show that AGN feedback is a relevant process for the formation of the central galaxies and for the determination of the mass distribution within clusters. I will also show that AGN feedback has an impact on the determination of the total mass in simulated clusters, an effect that deserves to be studied because of its relevance for the correct determination of the dark matter halo mass function.

Contents

Chapter 1

Introduction

Understanding the Universe, its origin, composition and evolution is one of the fundamental goals of science. Cosmology is the branch of science aimed at describing the properties of the Universe as a whole and at identifying the mechanisms that determine its evolution. Despite the existence of many open problems in Cosmology, scientists were able to develop a cosmological scenario that agrees with most of the observations of our Universe. Within this cosmological scenario, a well defined theory for the formation of the structures we observe in the Universe has been formulated. The study of the formation and the evolution of cosmic structures is a discipline at the boundary of Cosmology and Astrophysics.

In this Thesis I will refer to the standard cosmological scenario as Concordance Cosmological Model. Such model is characterized by a few free parameters, most of which have been now determined with good accuracy from observations. The Concordance Cosmological Model provides an excellent framework to study the many, complicated phenomena occurring throughout the cosmic time, chiefs among which are the formation and evolution of galaxies and clusters. An important requirement for any theory of structure formation is to reproduce the observed properties of the galaxy spatial distribution, their properties and morphologies. In this context, a successful theory has emerged in which cosmic structures grow from tiny fluctuations in the primordial cosmic density field, through gravitational instability. Analytical models coupled with numerical simulations are able to account for the evolution of such fluctuations from their onset (microscopic quantum fluctuations) to their gravitational collapse and subsequent formation of dynamically-stable, virialized structures.

Such theory applies to collisionless, self-gravitating types of matter, while standard particles, like nucleons, behave like a collisional, dissipative fluid. Following the cosmologists' jargon, the matter component composed of stan-

dard particles will be called "baryonic matter", since leptons provide a negligible contribution to the mass. The relevance of the gravitational instability theory stems for the observational evidence that only $\sim 1/6$ of the mass in the Universe is made of baryons. The largest fraction is dark, i.e. its presence is only inferred from the gravitational interaction with the surrounding baryons. This Dark Matter (DM) must have a very small cross-section for interactions with the electro-magnetic radiation and must be made of non-standard collisionless particles. Since it dominates the mass budget it also drives the evolution of cosmic structures, and the theory of gravitational instability can be safely applied, at least to a first approximation. Yet the evolution of luminous structures, made of baryons, is more difficult to work out because of the collisional, dissipative nature of the standard matter.

Current theories of galaxy formation suffer from several uncertainties. However, they all agree that luminous structures preferably form in correspondence of DM halos, i.e. the end-product of the gravitational instability process for the dark component. Baryonic matter that falls into a halo, initially in a gaseous form, cools down and forms stars within dynamically-stable systems that we call galaxies (White & Rees, 1978). The study of galaxy formation and evolution constitutes one of the main fields of modern Astronomy. Despite the simplicity of the standard picture, important details of the galaxy formation process still need to be properly understood. Given the complexity of the phenomena that take place during galaxy formation, it is now very common to resort to advanced simulation techniques to study the physics of the process.

A very important prediction of the Concordance Cosmological Model is the fact that small halos form earlier than larger halos, and they evolve in hierarchical fashion. Mergers and accretion of satellite halos are extremely relevant in shaping the properties of the most massive halos and their galaxies. Galaxy clusters are the largest collapsed structures in the local portion of the Universe and the study of their formation and complicated history provides a wealth of information that can be used to test galaxy formation theory.

In this Thesis, I will discuss several topics related to structure formation in a cosmological context. The results I will show are all relevant for a better understanding of the properties of galaxy clusters and the galaxies they host. In particular, I considered the problem of understanding the role of Active Galactic Nuclei (AGN) in structure formation. AGNs are some of the most powerful energy sources in the Universe and a fraction of their energy output is observed to be coupled to the integalactic gas in clusters of galaxies. Therefore, AGN constitute a non-negligible heating source for the intergalactic gas and influences the galaxy formation process. The effect of the presence of

AGN on baryonic matter is usually referred to as AGN feedback. I performed N-body and hydrodynamical simulations including AGN feedback and made predictions about the properties of massive galaxy clusters. The code used for the simulations is the multi-purpose code RAMSES.

The Thesis has the following structure:

- Chapter 1: Introduction to the Concordance Cosmological Model and to the galaxy formation theory.
- Chapter 2: Introduction to simulation techniques used in Cosmology. Introduction to the RAMSES code.
- Chapter 3 (Paper 1): A study of the effect of AGN feedback on the mass distribution in galaxy clusters simulated in a cosmological context.
- Chapter 4 (Paper 2): A study of the effect of AGN feedback on the properties of the central galaxies in galaxy clusters simulated in a cosmological context.
- Chapter 5 (Paper 3): A study showing that AGN feedback can dramatically influence the properties of the spatial distribution of DM in the central regions of galaxy clusters. The results were found using cosmological simulations.
- Chapter 6 (Paper 4): A study which confirms the results of Paper 3 using simulations of the progenitor of a galaxy cluster in isolation.
- Chapter 7: Preliminary results. A study of the effect of baryon physics on the dark matter halo mass function.

1.1 Introduction to the Concordance Cosmological Model - Hubble's Law

The 20th century was the theatre of mind-blowing developments in Physics and Astrophysics which influenced and radically modified the cosmological sciences. One of the breakthroughs in this field came with the discovery of Hubble's Law. In 1929 Edwin Hubble showed that distant galaxies are receding from us at a velocity proportional to their distance from us. This observation lead to the formulation of the famous Hubble's law:

$$v = H_0 d, \tag{1.1}$$

where v is the recessional velocity of the considered galaxy along the line of sight, d is its distance from the observer and H_0 is Hubble's constant. Due to the recessional velocity the energies of the photons emitted by galaxies are shifted to lower energies by Doppler effect. Let λ_{rest} be the rest frame wavelength of a photon at the time of emission and $\lambda_{obs} \geq \lambda_{rest}$ the wavelength of the same photon at the time of observation, then one can define the redshift z of the galaxy as:

$$z = \frac{\lambda_{obs} - \lambda_{rest}}{\lambda_{rest}}. \tag{1.2}$$

In the scientific jargon, it is commonly said that the wavelengths of the photons emitted by the galaxy are redshifted with respect to the rest frame wavelength. This phenomenon is known as Cosmological Redshift. The redshift value is a function of v (for $z \ll 1$ it is $cz \simeq v$), so Equation 1.1 can be used to associate a value of d to any redshift value measured through spectrum analysis. It must be stressed that Equation 1.1 is strictly valid only to a first approximation, because the motions of galaxies are not purely recessional, but are influenced by the gravitational pull of the surrounding galaxies.

1.2 The Cosmological Principle

Hubble's Law implies that the Universe is not stationary, but it expands. This means that H_0 can be interpreted as the expansion rate of the Universe, measured at the present epoch. The fact that the Universe is expanding can be derived from theory, making the some fundamental assumptions which represent the main hypothesis of the Concordance Model. First, one should assume the Theory of General Relativity (GR) to be the correct theory of gravitation. This is an important choice because gravity is the most relevant interaction on large scales. The second fundamental assumption is the Cosmological Principle which states that the Universe is homogeneous and isotropic when observed on sufficiently large scales or at sufficiently primordial times. Indeed this seems to be a good assumption at the present epoch, on scales greater than ~ 100 Mpc (1 Mpc $= 3.086 \times 10^{24}$ cm). The Cosmological Principle is in good agreement with the observed homogeneity and isotropy of the distribution of galaxies and radio sources, and with the isotropy of the Cosmic Microwave Background (CMB), a microwave band radiation field whose intensity is nearly constant across the sky.

In GR space-time is considered as a 4-dimensional manifold with an intrinsic curvature, so, in general, its geometry is non-Euclidean. Every point of space-time is called event and it is possible to define a space-time inter-

val between two events that is the generalization of the notion of distance in a 4-dimensional manifold. The Cosmological Principle implies that the infinitesimal space-time interval between two events can be calculated using the Friedmann-Robertson-Walker metric (FRW):

$$ds^2 = c^2dt^2 - a(t)^2 \left\{ \frac{dx^2}{1-kx^2} + x^2(d\theta^2 + sin^2\theta d\phi^2) \right\}. \tag{1.3}$$

$$\vec{r} = a(t)\vec{x}. \tag{1.4}$$

The quantity ds is the infinitesimal space-time interval between the considered events, c is the speed of light and t is the time coordinate (under our hypothesis we can define the same time in every point of space); $\vec{r}$ represents the physical spatial coordinates of each event and it is expressed as the product between the time-independent comoving spatial coordinates $\vec{x}$ and the dimensionless, time-dependent scale factor $a(t)$; with this assumption we allow the physical spatial coordinates to vary with time; it is customary to normalize the scale factor at the present epoch t_0, $a_0 = a(t_0) = 1$. The quantities θ and ϕ are the usual spherical angular coordinates. The quantity $k = \{-1, 0, +1\}$ is the curvature parameter and it represents the intrinsic curvature of space-time. From Equation 1.3 one sees that depending on k, space-time has a different metrical structure. If $k = +1$ the curvature is positive and the geometry of space-time is elliptical (non-Euclidean); if $k = 0$ the geometry of space-time is pseudo-Euclidean; if $k = -1$ the geometry of space-time is hyperbolic (non-Euclidean).

The redshift z of a photon emitted by a source which is moving away from us with recessional velocity $\vec{v}$ is a function of the scale factor, so it is also a function of time, in fact:

$$1 + z = \frac{a_0}{a(t)}. \tag{1.5}$$

Here t is the time associated to the photon emission. For a given cosmological model it is possible to calculate the relations $z(t)$ and $t(z)$. These two relations depend on the chosen cosmological model, with primordial times generally associated to high redshifts, while closer times are associated to low redshifts.

1.3 Friedmann's Equations

If one assumes FRW to describe the space-time metric on large scales, and the energy-momentum density in the Universe to be homogeneous, isotropic

and well described by a perfect fluid model, using Einstein's field equations, one obtains Friedmann's Equations which describe the evolution of the scale factor:

$$\left[\frac{\dot{a}(t)}{a(t)}\right]^2 = H(t)^2 = \frac{8\pi G}{3}\left[\sum_i \rho_i(t)\right] - \frac{kc^2}{a(t)^2}. \tag{1.6}$$

$$\left[\frac{\ddot{a}(t)}{a(t)}\right] = -\frac{4\pi G}{3}\left[\sum_i \rho_i(t) + 3\frac{p_i(t)}{c^2}\right]. \tag{1.7}$$

$H(t)$ is the Hubble parameter at time t, and it is defined so that its value at the present epoch t_0 is $H(t_0) = H_0$. The quantity $\rho_i(t)$ is the energy density of the i-th component of the Universe which contributes to its total energy density (matter, photons, neutrinos...) and $p_i(t)$ is its pressure. Equation 1.6 implies that $H(t)$ evolves with time depending on the contributions to the density and pressure of each component, and on the intrinsic curvature. This means that the whole space-time is able to expand (or to contract) due to its own gravity, generating the observed recessional motions of the galaxies.

According to GR, the fact that space-time is expanding implies that, in the past, there has been an epoch in which the whole Universe collapsed to a singularity. This epoch is placed at the origin of the time-axis ($t = 0$), so that t_0 corresponds to the age of the Universe. The global expansion following the initial singularity is commonly known as Big Bang. The validity of GR is not guaranteed for times $t < t_p$, where $t_p = \sqrt{\hbar G/c^5} \sim 10^{-43}$ s is the Planck time, because before t_p quantum effects may modify the physical laws that describe gravitational interactions. Since a quantum theory of gravitation able to describe the Universe at $t < t_p$ has not been developed yet, it is not clear whether the Big Bang singularity is inevitable or not. However, for times $t \gg t_p$ the quantum effects are negligible and GR is a valid theory. An important result that follows from Friedmann's Equations is the fact that at early epochs a $k = \pm 1$ Universe behaves like a $k = 0$ Universe, i.e. curvature effects are negligible.

While Equation 1.6 shows that the Universe is able to expand or contract, Equation 1.7 shows that the expansion (or contraction) may be either accelerated or decelerated, depending on the energy density ρ_i and pressure p_i of the components of Universe. This means that it is very important to understand, at any epoch, which component provides the dominant contribution to pressure and density.

Friedmann's Equations 1.6 and 1.7 are usually expressed in terms of many cosmological parameters which characterize the cosmological model: the density parameter Ω_{0i} and the Zel'dovich parameter w_i of the i-th component. In the next three Subections I define these important quantities and then I

use them to recast Friedmann's Equations.

1.3.1 The Zel'dovich parameter

The Zel'dovich parameter of the i-th component is defined as the quantity w_i such that its equation of state may be written as:

$$p_i = w_i \rho_i c^2. \tag{1.8}$$

In other words w_i is a macroscopic parameter used to account for the microphysics of the considered component. It is easy to verify that the Zel'dovich parameter of a fluid is proportional to the speed of sound inside the considered fluid, $c_s = \sqrt{\partial p_i / \partial \rho_i}$. The appropriate value for collisionless fluids is $w_i = 0$; for relativistic fluids like photons and neutrinos $w_i = 1/3$; finally, if considered as a fluid, the Cosmological Constant (see Section 1.4) has $w_i = -1$ (in this case no speed of sound is related to w_i). Taking into account the continuity equation for the i-th component:

$$\dot{\rho}_i c^2 + 3H(\rho_i c^2 + p_i) = 0, \tag{1.9}$$

one obtains the evolution of its energy density:

$$\rho_i(t) = \rho_{0i} a(t)^{-3[1+w_i]}. \tag{1.10}$$

The quantity $\rho_{0i} = \rho_i(t_0)$ is the present-time energy density. Depending on w_i, density will grow, be constant or decrease with time. If two different components have different w_i, then there can be an epoch when their energy densities are equal; this is called an equivalence epoch.

1.3.2 The density parameter

The density parameter of the i-th component, Ω_{0i}, is defined as the ratio between its present time energy density $\rho_{0i} = \rho_i(t_0)$ and the critical density ρ_{0c}:

$$\Omega_{0i} = \frac{\rho_{0i}}{\rho_{0c}}, \tag{1.11}$$

where the latter is defined as:

$$\rho_{0c} = \frac{3H_0^2}{8\pi G}, \tag{1.12}$$

and represents the density required to have a flat space-time. The present time total density parameter is the sum of the density parameters of each

component[1]:

$$\Omega = \sum_i \Omega_i. \tag{1.13}$$

The total density parameter and the density parameters of each component of the Universe are very important, because, together with H_0 and w_i, they uniquely determine the evolution of the scale factor $a(t)$, and the geometrical characteristics of the Universe.

1.3.3 The Expansion History of the Universe

In this Section, I show how Friedmann's Equations are expressed in terms of the parameters I just defined, then I discuss the cosmological implications of different values of Ω. The dependence of $a(t)$ from the cosmological parameters is easily obtained from Friedmann's Equations.

After some algebra from Equations 1.6 and 1.7 one obtains the so-called expansion history of the Universe:

$$H(t)^2 = H_0^2 \left\{ \left[\sum_i \Omega_i a(t)^{-3(1+w_i)} \right] - \frac{kc^2}{H_0^2 a(t)^2} \right\}, \tag{1.14}$$

and the evolution of its acceleration:

$$\left[\frac{\ddot{a}(t)}{a(t)} \right] = -\frac{H_0^2}{2} \left[\sum_i \Omega_i \left(1 + 3w_i\right) a(t)^{-3[1+w_i]} \right]. \tag{1.15}$$

From the analysis of Friedmann's Equations at $t = t_0$ one can find an important relation between Ω and the space-time curvature. It is easy to find that:

- $\Omega > 1$ implies $k = +1$, the Universe has an elliptical geometry (closed Universe).
- $\Omega = 1$ implies $k = 0$, the Universe has a pseudo-Euclidean geometry (flat Universe).
- $\Omega < 1$ implies $k = -1$, the Universe has an hyperbolic geometry (open Universe).

Moreover the sign of the quantity $(1 - \Omega)$ is a time-invariant, so that once the geometry is fixed, it cannot vary with time.

These results show that once H_0, the density parameters and the equations of state of the components are correctly determined, then the cosmological model is completely characterized and it can describe the overall properties of the Universe at any epoch after the Planck time.

[1]From here on I will drop the subscript 0 in the density parameters.

1.4 Observational constraints on Cosmology

An accurate measure of H_0 and of the Ω parameters of the different components is a very important goal for Cosmology, because it allows us to define the overall characteristics of space-time and of the Universe on large scales. Several efforts have been made to constrain these fundamental parameters, leading to the modern scenario, but the most important information probably comes from the following discoveries: the Cosmic Microwave Background Anisotropies, the existence of non-luminous matter, and the Cosmic Acceleration.

Cosmic Microwave Background Anisotropies are small fluctuations of the temperature of the CMB across the sky, i.e. small fluctuations of the energy density of electro-magnetic radiation (considered as a cosmological fluid) at the epoch of decoupling (see Section 1.6). From an accurate analysis of the angular correlation signal of these fluctuations it is possible to gain information about many cosmological parameters, including H_0 and Ω. The analysis conducted on the data taken from the Wilkinson Microwave Anisotropy Probe (WMAP), the Atacama Cosmology Telescope (ACT) and the South Pole Telescope (SPT), combined with observational constraints provided by distance measurements from Type Ia Supernovae and Baryon Acoustic Oscillations measurements (Hinshaw et al., 2012), allowed the accurate estimate of many cosmological parameters like the Hubble parameter $H_0 = 69.33 \pm 0.88$ Km s^{-1} Mpc^{-1}[2]. The curvature parameter is $\Omega_k = 1 - \Omega = -0.0027^{+0.0039}_{-0.0038}$, a value that provides strong support to a cosmological scenario with flat space-time. Moreover, measurements of the CMB temperature T_{CMB} allow estimates of the density parameter of photons, which turns out to be very small, $\Omega_\gamma = 2.469 \times 10^{-5} h^{-2}$ for $T_{CMB} = 2.725$ K.

Many observations of the dynamical properties of astrophysical objects like galaxies, galaxy groups and galaxy clusters provided other constraints on the density parameter of matter. Observations like the rotational velocities of spiral galaxies or velocity dispersion of galaxies within clusters suggest that the largest fraction of the mass in these structures is not luminous, i.e. it is not detectable with the usual techniques used in Astronomy. This mass component, dark matter (DM), does not show any sign of interaction with electro-magnetic radiation. DM manifests its existence only through its gravitational interaction with the surrounding luminous matter and with electro-magnetic radiation; for example, the presence of DM in galaxies influences the dynamics of stars, while DM in galaxy clusters deflect

[2] I will often use the dimensionless parameter $h = H_0/(100$ Km s^{-1} Mpc$^{-1})$ instead of H_0.

the light emitted by distant galaxies, generating the phenomenon known as gravitational lensing. None of the particles in the Standard Model of particle physics has such a small cross-section with electro-magnetic radiation, apart from neutrinos that, however, cannot be DM particles because of their relativistic nature. Therefore, the nature of DM is still unknown. Since the DM density is ~ 6 times than that of the ordinary matter, DM plays a crucial role in the formation and evolution of cosmic structures. Moreover, the structure formation scenario depends on the properties of DM particles. In particular, the observed large scale distribution of galaxies can be accounted for only if DM particles were non-relativistic at the epoch in which they decoupled from radiation, that is DM is cold. The Cold Dark Matter (CDM) model is now the reference scenario for structure formation in the Universe. Several studies suggest that matter, dark as well as luminous, may represent a large part of the cosmological energy density. The analysis by Hinshaw et al. (2012) shows that DM is the dominant component with a density parameter $\Omega_{DM} = 0.2408^{+0.0093}_{-0.0092}$, while the ordinary baryonic matter has $\Omega_b = 0.0472 \pm 0.0010$. However, the measured Ω_{DM} value is still not sufficient to account for the whole cosmological energy density ($\Omega = 1 > \Omega_m$), implying that its largest part ($\simeq 70\%$) must be represented by another unknown component.

At the end of the 1990s, observations of distant type Ia Supernovae (Riess et al., 1998) suggested that the current expansion of the Universe is accelerated. This phenomenon is known as Cosmic Acceleration. An accelerated expansion of the Universe may have different explanations depending on the adopted theory of gravitation; in the context of GR, Cosmic Acceleration can be explained introducing a Cosmological Constant Λ in Einstein's field equations, an extra term introduced by Einstein to obtain a static Universe. The Cosmological Constant may be interpreted as a contribution to the cosmic energy-momentum density, i.e. a cosmological fluid that manifests itself only on cosmological scales. In such a model the main feature of Λ is the fact that it contrasts gravity, behaving like a fluid with negative pressure. A Cosmological Constant has an equation of state $p_\Lambda = -\rho_\Lambda c^2$ (Zel'dovich parameter $w_\Lambda = -1$), with energy density constant with time. Cosmic Acceleration can also be produced by advocating other fluids with negative pressure and Zel'dovich parameter $w_{DE} < -1/3$: Dark Energy. The present theories of fundamental Physics are not able to explain the existence of such a fluid, moreover, there are several alternative theories of gravitation which try to explain Cosmic Acceleration without introducing the unknown Dark Energy component. However, GR has been verified in very different astrophysical situations (black holes, neutron stars, binary pulsars, gravitational lensing...) and will be considered as the reference theoretical framework of this Thesis.

1.5 Parameters of the Concordance Cosmological Model

The definition of the parameters defining the Concordance Cosmological Model is a thorny matter. As I discussed in the previous Section, there are still many open problems, the most important being the unknown nature of DM and Dark Energy. The problem of Dark Energy is of cardinal importance, because it directly questions the validity of the adopted theory of gravitation. Since there exist many alternative cosmological theories, it is important to understand why a model dominated by DM and a Cosmological Constant is considered as "standard".

The model has been developed in the context of GR, and it is the simplest model able to reproduce the observational data: a flat Universe with $\Omega = 1$, dominated by a Cosmological Constant Λ and by CDM particles (ΛCDM model). The fundamental parameters provided by observational constraints from CMB, Type Ia Supernovae and large scale galaxy distributions (Hinshaw et al., 2012) are:

- $\Omega_\Lambda = 0.712 \pm 0.010$ for the Cosmological Constant.
- $\Omega_{DM} = 0.2408^{+0.0093}_{-0.0092}$ for CDM.
- $\Omega_b = 0.0472 \pm 0.0010$ for baryonic matter.

The energy contribution from other particles is cosmologically negligible. Besides, the Zel'dovich parameters of these fluids are:

- $w_\Lambda = -1$ for the Cosmological Constant.
- $w_{DM} = 0$ for CDM.
- $w_b = 0$ for baryonic matter.

The Hubble parameter is fixed to the observed value $h = 0.6933 \pm 0.0088$. As I discussed in the previous Sections, these parameters are sufficient to completely define the expansion history of the Universe. The age of the Universe estimated through this model is $t_0 \approx 13.7$ Gyr, a value in agreement with the age of the oldest globular clusters (with an age of $\sim 12 - 13$ Gyr).

This model correctly describes the evolution of global properties like the abundance of light nuclei in the context of the cosmological Nucleosynthesis (see Section 1.6), but it cannot directly account for the build up of the cosmic structures and for the anisotropies in the CMB, since the Cosmological Principle is assumed.

1.6 A short history of the Universe

The aim of this Section is to provide a quick overview of the evolution of the Universe after Planck time ($t_p \sim 10^{-43}$ s), without focussing on the details.

1.6.1 Thermal evolution of cosmological fluids

The characterization of the thermal evolution of the cosmological fluids at any epoch is extremely important to describe the global features of the Universe, especially at early epochs. The evolution of the temperature of a cosmological fluid thermally independent from other components, i.e. decoupled, can be predicted considering that the overall expansion is an adiabatic process. Under such circumstances the continuity equation is valid:

$$\dot{\rho}c^2 + 3H(\rho c^2 + p), \tag{1.16}$$

where ρ is the density of the cosmological fluid, p is its pressure and H is Hubble's constant. The thermal history, $T(t)$ of cosmologically-relevant fluids like baryons and photons can be obtained from their equation of state and continuity equation.

If one assumes a fluid of non-relativistic baryons to be well described by an ideal gas equation of state, the energy contributions in Equation 1.16 come from the rest energy density $\rho_b c^2$, and from the kinetic energy $\frac{3}{2} n_b k_b T_b$, where n_b is the particle number density and T_b is the temperature of the fluid. The evolution of T_b is given by:

$$T_b \propto a^{-2} \propto (1+z)^2. \tag{1.17}$$

This means that T_b is expected to decrease together with ρ_b (Equation 1.10) during the expansion.

For a fluid of photons the Stefan-Boltzmann law holds: $\rho_\gamma c^2 = \sigma T^4$. If this relation is used together with the continuity equation, one obtains the evolution of the temperature T_γ of the photons:

$$T_\gamma \propto a^{-1} \propto (1+z). \tag{1.18}$$

T_γ is expected to decrease more slowly than T_b. Both Equations 1.17 and 1.18 hold in the present-time Universe where photons are decoupled from baryons and the two components evolve independently. However, a thermal evolution similar to the one of Equation 1.18 is found for the temperature of the photon-baryon plasma which dominates the Universe at early times, i.e. the temperature of the photon-baryon plasma evolves like that of the dominant

component alone: the photons. The Concordance Cosmological scenario is characterized by high temperatures at times close to the Big Bang singularity which decrease with time depending on the physics of the components of the Universe.

1.6.2 Primordial Universe and Inflation

Before the Planck time the Universe has peculiar features, since quantum effects may be important on the scale of the gravitational interactions. After Planck time these quantum effects can be neglected, and gravitation can be considered as independent from the other interactions (strong, weak and electro-magnetic). In this scenario, the primordial Universe is extremely homogeneous and isotropic and the main contribution to the energy density is due to photons and relativistic particle-anti-particle pairs, produced through quantum processes; in this primordial Universe the temperature is $kT \gtrsim 10^{15}$ Gev, so high that none of the known hadrons can form, meaning that we can only find photons, free quarks, gluons and leptons. Many fundamental Physics theories predict that at $t \sim 10^{-35}$ s the strong, weak and electro-magnetic interactions can be unified into a unique interaction. It is thought that some symmetry break in the physical laws of the primordial Universe may have created the three interaction we observe today, together with the disappearance of nearly all the anti-matter of the Universe during the baryogenesis, the process responsible for the formation of baryons.

The Primordial Universe should have gone through a short Inflationary Epoch in which the expansion of the Universe was accelerated and the scale factor increased exponentially. An Inflationary period has been advocated in the context of the Concordance Model to solve some apparent paradoxes: the flatness of the Universe at the present epoch, the isotropy of the CMB and the monopole abundance. In addition, the Inflationary Epoch is expected to produce the seeds for structure formation: microscopic quantum fluctuations are suddenly expanded to cosmological scales. Unfortunately, it is still not clear what physical process may have caused Inflation, even if there are many promising ideas.

1.6.3 From free quarks to atomic nuclei

After $t \sim 10^{-6}$ s, the temperature decreases down to $kT \sim 1$ Gev, due to the overall expansion, so that the quarks can aggregate to form hadrons (quark-hadron transition). Later, at $t \sim 10^{-2}$ s, when the temperature is $kT \sim 10$ Mev, the primordial plasma reaches physical conditions sufficient to trigger the first nuclear fusions between nucleons. This is the process known

as Big Bang Nucleosynthesis (BBN), which is responsible for the creation of ^{2}H, ^{3}He, ^{4}He and ^{7}Li nuclei starting from ^{1}H nuclei (protons) and neutrons. BBN is inefficient with respect to the nucleosynthesis in stars, due to the high number of photons-per-baryon and due to the fast temperature decrease of the Universe. For these reasons BBN is forced to stop at $t \sim 3$ mins, when $kT \leq 1$ Mev, before it can create nuclei heavier than ^{7}Li. BBN theory predicts the following mass fractions X:

- $X \sim 0.75$ for ^{1}H.
- $X \sim 10^{-5}$ for ^{2}H and ^{3}He.
- $X \sim 0.25$ for ^{4}He.
- $X \sim 10^{-10}$ for ^{7}Li.

BBN theory is considered as one of the greatest successes of the Big Bang scenario, since its predicted chemical abundances are in remarkable agreement with the ones observed in the Intergalactic Medium, the hydrogen rich gas which fills the empty spaces between galaxies. This fact is generally considered as one of the most important evidences of the validity of the Big Bang theory.

1.6.4 Plasma Era and Matter Era

After $t \sim$ s, a few 10^{-1} s after the beginning of BBN, the Universe is radiation dominated. More precisely the energy density is dominated by a photon-baryon plasma: photons and baryons are coupled through Thomson scattering, so that they can be considered as the constituents of a unique fluid. This epoch is usually called Plasma Era. The fact that photons continuously interact with baryons means that the Universe is optically thick. Early in this era, DM, which represent an independent fluid, decouples from the photon-baryon plasma. Since the densities of the photon-baryon plasma and of DM evolve differently with time (remind Equation 1.10), there will be an equivalence epoch between the DM and the plasma, when their densities will be equal. The redshift of the equivalence epoch is given by:

$$1 + z_{eq} \simeq 10^5 \Omega_{DM} h^2 \tag{1.19}$$

After the equivalence, DM becomes the dominant component, starting to govern the overall expansion of the Universe. This is the beginning of the Matter Era. During the expansion, the temperature and density of the photon-baryon plasma keep decreasing, until the physical conditions allow

the recombination of atomic nuclei and electrons, a process which leads to the formation of neutral atoms. During the transition, the interaction rate between baryons and photons slows down and becomes slower than the expansion-rate of the Universe at decoupling (redshift $z_{d,b\gamma} \sim 1100$, time $t_{d,b\gamma} \sim 10^5$ yr). After decoupling baryons and photons evolve separately: baryons will later constitute the luminous cosmic structures, photons will cool down to temperatures $T \sim 2.7$ K, becoming the observed CMB. From the decoupling age onwards the Universe becomes optically thin, allowing photons to travel long distances, without interacting with baryonic matter.

1.6.5 Formation and evolution of the structures

After decoupling the Universe has an age of only few 10^5 yr. The recombination process allows the Universe to become globally neutral. These epochs are usually called dark ages, since no luminous object has been formed yet and the only photons, belonging to the CMB, are being redshifted out of the optical band.

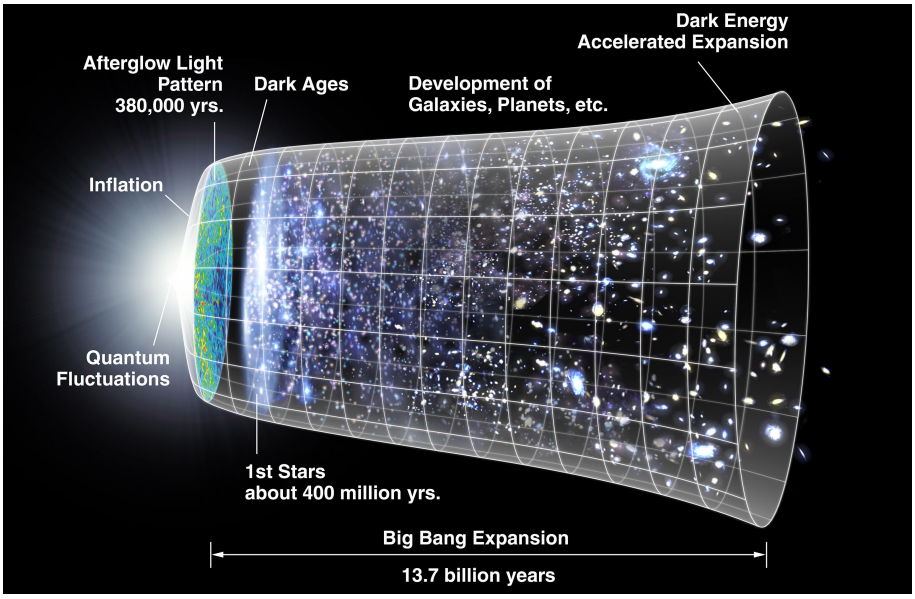

Figure 1.1: A representation of the formation and evolution of cosmic structures. All credits for this picture go to the NASA/WMAP team.

Fig. 1.1 is a representation of the formation and evolution of cosmic structures. The huge time interval between the end of the dark ages and the present time $t_0 \sim 13.7$ Gyr is spent forming the cosmic structures we

observe: free from the interactions with photons, baryons can fall into regions characterized by deep gravitational potential wells, previously formed by the DM. In these conditions, baryons start forming the firts stars. This stellar population is usually called Pop III, and it is thought to be constituted by massive (up to 100 $M_\odot$) and luminous O-B-like stars. Such stars are able to produce intense UV fluxes for relatively long times, even if their life is shorter than Pop II and Pop I stars. Pop III stars end their life forming black holes.

Astrophysical processes are usually considered as the main causes of the global reionization of the Universe: baryonic matter in every region of the observed Universe appears nearly completely ionized. The radiation emitted by Pop III stars and quasars may have ionized large regions of the Universe, explaining the small fraction of neutral hydrogen that survives in clouds. Its presence generates weak absorption lines in the spectra of distant and bright sources, like quasars, which constitute the so-called Ly-α forest. The redshift of the reionization epoch is thought to be $z \gtrsim 6$.

The ages following the reionization are characterized by the formation and hierarchical bottom-up evolution of the cosmic structures. In this scenario small structures form first and subsequently merge into larger objects in a hierarchical fashion. These structures form virialized objects, called Dark Matter Halos, in which a fraction of the available baryons falls and forms stars and galaxies (e.g. White & Rees (1978)).

1.6.6 Cosmic Acceleration and the Cosmological Constant

During the early stages of the evolution of the Universe, the Cosmological Constant provides a negligible contribution in Friedmann's Equations, however, since its energy density is constant, its contribution to the cosmic energy density increases with time and becomes dominant at $z \sim 1$, leading to the accelerate expansion of the Universe that we observe today. The Concordance Model predicts that such accelerated expansion will last forever.

1.7 Matter and Large Scale Structure of the Universe

Matter is the main constituent of the cosmic structures which populate the observed Universe. At the same time, according to the Concordance Cosmological Model, matter is one of the dominant components of the Universe, influencing the dynamics of its overall expansion. In the Concordance Cos-

mological Model the Universe is assumed to obey the Cosmological Principle. Obviously this assumption cannot be strictly correct, since the existence of stars and galaxies is itself a violation of the Cosmological Principle. Besides, a large number of inhomogeneities and anisotropies is detected in the spatial distribution of the astrophysical sources, especially on spatial scales $\ll 100$ Mpc. It is only on large scales ($\gg 100$ Mpc) that the Universe appears, to a first approximation, homogeneous and isotropic. Scientists developed a robust theoretical framework able to explain the way in which a primordial homogeneous and isotropic Universe is able to evolve and give birth to the observed structures. Theory is able to describe in a relatively simple way the formation of large scale DM structures which are thought to influence the formation of visible baryonic structures whose evolution is considerably more difficult to model.

In the first part of this Section, I will discuss the main theoretical aspects of the formation and evolution of DM structures in a standard ΛCDM Universe. In the second part I will describe the advantages of using numerical techniques to study the evolution of DM structures, then I will illustrate their main features. Hockney & Eastwood (1988), Plionis (2002) and Peacock (2003) can be considered as general reference for most of the subjects discussed in this Section.

1.7.1 Cosmological Perturbations

All the observed structures represent a deviation from the average density of the Universe, so it is natural to assume that they originated from the growth of little perturbations in the primordial, homogeneous and isotropic density field. From an observational viewpoint, the existence of such density perturbations is confirmed by the small fluctuations observed in the temperature of the CMB which has been emitted after decoupling, when the Universe was considerably younger. The hypothesis is that the little density perturbations form as quantum energy fluctuations before the Inflationary Epoch are amplified to cosmological scales by the Inflation and then evolve with time, increasing or decreasing their amplitude.

Let us first introduce the basic formalism to describe and characterize Cosmological Perturbations. Let V_u be a finite volume containing a continuous distribution of matter, with average density $\langle\rho\rangle$. The volume V_u must be large, so that it can be considered as a fair sample of the Universe, i.e. density fluctuations in the volume must be representative of the cosmic mean; a possible choice of V_u is a cube of side L, with $L \gg l_s$, where l_s is the maximum spatial scale at which there is significant structure due to perturbations. It is possible to construct a realisation of the Universe by dividing

it into independent cubic cells of volume V_u, with periodic boundary conditions at the face of each cube. This would be a poor choice, however, as the evolution would couple perturbations into nearby volumes. Instead one considers a cubic cell encompassed in the Hubble radius[3] and advocates the Ergodic Theorem to assume that the realization of the density field in that volume is representative of the cosmic mean.

In each point $\vec{x}$ contained in V_u we can define the density contrast $\delta(\vec{x})$ as:

$$\delta(\vec{x}) = \frac{\rho(\vec{x}) - \langle\rho\rangle}{\langle\rho\rangle}, \tag{1.20}$$

where $\rho(\vec{x})$ is the density in $\vec{x}$. The quantity $\delta(\vec{x})$ measures the deviation of $\rho(\vec{x})$ from the average value $\langle\rho\rangle$. If $\delta(\vec{x}) \ll 1$, then it is possible to express the density contrast in $\vec{x}$ as a superimposition of plane waves which evolve independently from the other ones. This means that it is possible to express $\delta(\vec{x})$ through the Fourier expansion:

$$\delta(\vec{x}) = \sum_{\vec{k}} \delta_{\vec{k}} e^{i\vec{k}\cdot\vec{x}}, \tag{1.21}$$

$$\delta_{\vec{k}} = \frac{1}{V_u} \int_{V_u} \delta(\vec{x}) e^{-i\vec{k}\cdot\vec{x}} d\vec{x}, \tag{1.22}$$

where $\delta_{\vec{k}}$ is the coefficient associated to the Fourier mode with wave vector $\vec{k}$. The amplitude of each wave vector is $k \propto 1/\lambda$, where λ is the comoving size of the region containing the considered mode of the perturbation.

In each fair sample of the Universe it is possible to perform a Fourier expansion of the density contrast. The resulting sets of $\delta_{\vec{k}}$ coefficients will have different amplitudes and phases. If we consider a huge number of realisations and assume that the phases of the different coefficients are random, which is the typical situation when fluctuations are small ($\delta \ll 1$) and each mode evolves independently, then we find that the density contrast is a stochastic variable with Gaussian statistics and average $\langle\delta\rangle = 0$. In other words the probability of finding a density contrast value between δ and $\delta + d\delta$ in a considered point of the volume V_u is:

$$p(\delta)d\delta = \frac{1}{\sqrt{2\pi\sigma^2}} \exp\left\{-\frac{\delta^2}{2\sigma^2}\right\} d\delta, \tag{1.23}$$

where $p(\delta)$ is the Probability Density Function (PDF) of the stochastic variable δ. Note that the density field is expected to have Gaussian statistic only

[3]The Hubble radius is the radius of the sphere containing all the points of space which are receding from the observer with velocity $v < c$, due to the overall expansion of the Universe.

as long as $\delta \ll 1$. The quantity σ^2 is the variance of the density contrast:

$$\langle \sigma^2 \rangle \equiv \sum_{\vec{k}} \langle |\delta_{\vec{k}}|^2 \rangle = \frac{1}{V_u} \sum_{k} \langle \delta_k^2 \rangle, \tag{1.24}$$

where all the averages are taken over an ensemble of different realisations of the Universe. The variance σ^2 represents the mean square amplitude of Cosmological Perturbations and it is the only free parameter in the Gaussian $p(\delta)$. The quantity $\langle |\delta_{\vec{k}}|^2 \rangle$ represents the contribution to the variance from the Fourier mode with wave vector $\vec{k}$, while $\langle \delta_k^2 \rangle$ is the contribution to σ^2 from Fourier modes with $|\vec{k}| = k$.

If we consider the quantities $\delta(\vec{x})$, $\delta_{\vec{k}}$, σ^2 in the limit $V_u \to +\infty$, we can express them in the following simplified forms:

$$\delta(\vec{x}) = \frac{1}{(2\pi)^3} \int_{\Re^3} \delta_{\vec{k}} e^{i\vec{k}\cdot\vec{x}} d\vec{k}, \tag{1.25}$$

$$\delta_{\vec{k}} = \int_{\Re^3} \delta(\vec{x}) e^{-i\vec{k}\cdot\vec{x}} d\vec{x}, \tag{1.26}$$

$$\sigma^2 = \frac{1}{2\pi^2} \int_0^{+\infty} P(k) k^2 dk. \tag{1.27}$$

The function $P(k) = \langle \delta_k^2 \rangle$ is called Power Spectrum and it is an extremely important quantity, since it can be used to describe the statistical features of the primordial density perturbations and of the Large Scale Structure of the Universe, as long as each k-mode evolves independently from each other. Moreover, it can be estimated from the spatial distribution of the objects that trace the cosmic density field, providing a wealth of cosmological information.

Another useful and closely related quantity for cosmological purposes is the Two-Point Spatial Correlation Function $\xi(\vec{r})$, which is defined by:

$$\xi(\vec{r}) = \langle \delta(\vec{x}) \delta(\vec{x} + \vec{r}) \rangle, \tag{1.28}$$

where $\vec{x}$ is an arbitrary point of the considered realisation of the Universe, and $\vec{r}$ is the spatial separation between $\vec{x}$ and $\vec{x}+\vec{r}$; $\langle ... \rangle$ represents the average over a statistical ensemble. From Equation 1.28 it is clear that $\xi(\vec{r})$ represents the spatial auto-correlation of the δ-field on the scale r. Note that σ^2 is just the Two-Point Spatial Correlation Function at zero-lag: $\sigma^2 = \xi(r = 0)$.

A general result, known as Wiener-Khintchine Theorem, demonstrates that $\xi(\vec{r})$ is the Fourier transform of $P(k)$:

$$\xi(\vec{r}) = \sum_{\vec{k}} \langle |\delta_{\vec{k}}^2| \rangle e^{-i\vec{k}\cdot\vec{r}}, \tag{1.29}$$

$$\xi(\vec{r}) = \frac{1}{(2\pi)^3}\int_{\Re^3} P(k)e^{-i\vec{k}\cdot\vec{r}}d\vec{k},\ \text{if } V_u \to +\infty. \tag{1.30}$$

Obviously both these relations can be inverted, giving:

$$\langle|\delta^2_{\vec{k}}|\rangle = \frac{1}{V_u}\int_{V_u} \xi(\vec{r})e^{i\vec{k}\cdot\vec{r}}d\vec{r}, \tag{1.31}$$

$$P(k) = \int_{\Re^3} \xi(\vec{r})e^{i\vec{k}\cdot\vec{r}}d\vec{r},\ \text{if } V_u \to +\infty. \tag{1.32}$$

All the quantities defined in this Section are used to characterize the continuous DM density field and can be used as cosmological tools.

1.7.2 Smoothed density contrast

The variance of the density contrast σ^2 is an important cosmological quantity since it represents the mean square amplitude of the density perturbations. However, the definition of Equation 1.27 is not always useful since it does not give information on the contributions of the different Fourier modes to the whole density field. A more useful quantity is the density contrast smoothed on a given spatial scale R. A smoothed continuous density field $\delta(\vec{x}, R)$ is defined as the convolution of the unsmoothed density contrast $\delta(\vec{x})$ with a filter function $F(|\vec{x}|, R)$:

$$\delta(\vec{x}, R) = \int_{\Re^3} \delta(\vec{y})F(|\vec{x} - \vec{y}|, R)d\vec{y}. \tag{1.33}$$

The filter function is chosen to select the physical information contained in spheres of radius R:

$$F(|\vec{x}|, R) \sim \begin{cases} R^{-3} & |\vec{x}| \ll R \\ 0 & |\vec{x}| \gg R \end{cases}, \tag{1.34}$$

$$\int_{\Re^3} F(|\vec{x}|, R)d\vec{x} = 1. \tag{1.35}$$

The variance of the smoothed density contrast σ^2_R is, then:

$$\sigma^2_R = \frac{1}{2\pi^2}\int_0^{+\infty} P(k)W^2(kR)k^2dk, \tag{1.36}$$

where $W(kR)$ is the Fourier transform of $F(|\vec{x}|, R)$ and it is often called window function, because it only selects contributions to σ^2_R from Fourier modes with $k \lesssim k_F \sim 1/R$.

Two standard filters are commonly used for the analysis of Cosmological Perturbations: the Top-Hat filter and the Gaussian filter. The Top-Hat filter selects mass in spherical regions of radius R_{TH} and it is defined by:

$$F_{TH}(\vec{x}, R_{TH}) = \frac{3}{4\pi R_{TH}^3}\Theta\left(1 - \frac{|\vec{x}|}{R_{TH}}\right), \tag{1.37}$$

where Θ is the Heaviside step function which introduces a sharp radial cut-off in the convolution of Equation 1.33. If a Top-Hat filter is used, the variance σ_R^2 can be considered as the variance on a characteristic mass scale $M = (4\pi/3)R_{TH}^3\langle\rho\rangle$ contained in a sphere of radius R_{TH}. The Top-Hat window function is:

$$W_{TH}(kR) = \frac{3(\sin kR_{TH} - kR_{TH}\cos kR_{TH})}{(kR_{TH})^3} \tag{1.38}$$

The Gaussian filter selects mass in spherical regions of characteristic radius R_G and it is defined by:

$$F_G(\vec{x}, R_G) = \frac{1}{(2\pi R_G^2)^{3/2}}\exp\left\{-\frac{|\vec{x}|}{2R_G^2}\right\}; \tag{1.39}$$

unlike the Top-Hat filter, this one has not sharp edges, so R_G is not the exact radius of the region from which the filter selects mass, but can be thought as a typical spatial scale. The mass contained in a volume of radius R_{TH} is equal to the mass contained in a Gaussian sphere of radius $R_G = 0.64R_{TH}$. Finally, the Gaussian window function is:

$$W_G(\vec{x}, R_G) = \exp\left\{-\frac{(kR_G)^2}{2}\right\}. \tag{1.40}$$

In the following discussion, I will frequently refer to the matter density field which, in all cases, must be considered as smoothed on a characteristic spatial scale R or, equivalently, on a mass scale M. For this reason, I will often drop the subscript "R", and substitute it with "M", when considering the smoothed density contrast $\delta(\vec{x}, R)$ or its variance σ_R^2.

1.7.3 Evolution of Cosmological Perturbations

The mechanism which determines the growth of Cosmological Perturbations is gravitational instability, first advocated by Sir Jeans to explain the formation of stars. Let's consider a cosmological fluid whose average density is perturbed by small fluctuations. If a volume of fluid is characterized by an

overdensity δ, then this perturbation will generate gravitational forces which will make the volume contract, increasing the amount of matter contained in the considered region. However, pressure forces between the elements of the fluid are expected to contrast gravitational forces during the contraction, so perturbations will continue their growth only if gravity wins over pressure, causing the development of the gravitational instability. If pressure forces win over gravity, then the gravitational instability cannot develop, and the perturbation is quickly suppressed. This picture must be adapted to DM which, being a collisionless fluid, is not pressure-supported. Indeed for DM a kinetic treatment would be needed and the results show that in this case the velocity dispersion plays the role of the pressure forces.

For simplicity, let's consider a perturbed Flat Matter-Dominated Universe (FMDU) where it is possible, to a first approximation, to ignore the presence of electro-magnetic radiation and of the Cosmological Constant. The evolution of a self-gravitating fluid with density contrast $\delta(\vec{x}, t)$ obeys the continuity, Euler and Poisson equations which, as long as $\delta(\vec{x}, t) \ll 1$, can be linearized. Then, the system of linearized equations can be solved analytically. In this linear regime, each Fourier mode evolves independently and the solution of the system can be expressed as a sum of plane waves in which only the Fourier coefficients evolve with time:

$$\delta(\vec{x}, t) = \sum_{\vec{k}} \delta_{\vec{k}}(t) e^{i\vec{k}\cdot\vec{x}}. \tag{1.41}$$

The evolution of $\delta_{\vec{k}}(t)$ would then obey the following differential equation:

$$\ddot{\delta}_{\vec{k}} + 2H\dot{\delta}_{\vec{k}}(t) + \left(\frac{k^2 c_s^2}{a^2} - 4\pi G\langle\rho\rangle\right)\delta_{\vec{k}} = 0, \tag{1.42}$$

where $H = H(t)$ and $a = a(t)$, c_s is the speed of sound in the fluid, $\langle\rho\rangle$ is the average density of the fluid. Besides, $k = |\vec{k}| = 2\pi/\lambda$ is the wave number.

Before discussing the solutions of Equation 1.42, it is useful to define the comoving Jeans Length λ_J:

$$\lambda_J = \sqrt{\frac{\pi c_s^2}{G\langle\rho\rangle a^2}}. \tag{1.43}$$

Note that for $\lambda = \lambda_J$ the third term on the left side of Equation 1.42 cancels.

The solutions of Equation 1.42 have different temporal evolution, depending on λ:

- $\lambda \ll \lambda_J$ ($c_s^2 k^2/a^2 \gg 4\pi G\langle\rho\rangle$): pressure forces overcome gravitational forces, so the perturbation cannot grow but oscillates as an acoustic wave.

- $\lambda \gg \lambda_J$ ($c_s^2 k^2/a^2 \ll 4\pi G\langle\rho\rangle$): gravitational forces overcome pressure forces and the amplitude of the perturbation can grow with time.

From this qualitative analysis we can conclude that all the perturbations with $\lambda \gg \lambda_J$ are able to grow until they form structures. Actually, the complete solution for $\lambda \gg \lambda_J$ perturbations is composed of two parts: a mode δ_+ which grows with time, a mode δ_- which decreases with time. In a FMDU we have:

$$\delta_+ \propto a(t) \propto t^{2/3} \propto (1+z)^{-1}, \tag{1.44}$$

$$\delta_- \propto a(t)^{-3/2} \propto t^{-1} \propto (1+z)^{3/2}. \tag{1.45}$$

The decreasing mode δ_- is suppressed after a short time, so that the only part of the initial perturbation that will contribute to the formation of structures is the growing mode δ_+.

In general, it is possible to write the linear evolution of $\delta_{\vec{k}}$ as:

$$\delta_{\vec{k}}(t) = \delta_+(t) + \delta_-(t) = \delta_+(t_i)D_+(t) + \delta_-(t_i)D_-(t), \tag{1.46}$$

where t_i is the time at which the perturbation starts its growth; $\delta_+(t_i)$ and $\delta_-(t_i)$ are the amplitudes of the growing and decreasing modes of the perturbation at some initial time t_i, while $D_+(t)$ and $D_-(t)$ account for their evolution.

The evolution of Cosmological Perturbations in the linear regime depends on the cosmological model, i.e. $D_+(t)$ and $D_-(t)$ have different functional behaviours depending on the cosmological parameters. The actual expression can be quite complicated, but analytic approximations exist also for the case with $\Lambda \neq 0$. It is possible to parametrize the linear growth of Cosmological Perturbations through the growth rate of linear matter perturbations f. This parameter measures the deviation of the function $\delta_+(a)$ in the chosen cosmological model from to the same function in a FMDU, and it is defined as:

$$f = \frac{d[\log(\delta_+)]}{d[\log(a)]}. \tag{1.47}$$

The growth rate strongly depends on the matter density parameter Ω_m. Generally, a good approximation for f is given by:

$$f(z) \simeq \Omega_m(z)^\gamma, \tag{1.48}$$

where $\gamma = 0.55$ in the standard Einsteinian Gravity scenario, but can be other values in alternative gravity scenarios.

1.7.4 Evolution of the linear Power Spectrum

The quantum origin of Cosmological Perturbations implies precise constraints of the functional behaviour of their primordial Power Spectrum. It is usual to assume that the primordial Power Spectrum $P_{pr}(k)$, at least in a certain interval in k, is given by a power law:

$$P_{pr}(k) \propto k^n, \tag{1.49}$$

where n is called spectral index. Observational constraints by Hinshaw et al. (2012) provide the value $n = 0.971 \pm 0.010$ for the spectral index of the primordial Power Spectrum.

The growth of density fluctuations will affect the slope and amplitude of the Power Spectrum. In the linear regime, when each Fourier mode evolves independently and with the same law (Equation 1.46), the spectrum does not change its shape but only its amplitude:

$$P(k,t) = D_+^2(t)P(k,t_i), \tag{1.50}$$

where t_i is some initial time. Therefore, in absence of additional effects, the Power Spectrum in the linear regime has the same slope of the primordial spectrum and its observation can place constraints on the mechanisms that have influenced primordial fluctuations, like the Inflation.

However, before decoupling, DM particles were coupled to the photon-baryon plasma, with the result of modifying the growth of the former component on different scales. To understand how the slope of the primordial spectrum of DM density perturbations can change in the period before decoupling, the following scales and effects must be considered:

- Jeans Length: perturbations of size $\lambda < \lambda_J(t)$ cannot grow but oscillate as acoustic waves. All perturbations of scale $\lambda < \lambda_J(t)$ will not contribute to structure formation.

- Free Streaming: since CDM is a collisionless fluid, CDM particles will possess a "broad" velocity distribution, so a large fraction of them will have high velocities. These particles are able to escape from overdense regions, causing the leveling out of the perturbations. This process is called Free Streaming and erases all perturbations with scale λ below the Free Streaming length $\lambda_{FS} \lesssim \lambda_J$, i.e. all oscillating perturbations are cancelled.

- Meszaros Effect: before the equivalence between DM and radiation the Universe is radiation-dominated. During this period DM perturbations

are not allowed to grow, since their characteristic growth rate is smaller than the expansion rate of the Universe; this effect causes stagnation of all perturbations of size $\lambda > \lambda_J$ which, in a matter-dominated Universe, would be allowed to grow. All perturbations in the DM are then frozen until equivalence.

All these phenomena modify the primordial Power Spectrum $P_{pr}(k)$. Their cumulative effect can be accounted for by the transfer function $T(k)$:

$$P_{lin}(k) = T^2(k)P_{pr}(k), \tag{1.51}$$

where $P_{lin}(k)$ is the Power Spectrum in the linear regime modified by all the cited phenomena. In a ΛCDM Universe $T(k)$ has the effect of removing power from high k modes, leaving the low k spectrum almost unchanged.

Perturbations in the baryonic component evolve in a different way. Before they decouple from radiation, these perturbations cannot grow due to viscous forces generated by the Thomson scattering between non-relativistic particles and photons (radiation drag). After decoupling, baryonic perturbations are free to grow. However, their evolution is strongly influenced by the gravitational forces generated by the already formed DM perturbations. As a consequence, part of the baryonic matter starts to fall into regions characterized by deep gravitational potential wells associated to DM fluctuations, and baryonic perturbations end up tracing DM perturbations.

Unlike DM, baryonic matter is collisional and dissipative. As a consequence it will only trace DM to first approximation and on scales large enough for dissipation and cooling/heating processes to be ignored. Additional interactions with electromagnetic-radiation and feedback effects from star formation processes will complicate the situation even further. The net effect is a mismatch between the spatial distribution of the DM and that of the baryons that is generally referred to as bias phenomenon.

1.7.5 Nonlinear evolution of Dark Matter perturbations

When $\delta \sim 1$ the linear approximation breaks down in many aspects. First of all, the Fourier modes do not evolve independently anymore but couple to each other, then the evolution of perturbations cannot be factorized in a time dependent and a space dependent part, reflecting the fact that perturbations are displaced by gradual pull of the surrounding matter. Since we are interested in cosmic structures with $\delta \gg 1$, we need to go beyond linear theory to trace the evolution of $\delta(\vec{x}, t)$ in the nonlinear regime.

There are many approaches to study the nonlinear evolution of Cosmological Perturbations. First of all, one can consider second (or higher) order terms in the perturbed continuity, Euler and Poisson equations. However this approach is mathematically challenging and adds little information to that provided by linear theory. An alternative is the kinematic approach called Zel'dovich Approximation. In this method the cosmological fluid is considered as composed of discrete particles. Be $\vec{q}$ the comoving Lagrangian coordinates of a particle at the reference time $t = 0$. The Zel'dovic Approximation assesses that the Eulerian, physical coordinate of the particle at time t can be expressed as:

$$\vec{r}(t) = a(t)[\vec{q} + b(t)\vec{P}(\vec{q})], \tag{1.52}$$

where $a(t)$ is the scale factor, $b(t)$ is a time dependent quantity which, for $t \to 0$ reduces to the linear growth factor $D_+(t)$; $\vec{P}(\vec{q})$ is a $\vec{q}$-only dependent vector field proportional to the peculiar velocities $\vec{v}_p$ at $t \to 0$. The peculiar velocities are generated by the gravitational forces and represent deviations over the recessional velocities. They are defined as:

$$\vec{v}_p \equiv \frac{d\vec{r}}{dt} - H\vec{r} = a(t)\frac{d\vec{x}}{dt}, \tag{1.53}$$

where $\vec{x}$ is the comoving coordinate of the particle. In other words, the Zel'dovich Approximation assumes that particles always move along straight lines where directions are defined by the vector field $\vec{P}(\vec{q})$, so given an initial displacement $\vec{q}$ and the corresponding peculiar velocities $\vec{v}_p$ (or $\vec{P}(\vec{q})$) we are able to predict the evolution of all the particles. The Zel'dovich approximation is capable of predicting the overall shape of the structures originated by the nonlinear growth of matter perturbations. The expected structures are of three types:

- Filaments: elongated structures which form by the gravitational collapse of a perturbation along two spatial directions and the expansion along the third direction.
- Pancakes: flat structures which form by the gravitational collapse of a perturbation along one spatial direction and the expansion along the other two.
- Voids: low density structures which form by the expansion of a perturbation along all spatial directions.

The Zel'dovich Approximation is valid as long as the trajectories of the particles do not intersect, however this happens when $\delta \to +\infty$, well beyond the linear condition breaks down.

An alternative, completely different way of following the evolution of the perturbations in the nonlinear regime is provided by the Spherical Collapse Model. Contrary to the Zel'dovich Approximation, no assumption is made on the dynamics. Instead an assumption is made on the symmetry of the problem, since the fluctuations are assumed to be spherical. Let's consider a spherical region of the Universe of initial radius R_i characterized by an average overdensity $\bar{\delta}_i$. Because of the spherical symmetry and thanks to Birkhoff's Theorem, the equations of motion of matter inside this region are the same as the ones that describe the evolution of the scale parameter $a(t)$ of the Universe. In other words the evolution of the perturbations is that of an isolated mini-universe with density different from the cosmological mean. All overdense regions with overdensity over a threshold, that depends on the cosmological model, will collapse under the effect of their own gravity. In practice, the only overdense regions that will collapse are those with:

$$\bar{\delta}_i > \frac{1-\Omega}{(1+z_i)\Omega}, \tag{1.54}$$

at some initial time t_i corresponding to redshift z_i. For spherical overdensities above the threshold the following qualitative evolution is expected:

1. Expansion: at the beginning the region expands under the effect of Hubble's flow, however the expansion is slowed down by the gravitational pull of the internal overdensity.

2. Turnover: at a certain time the gravitational pull generated by the internal overdensity causes the expansion to stop. Until turnover the Spherical Collapse Model can describe the growth of the fluctuations analytically.

3. Collapse and virialization: after the turnover the structure starts collapsing. Spherical Collapse Model is not valid anymore. Yet one can work out the collapse time (i.e. the time at which the overdensity collapses to a singularity) and the corresponding linear overdensity $\delta_c^{lin} \sim 1.69$. Collapse will never occur in practice, since dissipative effects will convert kinetic energy into random motions. At a certain time after the beginning of the collapse the system will reach virial equilibrium; the structure will be characterized by an average overdensity $\delta_{vir} \sim 200 - 400$. Isolated, collapsed structures of DM are called Dark Matter Halos.

As we shall see the Spherical Collapse Model is very useful, since it allows one to connect linear theory predictions to the actual evolution of cosmic

structures. For example at the collapse time the Spherical Collapse Model predicts $\delta_c^{SC} \sim 180$, corresponding to a linear overdensity $\delta_c^{lin} \sim 1.69$. This is very convenient to predict the properties of DM Halos, like their Mass Function, as we will see below. Obviously, Spherical Collapse is a simplistic model and has its own limits: real perturbations are not expected to be perfectly spherical, and the approximation breaks down when we have to consider the complex physical processes which lead the structures to virialization.

1.7.6 The Dark Matter Halos Mass Function

The best example of the success of the Spherical Collapse Model is provided by its predictions concerning the Dark Matter Halos Mass Function $n(M)$, which gives the number of DM Halos per unit volume with mass in the interval between M and $M+dM$. Press & Schechter (1974) (PS74) proposed a simple analytical model to calculate $n(M)$, in which the predictions of the Spherical Collapse Model and of the linear theory are used.

In the PS74 model one considers the linear DM density field $\delta_R(\vec{x}, t) = \delta_M$ smoothed on some spatial scale R corresponding to a mass M. If the smoothed density field is Gaussian, then the Probability Density Function of a density fluctuation δ_M is:

$$p_G(\delta_M)d\delta_M = \frac{1}{\sqrt{2\pi\sigma_M^2}} \exp\left\{-\frac{\delta_M^2}{2\sigma_M^2}\right\} d\delta_M, \tag{1.55}$$

where $\sigma_M^2 = \sigma_M^2(t)$ is the time-dependent variance of smoothed density field. The probability $P_{>\delta_c}(M)$ that at some point the overdensity δ_M exceeds a threshold δ_c which characterizes collapsed structures is:

$$P_{>\delta_c}(M) = \int_{\delta_c}^{+\infty} p_G(\delta_M)d\delta_M, \tag{1.56}$$

where a possible choice for the critical threshold is $\delta_c = 1.69$, the linear overdensity corresponding to collapsed structures with maximum density in the Spherical Collapse Model. $P_{>\delta_c}(M)$ is proportional to the number of collapsed structures ($\delta_M > \delta_c$), whether they are isolated or contained within denser structures which collapse with them. Since one is only interested in the number of structures with mass M that are collapsed and isolated (i.e. surrounded by underdense regions), one must subtract from $P_{>\delta_c}(M)$ the quantity $P_{>\delta_c}(M + dM)$, which is proportional to the number of collapsed objects with mass $M + dM$.

Note that the possibility that at a given time some object, which is collapsing on a scale M, can be later contained within a larger object has been

ignored. This is the so-called cloud-in-cloud problem. In practice, one should assume $P_{>\delta_c}(M)$ to be proportional to the probability that a given point has ever been contained in a collapsed object on mass scales $> M$. This is equivalent to assume that the only objects that exist on the scale M are the ones that just collapsed.

Another problem of the PS74 model is the fact that the contribution to structure formation from underdense regions is completely ignored, with the consequence that half of the mass is not accounted for. This problem is corrected, in a rather arbitrary way, by multiplying the Mass Function by a factor 2 to account for mass from the underdense regions which accretes onto overdense ones.

The PS74 Dark Matter Halos Mass Function can be obtained as follows:

$$n(M)dM = 2\frac{\langle\rho_M\rangle}{M}\left\{P_{>\delta_c}(M) - P_{>\delta_c}(M+dM)\right\} = \\ = 2\frac{\langle\rho_M\rangle}{M}\left|\frac{dP_{>\delta_c}}{d\sigma_M}\right|\left|\frac{d\sigma_M}{dM}\right|dM, \tag{1.57}$$

where $\langle\rho_M\rangle$ is the average density of DM, and $\langle\rho_M\rangle/M$ represents the average number of perturbations per unit volume. In the case where the dependence of σ_M from M can be expressed by a power law:

$$\sigma_M = \left(\frac{M}{M_0}\right)^{-\alpha}, \tag{1.58}$$

where M_0 is some characteristic mass, the Mass Function reads:

$$n(M) = \frac{2}{\sqrt{\pi}}\frac{\langle\rho_M\rangle\alpha}{M_*^2}\left(\frac{M}{M_*}\right)^{\alpha-2}\exp\left\{-\left(\frac{M}{M_*}\right)^{2\alpha}\right\}. \tag{1.59}$$

The Mass Function has a power law behaviour, with an exponential cut-off at $M > M_*$, with:

$$M_* = \left(\frac{2}{\delta_c^2}\right)^{1/2\alpha} M_0, \tag{1.60}$$

and α is related to the effective spectral index on the relevant mass scale.

Despite being a good approximation of the Mass Function on most mass scales, the PS74 model is not satisfactory under several aspects. First of all the assumption that collapsed structures form at the peaks of the linear density field is not justified, since matter moves away from the initial Lagrangian positions during the nonlinear evolution. The PS74 approach in which collapsed structures are identified through their overdensity is purely

statistical and this means that all the physical processes which can lead to the formation of a Halo of a given mass are ignored. This is a thorny matter since a Halo of mass M at a given instant may have formed through a variety of merger histories of smaller objects. Besides, the cloud-in-cloud problem causes errors in the process of counting Halos of a given mass scale, while the contribution to structure formation from underdense regions is not considered.

To deal with these problems Bond et al. (1991) and Lacey & Cole (1993) proposed an extension of the original Press & Schechter theory in which the cloud-in-cloud problem is tackled and solved. The Extended Press & Schechter Theory (EPST) succeeds in reproducing the PS74 Mass Function and its evolution throughout time, and provides a powerful formalism by which it is possible to reconstruct the rate at which a DM Halo of a given mass accretes matter through merger processes.

In the EPST approach we consider the smoothed DM density field δ_M at the generic point $\vec{x}$ of space and the mass variance $S(M) \equiv \sigma_M^2$. The function $S(M)$ is monotone, so a unique S value is associated to a given mass M, and vice versa. Since one is interested in studying the evolution of the Halo Mass Function throughout time, as well as their merger history, one should be able to characterize isolated, collapsed structures at any time t. One could consider all points $\vec{x}$ with $\delta_M(\vec{x}, t)$ above some time-independent threshold δ_c as contributions to collapsed structures. A more convenient choice is to consider the linear density field extrapolated to some fixed time t_0:

$$\delta_M(\vec{x}, t_0) = \delta_M(\vec{x}, t)\frac{D_+(t_0)}{D_+(t)}, \tag{1.61}$$

and account for the evolution throughout time using a time-dependent density threshold $\delta_c(t)$ that is progressively lowered throughout time. Thus, at some time t, all points with $\delta_M(\vec{x}, t_0) > \delta_c(t)$ are contained in collapsed structures. However, this assumption alone cannot solve the cloud-in-cloud problem, so one has to place additional conditions to select points contained in collapsed Halos.

In the EPST the evolution of the density field at the point $\vec{x}$ is represented by a trajectory $\delta_M(S)$ in the two-dimensional space defined by the pairs $(S(M), \delta_M)$. The trajectory is determined by the values of the Fourier coefficients of the density fluctuation field $\delta_{\vec{k}}$ in $\vec{x}$ (Equation 1.21), and begins at the point (0,0) of the $(S(M), \delta_M)$-space, corresponding to $M \to +\infty$ and $\delta_M = 0$, and evolves depending on the distribution of matter around $\vec{x}$. As long as the window function associated to the filter function is sharp in k-space, the Fourier modes evolve independently and the trajectories $\delta_M(S)$

are true Brownian random walks in the $(S(M), \delta_M)$-space. Points within collapsed structures at a given time t are represented by trajectories for which $\delta_M(S) > \delta_c(t)$ for some S. Since for a given position $\vec{x}$ the motions in the $(S(M), \delta_M)$-space are random, trajectories with different $S(M)$ can exceed the threshold. This means that there can be collapsed structures which are contained within larger collapsing objects. Then, to avoid the cloud-in-cloud problem and select isolated Halos, for any given point $\vec{x}$ one considers only the trajectory $\delta_M(S)$ which exceeds the threshold $\delta_c(t)$ with the minimum S possible, i.e. one considers $\vec{x}$ as contained in the collapsed structure with largest mass possible. If we denote the number density of trajectories at S in the interval δ_M to $\delta_M + d\delta_M$ as $Q(S, \delta_M)$, then its evolution in the $(S(M), \delta_M)$-space is described by a diffusion equation:

$$\frac{\partial Q}{\partial S} = \frac{1}{2}\frac{\partial^2 Q}{\partial \delta_M^2}. \tag{1.62}$$

Since the motions in the $(S(M), \delta_M)$-space are completely random, a trajectory can cross the threshold $\delta_M = \delta_c$ many times, a fact that should be avoided if one is interested to find the actual contribution to the collapsed structures. This problem can be solved placing a barrier at $\delta_M = \delta_c$ which absorbs trajectories and prevents multiple crossings of the threshold. The unique solution to Equation 1.62 with this boundary condition is:

$$Q(S, \delta_M)d\delta_M = \frac{1}{\sqrt{2\pi S}}\left[e^{-\frac{\delta_M^2}{2S}} - e^{-\frac{(\delta_M - 2\delta_c(t))^2}{2S}}\right] d\delta_M, \tag{1.63}$$

where the first exponential accounts for trajectories which cross the threshold from below it, while the second exponential accounts for trajectories which cross the threshold from above it, the latter being subtracted because it does not represent a physical contribution to the number of collapsed objects. The probability that a particular trajectory will be absorbed by the barrier in the interval S to $S + dS$ is:

$$f_S(S, \delta_c(t))dS = -\left[\frac{\partial}{\partial S}\int_{-\infty}^{\delta_c(t)} Q(S, \delta_M)d\delta_M\right] dS = -\left[\frac{1}{2}\frac{\partial Q}{\partial \delta_M}\right]_{-\infty}^{\delta_c(t)} dS =$$

$$= \frac{\delta_c(t)}{(2\pi)^{1/2} S^{3/2}} \exp\left\{-\frac{\delta_c^2(t)}{2S}\right\} dS. \tag{1.64}$$

The function $f_S(S, \delta_c(t))$ represents the fraction of mass associated to DM Halos in the range of masses M corresponding to the specified range in S. Therefore, the Dark Matter Halos Mass Function is:

$$n(M, t)dM = \frac{\langle \rho_M \rangle}{M} f_S(S, \delta_c(t)) \left|\frac{dS}{dM}\right| dM =$$

$$= \left(\frac{2}{\pi}\right)^{1/2} \frac{\langle \rho_M \rangle}{M^2} \frac{\delta_c(t)}{\sigma_M} \left| \frac{d \ln \sigma_M}{d \ln M} \right| \exp\left[-\frac{\delta_c^2(t)}{2\sigma_M^2} \right] dM, \tag{1.65}$$

which is with the Mass Function originally proposed by Press & Schechter 1974 in which the factor 2 is naturally accounted for.

1.8 Baryons in the Universe

Almost all information in Astrophysics is obtained by the observation of photons emitted by astrophysical objects. Since only standard matter has non negligible cross-section with electro-magnetic radiation, astrophysical observations provide direct information on the baryonic component, not on the DM.

The baryon cosmological density is well constrained by the abundance of light nuclei within the Big Bang Nucleosynthesis framework which provides $\Omega_b = \rho_b/\rho_c \sim 0.02h^{-2}$, in good agreement with the independent constraints provided by the analysis of the temperature fluctuations of the CMB.

In this Section, I provide an overview of the main features of the structures observed in the Universe and on the processes that lead to their formation.

1.8.1 Galaxies

Galaxies are gravitationally bound systems of stars, gas and dust with a typical size of a few kpc. All the observations show that there are many types of galaxies with very different features (shape, amounts of gas and dust, presence of star forming regions and substructures). One of the first classification criterions for galaxies, which is still in use, was proposed by Hubble, who classified their morphology. Further studies demonstrated that there is a correlation between other features of galaxies and their morphology. There are three main classes of galaxies:

- Disks: they constitute $\sim 68\%$ of all galaxies. Three different components are evident in their structure: a central spheroidal bulge with a few kpc radius; a few pc thin disk extending out to a few 10 kpc; a halo of radius up to ~ 100 kpc. They frequently show spiral structures that are thought to originate from rotating density waves producing shocks in the gas rich disk leading to star formation. The disk often hosts star forming regions, with young stellar populations. Their total mass varies in the range $M \sim 10^9 - 10^{12} M_\odot$.

- Ellipticals: they constitute $\sim 29\%$ of all galaxies. They have an ellipsoidal shape, old stellar populations and a very little amount of gas. Their total mass varies in a wide range: $M \sim 10^7 - 10^{13} M_\odot$.

- Irregulars: they constitute $\lesssim 3\%$ of all galaxies. These galaxies do not show a regular shape and their total mass is typically smaller with respect to the other two classes of galaxies: $M \sim 10^8 - 10^{10} M_\odot$. They often show regions characterized by bursts of star formation.

Spiral galaxies are generally considered as young stellar systems, due to their significant star forming activity, while ellipticals are characterized by older stellar populations. There is evidence that ellipticals may be the result of merger events, in which two or more galaxies merge, converting a large fraction of their gas content into stars during the process. The characteristic ellipsoidal shape would be obtained when the system reaches virial equilibrium, after a characteristic relaxation time (which depends on the complex processes which drive the relaxation). Besides, many irregular galaxies are considered to be systems which have undergone merging events and that have not reached yet the configurational equilibrium.

Galaxy dynamics provided the first widely-accepted evidence of DM. In particular, the evidence came from the rotational velocity of the spiral galaxies which, unlike the ellipticals, are rotationally-supported systems. The rotation curve, i.e. the rotational velocity as a function of the radius, was measured via spatially resolved spectroscopy and provided evidence that mass is present well beyond the optical radius which encompasses the region containing most of the visible matter (Rubin & Ford, 1970). The dynamical analysis of elliptical galaxies provided a similar evidence, showing that the velocity dispersion of the stars is larger than expected if the system were in virial equilibrium and were composed of luminous matter only. Both, rotational velocities in spirals and stellar velocity dispersions in ellipticals provided evidence that an excess of "dark"matter exists on galactic scales which dominates the total mass of the systems.

1.8.2 Groups and clusters of galaxies

Groups and clusters of galaxies are systems which contain large amounts of hot, X-ray emitting gas and a high number of galaxies. Groups of galaxies are non-virialized systems which contain less than 50 galaxies, with radii $R \lesssim 1.5$ Mpc; the temperature of the hot gas is $T \lesssim 10^7$ K. Clusters of galaxies are virialized structures containing more than 50 galaxies (rich clusters can contain hundreds of galaxies), with radii $R \gtrsim 1.5$ Mpc; the temperature of

the hot gas is $T > 10^7$ K. Galaxy groups are thought to be hosted by dark matter haloes with virial masses $10^{13} M_\odot \lesssim M_{\rm vir} \lesssim 10^{14} M_\odot$, while galaxy clusters are hosted by more massive halos of mass $M_{\rm vir} \gtrsim 10^{14} M_\odot$.

Clusters can be classified in many different ways, however, the simplest criterion is to divide them in two classes depending on their morphology:

- Regular/relaxed: they are characterized by very smooth and symmetric structure, and by high galaxy velocity dispersions; these facts are generally considered as evidences that regular cluster reached virial equilibrium. They have small fractions of spiral galaxies ($\lesssim 20\%$). Regular clusters represent roughly a half of all clusters.

- Irregular/unrelaxed: they are characterized by irregular internal structure and by low velocity dispersions; these systems have not reached virial equilibrium yet, either because they have formed recently or because they have undergone recent dynamical disturbance, like a major merging event. The fraction of spiral galaxies is higher with respect to regular clusters ($\gtrsim 40\%$).

The mass of galaxy clusters can be estimated using different methods. First through applications of the Virial Theorem (Zwicky (1933), the first work showing evidence of DM) and through the use of strong and weak gravitational lensing (Narayan & Bartelmann, 1996; Clowe et al., 2006). The total mass of galaxy clusters can also be estimated using X-ray observations (with e.g. Chandra, XMM-Newton, Suzaku) which allow the measurements of the gas density and temperature profiles: if hydrostatic equilibrium is assumed for the gas it is easy to estimate the total mass profile in the cluster. All methods indicate that clusters are dominated by DM, whereas stars and hot gas represent only $\sim 5\%$ and $\sim 15\%$, respectively, of the virial mass of the system.

Galaxy clusters are the largest collapsed structures observed in the Universe and represent important laboratories where one can test the theory of galaxy formation in the standard cosmological scenario, because of the many phenomena that shape their internal properties. Furthermore, the determination of their spatial distribution and their masses is extremely relevant for cosmology. Next generation galaxy and galaxy clusters surveys (e.g. DES, EUCLID, eROSITA) promise to measure quantities like the halo mass function with very high accuracy (at the % level). Such measurements will be used to constrain cosmological parameters and to study possible deviations from the Concordance Model. For these reasons the study of galaxy clusters represents one of the most fruitful and relevant fields for both Astrophysics and Cosmology.

Figure 1.2: Optical image of the Virgo cluster (image credit NASA).

1.8.3 Large Scale Structure and Galaxy Surveys

Galaxy redshift surveys are observational campaigns aimed at measuring the redshift of a large number of galaxies. Once the redshift is known, Hubble's Law can be used to assign distances to redshifts (within a given cosmological model). This allows the reconstruction of the 3D distribution of galaxies in the universe, which can be studied to recover cosmological information. For this purpose one needs to obtain the spectra (or detailed photometry) of a large number of objects. This became possible only in the late 1970s, with the advent of modern spectrographs and the possibility to perform multi-object spectroscopy over large fields of view.

Galaxy redshift surveys have become one of the most important tools in Cosmology. Recent, large redshift catalogues like the Sloan Digital Sky Survey (SDSS, Ahn et al. (2012)) contain more than 10^6 objects covering very large areas of the sky. On smaller angular scales the same strategy has been used to trace the galaxy distribution over larger distances, reaching $z > 0.7$ (VVDS, Garilli et al. (2008); DEEP2 http://deep.berkeley.edu/; zCOSMOS, Lilly et al. (2007); VIPERS Guzzo et al. (2013)).

The capability of tracing the Large Scale Structure using redshift surveys can be readily appreciated from Fig. 1.3 which shows the spatial distribution of the galaxies of the SDSS. Each dot represent a galaxy. On large scales, the spatial distribution of these objects is characterized by many overdense

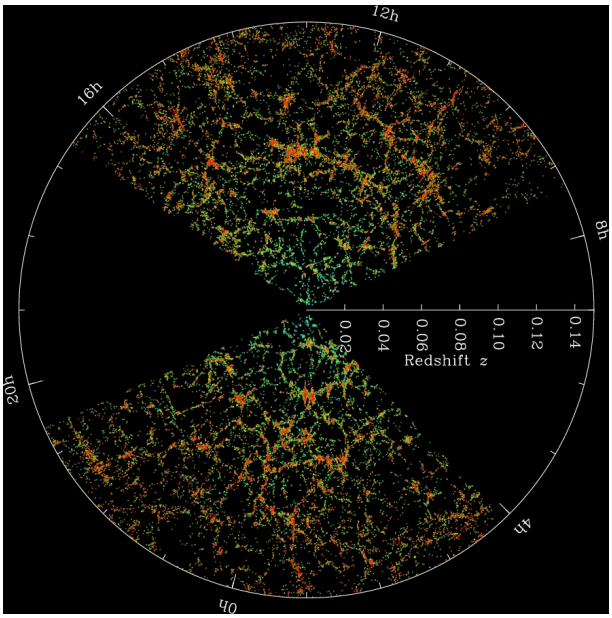

Figure 1.3: Spatial distribution of galaxies in a slice of the Sloan Digital Sky Survey (Ahn et al., 2012).

regions called superclusters, non-virialized systems composed by a great number of galaxies and galaxy clusters; these overdense regions surround large voids containing a very little number of objects; the overdense regions are connected by long filamentary structures.

The wealth of structures in Fig. 1.3 is revealed thanks to the large number of objects in the survey at $z \sim 0$, which allows to densely sample the distribution of luminous matter. Surveys at $z \sim 1$ probe similar volumes with $10^3 - 10^4$ galaxies, making more difficult to trace the Large Scale Structure. Yet, the analysis of the galaxy distribution at high redshifts represents the state of art, since it can provide most of the missing information (the nature of Dark Energy, the validity of the standard Einsteinian gravity, the evolution of cosmic structures throughout time) on the cosmological model. Future and ongoing surveys like the Dark Energy Survey and Euclid promise to accurately measure the distribution of galaxies and clusters up to redshift $z > 1$ in very large fields of view, providing data to conduct high precision cosmological studies.

1.9 The formation of baryonic structures

Although DM drives the evolution of cosmic structures, the fate of baryons is different from that of DM particles. Indeed the latter constitutes a collisionless fluid that interacts only through gravity, standard matter is both collisional and dissipative i.e. can interact with itself and with the electromagnetic radiation.

As a result, while it is relatively easy to follow the evolution of a collisionless, self-gravitating fluid in a cosmological framework (with N-body techniques, for example), it is much more difficult to trace the evolution of the baryonic component.

The collisional nature of the baryon fluid implies that we have to study its evolution in the realm of hydrodynamics. The fact that baryons can interact with electro-magnetic radiation means that we should also account for heating and cooling mechanisms, i.e. we need to address the problem of radiative transfer. Gas is accreted onto dark matter halos and as it cools it settles in disks at the halo centers. If sufficiently high densities and low temperatures are reached, gravitational instability can trigger the formation of stars (which represent yet an additional type of collisionless fluid), a process that must be modeled too. As the universe evolves the hierarchical growth of cosmological perturbations and the merging of pre-existing collapsed structures lead to the formation of larger and larger systems. Complex hydrodynamical processes influence the distribution of gas in halos, e.g. ram pressure can have the effect of stripping galaxies of their gas when they fall into a forming cluster, leading to the quenching of star formation. As gas falls into larger and larger halos, shocks can develop which lead to shock-heating of the inter-galactic medium. Furthermore, galaxy-galaxy and galaxy-environment interactions can modify the morphological and dynamical properties of the galaxies. For example, massive elliptical galaxies are thought to form as the result of the merger of disk galaxies whose original structure is completely destroyed by post-merger relaxation processes. Galaxy clusters are extremely complex systems where all the cited processes are simultaneously active.

A particularly relevant role in the formation of baryonic structures is thought to be played by the so-called feedback processes. As a result of star formation, feedback processes (supernovae explosions, stellar winds, and the related metal yield) modify the thermal and chemical state of the baryons in a complicated nonlinear fashion. The main function of stellar feedback is heating and adding momentum to the gas surrounding star-forming regions. The principal result is the quenching of star formation in the regions influenced by stellar feedback.

Another relevant feedback mechanism is related to the presence of super-

massive black holes in the spheroids of galaxies. Accretion of gas onto supermassive black holes is thought to trigger Active Galactic Nuclei (AGNs). Gas that settles in accretion disks around supermassive black holes can lose energy due to dissipative processes and transfer angular momentum outwards as it falls towards the black hole. This gas is eventually accreted. A fraction of the rest mass energy of the accreted gas is re-processed and emitted in various forms: emission of electro-magnetic radiation from the disk (the primary source is black-body-like UV-optical radiation from the optically thick disk, but a fraction of this radiation can be re-processed into the IR band the by dust and into the X-ray band by an hot gas corona surrounding the disk, via inverse-Compton interactions), relativistic jets produced by the accretion disks, acceleration of particles/cosmic rays, synchrotron emission from charged particles in magnetic fields. Part of this energy is observed to couple with the intergalactic medium resulting in a different form of feedback usually referred to as AGN feedback. The effect of AGN feedback is similar to that of stellar feedback: heating and expulsion of large quantities of gas from the central regions of dark matter halos, leading to the quenching of star formation. Evidence of the existence of AGN feedback comes from the observation of X-ray cavities and radio blobs in galaxy clusters (Fabian, 2012).

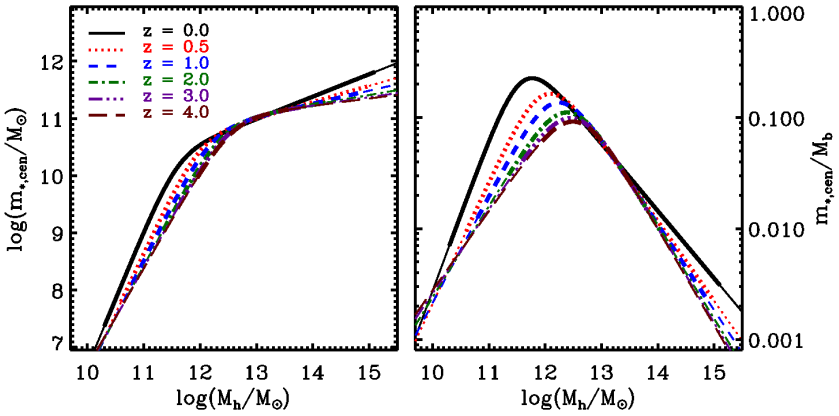

Figure 1.4: Results of abundance matching (Moster et al., 2013). Left: halo mass vs. mass of the central galaxy. Right: halo mass vs. baryon conversion efficiency (ratio between the stellar mass of the central galaxy and the total baryonic mass in the halo).

Fig. 1.4 shows the results of matching the mass function of central galaxies with the halo mass function predicted by numerical N-body simulations. This results show that the baryon conversion efficiency (ratio between the stellar

mass of the central galaxy and the total baryonic mass in the halo) peaks in halos of mass $M_{\rm h} \sim 3 \times 10^{11} M_{\odot}$, whereas it decreases in low mass halos hosting dwarf galaxies and in high mass halos hosting groups and clusters. The usual interpretation of this plot is that not all halos are equally efficient in converting gas into stars. Stellar feedback processes are thought to be responsible for the decrease in the baryon conversion efficiency in low mass halos, while AGN feedback is thought to be responsible for the same effect in high mass halos.

Altogether the processes involved in galaxy formation are very difficult to model. Indeed, at the moment, we do not have a self-consistent model to describe the formation of stars, galaxies, and their evolution in a cosmological framework. A viable approach to study the problem is provided by semi-analytical models in which the evolution of the baryonic component is calculated using simple analytical models, while the evolution of the DM is calculated either directly, using N-body simulations, or using Monte Carlo techniques that follow the merging history of DM Halos. Semi-analytical models suffer weakly from resolution limitations, especially when Monte-Carlo methods are used to generate halo merger histories. In this case, the resolution can be made arbitrarily high at a relatively small computational cost. Another advantage is the fact that the effects of varying assumptions or parameter choices can be easily investigated, making it possible to calculate a wealth of observable galaxy properties, like luminosities, sizes, mass-to-light ratios, bulge-to-disk ratios, circular velocities, etc. The main disadvantage is the need for simplifying assumptions in the calculation of gas features, like spherical symmetry or particular flow structures.

An alternative approach is provided by numerical hydrodynamic simulations in which the gravitational and hydrodynamical equations in an expanding universe are solved explicitly, using a variety of numerical techniques that have been specifically developed for this purpose. The advantage of using these methods is that the dynamics of the cooling gas are calculated in full generality, without the need of simplifying assumptions. The major disadvantage is that even with the best codes and the fastest computer available today, the attainable resolution is still some orders of magnitude below that required to resolve the formation and internal structure of individual galaxies in large, cosmological volumes. Besides, phenomenological models to include star formation and feedback processes in the simulations are required, due to the theoretical uncertainties concerning these phenomena.

1.10 The physics of galaxy clusters

The main aim of this Thesis is to identify the role of AGN feedback on the properties of galaxy clusters. Multi-wavelength observations of these systems revealed a complex structure. In this Section, I review the main observational properties of galaxy clusters and of some of the open problems concerning cluster physics that are discussed in more detail in the rest of the Thesis.

Figure 1.5 shows composite images of two massive clusters obtained combining results from multi-wavelength observations of clusters at low (left panel, Abell 1689) and high (right panel, SPT-CL J2106-5844) redshift. This picture helps to identify the main components of galaxy clusters: the luminous stars in galaxies, stars around galaxies, the hot Intracluster Medium (ICM) via its X-ray emission and the Sunyaev-Zel'dovich (SZ) effect by which the thermal energy of the hot ICM can be transferred to CMB photons via inverse Compton scattering.

In the case of the cluster Abell 1689 it is possible to observe the effects of the presence of a large quantity of dark matter: gravitational lensing distorts the images of background galaxies into extended cluster-centric arcs. At larger radii, the effect of gravitational lensing is weaker, however it can still be reliably measured by averaging the shapes of many background galaxies and comparing the average with the expected value for an isotropic distribution of shapes. Gravitational lensing directly probes the total mass distribution in clusters, and can be used to obtain very reliable estimated of cluster masses.

Besides gravitational lensing, several techniques are used to estimate cluster masses. X-ray instruments which are able to detect the thermal bremsstrahlung from the hot ($T > 10^8$ K) ICM can provide important information about the thermal state of this mass component. Combining these measurements with the simplifying assumptions that the ICM is in hydrostatic equilibrium and that the mass distribution is spherically symmetric, it is possible to obtain an estimate of the total mass profile in a cluster:

$$M(r) = -\frac{kTr}{\mu m_H G}\left(\frac{\partial \ln \rho}{\partial \ln r} + \frac{\partial \ln T}{\partial \ln r}\right) \tag{1.66}$$

where m_H is the mass of a Hydrogen atom, μ is the average molecular weight, T and ρ are the temperature and density of the gas, r is the distance from the cluster centre. Mass estimates obtained with this method are expected to be more reliable for relaxed clusters in which the configuration is approximately close to equilibrium, but less reliable for the most un-relaxed clusters.

Cluster mass measurements can be obtained also taking profit of the SZ effect. This effect is the result of high energy electrons distorting the CMB through inverse Compton scattering, in which the low energy CMB photons

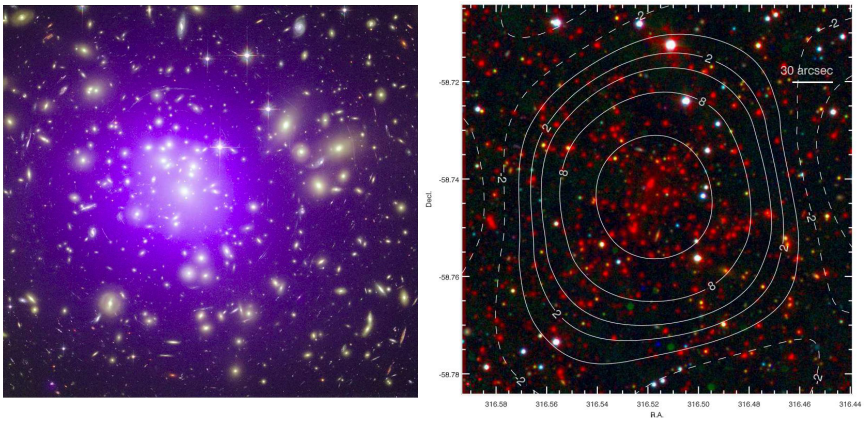

Figure 1.5: Left panel: the composite X-ray/optical image (556 kpc on a side) of the galaxy cluster Abell 1689 at redshift z = 0.18. The purple haze shows X-ray emission of the hot $T \sim 10^8$ K gas, obtained by the Chandra X-ray Observatory. Images of galaxies in the optical band, colored in yellow, are from observations performed with the Hubble Space Telescope. The long arcs in the optical image are caused by the gravitational lensing of background galaxies by matter in the galaxy cluster (Credit:X-ray: NASA/CXC/MIT; Optical: NASA/STScI). Right panel: the galaxy cluster SPT-CL J2106-5844 at $z = 1.133$, discovered via its Sunyaev-Zel'dovich (SZ) signal. The color image shows the Magellan/LDSS3 optical and Spitzer/IRAC mid-infrared measurements (corresponding to the blue-green-red color channels). The white contours correspond to the South Pole Telescope SZ significance values, as labeled, where dashed contours are used for the negative significance values. (Adapted from Kravtsov & Borgani (2012) and Foley et al. (2011)).

receive an average energy boost during collision with the high energy cluster electrons. Observations of the SZ effect in CMB maps allow to measure the so-called Comptonization parameter y for each line-of-sight, i.e. the integral of the number of collisions between photons and ICM electrons multiplied by the mean fractional energy change of photons per collision. The y parameter is given by:

$$y = \frac{\sigma_T}{m_e c^2} \int_{-\infty}^{+\infty} P_e(r) dl \tag{1.67}$$

where σ_T is the Thomson scattering cross section, m_e is the electron mass, c is the speed of light, l is the coordinate along the line-of-sight and $P_e(r)$ is the electron pressure profile. It is possible to integrate the y parameter over the solid angle Ω subtended by the cluster to obtain the so-called Y_{SZ} parameter. Once an analytical model is assumed for the pressure profile and the dark matter distribution, it is possible to obtain cluster mass estimates directly from SZ measurements.

When mass estimates from gravitational lensing are combined with independent measurements of the mass content in baryonic matter, it is possible to obtain estimates of the relative abundance of the different components. Dark matter constitutes the dominant mass component, whereas baryons constitute only up to 16% of the total mass. Recent results show that the abundance of baryons in clusters increases with halo mass but is typically below (or very close to) the cosmological average value (Lin et al., 2003; Gonzalez et al., 2007; Giodini et al., 2009; Vikhlinin et al., 2009; Andreon, 2010; Leauthaud et al., 2012; Lin et al., 2012). These studies also show that the stellar mass in clusters constitutes only up to $2 - 3\%$ of the total. This fact suggests that galaxy clusters are systems that are particularly inefficient in converting gas into stars.

The distribution of galaxies in clusters has very different properties than in the field. First of all, galaxy clusters usually have a very massive galaxy at their centres, the so-called brightest cluster galaxy (BCG). BCGs are typically surrounded by an extended halo of stellar mass, which can be detected only using very deep photometry (see e.g. Rudick et al. (2010)). This component is usually referred to as Intracluster Light (ICL). Gonzalez et al. (2007) showed that the BCG+ICL components account for $\sim 35\%$ of the total stellar luminosity measured in clusters. Galaxy clusters also contain a large number of satellite galaxies whose properties differ from those of the galaxies observed in the field. The abundance of elliptical and quiescent galaxies in clusters is larger than in the field (Dressler et al., 1997; Goto et al., 2003; Postman et al., 2005). The theoretical explanation of the larger abundance of elliptical galaxies is the fact that galaxy-galaxy interactions and mergers

are much more probable in high density environments like clusters. These interactions can lead to strong changes in the morphology of galaxies. The larger abundance of quiescent satellite galaxies is thought to be an effect of the ram pressure stripping of gas from galaxies orbiting in clusters (Abadi et al., 1999; McCarthy et al., 2008): as gas is removed from galaxies, the fuel necessary for star formation is slowly removed, leading to the decrease of the star formation rates. Satellite galaxies can also lose a significant amount of stellar mass while orbiting in clusters, due to tidal stripping. Results of numerical simulations suggest that the ICL is mainly composed of stars stripped from satellite galaxies orbiting in clusters (Puchwein et al., 2010).

Figure 1.6: Optical image of the BCG in the Fornax cluster. Credit: NASA, STScI.

Among the galaxies observed in clusters, BCGs constitute a completely different category. BCGs are the brightest and most massive galaxies observed in the Universe. Their stellar masses are in the range 10^{11} $M_{\odot}$ to 10^{12} $M_{\odot}$. BCGs are usually the largest galaxies that live at the bottom of the cluster dark matter halo. Their stars can be acquired in several ways. Some of the stars form within the rarest peaks collapsing at high redshift – those galaxies and their dark matter haloes quickly virialize through violent rapid merging and end up at the centre of the cluster. Stars can also be acquired

after the cluster formed through the dynamical friction and merging with other BCGs or with the most massive satellites of the cluster. Finally, the stars may form in situ from the cold gas that is expected to collect at the centre of the potential. BCGs are typically quiescent, red elliptical galaxies with very old stellar populations (McDonald et al., 2011). Figure 1.6 show an optical image of the BCG at the centre of the Fornax cluster, NGC 1399.

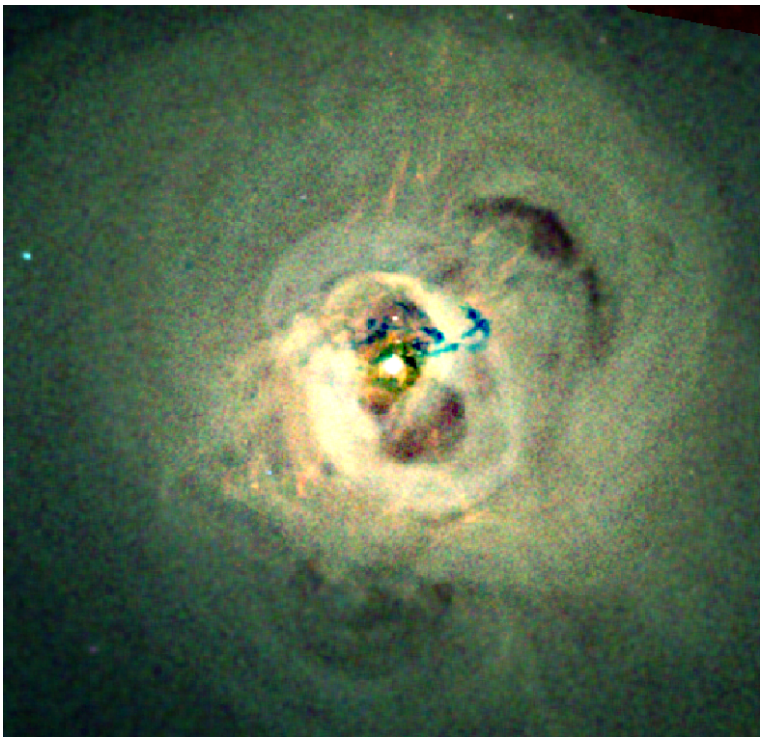

Figure 1.7: Chandra X-ray image of the Perseus cluster core. Red-Green-Blue depicts soft to hard X-rays Fabian (2012).

The low level of star formation observed in BCGs need to be understood in terms of gas physics. Spectroscopic X-ray observations of cluster core regions have shown that, despite strong X-ray emission of the hot gas, a very low amount of gas is able to cool down to low temperatures in these regions (Böhringer et al., 2001; Peterson et al., 2001; Fabian, 2012). This results are consistent with the low levels of star formation in BCGs, however they need to be explained in a context broader than that of the standard galaxy formation scenario. In particular, given the relatively short gas cooling times in cluster cores, an additional heating mechanism is needed to prevent gas from cooling down to low temperatures. There is growing observational consensus on the

idea that this heating mechanism is related to the interaction between AGNs at the centre of galaxies and the hot gas: AGN feedback. Observational evidence for AGN feedback is found in X-ray and radio observations of several clusters Fabian (2012).

AGN feedback is thought to operate in two different modes (Sijacki et al., 2007). The quasar mode, which occurs when the AGN is very luminous, is thought to be related to the high radiative efficiency of the AGN during phases in which the supermassive black hole accretes at its maximum rate (the Eddington limit). Direct observational evidence of quasar mode feedback is difficult to be found. The radio mode is thought to be related to the mechanical energy of radio-emitting jets often seen when the AGN is operating at a lower level, and is common in massive elliptical galaxies. Direct evidence of radio mode feedback is found directly through X-ray observations of the central galaxies of cool core clusters in the form of bubbles in the hot surrounding medium. Figure 1.7 shows a composite X-ray image of the Perseus cluster core: this striking image shows bubbles and cavities excavated by AGN feedback.

Despite the need for AGN feedback to explain the observed properties of the hot gas in cluster cores and of the BCG low star formation rates, its role in the different phases of the assembly of a galaxy cluster are poorly known. It is very important to understand the physical conditions required for AGN feedback to be effective, so that the phenomenon can be included in the standard scenario of galaxy formation. What is also poorly known is the effect that AGN feedback might have on other properties of galaxy clusters, like the mass distribution of the different cluster components (Duffy et al., 2010). For example, gas is not only heated by AGNs but can be also expelled from core regions, with significant dynamical consequences.

Furthermore, there is growing observational evidence for the existence of peculiar density distributions at the centers of clusters and it is not clear whether the formation of these features can be related to AGN activity. For example, the dark matter density profiles inferred for the sample of clusters observed by Newman et al. (2012) show very shallow slopes in the central regions ($r < 10$ kpc). This result is in tension with the typical results of N-body simulations which produce halos with cuspy central slopes (Navarro et al., 1996). Additionally, very shallow slopes are also observed in the surface brightness profiles of very massive elliptical galaxies, including BCGs, but in regions closer to the centres, $r < 3$ kpc (Kormendy, 1999; Quillen et al., 2000; Laine et al., 2003; Trujillo et al., 2004; Lauer et al., 2005; Côté et al., 2007; Kormendy et al., 2009).

To properly study these problems, it is required to include AGN feedback in our theoretical models for galaxy formation and study its effect. This

constitutes the main aim of this Thesis. The questions I try to answer in this work are the following:

- Does AGN feedback really allow to reproduce realistic properties for BCGs in clusters?
- Does AGN feedback influence the global distribution of matter in within the virial radius of clusters?
- Are the changes in the global mass distribution relevant for the determination of the total mass of clusters?

The theoretical tools used to answer these questions are numerical hydrodynamical simulations, as explained in more details in the next Chapter.

Bibliography

Abadi M. G., Moore B., Bower R. G., 1999, MNRAS, 308, 947

Ahn C. P., Alexandroff R., Allende Prieto C., Anderson S. F., Anderton T., Andrews B. H., Aubourg É., Bailey S., Balbinot E., Barnes R., et al. 2012, ApJS, 203, 21

Andreon S., 2010, MNRAS, 407, 263

Böhringer H., Belsole E., Kennea J., Matsushita K., Molendi S., Worrall D. M., Mushotzky R. F., Ehle M., Guainazzi M., Sakelliou I., Stewart G., Vestrand W. T., Dos Santos S., 2001, A&A, 365, L181

Bond J. R., Cole S., Efstathiou G., Kaiser N., 1991, ApJ, 379, 440

Clowe D., Bradač M., Gonzalez A. H., Markevitch M., Randall S. W., Jones C., Zaritsky D., 2006, ApJ, 648, L109

Côté P., Ferrarese L., Jordán A., Blakeslee J. P., Chen C.-W., Infante L., Merritt D., Mei S., Peng E. W., Tonry J. L., West A. A., West M. J., 2007, ApJ, 671, 1456

Dressler A., Oemler Jr. A., Couch W. J., Smail I., Ellis R. S., Barger A., Butcher H., Poggianti B. M., Sharples R. M., 1997, ApJ, 490, 577

Duffy A. R., Schaye J., Kay S. T., Dalla Vecchia C., Battye R. A., Booth C. M., 2010, MNRAS, 405, 2161

Fabian A. C., 2012, ARA&A, 50, 455

Foley R. J., Andersson K., Bazin G., de Haan T., Ruel J., Ade P. A. R., Aird K. A., Armstrong R., Ashby M. L. N., Bautz M., Benson B. A., Bleem L. E., Bonamente M., Brodwin M., Carlstrom J. E., Chang C. L., Clocchiatti A., et al. 2011, ApJ, 731, 86

Garilli B., Le Fèvre O., Guzzo L., Maccagni D., Le Brun V., de la Torre S., Meneux B., Tresse L., Franzetti P., Zamorani G., Zanichelli A., Gregorini L., Vergani D., et al. 2008, A&A, 486, 683

Giodini S., Pierini D., Finoguenov A., Pratt G. W., Boehringer H., Leauthaud A., Guzzo L., Aussel H., Bolzonella M., the COSMOS Collaboration 2009, The Astrophysical Journal, 703, 982

Gonzalez A. H., Zaritsky D., Zabludoff A. I., 2007, The Astrophysical Journal, 666, 147

Goto T., Yamauchi C., Fujita Y., Okamura S., Sekiguchi M., Smail I., Bernardi M., Gomez P. L., 2003, MNRAS, 346, 601

Guzzo L., Abbas U., Adami C., Arnouts S., Bel J., Bolzonella M., Bottini D., Branchini E., Burden A., Cappi A., Coupon J., Cucciati O., Davidzon I., de la Torre S., De Lucia G., et al. 2013, ArXiv e-prints

Hinshaw G., Larson D., Komatsu E., Spergel D. N., Bennett C. L., Dunkley J., Nolta M. R., Halpern M., Hill R. S., Odegard N., Page L., Smith K. M., Weiland J. L., et al. 2012, ArXiv e-prints

Hockney R. W., Eastwood J. W., 1988, Computer simulation using particles

Kormendy J., 1999, in D. R. Merritt, M. Valluri, & J. A. Sellwood ed., Galaxy Dynamics - A Rutgers Symposium Vol. 182 of Astronomical Society of the Pacific Conference Series, The Central Structure of Elliptical Galaxies and the Stellar-Dynamical Search for Supermassive Black Holes. pp 124–+

Kormendy J., Fisher D. B., Cornell M. E., Bender R., 2009, ApJS, 182, 216

Kravtsov A. V., Borgani S., 2012, ARA&A, 50, 353

Lacey C., Cole S., 1993, MNRAS, 262, 627

Laine S., van der Marel R. P., Lauer T. R., Postman M., O'Dea C. P., Owen F. N., 2003, AJ, 125, 478

Lauer T. R., Faber S. M., Gebhardt K., Richstone D., Tremaine S., Ajhar E. A., Aller M. C., Bender R., Dressler A., Filippenko A. V., Green R., Grillmair C. J., Ho L. C., Kormendy J., Magorrian J., Pinkney J., Siopis C., 2005, AJ, 129, 2138

Leauthaud A., George M. R., Behroozi P. S., Bundy K., Tinker J., Wechsler R. H., Conroy C., Finoguenov A., Tanaka M., 2012, ApJ, 746, 95

Lilly S. J., Le Fèvre O., Renzini A., Zamorani G., Scodeggio M., Contini T., Carollo C. M., Hasinger G., Kneib J.-P., Iovino A., Le Brun V., Maier C., Mainieri V., Mignoli M., Silverman J., et al. 2007, ApJS, 172, 70

Lin Y.-T., Mohr J. J., Stanford S. A., 2003, The Astrophysical Journal, 591, 749

Lin Y.-T., Stanford S. A., Eisenhardt P. R. M., Vikhlinin A., Maughan B. J., Kravtsov A., 2012, ApJ, 745, L3

McCarthy I. G., Frenk C. S., Font A. S., Lacey C. G., Bower R. G., Mitchell N. L., Balogh M. L., Theuns T., 2008, MNRAS, 383, 593

McDonald M., Veilleux S., Rupke D. S. N., Mushotzky R., Reynolds C., 2011, ApJ, 734, 95

Moster B. P., Naab T., White S. D. M., 2013, MNRAS, 428, 3121

Narayan R., Bartelmann M., 1996, ArXiv Astrophysics e-prints

Navarro J. F., Frenk C. S., White S. D. M., 1996, ApJ, 462, 563

Newman A. B., Treu T., Ellis R. S., Sand D. J., Nipoti C., Richard J., Jullo E., 2012, ArXiv e-prints

Peacock J. A., 2003, ArXiv Astrophysics e-prints

Peterson J. R., Paerels F. B. S., Kaastra J. S., Arnaud M., Reiprich T. H., Fabian A. C., Mushotzky R. F., Jernigan J. G., Sakelliou I., 2001, A&A, 365, L104

Plionis M., 2002, in Cotsakis S., Papantonopoulos E., eds, Cosmological Crossroads Vol. 592 of Lecture Notes in Physics, Berlin Springer Verlag, The Quest for the Cosmological Parameters. p. 147

Postman M., Franx M., Cross N. J. G., Holden B., Ford H. C., Illingworth G. D., Goto T., Demarco R., Rosati P., Blakeslee J. P., Tran K.-V., Benítez N., Clampin M., Hartig G. F., Homeier N., Ardila D. R., Bartko F., Bouwens R. J., et al. 2005, ApJ, 623, 721

Press W. H., Schechter P., 1974, ApJ, 187, 425

Puchwein E., Springel V., Sijacki D., Dolag K., 2010, MNRAS, 406, 936

Quillen A. C., Bower G. A., Stritzinger M., 2000, ApJS, 128, 85

Riess A. G., Filippenko A. V., Challis P., Clocchiatti A., Diercks A., Garnavich P. M., Gilliland R. L., Hogan C. J., Jha S., Kirshner R. P., Leibundgut B., Phillips M. M., Reiss D., Schmidt B. P., Schommer R. A., et al. 1998, AJ, 116, 1009

Rubin V. C., Ford Jr. W. K., 1970, ApJ, 159, 379

Rudick C. S., Mihos J. C., Harding P., Feldmeier J. J., Janowiecki S., Morrison H. L., 2010, ApJ, 720, 569

Sijacki D., Springel V., Matteo T. D., Hernquist L., 2007, Monthly Notices of the Royal Astronomical Society, 380, 877

Trujillo I., Erwin P., Asensio Ramos A., Graham A. W., 2004, AJ, 127, 1917

Vikhlinin A., Burenin R. A., Ebeling H., Forman W. R., Hornstrup A., Jones C., Kravtsov A. V., Murray S. S., Nagai D., Quintana H., Voevodkin A., 2009, ApJ, 692, 1033

White S. D. M., Rees M. J., 1978, MNRAS, 183, 341

Zwicky F., 1933, Helvetica Physica Acta, 6, 110

Chapter 2

Methods

This Chapter offers a description of the methods adopted to obtain the results showed in this Thesis. In the first Section the importance of numerical techniques applied to the study of the growth of cosmic structure is discussed. The second Section is dedicated to the description of the RAMSES code that was adopted to perform the numerical simulations analysed in detail in the published Papers which constitute the core of this Thesis.

2.1 The need for numerical cosmological simulations

In the hierarchical scenario of structure formation the collapse of small scale density perturbations happens before the collapse on larger scales. Large structures grow in a complex manner by the smooth accretion of mass, accretion of smaller collapsed structures and mergers. The large scale structure morphology is mainly determined by the dynamics of the cold dark matter (CDM) which constitutes the dominant fraction of matter in the universe. Nonetheless, a large quantity of physical processes related to the presence of baryonic matter in the universe can influence the properties of cosmic structure on the scale of galaxy clusters or lower. The properties of collapsed objects strongly depend on their history, e.g. galaxies accreted by a galaxy cluster can survive, evolve or be completely disrupted depending on the physical conditions of the intracluster medium and on the depth of the cluster potential well. Merging events are sources of complex hydrodynamical phenomena like shocks, turbulence and production of relativistic particles. Furthermore, these phenomena can lead to the amplification of intergalactic magnetic fields and to the acceleration of cosmic rays. All these processes can strongly modify the physical condition of the intergalactic and

interstellar media and influence the process of star formation in galaxies. The morphology of galaxies depends on the availability of cold ($T \lesssim 10^4$ K) gas, on the conditions of the intracluster medium, on dynamical processes acting within the galaxy, on the merger history and on the interaction with the environment. The formation and evolution of stars modify the physical properties of the surrounding environment, e.g. through stellar winds, radiation pressure and supernovae explosions, and these ends up influencing the star formation process itself. This phenomenon is usually referred to as stellar feedback. Several other processes are thought to be sources of feedback, in particular the presence of supermassive black holes in galaxies in their active phase as Active Galactic Nuclei.

The large variety of processes and the huge dynamic range of scales needed to be considered make the modeling of the growth of cosmic structure extremely challenging. A completely self-consistent and easily computable analytical model of structure formation does not exist. In order to model the relevant physical processes realistically scientists adopt numerical simulations based on solvers for the equations used to model the system. The main advantage of this approach is that simulations are able to follow the highly non-linear dynamics of structure formation. The drawbacks are represented by the fact that the solutions obtained through numerical simulations are approximate, can be affected by numerical errors and by the limited dynamic range resolved in the numerical realisations of the Universe.

2.1.1 Modeling of Cold Dark Matter

Cold dark matter in cosmological simulations is modeled as a self-gravitating collisionless fluid. N-body techniques are usually adopted to model the system: the phase-space distribution function $f(\mathbf{x}, \mathbf{p}, t)$ of the system is sampled by a set of N tracer particles whose momenta and positions are advanced in time according to the equations of Newtonian dynamics (see Subsection 2.2.3). The acceleration acting on each particle is only due to the self-gravity of the system and, for collisionless systems, can be computed as $-\bigtriangledown\phi$, where ϕ is the gravitational potential. The gravitational potential is determined as a solution of the Poisson equation $\Delta_x\phi = 4\pi G\rho$ (see Subsection 2.2.2), where ρ is the matter density field. Several algorithms exist for force calculation in numerical simulations:

- Direct summation: the total potential is obtained by summation of the contributions from each particle. For the standard version of the algorithm the computing time scales as N^2, where N is the number of particles. This algorithm can be very slow for a large number of

particles.

- Particle-Mesh method: the force and the density are considered as a fields computed on a cartesian mesh. Finite difference approximations and Fast Fourier Transform techniques are used to obtain the value of the force at the mesh nodes. Interpolation methods are used to compute the density field at the mesh nodes and to interpolate the force values back to the particles. The computing time scales as $N + N_g \log N_g$, where N is the number of particles and N_g is the number of mesh nodes. An obvious advantage is that the algorithm is much faster than direct summation for large N. The drawback of this algorithm is that the dynamic range can be strongly limited by the number of mesh nodes.

- Relaxation method: when Adaptive Mesh Refinement (see the Subsection 2.2.1) techniques are used the mesh can have arbitrarily shaped boundaries. The Poisson equation can be treated as a Dirichlet boundary problem. The potential is found using an iterative algorithm which starts with an initial guess for the solution and relaxes it to an "equilibrium"solution. The solution is usually obtained after a few iterations.

- Tree method: the potential is computed using a hierarchical multipole expansion. Distant particles are grouped in large cells and their gravity is accounted for by means of a single multipole force. The computing time scales as $N \log N$, making it much faster than direct summation for a large number of particles. The most relevant drawback of the standard tree technique is that the force computed via this algorithm is usually only an approximation of the true force.

- Hybrid methods: these algorithms are based on the splitting of the gravitational potential in two terms, a large scale one and a small scale one. The large scale component of the force can be computed using Particle-Mesh methods, while the small scale component is computed using more accurate methods. For example, in the so-called TreePM approach the small scale contribution is computed using the tree algorithm; in the so-called P^3M method the small scale contribution is computed using the direct summation algorithm.

For an interesting discussion on the most common techniques adopted for collisionless cosmological simulations, see e.g. Hockney & Eastwood (1988), Dolag et al. (2008) and references therein.

It is important to stress that in most codes adopted for cosmological simulations, the stellar component of baryonic matter is modeled adopting

N-body techniques identical to the ones just described, i.e. on the scales considered for cosmological simulations the stellar component is treated as a collisionless fluid.

2.1.2 Modeling of Baryonic Matter

The largest fraction of baryonic matter is usually modeled as an inviscid fluid for which Euler equations need to be solved (see Subsection 2.2.4). This fluid is gravitationally coupled to cold dark matter by means of the Poisson equation. There are several approaches to solve for the hydrodynamics, however the most common ones adopted in the field of cosmological simulations can be grouped in three broad classes:

- Grid-based methods (Eulerian): the Euler equations are solved on a fixed grid. These methods rely on finite difference approximations for the differential operators, interpolation techniques to compute the values of the fluid quantities at cell boundaries and on Riemann solvers to calculate fluxes at cell boundaries. Grid-based methods suffer from limited spatial resolution and can suffer from truncation errors. However, these methods can be coupled with Adaptive Mesh Refinement (see the Subsection 2.2.1) to obtain adaptive resolution and resolve the flow in a quasi-Lagrangian way.

- Smoothed Particle Hydrodynamics (SPH, Lagrangian): fluid elements are traced by particles and fluid quantities are computed by averaging on several particles via a weight function called SPH kernel. In this formalism, the SPH version of Euler equations can be used to evolve the properties and positions of the particles in time. High resolution can be obtained in dense regions, however degraded resolution is typically obtained in low density regions, due to the limited number of particles.

- Moving-mesh techniques: these techniques use meshes that move with the flow and they have been adopted to combine the advantages of grid-based methods with those of SPH methods. See e.g. Springel (2010).

Code comparison tests between grid-based and SPH-based codes have been performed, showing that grid-based methods can typically better resolve hydrodynamical instabilities (Agertz et al., 2007): the standard implementation of SPH introduces spurious pressure forces near contact discontinuities. Several modified versions of SPH have been proposed in the recent years with the aim of solving these problems; see e.g. Price (2012) for a review.

The Santa Barbara Cluster Comparison Project (Khokhlov, 1998) showed general agreement between the density and velocity dispersion profiles measured in a galaxy cluster simulated using codes with different hydrodynamical solvers (SPH and grid-based) but identical initial conditions. More disagreement was found in the X-ray properties and the baryon fractions. More recently, the Aquila Project (Scannapieco et al., 2012) compared the performances of hydrodynamical codes in shaping the properties of a massive galaxy. The same initial conditions were used for all the simulations but different implementations of feedback mechanisms were adopted by each group participating to the project. The results show that very different properties (stellar masses, gas masses, morphology) can be obtained for simulated galaxies when the implementation of feedback mechanisms is varied. This problem is strictly related to the limited dynamical range of cosmological simulations that forces scientists to adopt simplified phenomenological models, the so-called sub-grid models, to account for complex phenomena that take place at scales smaller than those resolved by the simulations, but influence the properties of the system at larger scales. Gas cooling/heating, the multiphase nature of the interstellar medium, star formation and all the feedback mechanisms implemented in state-of-art cosmological hydrodynamical simulations are accounted for by using simplified sub-grid models. Efforts are being made in implementing more realistic sub-grid models and in increasing the dynamic range of simulations to be able to self-consistently model small scale processes, with the aim of reducing the tension between the predictions of different codes which adopt different sub-grid implementations.

2.2 The RAMSES code

The results discussed in this Thesis were obtained by analysing high resolution N-body and hydrodynamical simulations performed with the RAMSES code (Teyssier, 2002). RAMSES is a multi-purpose code based on the Adaptive Mesh Refinement (AMR) technique, with a tree-based data structure used to allow recursive refinement of grid cells. The code is able to follow the simultaneous evolution of a collisionless fluid (used to model e.g. dark matter, stars) gravitationally coupled with an inviscid fluid (used to model baryonic matter). The evolution of the collisionless component is computed using N-body techniques, whereas the evolution of the inviscid fluid is followed adopting a hydrodynamical solver based on a second-order Godunov method. The gravitational coupling between the two fluid is obtained by considering the total density field and solving for the Poisson equation to compute the gravitational potential. When linked to the MPI libraries, RAMSES

can be run on massively parallel architectures, making the code suitable to solve a large amount of astrophysical problems that require high resolution and high dynamic range simulations.

2.2.1 Adaptive Mesh Refinement

The fundamental data structure in RAMSES is a *Fully Threaded Tree* (FTT) (Khokhlov, 1998): the simulation volume is split in groups of $2^{N_{dim}}$ contiguous cells called *octs*. Each oct belongs to a given level of refinement l. The base of the tree structure is a Cartesian grid (coarse grid) at level $l = 0$. The octs at each level are organised in a double linked list used to easily access the data structure. User-defined criteria can be used to split a cell at level l and create an oct at level $l + 1$ within it. This allows the user to obtain the required spatial resolution only in regions where that is needed. Each oct at level l points to the previous and the next oct in the linked list, but also to the parent cell at level $l - 1$, to the $2 \times N_{dim}$ neighboring parent cells at level $l - 1$ and to the $2^{N_{dim}}$ child octs at level $l + 1$. If a cell has no children it is called a *leaf cell*, otherwise it is called a *split cell*.

Time integration can be performed for each level independently. The user can choose to integrate all levels with the same time step Δt or to use a different time step for each level. When the latter choice is made, if level l is advanced in time with time step Δt_l, then level $l + 1$ is advanced in time using 2 time steps Δt^1_{l+1} and Δt^2_{l+1}, with a synchronization constraint $\Delta t_l = \Delta t^1_{l+1} + \Delta t^2_{l+1}$.

2.2.2 The Poisson solver

The computation of the gravitational potential $\phi(\mathbf{x})$ is essential to follow the evolution of self-gravitating systems. This means that the Poisson equation

$$\Delta_x \phi = 4\pi G \rho \tag{2.1}$$

needs to be solved at each time step in order to follow the evolution of the system.

In RAMSES the first step is computing the total density field $\rho(\mathbf{x})$. The collisionless fluid is represented by a distribution of N massive particles, whereas the inviscid fluid is represented by cell-based variables describing its state (density, velocity, pressure, etc.). Particles are organized in a linked list: all particles belonging to the same oct are linked together. First, a CIC scheme is used to calculate the contribution to the total density field from the collisionless particles. The total density field is computed as the sum of the contributions coming from the two fluids.

Once the total density field is known, the Poisson solver is used to compute the potential. The Poisson equation is solved level by level and boundary conditions are passed from the coarser to the finer grids via a linear interpolation. Boundary conditions are defined in temporary buffer regions surrounding the level domain. At level $l = 0$ the Poisson equation is solved using a standard Fast Fourier Transform (FFT) technique. At level $l > 0$ the potential is computed using the Gauss-Seidel (GS) relaxation method (Press et al., 1992). In two dimensions, for unit grid spacing, the basic GS iteration is given by

$$\phi_{i,j}^{n+1} = \frac{1}{4}(\phi_{i+1,j}^{n} + \phi_{i-1,j}^{n} + \phi_{i,j+1}^{n} + \phi_{i,j-1}^{n}) - \frac{1}{4}\rho_{i,j}. \tag{2.2}$$

The iteration is first applied to update the potential for 'black'cells defined by i odd (even) and j odd (even), and then to update the potential for 'red'cells defined by i odd (even) and j even (odd). Finally the result is corrected using the over-relaxation parameter ω:

$$\phi_{i,j}^{n+1} = \omega\phi_{i,j}^{n} + (1-\omega)\phi_{i,j}^{n+1}, \tag{2.3}$$

with $1 < \omega < 2$. The optimal value for ω for a $N \times N$ Cartesian grid is given by Press et al. (1992):

$$\omega \simeq \frac{2}{1 + \alpha\frac{\pi}{N}}, \tag{2.4}$$

with $\alpha = 1$ for Dirichlet boundary conditions and $\alpha = 2$ for periodic boundary conditions. The value of ω appropriate for an irregular AMR grid can be set looking at the average size of mesh patches at a given level, $\langle L \rangle$, which substitutes N in Equation 2.4. Empirical tests showed that $\langle L \rangle \sim 20$, and $\omega \sim 1.7$ are appropriate values for cosmological simulations.

2.2.3 N-body integrator

The evolution of the position and velocities of the particles composing a collisionless N-body system is described by the following equations of motion:

$$\frac{d\mathbf{x}_p}{dt} = \mathbf{v}_p \text{ and } \frac{d\mathbf{v}_p}{dt} = -\bigtriangledown_x \phi. \tag{2.5}$$

These equations are equivalent to the Vlasov-Poisson equations expressed in terms of particles.

In RAMSES a second-order midpoint scheme is adopted to advance the particles in time. This scheme reduces to the standard second-order leapfrog

scheme for constant time steps. First, the velocities and positions of the particles are updated by a predictor step

$$\mathbf{v}_p^{n+1/2} = \mathbf{v}_p^n - \bigtriangledown\phi^n \Delta t^n/2 \tag{2.6}$$

$$\mathbf{x}_p^{n+1} = \mathbf{x}_p^n + \mathbf{v}_p^{n+1/2}\Delta t^n. \tag{2.7}$$

Then a corrector step is performed:

$$\mathbf{v}_p^{n+1} = \mathbf{v}_p^{n+1/2} - \bigtriangledown\phi^{n+1} \Delta t^n/2 \tag{2.8}$$

The acceleration $-\bigtriangledown\phi$ is computed first on the mesh using a 5-points finite difference approximation of the gradient and then it is interpolated back to the particles of the current level. If a particle belongs to level l but its cloud lies partially outside the level volume, the acceleration is interpolated from the mesh of level $l-1$. If a particle exits level l with time step Δt_l, the corrector step is applied at level $l-1$, using Δt_l instead of Δt_{l-1}. This technique allows second-order accuracy in time when a single time step scheme is adopted, however only first-order accuracy in time can be obtained for the trajectories of particles crossing refinement boundaries. However, this worse accuracy turns out to have negligible effect on the particle distribution in cosmological simulations (see Teyssier 2002 for further details).

2.2.4 Hydrodynamical solver

The hydrodynamical solver implemented in RAMSES integrates the Euler equations describing an inviscid fluid expressed in their conservative form:

$$\frac{\partial\rho}{\partial t} + \bigtriangledown\cdot(\rho\mathbf{u}) = 0 \tag{2.9}$$

$$\frac{\partial}{\partial t}(\rho\mathbf{u}) + \bigtriangledown\cdot(\rho\mathbf{u}\otimes\mathbf{u}) + \bigtriangledown p = -\rho\bigtriangledown\phi \tag{2.10}$$

$$\frac{\partial}{\partial t}(\rho\mathrm{e}) + \bigtriangledown\cdot[\rho\mathbf{u}(\mathrm{e}+p/\rho)] = -\rho\mathbf{u}\cdot\bigtriangledown\phi \tag{2.11}$$

where ρ is the fluid mass density, $\mathbf{u}$ is the fluid velocity, e is the specific total energy and p is the thermal pressure. The system of equations is closed by the equation of state:

$$p = (\gamma-1)\rho\left(\mathrm{e} - \frac{u^2}{2}\right). \tag{2.12}$$

Equation 2.11 is conservative only when the source terms due to gravity are negligible. If this is not the case, the total energy is conserved at the percent level.

The numerical discretization adopted in RAMSES for Euler equations has the form

$$\frac{U_i^{n+1} - U_i^n}{\Delta t} + \frac{F_{i+1/2}^{n+1/2} - F_{i-1/2}^{n+1/2}}{\Delta x} = S_i^{n+1/2} \tag{2.13}$$

where U_i^n represents the cell averaged value of $(\rho, \rho\mathbf{u}, \rho\mathrm{e})$ at time t^n and cell i. The quantities $F_{i+1/2}^{n+1/2}$ represents time centered fluxes across cell interfaces and they are computed using a second-order Godunov Piecewise Linear Method (PLM) (Teyssier, 2002; Toro, 1997). Directional splitting can be applied according to the user's choice. The quantities $S_i^{n+1/2}$ represent the time centered gravitational source terms on the right hand sides of the Euler equations. The gravitational source terms are computed as:

$$S_i^{n+1/2} = \left(0, \frac{\rho_i^n \bigtriangledown \phi_i^n + \rho_i^{n+1} \bigtriangledown \phi_i^{n+1}}{2}, \frac{(\rho\mathbf{u})_i^n \bigtriangledown \phi_i^n + (\rho\mathbf{u})_i^{n+1} \bigtriangledown \phi_i^{n+1}}{2}\right). \tag{2.14}$$

Hydrodynamics is solved in each oct and boundary conditions are specified for each oct by 2 ghost zones in each side and in each direction. This means that $3^{N_{dim}}$ neighboring octs are used to provide boundary conditions to solve hydrodynamics for each oct. A Riemann solver (Toro, 1997) is used to compute the fluxes at cell interfaces. A recursive call of the same routine allows to advance the system in time at all different levels. At level l the procedure can be summarized as:

1. Generate refinements at level $l+1$ by interpolation of the variables at level l.

2. Calculate the time step Δt_l using the Courant Friedrich Levy (CFL) condition (Subsection 2.2.5) and the constraint $\Delta t_l \leq \Delta t_{l-1}$.

3. Advance the solution in time for level $l+1$, once for the single time step scheme, twice for the adaptive time step scheme.

4. Modify the time step Δt_l taking into account the constraint $\Delta t_l = \Delta t_{l+1}$ for the single time step scheme, or $\Delta t_l = \Delta t_{l+1}^1 + \Delta t_{l+1}^2$ for the adaptive time step scheme.

5. Compute boundary conditions by interpolation of level $l-1$ variables.

6. Compute fluxes at cell boundaries using the Godunov solver.

7. Replace the fluxes at coarse-fine interfaces by averaging the fluxes computed at level $l+1$.

8. For leaf cells update the variables using these fluxes. For split cells update the variables by averaging the updated variables of level $l + 1$.

9. Build a new refinement map.

As can be deduced from the description of this scheme, the solution at the coarse level is assumed to remain constant during the advance in time of the fine solution. The accuracy of the scheme at coarse-fine boundaries can be reduced from second to first-order in time in the adaptive time step case, however the global solution remains second-order accurate (Khokhlov, 1998; Teyssier, 2002).

2.2.5 Time step computation

The time step is computed for each level independently by taking into account several aspects of the modeled physical system. First of all, the evolution of the coupled N-body and hydrodynamical system can be accurately followed only if the time step is smaller than the minimum free-fall time:

$$\Delta t_l^1 = C_1 \times \min_l(t_{\rm ff}), \tag{2.15}$$

with $C_1 < 1$.

A second constraint comes from imposing particles to move only by a fraction of the local cell size Δx_l:

$$\Delta t_l^2 = C_2 \times \Delta x_l / \max_l(v_p), \tag{2.16}$$

with $C_2 < 1$.

A third constraint is imposed by the Courant Friedrich Levy condition for hydrodynamics:

$$\Delta t_l^3 = C_3 \times \Delta x_l / \max_l(|u_x| + c, |u_y| + c, |u_z| + c), \tag{2.17}$$

where c is the sound speed and (u_x, u_y, u_z) are the components of the fluid velocity. The quantity $C_3 < 1$ is the Courant factor.

For cosmological simulations a fourth requirement is imposed by requiring that the expansion factor $a_{\rm exp}$ should not vary more than $C_4 \simeq 10\%$ during one time step. This constraint can be expressed as

$$\Delta t_l^4 = C_4 \times \frac{a_{exp}}{\dot{a}_{exp}}. \tag{2.18}$$

The actual time step for level l is then taken to be the minimum of all the values enumerated above: $\Delta t_l = \min(\Delta t_l^1, \Delta t_l^2, \Delta t_l^3, \Delta t_l^4)$.

2.2.6 Galaxy formation with RAMSES

The RAMSES code is extremely suitable to study problems related to galaxy formation and dynamics: the N-body solver can be used to follow the evolution of dark matter and stars (modeled as a collisionless fluid), while the hydrodynamical solver can be used to follow the gaseous phase of the baryonic matter. Many physical processes that play a relevant role in galaxy formation have been modeled and implemented into the code. First of all, gas heating and cooling are both accounted for by the energy equation: a Sutherland & Dopita (1993) cooling function is adopted to model gas cooling, and the effect of a photo-ionizing UV background is accounted for following Haardt & Madau (1996). Star formation is implemented using a simple prescription to turn cold and dense gas into collisionless stellar particles (Rasera & Teyssier, 2006). Many works have been published on the implementation of feedback processes that regulate the star formation activity, e.g. supernovae feedback (Dubois & Teyssier, 2008; Agertz et al., 2012; Teyssier et al., 2013), and AGN feedback (Dubois et al., 2011; Teyssier et al., 2011; Dubois et al., 2012). Recently, RAMSES has been successfully used to study disk galaxy formation in the context of the ΛCDM cosmological scenario (Agertz et al., 2009; Agertz et al., 2011).

2.2.7 Interstellar medium, star formation and stellar feedback

The simulations presented in this Thesis adopt a sub-grid model for the interstellar medium (ISM) and for star formation. The dynamic range of these simulations is limited and does not allow to resolve the multi-phase structure of the ISM. We assume an effective equation of state (EOS) to capture the turbulent, multi-phase nature of the ISM. The model is based on a temperature floor given by

$$T_{\rm floor} = T_* \left(\frac{n_H}{n_*} \right)^{\Gamma - 1} \tag{2.19}$$

where $n_* = 0.1$ H/cc is the density threshold that defines the star forming gas, $T = 10^4$ K is a typical temperature mimicking thermal and turbulent motions in the ISM, and Γ is an effective polytropic index that controls the stiffness of the equation of state. The gas is allowed to be heated above $T_{\rm floor}$, but it is not allowed to cool below this threshold. Enforcing this temperature floor also allows the simulations to always resolve the Jeans length.

All cells whose density is $n_H > n_*$ are allowed to convert their gas into stars. Stars are represented by collisionless particles of mass m_*. The mass

of the stellar particles is limited by the minimum baryon resolution element, which is set by the resolution. Each stellar particle must be thought as representing an entire stellar population. Stellar particles are spawned at a rate given by

$$\dot{\rho}_* = \epsilon_* \frac{\rho_{\rm gas}}{t_{\rm ff}} \tag{2.20}$$

where $\rho_{\rm gas}$ is the total gas density within a cell, ϵ_* is the star formation efficiency and $\rho_{\rm gas}$ is the local free fall time defined by

$$t_{\rm ff} = \sqrt{\frac{3\pi}{32G\rho}}. \tag{2.21}$$

Supernovae feedback is also implemented in the code. For each star particle, we assume that 10 per cent of its mass will go supernova after 10 Myr. We consider a supernova energy of 10^{51} erg and 1 $M_\odot$ of ejected metals per 10 $M_\odot$ average progenitor mass. This supernovae feedback was implemented in the code using the "delayed cooling" scheme (Stinson et al., 2006) in which cooling in star forming cells is suppressed for 10 Myr.

2.2.8 Growth of Supermassive Black Holes and AGN feedback

Supermassive Black Holes (SMBHs) constitute the engine of Active Galactic Nuclei. The fuel is provided by gas that orbits around the black holes and is accreted onto them due to dissipative processes. A fraction of the rest mass energy of the accreted gas is converted in feedback energy that couples with the gas surrounding the AGN. The model here adopted does not resolve all the details of gas accretion and generation of feedback energy. It is aimed at capturing the features of the AGN feedback process relevant for galaxy formation simulations which do not resolve the small scales at which AGN physics takes place. This model is a modified version of the one adopted by Booth & Schaye (2009) for SPH simulations.

The seeds for SMBHs formation are thought to be either Pop III stars (Madau & Rees, 2001), or a result of direct collapse of baryonic material within low angular momentum halos (Bromm & Loeb, 2003; Begelman et al., 2006). In both cases the seed SMBHs are expected to grow quickly to $M_{\rm BH,s} = 10^5$ $M_\odot$ when they will start to interact with the environment and self-regulate their gas accretion rate. This black hole mass is at least one order of magnitude lower than the minimum SMBH mass observed in the $M_{\rm BH} - \sigma$ relation (Gebhardt et al., 2000; Gültekin et al., 2009), therefore $M_{\rm BH,s}$ can be considered to be the prototypical seed SMBH mass.

In this model, sink particles are used to simulate SMBHs, following the prescription of Krumholz et al. (2004). When the following conditions are met, a new SMBH is created in the simulation:

- The stellar density has to be greater than 0.1 H/cc ($2.4\times10^6 \mathrm{M}_\odot$ kpc^{-3}). This ensures that SMBHs form in stellar systems.
- The stellar 3D velocity dispersion is required to be greater than 100 km/s. With this condition the line-of-sight velocity dispersion is $\sigma_{1\mathrm{D}} \geq$ 60 km/s, in agreement with the observed $M_{\mathrm{BH}} - \sigma$ relation.
- The gas density has to be greater than 1 H/cc. With this conditions seed black holes form in the nuclear region of star forming disks.
- No other sink particle is present within 10 kpc. Seed SMBH will not be created within 10 kpc from an old SMBH residing at the center of a galaxy.

Each seed SMBH has a fixed mass $M_{\mathrm{BH}} = 10^5$ M$_\odot$ and a fixed radius $r_{\mathrm{sink}} = 4\Delta x$, where Δx is the spatial resolution in physical units. We assume that the SMBH mass is homogeneously distributed inside a sphere of radius r_{sink}, and we add this density distribution to the total mass density when solving the Poisson equation. Like dark matter and star particles, sink particles are advanced in time by interpolating the gravitational force back to the sink position using the inverse CIC scheme.

The SMBHs are allowed to grow by mass accretion from the surrounding gas. The mass accretion rate onto each SMBH is computed using a modified Bondi-Hoyle formula

$$\dot{M}_{\mathrm{BH}} = \alpha_{\mathrm{boost}} \frac{4\pi \mathrm{G}^2 M_{\mathrm{BH}}^2 \rho}{(c_{\mathrm{s}}^2 + u^2)^{3/2}} \tag{2.22}$$

where ρ, c_{s} and u are the average gas density, sound speed and relative velocity within the sink radius, all computed following the approach of Krumholz et al. (2004). The parameter α_{boost} was introduced by Springel et al. (2005) to account for unresolved multiphase turbulence in the SMBH environment, and its value was originally chosen as constant. Numerical studies by Booth & Schaye (2009) show that α_{boost} should instead be considered as a function of the local density: it should be close to unity in low density regions, it should increase in high density regions, in order to match the sub-grid model used for the unresolved turbulence in the disks. As proposed by Booth & Schaye (2009), we adopt

$$\begin{aligned} \alpha_{\mathrm{boost}} &= \left(\frac{n_{\mathrm{H}}}{n_*}\right)^2 \quad \text{if} \quad n_{\mathrm{H}} > n_* = 0.1 \text{ H/cc}, \\ \alpha_{\mathrm{boost}} &= 1 \quad \text{otherwise.} \end{aligned} \tag{2.23}$$

The choice for this particular form of $\alpha_{\rm boost}$ is strictly dependent on the chosen EOS for the gas.

Each SMBH is not allowed to accrete at a rate that exceeds the Eddington limit

$$\dot{M}_{\rm ED} = \frac{4\pi {\rm G} M_{\rm BH} m_{\rm p}}{\epsilon_{\rm r} \sigma_{\rm T} c} \quad \text{with} \quad \epsilon_{\rm r} \simeq 0.1. \tag{2.24}$$

where $\epsilon_{\rm r}$ is is the efficiency at which accreting gas rest mass energy is converted into radiation. To enforce this upper limit we always set the accretion rate to

$$\dot{M}_{\rm acc} = \min(\dot{M}_{\rm BH}, \dot{M}_{\rm ED}) \tag{2.25}$$

At each time step, a total gas mass of $\dot{M}_{\rm acc}\Delta t$ is removed from all cells within the sink radius, with the same weighting scheme as the one used to define average quantities (Krumholz et al., 2004). In order to prevent the gas density from vanishing or becoming negative, we do not remove more than 50% of the gas at each time step.

The adopted AGN feedback recipe allows SMBHs to have a self-regulated SMBH growth (Sijacki et al., 2007; Cattaneo & Teyssier, 2007; Booth & Schaye, 2009), by injecting thermal energy directly into the gas surrounding the black hole. This thermal energy is supposed to mimic the effect of different kinds of energy that an AGN can inject into the gas (radiation, high cosmic rays, jets...). If the black hole mass is too low, the amount of energy injected in the gas will not be able to heat it up, so it will remain cold and will accrete onto the SMBH at rates close to Eddington limit. In this case the SMBH growth can proceed exponentially with time, with e-folding time scale equal to the Salpeter time

$$t_{\rm S} = \frac{\epsilon_{\rm r} \sigma_{\rm T} c}{4\pi G m_{\rm p}} \approx 45{\rm Myr} \tag{2.26}$$

Feedback becomes efficient as long as the SMBH continues to grow, until the injected energy is enough to unbind the gas surrounding the black hole. In this regime accretion becomes Bondi-Hoyle limited and mass growth proceeds more slowly.

At each time step we compute the thermal energy injected in the gas surrounding each black hole as

$$\Delta E = \epsilon_{\rm c} \epsilon_{\rm r} \dot{M}_{\rm acc} c^2 \Delta t. \tag{2.27}$$

where $\epsilon_{\rm c}$ is the coupling efficiency, i.e. the fraction of radiated energy that is coupled with the surrounding gas. The correct value for ϵ_c can be set requiring the simulations to reproduce the observed $M_{\rm BH} - \sigma$ relation; we use the fiducial value $\epsilon_{\rm c} \simeq 0.15$ (Booth & Schaye, 2009). The energy ΔE is

not immediately injected in the gas, but its accumulated and stored in a new variable $E_{\rm AGN}$, so that we can avoid the gas instantly radiating away this energy via atomic line cooling. We release this energy within the sink radius when

$$E_{\rm AGN} > \frac{3}{2} m_{\rm gas} k_{\rm B} T_{\rm min} \tag{2.28}$$

where $m_{\rm gas}$ is the gas mass within the sink radius and $T_{\rm min}$ is the minimum feedback temperature. $T_{\rm min}$ should be chosen to be at least 10^7 K, the temperature above which line cooling is not very efficient, so that the resulting feedback is independent of the value of $T_{\rm min}$. In our simulations we adopt the fiducial value $T_{\rm min} = 10^7$ K. We distribute the energy within the sink radius in a volume weighted fashion.

This model allows us to phenomenologically reproduce the two extreme regimes in which AGN feedback is thought to work (Sijacki et al., 2007). "Quasar mode" is obtained in the case of cold dense gas accretion, more energy is required to reach the energy threshold. A large amount of energy is accumulated and released in a burst when the energy threshold is reached. "Radio mode" is obtained in the case of hot diffuse gas accretion, less energy is required to reach the threshold. Energy is injected in the gas in a quasi-continuous fashion.

2.2.9 Improvements to the AGN feedback scheme

The AGN feedback scheme we adopted for most of the results of this Thesis can be improved under several aspects. We are currently testing new options that may make the scheme more robust and realistic.

There are a few main issues that one needs to take care of when implementing AGN feedback schemes:

- Sink/black hole formation.
- Black hole dynamics and merging.
- Mass accretion onto sink particles.
- Feedback energy injection into the gas.

The theory of formation of primordial massive black holes predicts that these objects can be formed either as the end-product of the collapse of Pop III stars (Madau & Rees, 2001), or as result of direct collapse of baryonic material within low angular momentum halos (Bromm & Loeb, 2003; Begelman et al., 2006). Given these considerations, it is more natural to associate sink formation in cosmological simulations only to gas properties. In the new

version of the scheme, we do not form sink particles requiring that the stellar density is high enough. The scheme is based on a *clump finder* initially developed by Andreas Bleuler and modified by me to be used as a fundamental element of the AGN feedback scheme. The clump finder is a group of routines that are called at every coarse time step. The clump finder scans the AMR grid and finds density peaks above a given density threshold, then creates spatially disconnected patches which represent gas clumps associated to the density peaks. In the configuration used for the AGN feedback scheme, the density threshold is fixed in comoving units to $\rho_{\rm cf} \sim 10^{-29}$ g/cm^3 and all the peak patches that are physically connected are merged together. Our tests show that the final spatial distribution of peak patches matches quite well the gas contained in dark matter halos at high redshift, i.e. the regions where seed SMBH should form.

Sink particles are formed within peak patches only if the following conditions are met:

- The peak patch does not contain a sink particle within its boundaries.
- The peak patch is gravitationally bound.
- The accretion rate onto the central regions of the clump is high enough.

The accretion rate used for the third condition is computed as

$$\dot{M}_{\rm clump} = \frac{M_4}{t_{\rm ff}} \tag{2.29}$$

where $t_{\rm ff}$ is the local free fall time and M_4 is the gas mass enclosed within a spherical region of radius equal to $R_4 = 4\Delta x$, where Δx is the cell size. We form a sink only if $\dot{M}_{\rm clump} > 30$ M$_\odot$/yr. This choice allows sinks to be formed only in the most massive halos at high redshift.

The mass of the sinks at formation $M_{\rm BH,s}$ is not a fixed value anymore. By assuming that the SMBH initially accretes mass at the Eddington rate and that the SMBH is able to heat the surrounding gas to a temperature of 10^7 K during the Salpeter time $t_{\rm S}$, we get an estimate for the mass of the seed SMBH:

$$M_{\rm BH,s} = \frac{10^{-5}}{\epsilon_{\rm c}} \dot{M}_{\rm clump} t_{\rm S}. \tag{2.30}$$

The trajectory of sink particles is integrated as if they were N-body particles. However, in the new version of our scheme, we include a sub-grid model for the drag force experimented by a black hole from the gas in the wake it forms as it moves. For the drag force, we adopt the standard formulae of Ostriker (1999). Black holes do not merge instantly when their sink region

overlap, as in the older scheme. In the new scheme, we merge two sinks only if the kinetic energy associated associated to their relative motion is lower than the potential energy of the two body system. This allows black holes to orbit around each other for relatively long times before merging.

The scheme to compute the accretion rate onto the SMBH has been modified. Recent theoretical work showed that modified Bondi-Hoyle formulae like the one in Equation 2.22 can overestimate the accretion rate in case of cold, supersonic gas accretion (e.g. Hobbs et al. (2012)). In this case the accretion rate is better approximated by the free fall rate:

$$\dot{M}_{\rm ff} = \frac{M_{\rm gas}(r < \lambda_J)}{t_{\rm ff}(r < \lambda_J)} \tag{2.31}$$

where $M_{\rm gas}(r < \lambda_J)$ is the gaseous mass enclosed within a sphere of radius equal to the Jeans length λ_J, and $t_{\rm ff}(r < \lambda_J)$ is the free fall time in the same region. In the new scheme, we correct for this problem by introducing a new formula for the accretion rate which interpolates between the Bondi-Hoyle regime and the free fall regime. We compute the accretion rate onto SMBHs as:

$$\dot{M}_{\rm BH} = 4\pi\alpha_{\rm boost}\tilde{r}_B^2 v_B \rho \tag{2.32}$$

where $\alpha_{\rm boost}$ is the correction factor discussed in the previous section, $v_B = \sqrt{u^2 + c_{\rm s}^2}$, and $\tilde{r}_B$ is a modified Bondi radius defined by

$$\tilde{r}_B = \min(r_B, 4\Delta x) \tag{2.33}$$

with r_B equal to the standard Bondi radius:

$$r_B = \frac{GM_{\rm BH}}{v_B^2}. \tag{2.34}$$

In Equation 2.33 we limit the modified Bondi radius to a maximum value of four times the cell size Δx, i.e. to the minimum resolved Jeans length. With this choice, in the case of cold, supersonic ($u \gg c_{\rm S}$) gas accretion we recover the free fall rate in Equation 2.31. In the case of hot gas accretion, the formula simply reduces to the Bondi-Hoyle formula used in the older routine. To conclude, we limit the maximum accretion rate for each black hole to the Eddington limit, as in the old scheme.

Finally, the energy injection scheme has been also modified. We still use the same formulae discussed in the previous Section, however we decided to distribute the feedback energy within the sink radius in a mass weighted fashion. This choice seems to make our new scheme more robust against changes in resolution, however the scheme is still being tested and we do not have conclusive results yet.

Further improvements to the AGN feedback routines in the RAMSES code can be made by introducing more detailed models for the energy injection. For example, Dubois et al. (2012) introduced a technique to explicitly include mechanical feedback from jets in radio mode, while still using thermal feedback for the quasar mode. Interesting efforts still need to be made to develop schemes to include radiative feedback in quasar mode (e.g. Debuhr et al. (2011)), or the effect of cosmic rays streaming and their non-thermal contribution to the gas pressure (e.g. Fujita & Ohira (2011)). Furthermore, the problem might need to be studied in the context of magnetohydrodynamics, due to the significant contribution expected from magnetic pressure in cluster cores and due to the acceleration of cosmic rays due to Fermi mechanisms.

Bibliography

Agertz O., Kravtsov A. V., Leitner S. N., Gnedin N. Y., 2012, ArXiv e-prints

Agertz O., Moore B., Stadel J., Potter D., Miniati F., Read J., Mayer L., Gawryszczak A., Kravtsov A., Nordlund Å., Pearce F., Quilis V., Rudd D., Springel V., Stone J., Tasker E., Teyssier R., Wadsley J., Walder R., 2007, MNRAS, 380, 963

Agertz O., Teyssier R., Moore B., 2009, Monthly Notices of the Royal Astronomical Society: Letters, 397, L64

Agertz O., Teyssier R., Moore B., 2011, MNRAS, 410, 1391

Begelman M. C., Volonteri M., Rees M. J., 2006, Monthly Notices of the Royal Astronomical Society, 370, 289

Booth C. M., Schaye J., 2009, Monthly Notices of the Royal Astronomical Society, 398, 53

Bromm V., Loeb A., 2003, The Astrophysical Journal, 596, 34

Cattaneo A., Teyssier R., 2007, Monthly Notices of the Royal Astronomical Society, 376, 1547

Debuhr J., Quataert E., Ma C.-P., 2011, MNRAS, 412, 1341

Dolag K., Borgani S., Schindler S., Diaferio A., Bykov A. M., 2008, Space Sci. Rev., 134, 229

Dubois Y., Devriendt J., Slyz A., Teyssier R., 2012, MNRAS, 420, 2662

Dubois Y., Devriendt J., Teyssier R., Slyz A., 2011, ArXiv e-prints

Dubois Y., Teyssier R., 2008, Astronomy and Astrophysics, 477, 79

Fujita Y., Ohira Y., 2011, ApJ, 738, 182

Gebhardt K., Bender R., Bower G., Dressler A., Faber S. M., Filippenko A. V., Green R., Grillmair C., Ho L. C., Kormendy J., Lauer T. R., Magorrian J., Pinkney J., Richstone D., Tremaine S., 2000, The Astrophysical Journal, 539, L13

Gültekin K., Richstone D. O., Gebhardt K., Lauer T. R., Tremaine S., Aller M. C., Bender R., Dressler A., Faber S. M., Filippenko A. V., Green R., Ho L. C., Kormendy J., Magorrian J., Pinkney J., Siopis C., 2009, The Astrophysical Journal, 698, 198

Haardt F., Madau P., 1996, Astrophysical Journal v.461, 461, 20

Hobbs A., Power C., Nayakshin S., King A. R., 2012, MNRAS, 421, 3443

Hockney R. W., Eastwood J. W., 1988, Computer simulation using particles

Khokhlov A., 1998, Journal of Computational Physics, 143, 519

Krumholz M. R., McKee C. F., Klein R. I., 2004, The Astrophysical Journal, 611, 399

Madau P., Rees M. J., 2001, The Astrophysical Journal, 551, L27

Ostriker E. C., 1999, ApJ, 513, 252

Press W. H., Teukolsky S. A., Vetterling W. T., Flannery B. P., 1992, Cambridge: University Press

Price D. J., 2012, Journal of Computational Physics, 231, 759

Rasera Y., Teyssier R., 2006, Astronomy and Astrophysics, 445, 1

Scannapieco C., Wadepuhl M., Parry O. H., Navarro J. F., Jenkins A., Springel V., Teyssier R., Carlson E., Couchman H. M. P., Crain R. A., Dalla Vecchia C., Frenk C. S., Kobayashi C., Monaco P., Murante G., Okamoto T., et al. 2012, MNRAS, 423, 1726

Sijacki D., Springel V., Matteo T. D., Hernquist L., 2007, Monthly Notices of the Royal Astronomical Society, 380, 877

Springel V., 2010, MNRAS, 401, 791

Springel V., Matteo T. D., Hernquist L., 2005, Monthly Notices of the Royal Astronomical Society, 361, 776

Stinson G., Seth A., Katz N., Wadsley J., Governato F., Quinn T., 2006, Monthly Notices of the Royal Astronomical Society, 373, 1074

Sutherland R. S., Dopita M. A., 1993, ApJS, 88, 253

Teyssier R., 2002, Astronomy and Astrophysics, 385, 337

Teyssier R., Moore B., Martizzi D., Dubois Y., Mayer L., 2011, MNRAS, 414, 195

Teyssier R., Pontzen A., Dubois Y., Read J. I., 2013, MNRAS, p. 493

Toro E. F., 1997, Berlin: Springer

Overview of the results

In this small Section, I offer a short overview of the results obtained with the methods:

- Paper 1: Cosmological hydrodynamical simulations are performed to show that the mass distribution of gas and stars in galaxy clusters in simulations including AGN feedback is very different from that observed in simulations neglecting this effect. A careful study of resolution effects is performed. The simulations with AGN feedback are the only ones that provide a good match to the observational data.

- Paper 2: The simulations of Paper 1 are analysed to study the properties of BCGs. Only the simulations including AGN feedback reproduce BCG properties that match the ones of observed galaxies. These include galaxy stellar mass, velocity dispersion, size and kinematic properties. A cored stellar density profile is also measured.

- Paper 3: The density profiles of the cluster analysed in Paper 1 have peculiar properties. In the case including AGN feedback, density cores of similar size are found in the dark matter profile and in the stellar mass profile. The formation of these cores is related to violent gas dynamical processes induced by AGN feedback.

- Paper 4: New simulations are performed. The progenitor of a galaxy cluster in isolation is provided with a controlled supply of cold gas that feeds the central AGN. These simulations confirm the result found in Paper 3: gas dynamical processes induced by AGN feedback can generate density cores at the centre of galaxy clusters.

- Preliminary results – This manuscript might need revisions before submission to a peer reviewed journal. A large sample of cosmological hydrodynamical simulations is performed. The effect of baryon physics on the halo mass function is studied. The novel part of this work is the inclusion of AGN feedback effects in the model.

Chapter 3

First Publication - Mass distribution in galaxy clusters: the role of Active Galactic Nuclei feedback

Published on MNRAS

Monthly Notices
of the
ROYAL ASTRONOMICAL SOCIETY

Mon. Not. R. Astron. Soc. **414,** 195–208 (2011) doi:10.1111/j.1365-2966.2011.18399.x

Mass distribution in galaxy clusters: the role of Active Galactic Nuclei feedback

Romain Teyssier,[1,2]★ Ben Moore,[1] Davide Martizzi,[1] Yohan Dubois[3] and Lucio Mayer[1]

[1]*Institute for Theoretical Physics, University of Zurich, CH-8057 Zürich, Switzerland*
[2]*CEA Saclay, DSM/IRFU/SAP, Bâtiment 709, F-91191 Gif-sur-Yvette, Cedex, France*
[3]*Department of Astrophysics, University of Oxford, Keble Road, Oxford OX1 3RH*

Accepted 2011 January 14. Received 2011 January 14; in original form 2010 March 24

ABSTRACT

We use 1-kpc resolution cosmological Adaptive Mesh Refinement (AMR) simulations of a Virgo-like galaxy cluster to investigate the effect of feedback from supermassive black holes on the mass distribution of dark matter, gas and stars. We compared three different models: (i) a standard galaxy formation model featuring gas cooling, star formation and supernovae feedback, (ii) a 'quenching' model for which star formation is artificially suppressed in massive haloes and finally (iii) the recently proposed active galactic nucleus (AGN) feedback model of Booth and Schaye. Without AGN feedback (even in the quenching case), our simulated cluster suffers from a strong overcooling problem, with a stellar mass fraction significantly above observed values in M87. The baryon distribution is highly concentrated, resulting in a strong adiabatic contraction (AC) of dark matter. With AGN feedback, on the contrary, the stellar mass in the brightest cluster galaxy (BCG) lies below observational estimates and the overcooling problem disappears. The stellar mass of the BCG is seen to increase with increasing mass resolution, suggesting that our stellar masses converge to the correct value from below. The gas and total mass distributions are in better agreement with observations. We also find a slight deficit ($\sim$10 per cent) of baryons at the virial radius, due to the combined effect of AGN-driven convective motions in the inner parts and shock waves in the outer regions, pushing gas to Mpc scales and beyond. This baryon deficit results in a slight *adiabatic expansion* of the dark matter distribution that can be explained quantitatively by AC theory.

Key words: black hole physics – methods: numerical – galaxies: clusters: general – galaxies: formation – cosmology: theory – large-scale structure of Universe.

1 INTRODUCTION

Galaxy clusters are ideal laboratories to study galaxy formation in a dense environment. Galaxies in clusters are observed in many morphological types, from blue extended spirals to red massive elliptical spheroids. The origin of the morphological evolution of galaxies in clusters is still poorly understood. Tidal and ram pressure stripping trigger fast evolution in the properties of accreted satellites, while complex gas cooling and heating processes control the amount of stripped gas that can actually reach the central region of the cluster. In this context, the origin of brightest cluster galaxies (BCGs) still raises many questions. In the current cosmological framework, the formation of galaxies at the bright end of the luminosity function is still affected by the so-called 'overcooling problem': using both semi-analytical models and computer simulations, it has been shown that the massive galaxies are predicted to be too bright and too blue when compared to massive galaxies in the nearby Universe (see the recent review by Borgani & Kravtsov 2009). As a consequence, these models find a stellar content in massive clusters that is significantly above the observed values (Kravtsov, Nagai & Vikhlinin 2005), even including rather extreme supernovae feedback recipe (Borgani et al. 2004).

In order to overcome this issue, feedback from supermassive black holes (SMBH) have been proposed as a mechanism to prevent gas from accumulating in the cluster core. The so-called active galactic nucleus (AGN) feedback scenario has received support from theoretical considerations (Tabor & Binney 1993; Ciotti & Ostriker 1997; Silk & Rees 1998), but the strongest evidence comes from the correlated observations of X-ray cavities and radio blobs in massive clusters. These features are usually interpreted as buoyantly rising bubbles of high-entropy material injected in the cluster

★E-mail: romain.teyssier@cea.fr

core by jets of relativistic particles. Detailed models of bubbles (Churazov et al. 2001; Ruszkowski, Brüggen & Begelman 2004; Brüggen, Ruszkowski & Hallman 2005) and jets (Reynolds, Heinz & Begelman 2001; Omma et al. 2004; Cattaneo & Teyssier 2007) have been proposed in the context of cluster cores heating, usually based on spherically or planar symmetric, idealized cluster configurations. Based on simple energetic arguments, it is possible to relate the growth of SMBHs at the centre of massive galaxy spheroids to the energy required to unbind the overcooling gas (Silk & Rees 1998). The idea of star formation being regulated by AGN feedback at the high-mass end of the galaxy mass function has been applied first quite successfully to hydrodynamical simulations of galaxy merger (Di Matteo, Springel & Hernquist 2005) and then to semi-analytical models of galaxy formation (Bower et al. 2006; Cattaneo et al. 2006; Croton et al. 2006; De Lucia & Blaizot 2007; Cattaneo et al. 2009).

AGN feedback models have been included only recently in cosmological simulations of galaxy groups and clusters (Sijacki et al. 2007; Puchwein, Sijacki & Springel 2008; McCarthy et al. 2010). Although the detailed physical modelling of SMBHs growth usually differs (Sijacki et al. 2007; Booth & Schaye 2009), these simulations, exclusively based on the GADGET code (Springel 2005), have obtained very encouraging results regarding the global properties of the simulated clusters (Puchwein et al. 2008; Fabjan et al. 2010; McCarthy et al. 2010; Puchwein et al. 2010). In this paper, we report on the first AMR high-resolution simulation of a Virgo-like cluster, following both SMBH and star formation, with the associated feedback. A companion paper is exploring the properties of a jet-based, AGN feedback model (Dubois et al. 2010). We use the AMR code RAMSES, which differs significantly from the other code used so far to model AGN feedback in a fully cosmological simulation, namely the GADGET code. Although AMR schemes suffer from larger advection errors than smoothed particle hydrodynamics (SPH), which is a strictly Galilean invariant method, there are some definitive advantages of using AMR in this context: although the total energy (kinetic + thermal + potential) is conserved only at the percent level, it is strictly conserving for the fluid energy (kinetic + thermal), which is very important in presence of strong shocks, and it captures hydrodynamical instabilities more realistically (Agertz et al. 2007; Wadsley, Veeravalli & Couchman 2008; Mitchell et al. 2009), which is very important in presence of convective motions of buoyant gas. It also captures gas stripping of infalling satellites due to hydrodynamical instabilities more realistically than standard implementations of SPH (Agertz et al. 2007).

We have adapted the SMBH growth model of Booth & Schaye (2009) to the sink particle method for AMR presented by Krumholz, McKee & Klein (2004). With respect to the previous work of Booth & Schaye (2009) and follow-up papers, we have made significant improvements over the OWL simulations suites in terms of mass and spatial resolution, but only for one single zoom-in simulation of a Virgo-like cluster. Recently, Puchwein et al. (2008) and Puchwein et al. (2010) have also used the GADGET code, but a different AGN feedback model, to perform zoom-in simulations of groups and clusters of galaxies, with however a mass resolution and a gravitational softening length not as good as the one we used in our high-resolution case. Note also that the minimum smoothing length in these SPH simulations is usually much smaller than the gravitational softening length. In this paper, we have specifically chosen a Virgo-like cluster, in order to compare our results with the very detailed observations that are available for this well-known astronomical object. We will focus here on the mass distribution of the three main components, namely dark matter, gas and stars.

The paper is organized as follows. Section 2 is dedicated to numerical methods and physical ingredient (cooling, star formation and AGN feedback), while Section 3 presents our results, comparing our three models. The Section 4 is left for discussion.

2 NUMERICAL METHODS

In this section, we describe the numerical techniques and the initial conditions we used to model our Virgo-like cluster. As it is now customary for cosmological simulations, we used a zoom-in (or volume renormalization) technique to focus our computational resources on a specific region of a 100 Mpc h^{-1} periodic box. We adopt a standard Λ cold dark matter (ΛCDM) cosmology with $\Omega_{\rm m} = 0.3, \Omega_\Lambda = 0.7, \Omega_{\rm b} = 0.045$ and $H_0 = 70\,{\rm km\,s^{-1}\,Mpc^{-1}}$. We have adopted the Eisenstein & Hu (1998) transfer function and the GRAFIC package (Bertschinger 2001) in its parallel implementation MPGRAFIC (Prunet et al. 2008) to generate our initial conditions. From a first low-resolution dark matter only (DMO) run, we built a catalogue of candidate haloes whose virial masses lie in the range $(1–2) \times 10^{14}\,{\rm M_\odot}\,h^{-1}$. From this catalogue, we have extracted our final halo based on its mass assembly history; its final mass ($M_{\rm vir} \simeq 10^{14}\,{\rm M_\odot}$) is already in place around $z = 1$, so it can be considered as a well-relaxed cluster by $z = 0$. The final halo mass has been measured to be $M_{\rm 200c} = 1.04 \times 10^{14}\,{\rm M_\odot}$ or $M_{\rm 500c} = 7.80 \times 10^{13}\,{\rm M_\odot}$, where index 'c' refers to the critical density.

2.1 Simulation parameters

We have performed two simulations, one at low resolution, for which the initial grid effective size was 1024^3, and one at high resolution, with effective grid size of 2048^3. From this initial grid, we have extracted high-resolution particles only in the Lagrangian volume of the halo, and we have used larger and larger mass particles to sample the cosmological volume, so that the total number of particles in the box was 5.2×10^6 (22×10^6) for only 2.6×10^6 (19×10^6) in the central region, and 10^6 (8×10^6) inside the final virial radius for the low-resolution (high-resolution) simulation. The dark matter particle mass is therefore 6.5×10^7 (8.2×10^6) ${\rm M_\odot}\,h^{-1}$ and the baryons resolution element mass is 1.2×10^7 (1.4×10^6) ${\rm M_\odot}\,h^{-1}$ (see Table 1).

The AMR grid was initially refined to the same level of refinement than the particle grid (1024^3 and 2048^3), and seven more levels of refinements were considered. We imposed the spatial resolution to remain roughly constant in physical units, so that the minimum grid cell stayed close to $\Delta x_{\rm min} = L/2^{\ell_{\rm max}}$ with $\ell_{\rm max} = 17$ (18) at $z = 0$. We therefore reached a spatial resolution of $\Delta x_{\rm min} \simeq 1$ kpc for the low-resolution simulation and $\Delta x_{\rm min} \simeq 500$ pc for the high-resolution one. The grid was dynamically refined up to this resolution using a quasi-Lagrangian strategy; when the dark matter or baryons mass in a cell reaches eight times the initial mass resolution, it is split into eight children cells. We reached $z = 0$ with 14×10^6 (68×10^6) cells for the low- (high-) resolution run, including split cells.

Table 1. Mass resolution for dark matter particles, gas cells and star particles, and spatial resolution (in physical units) for our two sets of simulations.

Run	$m_{\rm cdm}$	$m_{\rm gas}$ ($10^6\,{\rm M_\odot}$)	m_*	$\Delta x_{\rm min}$ (kpc h^{-1})
Low resolution	65	12	2.4	0.76
High resolution	8.2	1.4	0.3	0.38

Gas dynamics is modelled using a second-order unsplit Godunov scheme (Teyssier 2002; Teyssier, Fromang & Dormy 2006; Fromang, Hennebelle & Teyssier 2006) based on the HLLC Riemann solver (Toro, Spruce & Speares 1994). We assume a perfect gas equation of state (EOS) with $\gamma = 5/3$. Gas metallicity is advected as a passive scalar, and is self-consistently accounted for in the cooling function. We also considered the standard homogeneous UV background of Haardt & Madau (1996), but we modified the starting redshift, extrapolating the average intensity from $z_{\rm reion} = 6$ to 12, in order to account for the early reionization expected in such a protocluster regions (Iliev et al. 2008).

2.2 Galaxy formation physics

As gas cools down and settles into centrifugally supported discs, we need to provide a realistic model for the interstellar medium (ISM). Since the ISM is inherently multiphase and highly turbulent, it is beyond the scope of present-day cosmological simulations to try to simulate it self-consistently. It is customary to rely on subgrid models, providing an effective EOS that capture the basic turbulent and thermal properties of this gas. Models with various degrees of complexity have been proposed in the literature (Yepes et al. 1997; Springel & Hernquist 2003; Schaye & Vecchia 2008). We follow the simple approach based on a temperature floor given by a polytropic EOS for gas:

$$T_{\rm floor} = T_* \left(\frac{n_{\rm H}}{n_*}\right)^{\Gamma-1}, \quad (1)$$

where $n_* = 0.1$ H/cc is the density threshold that defines the star-forming gas, $T_* = 10^4$ K is a typical temperature mimicking both thermal and turbulent motions in the ISM, and $\Gamma = 5/3$ is the polytropic index controlling the stiffness of the EOS. Gas is able to heat above this floor, but cannot cool down below it. Note that because of this temperature floor, the Jeans length in our galactic disc is always resolved. We also consider star formation using a similar phenomenological approach. In each cell with gas density larger than n_*, we spawn new star particles at a rate given by

$$\dot{\rho}_* = \epsilon_* \frac{\rho_{\rm gas}}{t_{\rm ff}} \quad \text{with} \quad t_{\rm ff} = \sqrt{\frac{3\pi}{32 G \rho}}, \quad (2)$$

where $t_{\rm ff}$ is the free-fall time of the gaseous component and $\epsilon_* = 0.01$ is the star formation efficiency. The star particle mass depends on the resolution and was chosen to be 2.4×10^6 (3×10^5) $\mathrm{M}_\odot$ for the low (high) resolution run. For each star particle, we assume that 10 per cent of its mass will go supernova after 10 Myr. We consider a supernova energy of 10^{51} erg and 1 $\mathrm{M}_\odot$ of ejected metals per 10 $\mathrm{M}_\odot$ average progenitor mass. This supernovae feedback was implemented in the RAMSES code using the 'delayed cooling' scheme (Stinson et al. 2006).

Up to this point, we use rather standard galaxy formation recipe, which have proven only recently to be quite successful in reproducing the properties of field spirals (Mayer, Governato & Kaufmann 2008; Governato et al. 2009, 2010; Agertz, Teyssier & Moore 2011). These recipes have been shown to reproduce basic galaxy properties like Kennicutt–Schmidt law, star formation rates and galactic winds (Dubois & Teyssier 2008; Devriendt et al. 2010; Agertz et al. 2011). The same recipe are only marginally successful when one considers small groups (Feldmann et al. 2010), but they fail on cluster scales (Borgani et al. 2004; Kravtsov et al. 2005; Borgani & Kravtsov 2009). In the present paper, in order to check that our results are compatible with previous work, and to set a reference point, we have performed simulations with only standard galaxy formation physics (labelled SF runs in the followings).

2.3 Star formation quenching

The main problem we have to face in standard cosmological simulations on cluster scales is the striking excess of mass locked into stars. Using rather extreme stellar feedback models, previous authors report that the simulated stellar mass fraction lies in the range 35–60 per cent, depending on the cluster mass (Borgani & Kravtsov 2009). Since only 10 per cent of the baryonic mass is observed in the galaxies, this would require a large amount of stars hidden in a diffuse component such as the intracluster light (ICL). This last scenario is however severely constrained by observations of the ICL (Gonzalez, Zaritsky & Zabludoff 2007) and does not appear to be plausible.

There is growing theoretical and observational evidence that star formation is shut down above a critical halo mass $M_{\rm c} \simeq 6 \times 10^{11}\,\mathrm{M}_\odot$ (Cattaneo et al. 2006). Birnboim & Dekel (2003) have proposed that this critical mass is related to the stability of accretion shocks, and to a transition from cold to hot mode of gas accretion. Although this transition in the nature of the accretion flows has been confirmed by numerical simulations (Kereš et al. 2005; Ocvirk, Pichon & Teyssier 2008; Dekel, Sari & Ceverino 2009b), the simulated star formation was not observed to decrease significantly above the critical mass (Ocvirk et al. 2008). This might be due to insufficient mass and spatial resolution, so that heating processes, not properly captured, cannot balance radiative cooling (Naab et al. 2007). On a different side, Cattaneo et al. (2006) argued that this modification of the halo properties may create favourable conditions for AGN feedback to be effective, but AGN feedback is still needed to prevent the overcooling problem above the critical mass (Dekel & Birnboim 2006). Without specifying the underlying heating process, the critical mass argument boils down to stopping (or quenching) gas cooling and star formation in the central galaxy for halo masses larger than $\sim 10^{12}\,\mathrm{M}_\odot$.

In this paper, in order to test this hypothesis, we have used a simple phenomenological model to quench star formation in massive galaxies. Since our standard model (SF runs) obviously suffers from a strong overcooling problem, we need to actively suppress gas cooling and star formation above the critical mass. If the stellar mass density is greater than 0.1 H/cc, and if the stellar 3D velocity dispersion is greater than 100 km s^{-1}, we switch off star formation and gas cooling. In this way, star formation in discs is unaffected, since the velocity dispersion is smaller than the chosen threshold. On the other hand, star formation is suppressed in massive spheroids. The main advantage of this quenching model is its simplicity; although it captures the scenario proposed by Cattaneo et al. (2006), it does not require any complex AGN feedback model, nor the mass and spatial resolution reached by Naab et al. (2007) in their early-type galaxy simulation. However, as we demonstrate in this paper, this simple approach does not solve the overcooling problem in our Virgo cluster simulation.

2.4 SMBH growth and associated feedback

Besides our standard galaxy formation and our quenching scenario simulations, we explore a model for which SMBH growth and feedback is considered. In a nutshell, our recipe is based on the sink particle method for grid-based codes designed by Krumholz et al. (2004), with the AGN feedback model proposed by Booth & Schaye (2009). We shall now briefly summarize these techniques.

2.4.1 Seed particles

In the two main competing SMBH formation models: slow growth from Population III stars (Madau & Rees 2001) or direct collapse of a low angular momentum halo (Bromm & Loeb 2003; Begelman, Volonteri & Rees 2006), the seed SMBH is believed to grow quickly to $10^5\,\mathrm{M}_\odot$, before starting to affect its environment and enter the self-regulated regime. Although the question of intermediate mass black holes is still vigorously debated, this characteristic mass is often considered as the initial seed SMBH mass (Li et al. 2006; Pelupessy, Di Matteo & Ciardi 2007), since it is 1 order of magnitude smaller than the smallest SMBH observed on the $M_{\rm BH}$–σ relation (Gebhardt et al. 2000; Gültekin et al. 2009). At each main time-step during the course of the simulation, we identify potential candidate regions for seed black hole formation using the following criteria:

(i) the stellar density has to be greater than 0.1 H/cc;
(ii) the stellar 3D velocity dispersion has to be greater than $100\,\mathrm{km\,s^{-1}}$;
(iii) the gas density has to be greater than 1 H/cc;
(iv) no other sink particle is present within 10 kpc.

If these four conditions are fulfilled, we create a sink particle of fixed mass $M_{\rm BH} = 10^5\,\mathrm{M}_\odot$. These particles represent our seed black holes. Note that our third condition ensures that seed black holes form in the nuclear region of star-forming discs, where the gas density is probably much larger than 1 H/cc. Because of our limited resolution, we cannot choose an arbitrary high-density threshold, otherwise SMBH will never form. On the other hand, because star formation is a very inefficient process, large enough galaxies devoid of SMBH will always reach this gas density threshold and trigger SMBH seeding. Our second condition requires a minimum line-of-sight velocity dispersion $\sigma_{\rm 1D} \simeq 60\,\mathrm{km\,s^{-1}}$, in agreement with the observed $M_{\rm BH}$–σ relation (Gebhardt et al. 2000; Gültekin et al. 2009). Our last condition ensures that no new seed SMBH will be created in a galaxy that is already hosting an old SMBH (or at least within 10 kpc from its centre).

2.4.2 Sink particle evolution

Each black hole is considered as a sink particle, as defined in Krumholz et al. (2004). We recall briefly the method here. We consider around each black hole a sphere of fixed physical radius $r_{\rm sink} = 4\Delta x$, where Δx is our spatial resolution in physical units, so that $r_{\rm sink} \simeq 4$ kpc (2 kpc) for the low- (high-) resolution run. We assume that the SMBH mass distribution inside the sink is homogeneous, and this homogeneous sphere is added to the total mass density when solving for the Poisson equation. The sink particle is then advanced in time by interpolating the gravitational force back to the sink position using the inverse CIC scheme. For each sink, we compute the Bondi–Hoyle accretion rate:

$$\dot{M}_{\rm BH} = \alpha_{\rm boost}\frac{4\pi \mathrm{G}^2 M_{\rm BH}^2 \rho}{\left(c_{\rm s}^2 + u^2\right)^{3/2}}, \tag{3}$$

where ρ, $c_{\rm s}$ and u are the average gas density, sound speed and relative velocity within the sink radius. These average quantities are computed following the scheme proposed by Krumholz et al. (2004). The parameter $\alpha_{\rm boost}$ was introduced by Springel, Di Matteo & Hernquist (2005) to account for unresolved multiphase turbulence in the SMBH environment. Although this parameter was first chosen constant at $\alpha_{\rm boost} \simeq 100$ (Springel et al. 2005), Booth & Schaye (2009) argued that this parameter should be close to one in low-density regions, while its value should increase in high-density regions, in order to match the subgrid model used for the unresolved turbulence in the discs. Based on extensive numerical experiments, they proposed the following phenomenological model to boost Bondi–Hoyle accretion:

$$\begin{aligned} \alpha_{\rm boost} &= \left(\frac{n_{\rm H}}{n_*}\right)^2 \quad \text{if } n_{\rm H} > n_* = 0.1\ \mathrm{H/cc}, \\ \alpha_{\rm boost} &= 1 \qquad\qquad \text{otherwise}. \end{aligned} \tag{4}$$

Note that this model has no real physical justification, and that it depends crucially on the underlying EOS model. We have been very careful in using this boost factor in conjunction with the same EOS model (see equation 1) as in Booth & Schaye (2009).

As advocated by Springel et al. (2005), the accretion rate on to the SMBH cannot exceed its Eddington limit given by

$$\dot{M}_{\rm ED} = \frac{4\pi \mathrm{G} M_{\rm BH} m_{\rm p}}{\epsilon_r \sigma_{\rm T} c} \quad \text{with } \epsilon_r \simeq 0.1, \tag{5}$$

so that the final accretion rate is computed using $\dot{M}_{\rm acc} = \min(\dot{M}_{\rm BH}, \dot{M}_{\rm ED})$. At each time-step, a total gas mass of $\dot{M}_{\rm acc}\Delta t$ is removed from all cells within the sink radius, with the same weighting scheme as the one used to define average quantities (Krumholz et al. 2004). In order to prevent the gas density to vanish or become negative, we allow a maximum of 50 per cent gas removal at each time-step.

2.4.3 AGN feedback

In the proposed model for SMBH growth, a key ingredient is the associated feedback model. As demonstrated by many authors (Sijacki et al. 2007; Cattaneo & Teyssier 2007; Booth & Schaye 2009), the Bondi–Hoyle accretion model allows the SMBH growth history to be self-regulated by injecting thermal energy in the surrounding gas: if the SMBH mass is too small, the associated feedback will be inefficient and the surrounding gas will remain cold and dense, boosting the accretion rate up to the Eddington limit. The SMBH mass will grow exponentially fast, with e-folding timescale equal to the Salpeter time, $t_{\rm S} \simeq 45$ Myr. As soon as the black hole mass is large enough, feedback processes heat and eventually unbind the surrounding gas, so that the accretion rate drops and becomes Bondi–Hoyle-limited. This bimodal behaviour is illustrated in Fig. 1, where one can see the time evolution of the accretion rate of the most massive SMBH in the simulated region. Short bursts of Eddington-limited accretion are followed by long quiescent epochs of Bondi–Hoyle-limited accretion, self-regulated by SMBH feedback.

In order to allow for this self-regulated SMBH growth, efficient feedback schemes are mandatory. Although we do see clear signatures of AGN feedback in clusters (Arnaud et al. 1984; Fabian et al. 2000; McNamara et al. 2001), the physical processes at the origin of this energy injection are still unclear: radiative feedback (Ciotti & Ostriker 2001), cosmic rays (Brüggen et al. 2002; Chandran & Rasera 2007) or strong shocks [see the review of Begelman (2004)]. A common property of these various models is that they require a very good spatial resolution to be captured realistically in hydrodynamical simulations. The most advanced modelling so far has been using AGN-driven bubbles (Churazov et al. 2001; Ruszkowski et al. 2004; Brüggen et al. 2005) or jets (Reynolds et al. 2001; Omma et al. 2004; Cattaneo & Teyssier 2007), leading to turbulent convective motions and 'shocklets' escaping the cluster core (Chandran & Rasera 2007; Rasera & Chandran 2008; Sharma

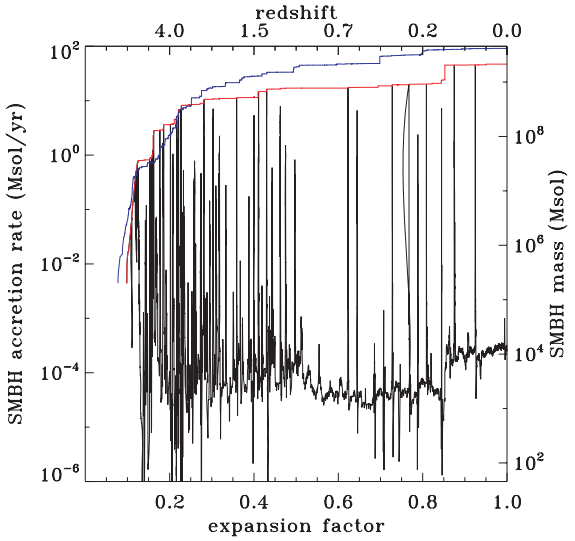

Figure 1. Time evolution of the accretion rate of the largest SMBH in the cluster. The Eddington limit is shown as the red line, the corresponding SMBH mass indicated on the right-hand axis. The high-resolution simulation finds a similar (within a factor of 2) SMBH mass (shown in blue). We clearly see two modes of accretion, with episodic bursts for which the SMBH accretes at or close to the Eddington limit, and long periods in between for which the SMBH accretion rate is at or close to the Bondi rate.

et al. 2009). In some case, depending on the injected energy, these AGN-driven flows can drive strong shock waves that can travel to very large distances (Baldi et al. 2009). In current cosmological simulations, numerical resolution does not allow these effects to be self-consistently modelled. As it is customary under these circumstances, we rely on a more phenomenological model.

In the cosmological context, the model proposed by Booth & Schaye (2009) appears to be easier to implement than the one proposed by Sijacki et al. (2007). Moreover, it relies on only one main free parameter, the coupling efficiency ϵ_c, that can be calibrated to the observed M_{BH}–σ relation to the fiducial value $\epsilon_c \simeq 0.15$ (Booth & Schaye 2009). We have adapted their model to the RAMSES code, using the following approach: at each time-step, we compute the SMBH feedback energy as a fixed fraction of the rest mass energy of the accreted gas, multiplied by the 'coupling efficiency' ϵ_c:

$$\Delta E = \epsilon_c \epsilon_r \dot{M}_{acc} c^2 \Delta t. \quad (6)$$

This energy is not released immediately in the surrounding gas. It is instead accumulated over many time-steps and stored into a new SMBH-related variable E_{AGN}, so that we can avoid atomic line cooling to radiate this energy instantaneously. Following the trick proposed by Booth & Schaye (2009), we release this accumulated energy inside the sink radius when

$$E_{AGN} > \frac{3}{2} m_{gas} k_B T_{min}, \quad (7)$$

where m_{gas} is the gas mass within the sink radius and T_{min} is the minimum feedback temperature. As soon as T_{min} is chosen above 10^7 K, the critical temperature below which metal line cooling becomes very efficient, the resulting feedback scheme does not depend on the chosen value for T_{min}. We adopt here $T_{min} = 10^7$ K. As can be seen on the previous equation, this threshold energy depends directly on the gas density in the environment of the black hole. When dense and cold gas is present, more energy is required to reach the threshold. After enough mass has been accreted, a strong burst of energy is released, that will unbind the surrounding dense gas. On the other hand, when only diffuse, hot gas is present, the threshold energy is much easier to reach, and feedback proceeds in a quasi-continuous fashion. In some sense, based on this rather simple recipe, we can account for both the 'quasar mode' and the 'radio mode' of the AGN feedback model of Sijacki et al. (2007).

3 RESULTS

In this section, we describe the properties of our simulated cluster for the three different models, labelled 'SF', 'quenching' and 'AGN' in most of the figures. We will focus our analysis in the final mass distribution, and compare, whenever it is possible, to actual Virgo cluster data. We present mostly low-resolution data, although we also compare low- and high-resolution results to discuss convergence properties.

3.1 SMBH growth and feedback

In Fig. 1, we show the accretion rate of the most massive SMBH as a function of expansion factor. This plot is relevant only for the 'AGN' simulation. Also shown is the Eddington accretion rate, directly proportional to the SMBH mass. It appears quite clearly in this plot that the most massive SMBH grows discontinuously, during very short Eddington-limited accretion events, or, at late time, by accreting other black holes, in good agreement with semi-analytical predictions from Malbon et al. (2007). In the low-resolution simulation, the final mass reaches $M_{BH} \simeq 2.1 \times 10^9$ M$_\odot$ after a last merger around $a \simeq 0.85$. In the high-resolution simulation, the SMBH mass is twice as large, with a slightly different evolution, and reaches the final value of $M_{BH} \simeq 4.2 \times 10^9$ M$_\odot$. The SMBH mass in M87 has been estimated around 4×10^9 M$_\odot$ using dynamical constraints (Macchetto et al. 1997; Gebhardt & Thomas 2009; Gültekin et al. 2009), in very good agreement with our high-resolution prediction. Note that M87 SMBH is close to the M_{BH}–σ relation (Gültekin et al. 2009). Since the free parameter ϵ_c was calibrated to $\epsilon_c = 0.15$ by Booth & Schaye (2009) on the M_{BH}–σ relation, our AMR simulation appears to be consistent with their SPH results.

The SMBH activity, quite strong before $z = 1$, declines slightly until the present epoch. In our simulation, this early activity is due to an early phase of frequent mergers feeding the SMBHs very efficiently. Strong and repeated outbursts of energy are launching strong shock waves in the intergalactic medium (IGM), rising the IGM entropy within the whole protocluster region. This early epoch can therefore be considered as representative of the pre-heating scenario advocated by several authors to explain structural properties of galaxy clusters (Kaiser 1991; Ponman, Cannon & Navarro 1999; Babul et al. 2002; Davé, Oppenheimer & Sivanandam 2008). On the other hand, at later epochs ($z < 1$), when the cluster mass is finally assembled, AGN feedback prevent gas from overcooling and from accumulating in the core. This is well illustrated by the sequence of temperature maps shown in Fig. 2, just after the strong AGN outburst occurring at $a \simeq 0.62$ (see Fig. 1). The first image show the mass-weighted projected temperature within the whole cluster, just at the time of the outburst. Slightly after (in the second frame), the whole cluster has been significantly heated, with buoyantly driven plumes of hot gas escaping the cluster core (Cattaneo & Teyssier 2007; Chandran & Rasera 2007; Rasera & Chandran 2008; Sharma et al. 2009). In the next frame, a strong shock, visible as a sharp temperature discontinuity, develops close to and beyond the virial radius. The last frame shows the cluster back to hydrostatic equilibrium, waiting for the next AGN outburst. Note that in the core region, where the density is high enough for X-ray detections, only

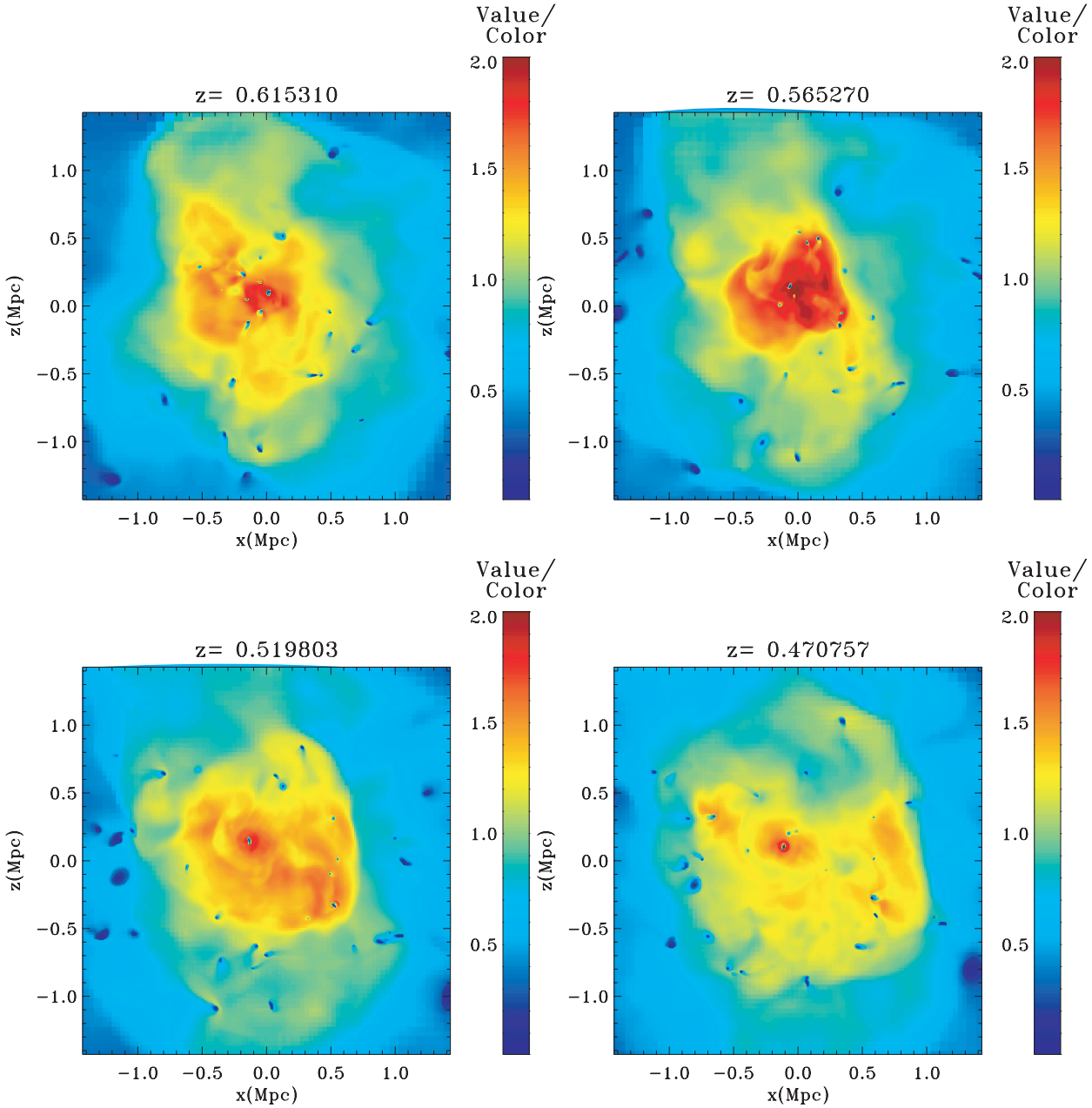

Figure 2. Maps of the mass-weighted temperature of the simulated cluster at four different redshifts. Units are in keV. The first redshift in the series corresponds to the strong SMBH outburst seen in Fig. 1 around $a \simeq 0.62$.

buoyantly rising bubbles are seen. In our simulation, shock waves form only in the outer part of the cluster, with a Mach number of a few. Because of the rather low gas density, we believe that their detection is quite challenging, explaining why there is so little evidence of their presence (Bourdin et al. 2004).

Although the feedback recipe does not explicitly account for it, the AGN energy deposition typically proceeds in two modes: a strong, energetic mode or 'quasar mode', which in our case corresponds to the Eddington luminosity and reaches 5×10^{46} erg s^{-1}, and a quiescent mode or 'radio mode', with a Bondi–Hoyle-limited luminosity of 5×10^{41} erg s^{-1}. If we now take into account the coupling efficiency parameter $\epsilon_c = 0.15$ in our energy estimate, using, from Fig. 1, $\dot{M}_{acc} \simeq 10^{-4}\,M_\odot\,yr^{-1}$ into equation (6), we obtain a total luminosity of 9×10^{40} erg s^{-1} during radio mode. Although the X-ray luminosity of the active nucleus of M87 observed with *Chandra* is $L_{X,0.5-7\,keV} \simeq 7 \times 10^{40}$ erg s^{-1} (Di Matteo et al. 2003), quite close to our total luminosity in the radio mode, the mechanical power of the observed jet is significantly larger $P_{jet} \simeq 3.3 \times 10^{43}$ erg s^{-1} (Allen et al. 2006). This is consistent with observational estimates of the Bondi accretion rate in M87, around $\dot{M}_{acc} \simeq 10^{-1}\,M_\odot\,yr^{-1}$ (Di Matteo et al. 2003; Allen et al. 2006) and a coupling efficiency $\epsilon_c \simeq 0.2$ (Allen et al. 2006). This suggests that M87 SMBH lies in an intermediate state, between our radio and quasar modes. Nevertheless, the fact that our final black hole mass match well observational constraints of M87 is of great importance; it means that the *available* rest mass energy that the black hole can release into the forming cluster over its entire history is consistent with M87. This does not mean that the actual amount of energy

deposited into the X-ray emitting gas *today* is correct. With these limitations in mind, we can now predict the global properties of our simulated Virgo cluster, in particular the mass distribution in stars, gas and dark matter.

3.2 The mass distribution of stars and gas

We have plotted in Fig. 3 the surface brightness of our simulated Virgo cluster in the SDSS i band. One clearly sees many satellite galaxies orbiting around the BCG and a rich structure in the ICL component. In the SF case, the BCG appears as a very bright, gas-rich and disc-like object. We have also plotted in Fig. 4 the stellar mass profile from this SF simulation; we see immediately that the BCG stellar mass (measured at 20 kpc from the centre) is a factor of 10 too large, when compared to the observational estimate of Gebhardt & Thomas (2009). This is the classical result of the overcooling problem that occurs for cluster simulations with standard galaxy formation physics. Our second scenario, the quenching run, partially alleviates this problem. As can be seen on the surface brightness maps (Fig. 3), the BCG and the most massive satellites are now much dimmer. The total stellar mass within 100 kpc is in much better agreement with observations, although still slightly larger. The stellar mass profile, shown in Fig. 4, is however significantly different. When one looks now at the gas distribution in the cluster, it becomes quite obvious that this quenching scenario is far from being a viable solution. We have plotted in Fig. 3 the mass-weighted, projected gas density. We see a massive gas clump in the cluster core for both the SF and the quenching runs. For sake of comparison, we have plotted the simulated gas density profiles for our simulations and the best-fitting β-model for M87 from Churazov et al. (2008). The gas density is the SF run is a factor of 100 too large in the core of the cluster, and it is even worse for the quenching scenario, by an additional factor of 2. We therefore conclude that for both SF and quenching models, the simulated cluster suffers from a strong overcooling problem, with the build up of a dense, concentrated BCG, for which the stellar mass or the gas mass (or both) are in far in excess of those observed in M87.

We now turn to the analysis of our AGN model. The stellar surface brightness map is by far the dimmest of our three models: star formation has been dramatically reduced, even more than our quenching scenario. The stellar mass profile is now below the observational constraints by a factor of 3 at 100 kpc (see Fig. 4), and there is less apparent structure in the ICL component. AGN feedback has been quite successful in regulating star formation in the cluster. The gas distribution has also been profoundly affected by the SMBH model. First, no large, gas-rich disc is visible in the projected gas density map: the overcooling problem has been efficiently removed. We see in Fig. 5 that the dense unrealistic gas core has disappeared. When compared to the best-fitting β-model proposed by Churazov et al. (2008) for M87, the agreement is much better. Note that the cooling flow, although dramatically reduced, is still present in the AGN run, and it can be detected as the density enhancement within the central 10 kpc of the cluster. Interestingly, the knee in the gas density profile seen around 10 kpc in our model is also present in the data, although much weaker and at $\sim$5 kpc from the centre (Churazov et al. 2008 see Fig. 5 in their paper), suggesting the presence of a weak cooling flow in M87. Another important difference between the SF/quenching runs and the AGN run can be seen at large radii in the gas distribution: the gas density in the AGN case is 30 per cent larger, showing that gas have been removed from the core and stored at large radii (beyond the virial radius) by strong shocks similar to the one shown in Fig. 2.

3.3 The effect of mass resolution

Using our high-resolution simulation with AGN feedback, we would like to estimate the effect of numerical resolution on our results. We see in Fig. 6 the stellar mass profiles for the low- and the high-resolution runs at the final redshift. Contrary to what is often claimed in the literature, we do see a strong effect of mass (and spatial) resolution in the stellar mass distribution. The effect is stronger for the BCG close to the centre (the stellar mass has increased by a factor of 4 at 20 kpc) than for the cluster as a whole (the total stellar mass within the virial radius has increased only by a factor of 2). The effect of mass resolution is smaller for the other components (gas and dark matter).

The strong effect of mass resolution on the star formation history of the simulated halo can be interpreted easily by comparing the minimum resolved halo mass (optimistically set to 100 dark matter particles) to the minimum mass for star-forming haloes based on atomic cooling arguments (Gnedin 2000; Hoeft et al. 2006; Rasera & Teyssier 2006). This minimum mass (also referred to as the filtering mass) starts around 10^7 M$_\odot$ before reionization and then rises steadily as $(1+z)^{3/2}$ from redshift 6–7 to the final epoch. Resolving this minimum mass before reionization will require a dark matter particle mass below 10^5 M$_\odot$, a rather strong requirement for cluster-scale cosmological simulation. A more flexible criterion based on resolving the majority ($\sim$80 per cent) of star-forming haloes gives a less stringent limit around $M_{\rm min} \simeq 10^8$ M$_\odot$ (Iliev et al. 2007). Nevertheless, our low-resolution run falls short of the corresponding required dark matter particle mass by 65, while our high-resolution run is 'only' a factor of 8 above the limit. As explained in De Lucia & Blaizot (2007), BCGs are 'fundamentally hierarchical' objects, that formed their stars very early (80 per cent before $z = 3$) and assembled late (after $z = 0.5$, in average). This effect is directly related to the suppression of cooling flows and the associated star formation by AGN feedback. This early star formation occurs in rather small mass haloes (De Lucia & Blaizot 2007) in which star formation proceeds through accretion of diffuse gas in cold streams (Dekel et al. 2009b). Although BCGs are quite massive objects, it is of great importance to resolve properly the earliest epoch of star formation, in order to account for all the stellar mass in these objects. Puchwein et al. (2010) have reported a similar effect in their SPH simulation, although they mentioned a significantly smaller effect ($\sim$20 per cent) with a different, may be more robust feedback model.

Another interpretation to the rather large resolution effect we see in our simulation is an evolution in the efficiency of AGN feedback. The AGN thermal energy deposition is performed within a sphere of four cells radius. The high-resolution run will therefore deposit the energy deeper into the halo potential well. This might result in a reduced overall efficiency. Using the same model than in this paper, Booth & Schaye (2009) have also reported a rather strong dependence of the computed star formation rate on mass resolution (see their fig. 6b). Another solution we would like to explore in the future is to recalibrate the AGN feedback model parameters as a function of mass resolution, in order to overcome these limitations.

For both the low- and the high-resolution simulations, we see in Fig. 6 that the stellar mass profile has evolved only slightly between $z = 1$ and 0. Inside the BCG, we see stars expanding slightly, while the stellar halo grows in mass more substantially, by almost a factor of 2. This evolution is in good qualitative agreement with the group-scale simulation reported by Feldmann et al. (2010). Using our highest resolution simulation, we observe that the agreement

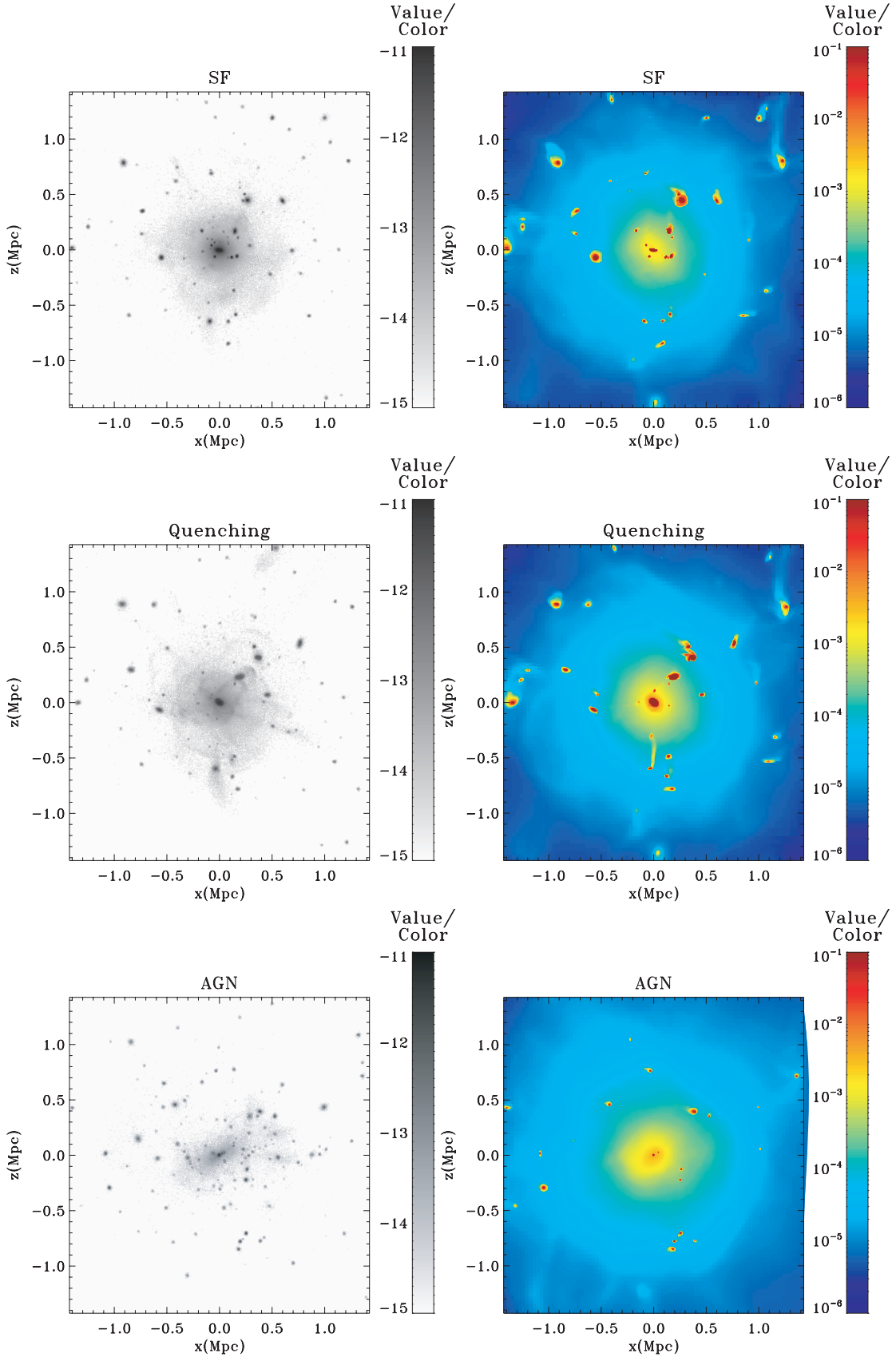

Figure 3. Maps of the projected stellar luminosity (left-hand panels, units are *I*-band absolute magnitude) and gas mass-weighted density (right-hand panels, units are in H per cc) in the simulated cluster at $z = 0$ for our three models.

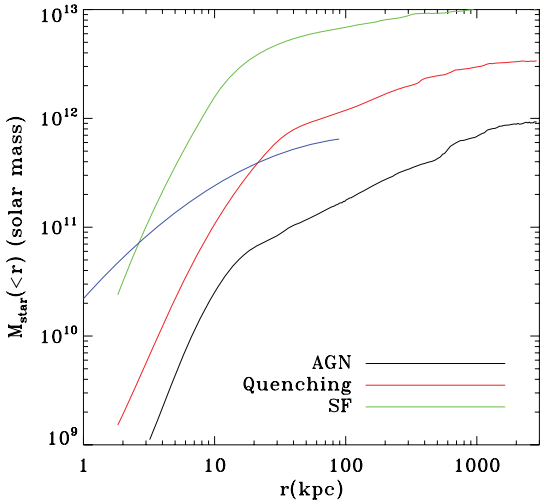

Figure 4. Cumulative stellar mass profile for our simulated cluster at $z = 0$. The blue line is the stellar mass profile of M87 from Gebhardt & Thomas (2009).

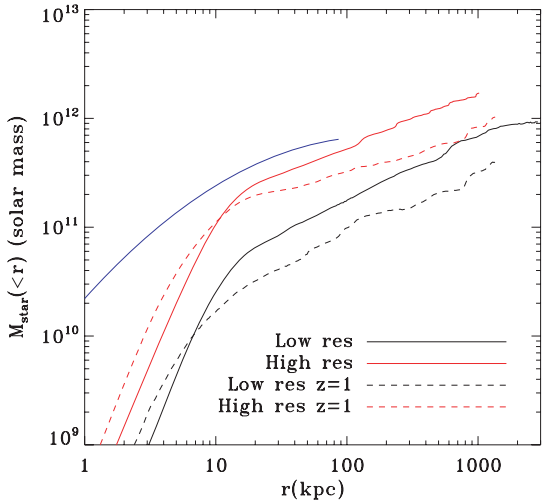

Figure 6. Effect of the mass resolution on the stellar mass profiles from our AGN model. The blue line is the stellar mass profile of M87 from Gebhardt & Thomas (2009).

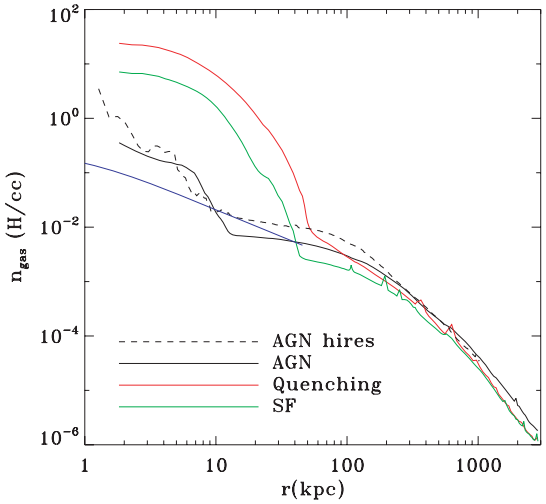

Figure 5. Gas density profile for our simulated cluster at $z = 0$. The blue line is the fit of the gas density using the X-ray emissivity profile of M87 from Churazov et al. (2008).

with M87 stellar distribution is very good between 10 and 100 kpc. It however still deviates quite strongly with observations within the inner 10 kpc. We therefore conclude that our model with AGN feedback seems to converge *from below* to the correct stellar mass distribution. It is worth stressing that the same analysis can be made for our quenching run, and that its converged stellar mass ends up being significantly above the observational limit. From this, we conclude that AGN feedback is necessary, not only to regulate star formation inside massive galaxies, but also to destroy and remove the gas supply in satellite galaxies.

3.4 The distribution of dark matter

One important consequence of the overcooling problem is to modify significantly the properties of the dark matter halo. We have plotted in Fig. 7 the projected dark matter density for our three models, and for the corresponding pure dark matter simulation. We immediately see that the dark haloes in the overcooled runs (SF and quenching) are denser and rounder than the pure dark matter case. With AGN feedback, we basically recover the halo shape and distribution of the pure dark matter case. The effect of gas cooling on the dark halo has been interpreted in terms of adiabatic contraction (AC) of the particle orbits (Blumenthal et al. 1986; Gnedin et al. 2004), meaning that individual orbits are compressed inwards, while conserving the adiabatic invariant $\mathcal{I} = rM(<r)$. The global shape change has been also interpreted by Debattista et al. (2008) as a transition from boxy orbits to more circular ones. These effects have been studied quite extensively at galactic scales, where they are probably more relevant (Pedrosa, Tissera & Scannapieco 2009; Abadi et al. 2010). Although we are dealing with a much larger object, we recover very similar properties for our dark halo, because of overcooling. We have plotted in Fig. 9 the cumulative dark matter mass profiles for our three runs, plus the DMO simulation. The DMO profile has been multiplied by 85 per cent to allow a direct comparison with the baryonic runs; it is fitted with an accuracy better than 5 per cent down to 10 kpc by a Navarro–Frenk–White (NFW) profile with a concentration parameter $c = 7.5$. The fit is shown as the blue dotted line on the same figure. The dark matter profiles for the SF and quenching runs are very similar, except in the very centre of the cluster. They all appear significantly adiabatically contracted. Interestingly enough, the AGN case appears slightly expanded, when compared to the DMO simulation. We will now use AC theory to explain these trends.

Gnedin et al. (2004) have revisited the original paper of Blumenthal et al. (1986) on AC theory, stressing that the original assumption of purely circular orbits was leading to an overestimate of the baryon-induced dark halo contraction. They presented a numerical implementation for their modified AC theory in which the particle orbit distribution was allowed some radial components and predicted the contracted dark matter distribution, given the initial dark matter profile and the final baryonic distribution. We present in Appendix A a simple analytical model to account for the adiabatic contraction of the dark halo, based on Gnedin et al. (2004) theory.

In Fig. 8 we have plotted the total baryonic mass $M_{\rm bar}$ as a function of the final radius for our three different models. Although the actual distributions are different from our simple model, we have fitted them using a constant surface density, truncated disc of mass $m_{\rm d}$ and size $r_{\rm d}$. The fits are very similar in the SF and

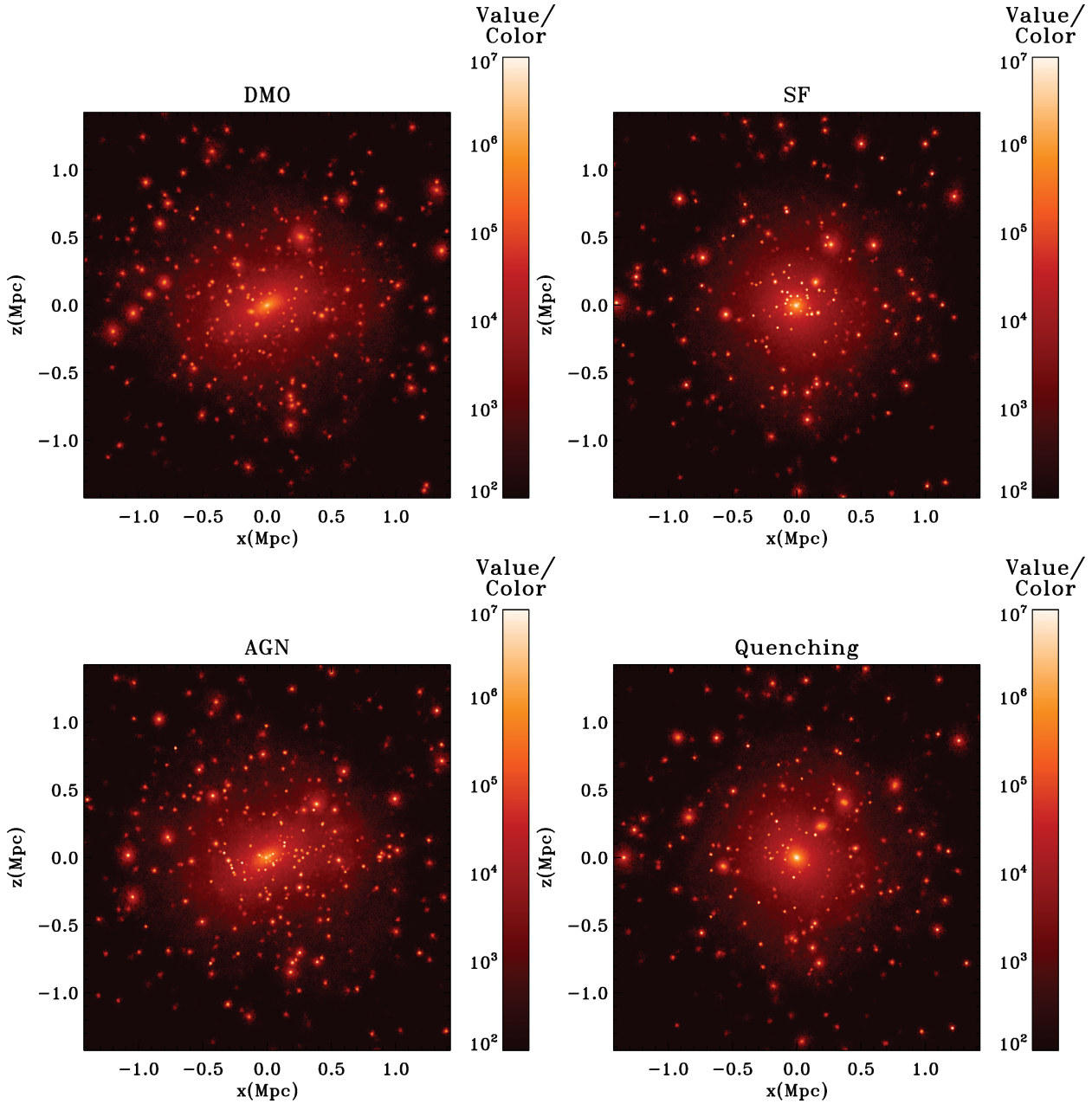

Figure 7. Maps of the dark matter overdensity distribution in the simulated cluster at $z = 0$ for our three models. Also shown for comparison is the dark matter density map we have obtained in a DMO simulation of the same cluster.

quenching cases, so we have used only one model with $m_d \simeq 5 \times 10^{12}\,M_\odot$ and $r_d \simeq 20$ kpc. These values, consistent with the mass of our simulated BCG (including the concentrated gas component in the quenching case) are much larger than any observed BCG in haloes of similar masses, and are again a manifestation of the overcooling problem. In this case of strong baryonic concentration, our analytical model with $r_d \ll r_s$ applies (see Appendix A). We have plotted the corresponding AC theory prediction in Fig. 9 as the dotted line, showing convincingly that the Gnedin et al. (2004) model, in our simplified formulation, works quite well; the fit is better than 20 per cent down to 10 kpc in radius. Within 10 kpc, our fit is not as good. We believe that since we are entering the scale of both the disc and the dark matter inner region ($r < r_s$), the adiabatic contraction model does not apply anymore. When the halo first forms and virializes at high redshift, the baryon fraction in star and gas during violent relaxation is likely to play an important role, explaining why the dark matter profiles in the SF and quenching runs differ below 10 kpc, although the total baryon mass profiles are very similar at redshift zero.

The AGN feedback model gives us a much more extended baryonic mass profile. We have fitted it using the constant surface density truncated disc model with parameters $m_d \simeq 2 \times 10^{13}\,M_\odot$ and $r_d \simeq 700$ kpc. We can see in Fig. 8 that our fit is far from being perfect (especially within the BCG), but it captures roughly the total baryon distribution, which is now mostly dominated by the hot extended gaseous halo. The values for m_d and r_d are now closer to the total mass and total size of the hot halo than those of the BCG. In this case, the AC prediction cannot be worked out analytically. We have

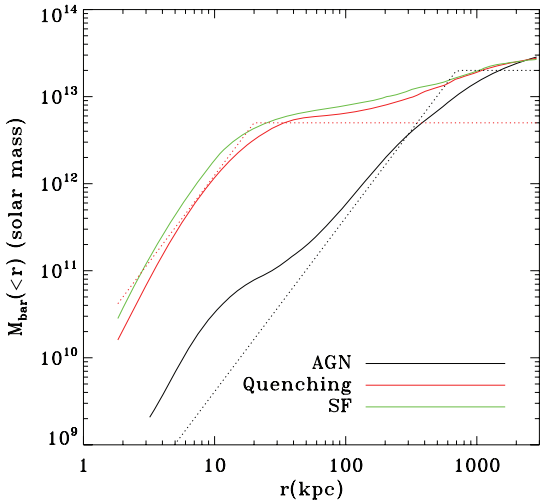

Figure 8. Cumulative total baryonic mass profile (gas + stars) in the simulated cluster at $z = 0$. The dotted lines are fits to the measured profiles for our simple model of adiabatic contraction of the dark halo.

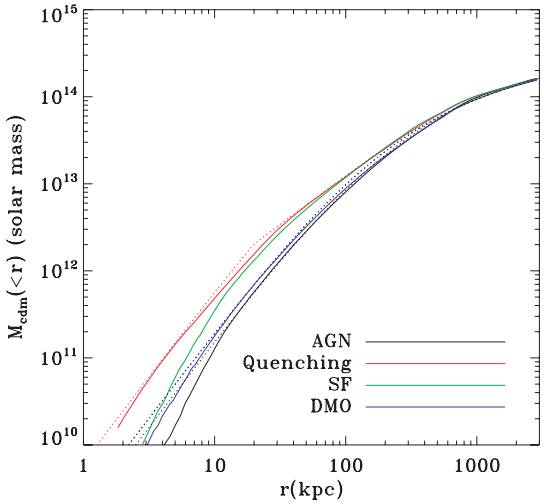

Figure 9. Cumulative dark matter mass measured in our three models at $z = 0$. Also shown in blue is the profile we obtained in the DMO simulation. In each case, the dotted line corresponds to our analytical model of adiabatic contraction. Note that in the AGN feedback case, we see a slight adiabatic expansion of the dark halo.

therefore solved for the real root of the third-order polynomial defined by equation (A1) and plotted the result in Fig. 9. Again, the prediction from Gnedin et al. (2004) theory is very close (within 20 per cent above 10 kpc) to the measured dark matter profile. In the AGN feedback case, we see that the dark matter has expanded slightly, when compared to the pure dark matter case, and that this 'adiabatic expansion' appears to be well captured by the same adiabatic invariant for the orbits of dark matter particle. Note that this expansion is very small, as it affects the dark matter mass distribution by less than a few per cent. We have also checked that using the complete numerical solution of Gnedin et al. (2004) in conjunction with the simulated baryon mass profile (instead of our simple disc model) does not affect our conclusions.

A good diagnostic of how much concentrated the simulated halo should be to match the observations is to compare the total mass profile with the one derived from dynamical arguments using M87 optical and X-ray data (see Fig. 10). Gebhardt & Thomas (2009)

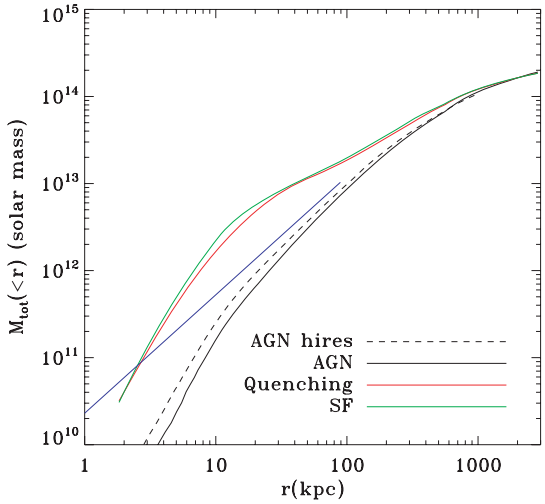

Figure 10. Cumulative total mass profile (baryons + dark matter) in the simulated cluster at $z = 0$. The blue line is the mass profile deduced from stellar kinematics and X-ray data (Gebhardt & Thomas 2009).

have derived a complex mass model for M87, including the presence of a central SMBH, stellar BCG and dark matter halo. Their mass model is compared to our total mass profiles from our three different models in Fig. 10. The SF and quenching models are too much concentrated and overestimate the total mass by a factor of 2–4 in the inner 100 kpc. The AGN model is in much better agreement, although slightly below, for both the low- and high-resolution runs.

Another diagnostic on the total mass distribution is the temperature profile of the hot, X-ray emitting gas. We have plotted in Fig. 11 the mass-weighted temperature profile for our various simulations. The temperature at 100 kpc is 3 keV in the AGN case, in good agreement with the observed value of 2.8 ± 0.2 keV (Churazov et al. 2008). Without AGN feedback, we obtain a larger temperature (around 6 keV) because of the higher mass concentration. If one looks at the temperature profile, we do not get a good match with X-ray data, even including AGN feedback. We are slightly hotter than the observations between 10 and 100 kpc, and within 10 kpc, we see a sharp drop of temperature, due to cooling gas

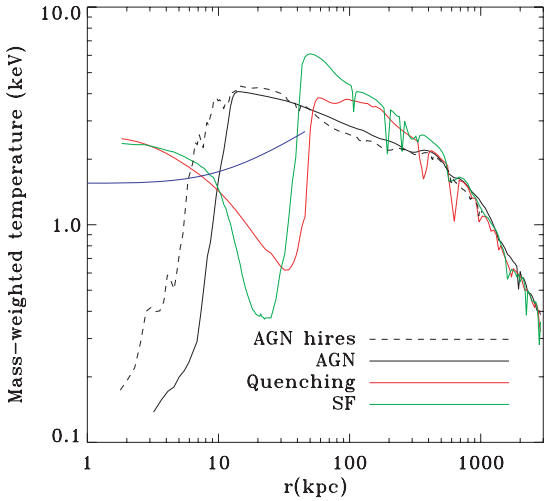

Figure 11. Mass-weighted gas temperature profile in the simulated cluster at $z = 0$. The blue line is the temperature profile inferred from X-ray data in Virgo (Churazov et al. 2008).

feeding the central galaxy and sinking towards the central AGN. We have checked that hydrostatic equilibrium is satisfied down to 10 kpc. Matching X-ray temperature profiles will probably require additional physics, such as cosmic rays propagation and magnetic fields, and/or a more realistic AGN feedback scheme.

3.5 The baryon fraction

The most important consequence of the disappearance of the overcooling problem is that we expect the baryonic mass distribution to be in much better agreement with observational constraints. Using X-ray data, it is indeed possible to estimate the gas profile in large clusters, while the stellar mass can be measured using optical data. Gonzalez et al. (2007) have computed the baryon mass fraction within r_{500} for a large sample of groups and clusters. They have found a slight deficit of baryons $f_{\rm bar} = 0.133 \pm 0.004$, when compared to the universal baryon fraction as measured by *Wilkinson Microwave Anisotropy Probe* (*WMAP*) $\Omega_{\rm b}/\Omega_{\rm m} = 0.176 \pm 0.008$ (Spergel et al. 2003, 2007). From Fig. 12, we see that the SF and quenching runs show a slight baryon *excess* with $f_{\rm bar} \simeq 0.16$ while our universal baryon fraction $\Omega_{\rm b}/\Omega_{\rm m}$ was set to 0.15 in our simulation (see Table 2). This is a direct consequence of overcooling (Kravtsov et al. 2005). On the contrary, the AGN model shows a clear baryon *deficit* with $f_{\rm bar} \simeq 0.13$, in striking agreement with the observed average value. Note however that we used a universal baryon fraction lower than the *WMAP* estimate, so that we cannot claim that our model is fully consistent with the data yet. Nevertheless, this baryon deficit in our model is the consequence of the repeated effect of AGN-driven shocks and convective motions, pushing gas outside the virial radius. One can see from the local baryon fraction profile in Fig. 12 that this gas accumulates in a region between 1 and 2 virial radii around the cluster, beyond which the cumulative baryon fraction converges to the universal one.

Our SF model compares very well to the AMR simulation performed by Kravtsov et al. (2005), showing a slight excess of baryon at the virial radius. From these standard galaxy formation models, we obtain gas properties that compare favourably to X-ray data (Nagai, Kravtsov & Vikhlinin 2007). We see indeed in Fig. 12 that in the SF model, the gas mass fraction is slowly decreasing towards the centre, with a significant deficit at the virial radius. This behaviour is traditionally explained by the joint effect of cooling and star formation (Voit & Bryan 2001). The price to pay is however to form too many stars and cold gas in the cluster, as confirmed by previous numerical models (Borgani et al. 2004; Kravtsov et al. 2005; Borgani & Kravtsov 2009). Our simple quenching model is making things better for the stellar component, but now the gas mass distribution is too concentrated (see Fig. 12). Only with AGN feedback can we obtain a small stellar mass fraction and at the same time a small gas fraction. We note however that, in our AGN model, the gas mass profile is not as steep as suggested by X-ray data. We could probably reproduce the gas profile of the SF model using another, more efficient AGN feedback scheme.

Recently, Puchwein et al. (2010) have simulated a large number of groups and clusters with the SPH code GADGET, using a mass resolution that is only about a factor 2 lower than ours and a spatial resolution of 2.5kpc (compared to 1 kpc at low resolution or 0.5 kpc at high resolution here). Nevertheless, they also found that with AGN feedback, the total baryon fraction was below the universal value. More interestingly, using a high universal baryon fraction ($\Omega_{\rm b}/\Omega_{\rm m} = 0.165$), they report a stellar mass fraction of $f_* \simeq 0.05$, quite independent of the parent halo mass. In our case, for our Virgo-like cluster with $M_{\rm vir} \simeq 10^{14}\,{\rm M}_\odot$, we obtained $f_* \simeq 0.01$ in the low-resolution case and $f_* \simeq 0.02$ in our high-resolution simulation. Our value is in better agreement with the observational estimate proposed by Lin, Mohr & Stanford (2003, 2004), while the higher value found by Puchwein et al. (2010) is in better agreement with the observations reported in Gonzalez et al. (2007). Using the COSMOS survey, Giodini et al. (2009) have estimated stellar mass fractions for a large sample of galaxy clusters and groups.

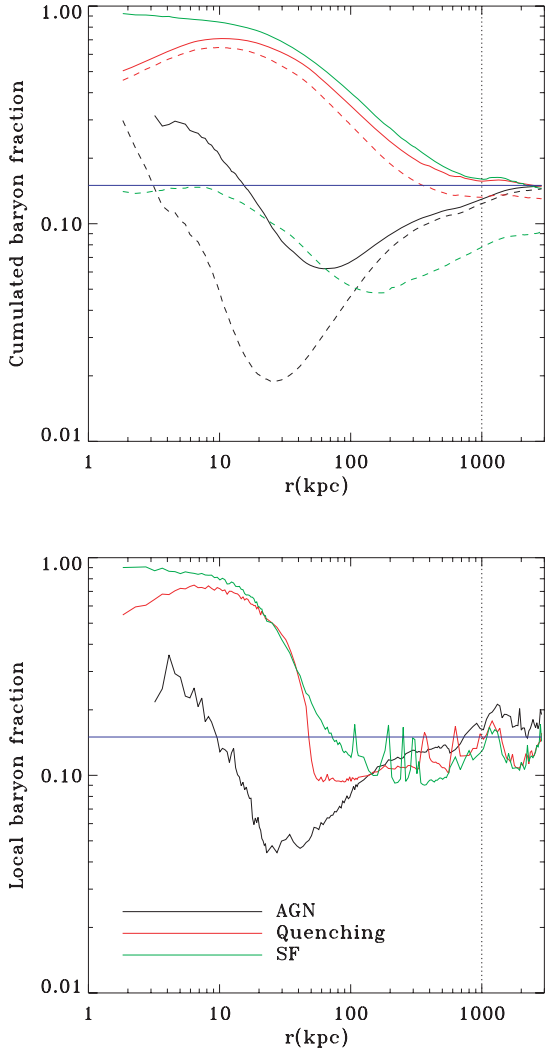

Figure 12. Cumulative (top panel) and local (bottom panel) baryon fractions at redshift $z = 0$ in the simulated cluster. The universal baryon fraction is shown as the blue horizontal line, while the virial radius is indicated by the dashed vertical line. Each model is labelled using the standard colour scheme. In the AGN feedback case, we observe a slight deficit (∼10 per cent) of baryon within the virial radius. Using the local baryon fraction, we see that these missing baryons are located in between $R_{\rm vir}$ and $2R_{\rm vir}$. In the upper panel, the cumulative gas fraction is also shown as a dashed line.

Table 2. Mass fractions inside the virial radius for our three different models. The universal baryon fraction we used in this paper is 15 per cent.

Run	$M^{\rm tot}_{\rm 200c}$	$f_{\rm bar}$ (per cent)	f_* (per cent)	$f_{\rm gas}$ (per cent)
SF	$1.2 \times 10^{14}\,{\rm M}_\odot$	16	8	8
Quenching	$1.2 \times 10^{14}\,{\rm M}_\odot$	16	3	13
AGN	$1.1 \times 10^{14}\,{\rm M}_\odot$	13	1	12

For our simulated halo mass, $M_{500c} \sim 8 \times 10^{13}\,M_{\odot}$, they report stellar mass fraction ranging from 2 to 5 per cent. Using the original feedback model of Booth & Schaye (2009) in the GADGET code, Duffy et al. (2010) have also computed the predicted baryon and stellar mass fraction of a large sample of groups extracted from a cosmological simulation. Although they report a similar baryon deficit within the virial radius, they obtained $f_* \simeq 0.03$ for an even larger universal baryon fraction $\Omega_b/\Omega_m = 0.18$. We see that there is a consensus about a strong reduction of the stellar mass fraction in groups and clusters, thanks to AGN feedback. The extent of this reduction seems to depend quite sensitively on the details of each implementation, and possibly on the nature of the code (SPH versus AMR). As suggested by observations also, we note that the exact stellar and baryon fraction probably varies from halo to halo. We would like also to stress that all the reported simulations, including ours, are probably not fully converged yet.

4 SUMMARY AND CONCLUSIONS

We have simulated the formation of a Virgo-sized galaxy cluster to study the effects of feedback on the overcooling problem. The impact of AGN feedback on the distribution of the baryonic mass is strong, and in good agreement with previous SPH simulations; star formation in massive galaxies is drastically reduced. At the same time, leftover gas is very efficiently removed from the core of the parent haloes, where it would have otherwise accumulated. In order to quantify the effect of AGN feedback, we have run two other reference simulations: one model with only star formation and supernovae feedback (the standard scenario), and one model for which we have artificially prevented star formation to occur in massive enough spheroids (the quenching scenario).

A detailed comparison of the three models clearly demonstrates that AGN feedback is needed to control star formation in the central BCG, but also to unbind the overcooling gas from the cluster core. We also clearly identify the effect of the baryon dynamics on the dark matter mass distribution on large scale. Interestingly enough, in case of AGN feedback, we observe the adiabatic expansion of the dark halo, an effect well modelled by the AC theory of Gnedin et al. (2004). A comparison of our simulation results with observational data for Virgo and its central galaxy M87 rules out the standard model, but also the quenching model. On the contrary, our simulation with AGN feedback, although not fully converged yet, shows a much better agreement with M87 data in term of mass distribution. In particular, we obtain a significantly reduced baryon fraction within the virial radius, in agreement with observations compiled by Lin et al. (2003) and Gonzalez et al. (2007). We clearly identify in our simulation that gas is removed from the core of the cluster by convective motions and/or strong shocks, and accumulates in a region just outside the virial radius. When compared to gas profiles inferred from X-ray data, our AGN model produces too shallow gas distribution, suggesting that we probably need even more powerful feedback processes.

Our cluster formation simulations with AGN feedback have not fully converged yet – as we increase the resolution, we find a stellar mass profile for the BCG that is in better agreement with observations, but it is still too low by about a factor of 2. We are still missing the lowest mass galaxy population, which could provide the missing stellar mass in the central elliptical galaxy. We also note that, in the current picture, AGN feedback is a morphologically dependent process; it only directly affects galaxies with SMBHs, i.e. galaxies with a significant bulge/spheroid component. Higher resolution studies would be needed, in order to reliably model this distinction, so that star formation in discy galaxies is not artificially suppressed.

ACKNOWLEDGMENTS

We thank our anonymous referee for helpful suggestions that greatly improved the quality of the paper. RT thanks Andrey Kravtsov for stimulating comments. All simulations were performed on the Cray XT-5 cluster at CSCS, Manno, Switzerland. We thank the CTS for supporting the astrophysical fluids program at the University of Zürich.

REFERENCES

Abadi M. G., Navarro J. F., Fardal M., Babul A., Steinmetz M., 2010, MNRAS, 407, 435
Agertz O. et al., 2007, MNRAS, 380, 963
Agertz O., Teyssier R., Moore B., 2011, MNRAS, 410, 1391
Allen S. W., Dunn R. J. H., Fabian A. C., Taylor G. B., Reynolds C. S., 2006, MNRAS, 372, 21
Arnaud K. A., Fabian A. C., Eales S. A., Jones C., Forman W., 1984, MNRAS, 211, 981
Babul A., Balogh M. L., Lewis G. F., Poole G. B., 2002, MNRAS, 330, 329
Baldi A., Forman W., Jones C., Kraft R., Nulsen P., Churazov E., David L., Giacintucci S., 2009, ApJ, 707, 1034
Begelman M. C., 2004, in Ho L. C., ed., Coevolution of Black Holes and Galaxies. Cambridge Univ. Press, Cambridge, p. 374
Begelman M. C., Volonteri M., Rees M. J., 2006, MNRAS, 370, 289
Bertschinger E., 2001, ApJS, 137, 1
Birnboim Y., Dekel A., 2003, MNRAS, 345, 349
Blumenthal G. R., Faber S. M., Flores R., Primack J. R., 1986, ApJ, 301, 27
Booth C. M., Schaye J., 2009, MNRAS, 398, 53
Borgani S., Kravtsov A., 2009, preprint (arXiv:0906.4370)
Borgani S. et al., 2004, MNRAS, 348, 1078
Bourdin H., Sauvageot J.-L., Sleszak E., Bijaoui A., Teyssier R., 2004, A&A, 414, 429
Bower R. G., Benson A. J., Malbon R., Helly J. C., Frenk C. S., Baugh C. M., Cole S., Lacey C. G., 2006, MNRAS, 370, 645
Bromm V., Loeb A., 2003, ApJ, 596, 34
Brüggen M., Kaiser C. R., Churazov E., Enßlin T. A., 2002, MNRAS, 331, 545
Brüggen M., Ruszkowski M., Hallman E., 2005, ApJ, 630, 740
Cattaneo A., Teyssier R., 2007, MNRAS, 376, 1547
Cattaneo A., Dekel A., Devriendt J., Guiderdoni B., Blaizot J., 2006, MNRAS, 370, 1651
Cattaneo A. et al., 2009, Nat, 460, 213
Chandran B. D. G., Rasera Y., 2007, ApJ, 671, 1413
Churazov E., Brüggen M., Kaiser C. R., Böhringer H., Forman W., 2001, ApJ, 554, 261
Churazov E., Forman W., Vikhlinin A., Tremaine S., Gerhard O., Jones C., 2008, MNRAS, 388, 1062
Ciotti L., Ostriker J. P., 1997, ApJ, 487, L105
Ciotti L., Ostriker J. P., 2001, ApJ, 551, 131
Croton D. J. et al., 2006, MNRAS, 365, 11
Davé R., Oppenheimer B. D., Sivanandam S., 2008, MNRAS, 391, 110
De Lucia G., Blaizot J., 2007, MNRAS, 375, 2
Debattista V. P., Moore B., Quinn T., Kazantzidis S., Maas R., Mayer L., Read J., Stadel J., 2008, ApJ, 681, 1076
Dekel A., Birnboim Y., 2006, MNRAS, 368, 2
Dekel A. et al., 2009a, Nat, 457, 451
Dekel A., Sari R., Ceverino D., 2009b, ApJ, 703, 785
Devriendt J. et al., 2010, MNRAS, 403, L84
Di Matteo T., Allen S. W., Fabian A. C., Wilson A. S., Young A. J., 2003, ApJ, 582, 133
Di Matteo T., Springel V., Hernquist L., 2005, Nat, 433, 604
Dubois Y., Teyssier R., 2008, A&A, 477, 79

Dubois Y., Devriendt J., Slyz A., Teyssier R., 2010, MNRAS, 409, 985
Duffy A. R., Schaye J., Kay S. T., Vecchia C. D., Battye R. A., Booth C. M., 2010, MNRAS, 405, 2161
Eisenstein D. J., Hu W., 1998, ApJ, 496, 605
Fabian A. C. et al., 2000, MNRAS, 318, L65
Fabjan D., Borgani S., Tornatore L., Saro A., Murante G., Dolag K., 2010, MNRAS, 401, 1670
Feldmann R., Carollo C. M., Mayer L., Renzini A., Lake G., Quinn T., Stinson G. S., Yepes G., 2010, ApJ, 709, 218
Fromang S., Hennebelle P., Teyssier R., 2006, A&A, 457, 371
Gebhardt K., Thomas J., 2009, ApJ, 700, 1690
Gebhardt K. et al., 2000, ApJ, 539, L13
Giodini S. et al. (the COSMOS Collaboration), 2009, ApJ, 703, 982
Gnedin N. Y., 2000, ApJ, 542, 535
Gnedin O. Y., Kravtsov A. V., Klypin A. A., Nagai D., 2004, ApJ, 616, 16
Gonzalez A. H., Zaritsky D., Zabludoff A. I., 2007, ApJ, 666, 147
Governato F. et al., 2009, MNRAS, 398, 312
Governato F. et al., 2010, Nat, 463, 203
Gültekin K. et al., 2009, ApJ, 698, 198
Haardt F., Madau P., 1996, ApJ, 461, 20
Hoeft M., Yepes G., Gottlöber S., Springel V., 2006, MNRAS, 371, 401
Iliev I. T., Mellema G., Shapiro P. R., Pen U.-L., 2007, MNRAS, 376, 534
Iliev I. T., Shapiro P. R., McDonald P., Mellema G., Pen U.-L., 2008, MNRAS, 391, 63
Kaiser N., 1991, ApJ, 383, 104
Kereš D., Katz N., Weinberg D. H., Davé R., 2005, MNRAS, 363, 2
Kravtsov A. V., Nagai D., Vikhlinin A. A., 2005, ApJ, 625, 588
Krumholz M. R., McKee C. F., Klein R. I., 2004, ApJ, 611, 399
Li C., Kauffmann G., Wang L., White S. D. M., Heckman T. M., Jing Y. P., 2006, MNRAS, 373, 457
Lin Y.-T., Mohr J. J., Stanford S. A., 2003, ApJ, 591, 749
Lin Y.-T., Mohr J. J., Stanford S. A., 2004, ApJ, 610, 745
McCarthy I. G. et al., 2010, MNRAS, 406, 822
Macchetto F., Marconi A., Axon D. J., Capetti A., Sparks W., Crane P., 1997, ApJ, 489, 579
McNamara B. R. et al., 2001, ApJ, 562, L149
Madau P., Rees M. J., 2001, ApJ, 551, L27
Malbon R. K., Baugh C. M., Frenk C. S., Lacey C. G., 2007, MNRAS, 382, 1394
Mayer L., Governato F., Kaufmann T., 2008, Advanced Sci. Lett., 1, 7
Mitchell N. L., McCarthy I. G., Bower R. G., Theuns T., Crain R. A., 2009, MNRAS, 395, 180
Naab T., Johansson P. H., Ostriker J. P., Efstathiou G., 2007, ApJ, 658, 710
Nagai D., Kravtsov A. V., Vikhlinin A., 2007, ApJ, 668, 1
Ocvirk P., Pichon C., Teyssier R., 2008, MNRAS, 390, 1326
Omma H., Binney J., Bryan G., Slyz A., 2004, MNRAS, 348, 1105
Pedrosa S., Tissera P. B., Scannapieco C., 2009, MNRAS, 395, L57
Pelupessy F. I., Di Matteo T., Ciardi B., 2007, ApJ, 665, 107
Ponman T. J., Cannon D. B., Navarro J. F., 1999, Nat, 397, 135
Prunet S., Pichon C., Aubert D., Pogosyan D., Teyssier R., Gottloeber S., 2008, ApJS, 178, 179
Puchwein E., Sijacki D., Springel V., 2008, ApJ, 687, L53
Puchwein E., Springel V., Sijacki D., Dolag K., 2010, MNRAS, 406, 936
Rasera Y., Chandran B., 2008, ApJ, 685, 105
Rasera Y., Teyssier R., 2006, A&A, 445, 1
Reynolds C. S., Heinz S., Begelman M. C., 2001, ApJ, 549, L179
Ruszkowski M., Brüggen M., Begelman M. C., 2004, ApJ, 611, 158
Schaye J., Vecchia C. D., 2008, MNRAS, 383, 1210
Sharma P., Chandran B. D. G., Quataert E., Parrish I. J., 2009, ApJ, 699, 348
Sijacki D., Springel V., Di Matteo T., Hernquist L., 2007, MNRAS, 380, 877
Silk J., Rees M. J., 1998, A&A, 331, L1
Spergel D. N. et al., 2003, ApJS, 148, 175
Spergel D. N. et al., 2007, ApJS, 170, 377
Springel V., 2005, MNRAS, 364, 1105
Springel V., Hernquist L., 2003, Astrophys. Supercomput. Part. Simulations, 208, 273
Springel V., Di Matteo T., Hernquist L., 2005, MNRAS, 361, 776
Stinson G., Seth A., Katz N., Wadsley J., Governato F., Quinn T., 2006, MNRAS, 373, 1074
Tabor G., Binney J., 1993, MNRAS, 263, 323
Teyssier R., 2002, A&A, 385, 337
Teyssier R., Fromang S., Dormy E., 2006, J. Comput. Phys., 218, 44
Toro E. F., Spruce M., Speares W., 1994, Shock Waves, 4, 25
Voit G. M., Bryan G. L., 2001, Nat, 414, 425
Wadsley J. W., Veeravalli G., Couchman H. M. P., 2008, MNRAS, 387, 427
Yepes G., Kates R., Khokhlov A., Klypin A., 1997, MNRAS, 284, 235

APPENDIX A: ADIABATIC CONTRACTION MODEL

If one defines the initial radius of each dark matter shell as r_i and its final, adiabatically contracted value r_f, Abadi et al. (2009) have proposed to capture Gnedin et al. (2004) model using the following simplified model:

$$\frac{r_\mathrm{f}}{r_\mathrm{i}} = 1 + \alpha\left(\frac{M_\mathrm{i}}{M_\mathrm{f}} - 1\right) \quad \text{with } \alpha \simeq 0.68. \tag{A1}$$

The original Blumenthal et al. (1986) can be recovered using $\alpha = 1$. The final cumulative mass distribution is computed using

$$M_\mathrm{f} = M_\mathrm{dm}(r_\mathrm{f}) + M_\mathrm{bar}(r_\mathrm{f}) = f_\mathrm{dm} M_\mathrm{i}(r_\mathrm{i}) + M_\mathrm{bar}(r_\mathrm{f}), \tag{A2}$$

where we have assumed that the initial dark matter mass is conserved during AC. The initial dark matter distribution is described using the analytical NFW profile:

$$M_\mathrm{i}(r_\mathrm{i}) = M_{200}\frac{\log(1+x) - x/(1+x)}{\log(1+c) - c/(1+c)}, \tag{A3}$$

where $x = r_\mathrm{i}/r_\mathrm{s}$ and $r_\mathrm{s} = r_{200}/c$. M_{200} is the total virial mass. For the baryonic distribution, we assume a constant surface density disc with size r_d and mass m_d, so that

$$M_\mathrm{bar}(r_\mathrm{f}) = m_\mathrm{d}\left(\frac{r_\mathrm{f}}{r_\mathrm{d}}\right)^2. \tag{A4}$$

The dark matter mass fraction is computed using $f_\mathrm{d} = 1 - m_\mathrm{d}/M_{200}$. The model we considered in equation (A4) for the baryonic mass distribution has been chosen that simple on purpose; inserting equation (A4) into the AC relation in equation (A1), one clearly sees that we have to find the only real root of a third-order polynomial equation with unknown $r_\mathrm{f}/r_\mathrm{i}$. This can be done quite easily with any root finder. In case the disc size is small enough (namely if $r_\mathrm{d} \ll r_\mathrm{s}$), the AC model is fully tractable analytically by noting that for $x \ll 1$, one has $M_\mathrm{i} \propto x^2$. We therefore have

$$\frac{r_\mathrm{f}}{r_\mathrm{i}} = 1 + \alpha\left[\frac{M_\mathrm{i}(r_\mathrm{i})}{f_\mathrm{d} M_\mathrm{i}(r_\mathrm{i}) + m_\mathrm{d}} - 1\right] \quad \text{for } r_\mathrm{f} \geq r_\mathrm{d} \tag{A5}$$

$$\frac{r_\mathrm{f}}{r_\mathrm{i}} \simeq \text{constant} \quad \text{for } r_\mathrm{f} < r_\mathrm{d}, \tag{A6}$$

where the constant can be determined by continuity.

This paper has been typeset from a TEX/LATEX file prepared by the author.

Chapter 4

Second Publication - The formation of the brightest cluster galaxies in cosmological simulations: the case for active galactic nucleus feedback

Published on MNRAS

Monthly Notices
of the
ROYAL ASTRONOMICAL SOCIETY

Mon. Not. R. Astron. Soc. **420,** 2859–2873 (2012) doi:10.1111/j.1365-2966.2011.19950.x

The formation of the brightest cluster galaxies in cosmological simulations: the case for active galactic nucleus feedback

Davide Martizzi,[1]★ Romain Teyssier[1,2] and Ben Moore[1]

[1]*Institute for Theoretical Physics, University of Zurich, CH-8057 Zürich, Switzerland*
[2]*CEA Saclay, DSM/IRFU/SAP, Bâtiment 709, F-91191 Gif-sur-Yvette Cedex, France*

Accepted 2011 October 4. Received 2011 October 4; in original form 2011 June 27

ABSTRACT

We use 500 pc resolution cosmological simulations of a Virgo-like galaxy cluster to study the properties of the brightest cluster galaxy (BCG) that forms at the centre of the halo. We compared two simulations; one incorporating only supernova feedback and a second that also includes prescriptions for black hole growth and the resulting active galactic nucleus (AGN) feedback from gas accretion. As previous work has shown, with supernova feedback alone we are unable to reproduce any of the observed properties of massive cluster ellipticals. The resulting BCG rotates quickly, has a high Sérsic index, a strong mass excess in the centre and a total central density profile falling more steeply than isothermal. Furthermore, it is far too efficient at converting most of the available baryons into stars which is strongly constrained by abundance matching. With a treatment of black hole dynamics and AGN feedback the BCG properties are in good agreement with data: they rotate slowly, have a cored surface density profile, a flat or rising velocity dispersion profile and a low stellar mass fraction. The AGN provides a new mechanism to create cores in luminous elliptical galaxies; the core expands due to the combined effects of heating from dynamical friction of sinking massive black holes and AGN feedback that ejects gaseous material from the central regions.

Key words: black hole physics – methods: numerical – galaxies: clusters: general – galaxies: formation – cosmology: theory – large-scale structure of Universe.

1 INTRODUCTION

In the standard Λ cold dark matter (ΛCDM) cosmological scenario, galaxy formation proceeds hierarchically and galaxy clusters are the largest and most recently assembled bound systems in the universe. The entire Hubble sequence can be found in galaxy clusters; from blue extended spirals to red massive elliptical spheroids. For this reason galaxy clusters can be considered as ideal environments for the study of galaxy formation and evolution. The brightest cluster galaxy (BCG) is usually the largest galaxy that lives at the bottom of the cluster dark matter halo. Its stars can get there in a number of ways. Some of the stars will form within the rarest peaks collapsing at high redshift – those galaxies and their dark matter haloes quickly virialize through violent rapid merging and end up at the centre of the cluster. Stars can also be acquired after the cluster formed through the dynamical friction and merging with other BCGs or with the most massive satellites of the cluster. Finally, the stars may form in situ from the cold gas that is expected to collect at the centre of the potential. The satellite galaxies themselves can undergo further evolution inside the cluster due to the interaction with the hot intracluster medium, or gravitational interactions with the cluster potential and other massive galaxies. There is growing evidence that present-day massive galaxies are formed in two phases (Oser et al. 2010): at redshift $z \gtrsim 2$ stars are formed within galaxies from infalling cold gas and at redshift $z \lesssim 3$ galaxies mainly grow through accretion of stellar material. Massive early-type galaxies can assemble more than half of their present-day mass through dry minor mergers at $z \lesssim 2$ (Naab, Johansson & Ostriker 2009). These processes affect their star formation histories and their morphological appearance.

Explaining the formation of very massive BCGs at the centre of galaxy clusters is one of the most challenging open problems in galaxy formation research. Standard galaxy formation models in the context of ΛCDM cosmology are affected by the so-called 'overcooling problem': massive galaxies are predicted to be too bright and too blue when compared to massive galaxies in the nearby universe (Borgani & Kravtsov 2009). These models find a stellar content in massive cluster galaxies, which is significantly above the observed values (Kravtsov, Nagai & Vikhlinin 2005), even if extreme supernova feedback recipes are included (Borgani et al. 2004). One scenario that has been proposed to solve this problem involves feedback processes from supermassive black holes (SMBHs), usually referred to as active galactic nucleus (AGN) feedback. Theoretical considerations (Tabor & Binney 1993; Ciotti & Ostriker 1997; Silk & Rees 1998) suggest that these processes

★E-mail: martdav@physik.uzh.ch

should provide enough energy to prevent gas from accumulating in the central regions of galaxy clusters thus quenching star formation. Semi-analytical models including AGN feedback coupled with *N*-body simulations have shown that most of the stellar mass in present-time BCGs was assembled through dry minor mergers, following a phase of quiescent star formation influenced by feedback processes (Lucia & Blaizot 2007). The strongest evidence supporting the existence of AGN feedback is provided by observations of X-ray cavities and radio cavities in galaxy clusters. These have been interpreted as buoyantly rising bubbles of high-entropy material injected in the cluster core by jets of relativistic particles. The success of numerical hydrodynamical simulations including AGN-driven buoyantly rising bubbles in reproducing masses and colours of observed BCGs has been shown by Sijacki & Springel (2006). Thus, AGN feedback is expected to play a significative role in shaping the properties of BCGs.

In this paper we use two high-resolution cosmological simulations of a Virgo-like cluster, with and without AGN feedback. The simulations were performed by Teyssier et al. (2011) using the AMR code RAMSES (Teyssier 2002). Teyssier et al. (2011) showed that combining high spatial resolution and the effects of AGN feedback it is possible to bring the stellar content in the cluster closer to the observed values, while a model without AGN feedback totally fails. Here, we use the same simulations to study the effect of AGN feedback on the massive BCGs that form at the centre of the cluster. The main questions we want to address are as follows.

(i) What are the differences between the properties of the BCG when we include AGN feedback and when we do not? We consider structural as well as kinematic quantities to address this problem, including ellipticities, masses, velocity dispersions, rotational velocities and stellar surface density profiles.

(ii) What are the main ingredients that determine the evolution of the BCG? Massive elliptical galaxies are expected to form through a long series of dry minor mergers (Naab et al. 2007, 2009), but processes connected to SMBHs and AGN feedback may also influence their evolution.

(iii) Recent results showed that it is possible to reproduce some of the properties of massive elliptical galaxies in the field and in galaxy groups neglecting AGN feedback (Naab et al. 2009; Feldmann et al. 2010). Is it possible to do the same for BCGs in massive galaxy clusters? If not, can the problem be solved by invoking AGN feedback?

The paper is organized as follows: the first section is dedicated to the numerical methods and the subgrid recipes adopted for our simulations (cooling, star formation and AGN feedback), while the second section presents our results, comparing our models with observational data and other numerical simulation studies. The final section is left for discussion.

2 NUMERICAL TECHNIQUES

In this section we describe the numerical methods and the initial conditions used to model the Virgo-like cluster we will study in this paper. We consider two numerical cosmological simulations that have been presented by Teyssier et al. (2011). They were performed using the zoom-in technique which allows us to obtain the required effective resolution in selected regions of the computational domain. We consider a periodic cubic box of the universe of side 100 Mpc h^{-1} that has the standard ΛCDM cosmological parameters, with $\Omega_{\rm m} = 0.3$, $\Omega_\Lambda = 0.7$, $\Omega_{\rm b} = 0.045$, $\sigma_8 = 0.77$ and $H_0 = 70\ {\rm km\,s^{-1}\,Mpc^{-1}}$. We used the Eisenstein & Hu (1998) transfer function and the GRAFIC package (Bertschinger 2001) in its parallel implementation MPGRAFIC (Prunet et al. 2008) to generate our initial conditions. We first ran a low-resolution dark-matter-only simulation, then we identified dark matter haloes at $z = 0$. From the original halo catalogue we constructed a set of candidate haloes whose virial masses lie in the range 10^{14}–$2 \times 10^{14}\ {\rm M_\odot}\,h^{-1}$. Finally, we identified our final halo based on its assembly history: most of its mass is already in place at $z = 1$, therefore it can be considered as relaxed at $z = 0$. Its final virial mass is $M_{\rm vir} \simeq 10^{14}\ {\rm M_\odot}$ and $M_{200{\rm c}} = 1.04 \times 10^{14}\ {\rm M_\odot}$ or $M_{500{\rm c}} = 7.80 \times 10^{13}\ {\rm M_\odot}$, where index c refers to the critical density. We stress that our aim is not to exactly reproduce the properties of the Virgo cluster, which is a relatively unrelaxed cluster, but to study the effect of AGN feedback on the formation of the central galaxy in a cluster with a similar mass. We select a relatively relaxed halo: this allows us to focus on this effect without having to deal with a very complex merger history. The Virgo-like halo was then resimulated at higher resolution including dark matter and baryons.

2.1 The simulations

The two cosmological hydrodynamical simulations considered in this paper were performed using the AMR code RAMSES (Teyssier 2002). The initial grid had an effective size of 2048^3 and it has been used to extract a set of high-resolution dark matter particles only in the Lagrangian volume of the halo, while a lower resolution has been used to sample the rest of the periodic box. As a result we have 22×10^6 particles in the cosmological box, 19×10^6 particles in the high-resolution region and 8×10^6 particles within the virial radius of the halo at $z = 0$. This means that in the high-resolution region we have a dark matter particle mass of $8.2 \times 10^6\ {\rm M_\odot}\,h^{-1}$ and a resolution element mass of $1.4 \times 10^6\ {\rm M_\odot}\,h^{-1}$ for the baryonic component.

The AMR grid used to solve the hydrodynamical equations was initially refined to the same level as the particle grid (2048^3, level $\ell = 11$), but seven more levels of refinement were considered during the run (level $\ell_{\rm max} = 18$). We used a refinement criterion that allowed spatial resolution to be nearly constant in physical units; in this way the minimum cell physical size was always close to $\Delta x_{\rm min} = L/2^{\ell_{\rm max}} \simeq 500\ {\rm pc}\,h^{-1}$. The grid was dynamically refined using a quasi-Lagrangian strategy: when the dark matter or baryonic mass in a cell reaches eight times the initial mass resolution, it is split into eight children cells. The mass and spatial resolutions of our simulations are shown in Table 1.

2.2 Modelling the baryonic processes

Gas dynamics is modelled using a second-order unsplit Godunov scheme (Teyssier 2002; Fromang, Hennebelle & Teyssier 2006; Teyssier, Fromang & Dormy 2006) based on the HLLC Riemann solver and the MinMod slope limiter (Toro, Spruce & Speares 1994). We assume a perfect gas equation of state (EOS) with $\gamma = 5/3$. Part of the galaxy formation process has been calculated using subgrid

Table 1. Mass resolution for dark matter particles, gas cells and star particles, and spatial resolution (in physical units) for our two simulations.

$m_{\rm cdm}$ ($10^6\ {\rm M_\odot}\,h^{-1}$)	$m_{\rm gas}$ ($10^6\ {\rm M_\odot}\,h^{-1}$)	m_* ($10^6\ {\rm M_\odot}\,h^{-1}$)	$\Delta x_{\rm min}$ (kpc h^{-1})
8.2	1.4	0.3	0.38

models, since a correct modelling of the turbulent and multiphase interstellar medium (ISM) is beyond the reach of present-day cluster simulations. In both simulations:

(i) *The ISM* has been modelled using a very simple EOS for the gas

$$T_{\rm floor} = T_* \left(\frac{n_{\rm H}}{n_*}\right)^{\Gamma-1}, \quad (1)$$

where $n_* = 0.1$ H cc^{-1} is the density threshold that defines the star-forming gas, $T_* = 10^4$ K is a typical temperature mimicking both thermal and turbulent motions in the ISM and $\Gamma = 5/3$ is the polytropic index controlling the stiffness of the EOS. Gas cannot cool below the temperature floor, while it can be heated above.

(ii) *Gas cooling* is followed according to the Sutherland & Dopita (1993) cooling function. We take into account H, He and metal cooling. Gas metallicity is advected as a passive scalar, and is self-consistently accounted for in the cooling function. We also considered the effect of the standard homogeneous ultraviolet background of Haardt & Madau (1996), but we modified the starting redshift, extrapolating the average intensity from $z_{\rm reion} = 6$ to 12. This extrapolation is justified by the fact that early reionization is expected in protocluster regions (Iliev et al. 2008).

(iii) *Star formation* is implemented using the following simple model. We create new star particles in cells with gas density larger than n_*. The mass of the star particles depends on resolution; in the present case we have chosen $3 \times 10^5\,{\rm M}_\odot\,h^{-1}$. The formation rate of star particles is given by

$$\dot{\rho}_* = \epsilon_* \frac{\rho_{\rm gas}}{t_{\rm ff}} \quad \text{with} \quad t_{\rm ff} = \sqrt{\frac{3\pi}{32 G \rho}} \quad (2)$$

where $t_{\rm ff}$ is the local free-fall time of the gaseous component and $\epsilon_* = 0.01$ is the star formation efficiency.

(iv) *Supernova feedback* is implemented in the code. A 10 per cent mass fraction of each star particle is ejected in supernovae explosions after 10 Myr. We assume that the supernova energy is 10^{51} erg. We also include metal enrichment from supernovae: 1 $\rm M_\odot$ of metals per 10 $\rm M_\odot$ average progenitor mass is ejected in the ISM. This value for the metal yield has been chosen to match, on average, the metal enrichment from massive stars (Woosley & Weaver 1995). Supernova feedback is modelled using the 'delayed cooling' scheme (Stinson et al. 2006), i.e. we shut down gas cooling for 50 Myr in the cells surrounding a star particle going supernova. Since regions where feedback acts are typically very dense, this technique prevents gas from fastly radiating away the feedback energy. See Agertz, Teyssier & Moore (2011) for more details.

It has been shown that these galaxy formation recipes are able to successfully reproduce the properties of spiral galaxies in the field (Mayer, Governato & Kaufmann 2008; Governato et al. 2009, 2010; Agertz, Teyssier & Moore 2011) as well as other observed galaxy properties like the Kennicutt–Schmidt law, star formation rates, galactic winds (Dubois & Teyssier 2008; Devriendt et al. 2010; Agertz et al. 2011). On galaxy group scales the same recipes are less successful in reproducing the observed properties (Feldmann et al. 2010), while on galaxy cluster scales they fail (Borgani et al. 2004; Kravtsov et al. 2005; Borgani & Kravtsov 2009). In simulated galaxy clusters similar sets of phenomenological models produce overcooling of gas that leads to the formation of a higher fraction of stars than observed in real systems (Borgani & Kravtsov 2009). It has been argued that star formation is quenched in haloes more massive than $M_{\rm c} \simeq 6 \times 10^{11}\,{\rm M}_\odot$ (Cattaneo et al. 2006), and this mass threshold is thought to be related to the stabilization of gas accretion shocks and to the transition from cold to hot gas accretion (Birnboim & Dekel 2003), although additional physical processes are required to prevent overcooling. The favoured theoretical scenario proposed to solve the overcooling problem involves the role of AGN feedback in haloes of mass $M > M_{\rm c}$. Gas accretion favours AGN activity and the related feedback on the gas (Cattaneo et al. 2006). AGN feedback is expected to provide enough energy to heat up gas in haloes and partially blow it away, thus preventing further star formation. The analysis of cosmological simulations of galaxy groups and clusters including AGN feedback like the ones of Puchwein, Sijacki & Springel (2008) support this scenario.

The two simulations of the Virgo-like cluster we are considering differ substantially. The first run has been performed using only the galaxy formation recipes described above, without considering the presence of SMBHs and neglecting AGN feedback, therefore after much thought of a clever acronym, we call it the AGN-OFF run. In the second run we include SMBHs and we take into account AGN feedback; we call it the AGN-ON run.

2.3 SMBH growth and AGN feedback in the simulations

The seeds for SMBH formation are thought to be either Population III stars (Madau & Rees 2001), or a result of direct collapse of baryonic material within low angular momentum haloes (Bromm & Loeb 2003; Begelman, Volonteri & Rees 2006). In both cases the seed SMBHs are expected to grow relatively quickly to $M_{\rm BH,s} = 10^5\,{\rm M}_\odot$ when they will start to interact with the environment and self-regulate their gas accretion rate. The fact that this black hole mass is at least one order of magnitude lower than the minimum SMBH mass observed in the $M_{\rm BH}$–σ relation (Gebhardt et al. 2000; Gültekin et al. 2009) allows us to consider $M_{\rm BH,s}$ as the prototypical seed SMBH mass.

In our model, we use sink particles to simulate SMBHs, following the prescription of Krumholz, McKee & Klein (2004). When the following conditions are met, we create a new SMBH in the simulation.

(i) The stellar density has to be greater than 0.1 H cc^{-1} ($2.4 \times 10^6\,{\rm M}_\odot\,{\rm kpc}^{-3}$). This ensures that SMBHs form in stellar systems.

(ii) The stellar 3D velocity dispersion has to be greater than 100 km s^{-1}. With this condition we require that the line-of-sight velocity dispersion is $\sigma_{\rm 1D} \geq 60$ km s^{-1}, in agreement with the observed $M_{\rm BH}$–σ relation.

(iii) The gas density has to be greater than 1 H cc^{-1}. With this condition we are sure that seed black holes form in the nuclear region of star-forming discs.

(iv) No other sink particle is present within 10 kpc. No new seed SMBH will be created within 10 kpc from an old SMBH residing at the centre of a galaxy.

Each seed SMBH has a fixed mass $M_{\rm BH} = 10^5\,{\rm M}_\odot$ and a fixed radius $r_{\rm sink} = 4\Delta x \simeq 2$ kpc, where Δx is the spatial resolution in physical units. We assume that the SMBH mass is homogeneously distributed inside a sphere of radius $r_{\rm sink}$, and we add this density distribution to the total mass density when solving the Poisson equation. Like dark matter and star particles, sink particles are advanced in time by interpolating the gravitational force back to the sink position using the inverse CIC scheme.

A key ingredient in our simulations is AGN feedback from SMBHs. On the theoretical side, it is thought that AGN feedback energy could be transported through the gas by several processes, e.g. radiative feedback (Ciotti & Ostriker 2001) or strong shocks

(Begelman 2004; Dubois et al. 2011; Gaspari et al. 2011). Additional feedback may come from production of cosmic rays (Brüggen et al. 2002; Chandran & Rasera 2007). On the theoretical side, all these processes are very complex to model self-consistently and therefore are very challenging to be reproduced in hydrodynamical simulations. Additional difficulties include the very high spatial resolution required to study these processes in a detailed way, although it is not only a matter of resolution but also of proper physical modelling. Even in state-of-the-art cosmological hydrodynamical simulations it is not possible to model these processes in a self-consistent way, so that a phenomenological treatment of the problem must be chosen.

Mass accretion on to SMBHs and AGN feedback are implemented using a modified version of the Booth & Schaye (2009) model which was originally developed for smoothed particle hydrodynamics (SPH) simulations. This model is a modified version of that proposed by Springel, Matteo & Hernquist (2005). We compute the mass accretion rate on to each SMBH using a modified Bondi–Hoyle formula

$$\dot{M}_{\rm BH} = \alpha_{\rm boost} \frac{4\pi {\rm G}^2 M_{\rm BH}^2 \rho}{\left(c_{\rm s}^2 + u^2\right)^{3/2}}, \tag{3}$$

where ρ, $c_{\rm s}$ and u are the average gas density, sound speed and relative velocity within the sink radius, all computed following the approach of Krumholz et al. (2004). The parameter $\alpha_{\rm boost}$ was introduced by Springel et al. (2005) to account for unresolved multiphase turbulence in the SMBH environment, and its value was originally chosen as constant. Numerical studies by Booth & Schaye (2009) show that $\alpha_{\rm boost}$ should instead be considered as a function of the local density: it should be close to unity in low-density regions, it should increase in high-density regions, in order to match the subgrid model used for the unresolved turbulence in the discs. As proposed by Booth & Schaye (2009), we adopt

$$\begin{aligned} &\alpha_{\rm boost} = \left(\frac{n_{\rm H}}{n_*}\right)^2 \quad \text{if } n_{\rm H} > n_* = 0.1\ {\rm H\,cc^{-1}}, \\ &\alpha_{\rm boost} = 1 \text{ otherwise.} \end{aligned} \tag{4}$$

We stress that the choice for this particular form of $\alpha_{\rm boost}$ is strictly dependent on the chosen EOS for the gas.

Equation (3) does not provide any upper limit for the accretion rate; however, it cannot exceed the Eddington limit

$$\dot{M}_{\rm ED} = \frac{4\pi {\rm G} M_{\rm BH} m_{\rm p}}{\epsilon_{\rm r} \sigma_{\rm T} c} \quad \text{with} \quad \epsilon_{\rm r} \simeq 0.1. \tag{5}$$

where $\epsilon_{\rm r}$ is the efficiency at which accreting gas rest-mass energy is converted into radiation. To enforce this upper limit we always set the accretion rate to

$$\dot{M}_{\rm acc} = \min(\dot{M}_{\rm BH}, \dot{M}_{\rm ED}). \tag{6}$$

At each time-step, a total gas mass of $\dot{M}_{\rm acc}\Delta t$ is removed from all cells within the sink radius, with the same weighting scheme as the one used to define average quantities (Krumholz et al. 2004). In order to prevent the gas density from vanishing or becoming negative, we remove no more than 50 per cent of the gas at each time-step.

In our simulations, AGN feedback is implemented in a way that allows self-regulated SMBH mass growth (Cattaneo & Teyssier 2007; Sijacki et al. 2007; Booth & Schaye 2009), by injecting thermal energy directly into the gas surrounding the black hole. If the black hole mass is too low, the amount of energy injected in the gas will not be able to heat it up, so it will remain cold and will accrete on to the SMBH at rates close to Eddington limit. In this case the SMBH growth can proceed exponentially with time, with e-folding time-scale equal to the Salpeter time

$$t_{\rm S} = \frac{\epsilon_{\rm r}\sigma_{\rm T} c}{4\pi G m_{\rm p}} \approx 45\ {\rm Myr}. \tag{7}$$

Feedback will become more efficient as long as the SMBH continues to grow, until the injected energy is enough to unbind the gas surrounding the black hole. In this regime accretion will become Bondi–Hoyle limited and mass growth will proceed more slowly. Fig. 1 shows the time evolution of the accretion rate of the most massive SMBH in the simulated region. Short bursts of Eddington-limited accretion are followed by long quiescent epochs of Bondi–Hoyle limited accretion, self-regulated by SMBH feedback.

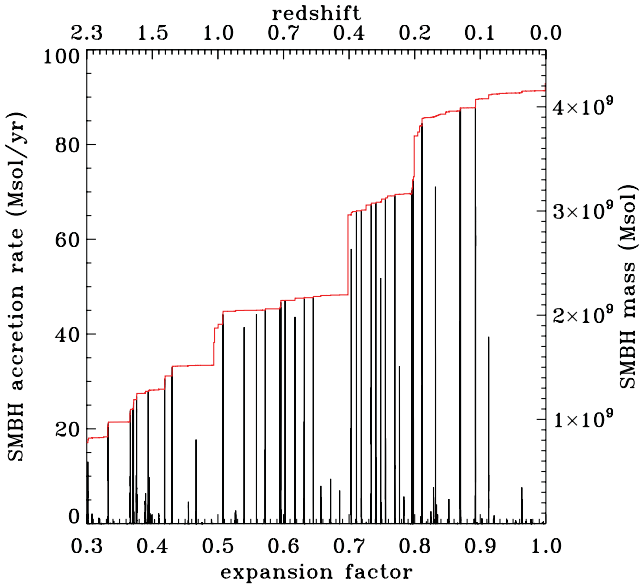

Figure 1. Time evolution of the SMBH mass in red, and of its instantaneous accretion rate in black.

At each time-step we compute the thermal energy injected in the gas surrounding each black hole as

$$\Delta E = \epsilon_{\rm c} \epsilon_{\rm r} \dot{M}_{\rm acc} c^2 \Delta t, \tag{8}$$

where $\epsilon_{\rm c}$ is the coupling efficiency, i.e. the fraction of radiated energy that is coupled with the surrounding gas. The correct value for ϵ_c can be set requiring the simulations to reproduce the observed $M_{\rm BH}$–σ relation; we use the fiducial value $\epsilon_{\rm c} \simeq 0.15$ (Booth & Schaye 2009). The energy ΔE is not immediately injected in the gas, but its accumulated and stored in a new variable $E_{\rm AGN}$, so that we can avoid the gas instantly radiating away this energy via atomic line cooling. We release this energy within the sink radius when

$$E_{\rm AGN} > \frac{3}{2} m_{\rm gas} k_{\rm B} T_{\rm min}, \tag{9}$$

where $m_{\rm gas}$ is the gas mass within the sink radius and $T_{\rm min}$ is the minimum feedback temperature. $T_{\rm min}$ should be chosen to be at least 10^7 K, the temperature above which line cooling is not very efficient, so that the resulting feedback is independent of the value of $T_{\rm min}$. In our simulations we adopt the fiducial value $T_{\rm min} = 10^7$ K.

This model allows us to phenomenologically reproduce the two extreme regimes in which AGN feedback is thought to work (Sijacki et al. 2007).

(i) 'Quasar mode': in the case of cold dense gas accretion, more energy is required to reach the energy threshold. A large amount

of energy is accumulated and released in a burst when the energy threshold is reached.

(ii) 'Radio mode': in the case of hot diffuse gas accretion, less energy is required to reach the threshold. Energy is injected in the gas in a quasi-continuous fashion.

In the next section we will show how the presence or lack of SMBHs and their feedback can heavily influence the structure of massive galaxies in clusters.

3 RESULTS

In this section, we compare the properties of the BCGs in our two simulations to show the strong differences between the two models. We also compare our results with the two observational samples of early-type galaxies at $z \approx 0$ and 1 analysed by van der Wel et al. (2008). We stress that BCGs are particular kinds of early-type galaxies, so we make an additional comparison with the BCG sample analysed by Brough et al. (2011) to show that our results are robust. A final comparison is made with the cosmological hydrodynamical simulations performed by Naab et al. (2009) (a massive early-type galaxy) and Feldmann et al. (2010) (the central galaxy of a group).

3.1 Identification of the BCGs

We identified galaxies in our simulations with the AdaptaHOP algorithm (Aubert, Pichon & Colombi 2004), using the version implemented and tested by Tweed et al. (2009). This version of the algorithm allows us to use the most massive substructure method (MSM) to identify haloes as well as their substructures, along with their centres, virial radii and masses. Galaxy centres were identified by running the same halo finder using the star particles. In each of the analysed snapshots, we defined the BCG as the object with the largest stellar mass; we verified that such a definition of the BCG also selects the galaxy closest to the cluster halo centre.

In both simulations, the BCGs are surrounded by fairly smooth stellar haloes extending to beyond 50 kpc. Similar stellar haloes around BCGs have been found in numerical simulations by other authors (Puchwein et al. 2010) and are similar to the intracluster light observed in galaxy clusters (Lin, Mohr & Stanford 2003; Gonzalez, Zaritsky & Zabludoff 2007; Giodini et al. 2009; Rudick et al. 2010). There is no clear separation between the BCG and the intracluster stars, so just for accounting and comparison purposes, a criterion should be chosen to decide how to separate the central galaxy from the stellar halo. We consider as part of the BCGs all the regions where the stellar density is larger than $2.5 \times 10^6\ \mathrm{M}_\odot\ \mathrm{kpc}^{-3}$. This choice is justified by the fact that lowering the density threshold by a factor of 2 does not influence the values of the measured stellar masses by more than 5 per cent. We also checked that the mass estimates we obtain using this criterion are robust by comparing them with estimates obtained using two additional methods: (i) we substituted the 3D density threshold with an equivalent surface density threshold; (ii) we use a criterion similar to that used by Naab et al. (2009), where the BCG is identified as the set of star particles enclosed in a spherical region of fixed physical radius. The variations in stellar mass were always less than 5 per cent, therefore we consider the masses obtained with the stellar density criterion as our fiducial values.

We find that the BCG mass at $z = 0$ is $M_{\rm star} = 3.484 \times 10^{12}\ \mathrm{M}_\odot$ in the AGN-OFF run and $M_{\rm star} = 2.243 \times 10^{11}\ \mathrm{M}_\odot$ in the AGN-ON run. At $z = 1$ we find $M_{\rm star} = 1.637 \times 10^{12}\ \mathrm{M}_\odot$ in the AGN-OFF run and $M_{\rm star} = 1.697 \times 10^{11}\ \mathrm{M}_\odot$ in the AGN-ON run. At both redshifts the total stellar mass of the BCG in the AGN-OFF simulations are almost 10 times larger. This fact implies that star formation quenching due to AGN feedback processes is very efficient in our model and has significantly changed the star formation history already by a redshift $z = 1$.

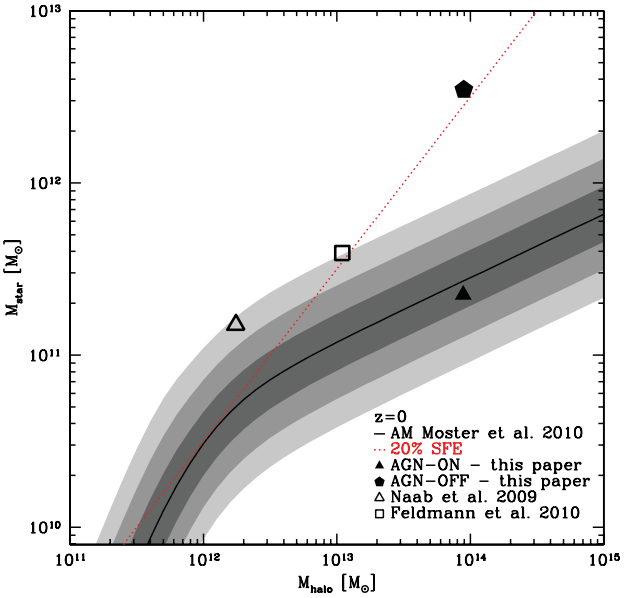

Figure 2. Comparison of the stellar-versus-halo mass relation in four early-type galaxies from different cosmological simulations (filled and empty black dots). The red dotted line represents the relation expected for a 20 per cent star formation efficiency from the universal baryon fraction. The solid black line is the prediction from abundance matching (Moster et al. 2010). The grey shaded areas represent the 1σ, 2σ and 3σ scatter bars around the average relation.

In Fig. 2 we show the comparison of the stellar-versus-halo mass relation for the BCGs in our AGN-ON/OFF simulations with the predictions of abundance matching (Moster et al. 2010) (black solid line). The BCG mass predicted by the AGN-OFF model deviates more than 3σ from the average relation obtained through abundance matching. Without feedback, the BCG forms stars at an efficiency of 20 per cent from the cosmic available baryon fraction, thus it lies close to the dotted red line. On the contrary, the AGN-ON model prediction is remarkably close to the average relation and well inside the 1σ scatter bars. For comparison with recent simulations of massive early-type galaxies that do not include AGN feedback, we show the results of Naab et al. (2009) and Feldmann et al. (2010). The mass of the central group galaxy simulated by these authors are both $\sim 3\sigma$ above the average relation; also in this case the result is close to the simplified model with 20 per cent star formation efficiency. This suggests that AGN feedback could well be the mechanism that reduces the star formation efficiencies in massive galaxies.

3.2 Star formation rates

The star formation history of the BCG galaxy in our simulations can be used to quantify the efficiency of the star formation quenching produced by our AGN feedback model. The difference between the star formation history between the AGN-ON and AGN-OFF simulations is striking. Fig. 3 shows the rate at which stars found in the BCG at $z = 0$ have been formed as a function of time. At the

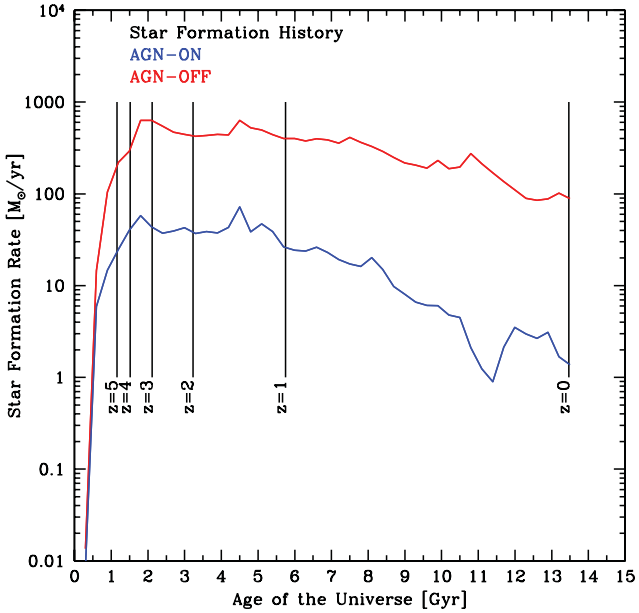

Figure 3. Star formation rate in the BCG as a function of time.

beginning of the simulation (age of the Universe <1 Gyr), when SMBHs have not formed yet the star formation rates in the AGN-ON (blue line) and AGN-OFF (red line) galaxies are almost indistinguishable. Later on AGN feedback starts to play its role in quenching star formation: the difference between the star formation rate in the two models is almost a factor of 10, with the difference increasing towards $z = 0$. Hirschmann et al. (2011) compare star formation rates of a wide variety of semi-analytical models and numerical hydrodynamical zoom simulations: they also find that the difference between the star formation rates in models including AGN and models do not including this effect is striking, however smaller than in our AGN-ON run. A similar result has been found by van de Voort et al. (2011). A comparison with these results suggests that our AGN feedback model is particularly efficient in quenching star formation. It should be stressed that such high feedback efficiency is expected because the resolution we reach is sufficient to resolve massive galaxies where SMBH reside already at $z \gtrsim 6$, thus AGN feedback starts playing its role in quenching star formation at very early times. It is interesting to note how in both the simulations the star formation rate peaks before redshift $z = 1$ and decreases towards $z = 0$. The fact that star formation is extremely quenched between $z = 1$ and 0 in the AGN-ON model is also in agreement with the results of recent semi-analytical models of BCGs (Lucia & Blaizot 2007). Some starburst events are evident as peaks in the star formation rates at different times, while periods of strong AGN activity appear as sudden decreases of the star formation rate. This simple test shows how our simple AGN feedback model is indeed able to quench star formation, decreasing the stellar mass observed in the BCG.

3.3 Ellipticity and velocity distribution of stars in the BCGs

We constructed mock images of the central region of the simulated galaxy clusters to detect further differences between the two models. Fig. 4 shows a set of such images at $z = 1$ and 0, where the colour of each pixel represents the flux in the g' band. We have chosen the same spatial and colour scales in all the pictures to show the remarkable difference in sizes between the AGN-ON and AGN-OFF simulations. The AGN-OFF BCG is much more extended than the AGN-ON one, at $z = 1$ as well as at $z = 0$, i.e. the global size of the galaxies scales with their mass. However, the half-light isophotes (black contours) show that the stellar light is more concentrated in the AGN-OFF BCG than in the AGN-ON one. This implies that the surface density profile of the AGN-ON galaxy is shallow when compared to the AGN-OFF one; this is indeed the case as we will show in Section 3.4.

To estimate the range of possible ellipticities an observer would see, we view the simulations from different angles and make the same surface brightness images. We then fit the half-light isophotes with ellipses and estimate their ellipticity $\epsilon = 1 - b/a$, where b and a are the semiminor and semimajor axes of the ellipses. In this way we give the range of possible ellipticities for our galaxies. At $z = 0$ the AGN-ON BCG has $\epsilon = [0.123, 0.155]$, while the AGN-OFF BCG has $\epsilon = [0.257, 0.498]$; both ranges are consistent with values typical of spheroidal systems, but the AGN-ON galaxy is slightly more spherical. At $z = 1$ we have $\epsilon = [0.201, 0.424]$ for the AGN-ON BCG, and $\epsilon = [0.120, 0.721]$ for the AGN-OFF BCG; at this redshift, the AGN-ON galaxy is slightly more spheroidal than at $z = 0$, while the ellipticity of the AGN-OFF galaxy is more typical of flattened ellipsoidal systems.

Fig. 5 shows the average line-of-sight velocity maps for the stars in the central region of the cluster at $z = 0$ and 1. The AGN-OFF BCG hosts a rotating disc with a rotational velocity of a few hundred km s^{-1}, both at $z = 1$ and 0. Interestingly, in the AGN-ON case there is no evidence for rotation at $z = 0$, while at $z = 1$ there is evidence for very slow rotation. These maps should be compared with those in Fig. 6 that shows the line-of-sight velocity dispersion of the stars in the central region. The AGN-OFF velocity dispersion at $z = 0$ is highly peaked in the centre, where it is larger than $\sim$750 km s^{-1}, and it decreases rapidly towards the external parts of the BCG. On the contrary, the AGN-ON velocity dispersion at $z = 0$ does not peak in the centre, but it increases towards the outskirts of the BCG (we will discuss this topic in greater detail in the next subsection). At $z = 1$ the velocity dispersion is centrally peaked in both the simulations, but the values are at least a factor of 2 larger in the AGN-OFF case than in the AGN-ON case. If we rotate the galaxies edge-on and we account only for the regions within the half-light isophotes at $z = 0$, we measure a mean $v/\sigma \sim 0.65$ for the AGN-OFF BCG and $v/\sigma \sim 0.08$ for the AGN-ON BCG. At $z = 1$ we find $v/\sigma \sim 0.82$ for the AGN-OFF BCG and $v/\sigma \sim 0.16$ for the AGN-ON BCG.

It is interesting to compare the $(\epsilon, v/\sigma)$ values with those observed in early-type galaxies, despite the fact that BCGs are a particular subcategory of these objects. Cappellari et al. (2007) and Emsellem et al. (2007) used 2D spectroscopy measurements from the SAURON survey (Bacon et al. 2001; de Zeeuw et al. 2002) and analysed the orbital structure of 48 nearby S0 and E galaxies. They divide the galaxies in their sample into two groups: *slow rotators* with $\epsilon \lesssim 0.3$, $v/\sigma \lesssim 0.2$ and low specific angular momentum, and *fast rotators* with $\epsilon \lesssim 0.7$, $v/\sigma \gtrsim 0.2$ and a high specific angular momentum. Including the effects of AGN feedback in our simulations moved our BCG from the class of fast rotating early-type galaxies to that of the slow rotators.

The SAURON galaxies are not chosen to be central cluster galaxies, so we can also directly compare our simulations with the central galaxy in the Virgo cluster, M87 (NGC 4486), which is also a slow rotator; according to Cappellari et al. (2007), M87 has $(\epsilon, v/\sigma) = (0.04, 0.02)$, values that are consistent with the AGN-ON BCG simulation. This close match with M87 is interesting, given that in our simulations we only selected the Virgo-like halo based on its virial mass and merger history.

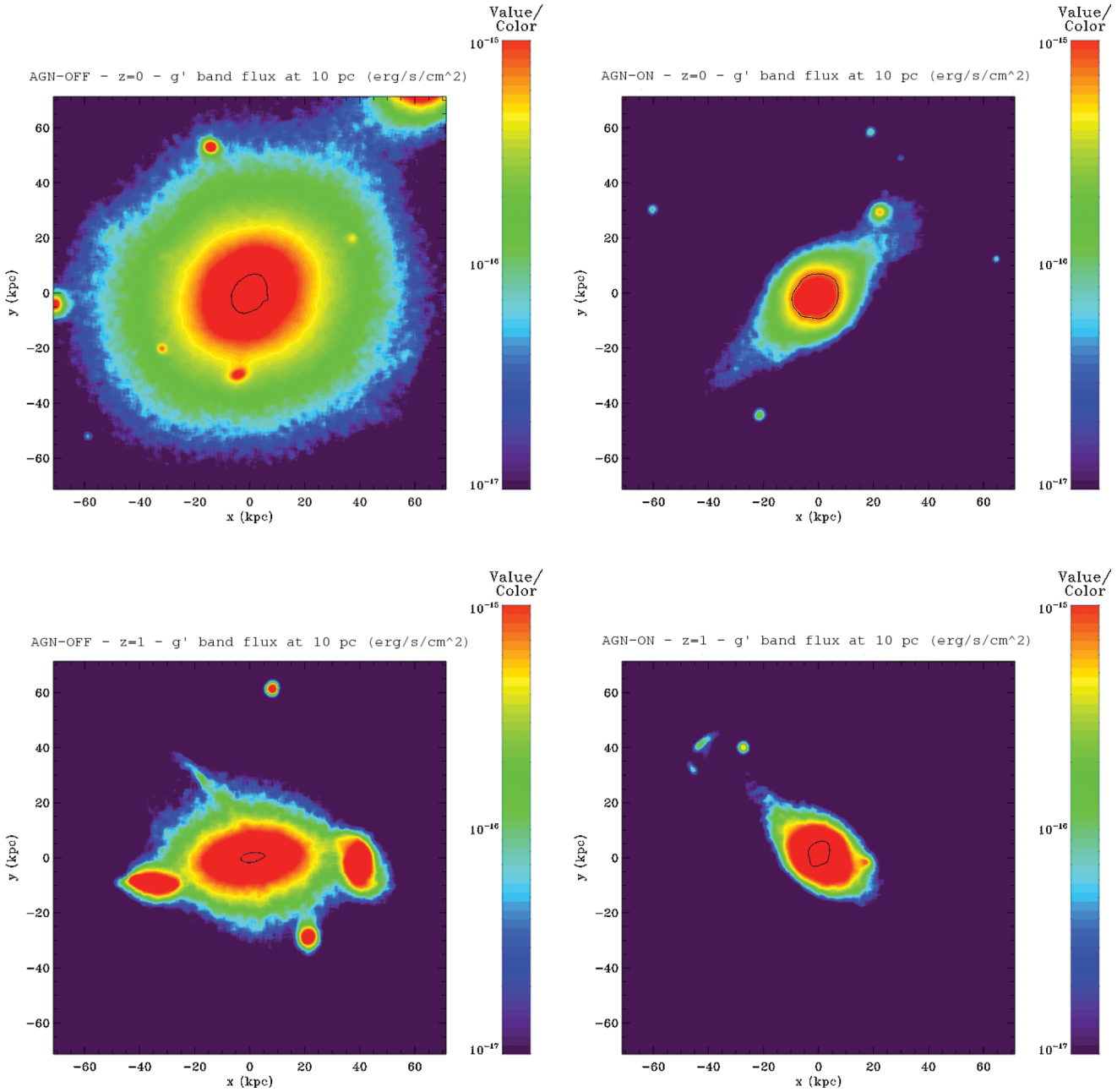

Figure 4. Fluxes in the g' band of the BCG projected along the z-axis of the periodic box. We filtered out all pixels with flux $<10^{-17}$ erg s^{-1} cm^{-2}. Top left: $z = 0$, AGN-OFF. Top right: $z = 0$, AGN-ON. Bottom left: $z = 1$, AGN-OFF. Bottom right: $z = 1$, AGN-ON. The black contours represent the half-light isophotes.

3.4 Rotational velocity, velocity dispersion and stellar mass surface density profiles

Here we analyse the circular velocity and velocity dispersion profiles of the two galaxies at $z = 0$ (Fig. 7 , left-hand panel) to further explore the structural and kinematic properties of our BCG simulations. The rotational velocity (filled symbols) of the AGN-ON BCG within $R_{\rm eff}$ (blue dashed line) is never larger than 25 km s^{-1} and its value is slightly growing with the distance from the centre. The line-of-sight velocity dispersion profile is nearly constant within the BCG, $250 \lesssim \sigma \lesssim 300$ km s^{-1} within $R_{\rm eff}$. Within this characteristic radius the galaxy is always dominated by random motions and has a very little rotation.

The AGN-OFF BCG has very different properties. Its velocity dispersion profile is maximum in the central region and decreases with radius; the rotational velocity increases with distance from the centre, peaking just before $R_{\rm eff}$ is reached, then decreases again. Within $R_{\rm eff}$ the AGN-OFF galaxy is still dominated by random motions; however, the rotational velocity is a significant fraction of the velocity dispersion ($\gtrsim$0.45). Whilst rotating disc-like structures in fast rotators have been observed (Krajnović et al. 2008), the peak $v_{\rm rot}$ value of our AGN-OFF simulation is a factor of ∼2–3 larger than the typical values measured for the fastest rotators.

The velocity dispersion profiles measured for M87 (Murphy, Gebhardt & Adams 2011) are comparable with those of our AGN-ON BCG, at least beyond the spatial resolution limit. In SAURON

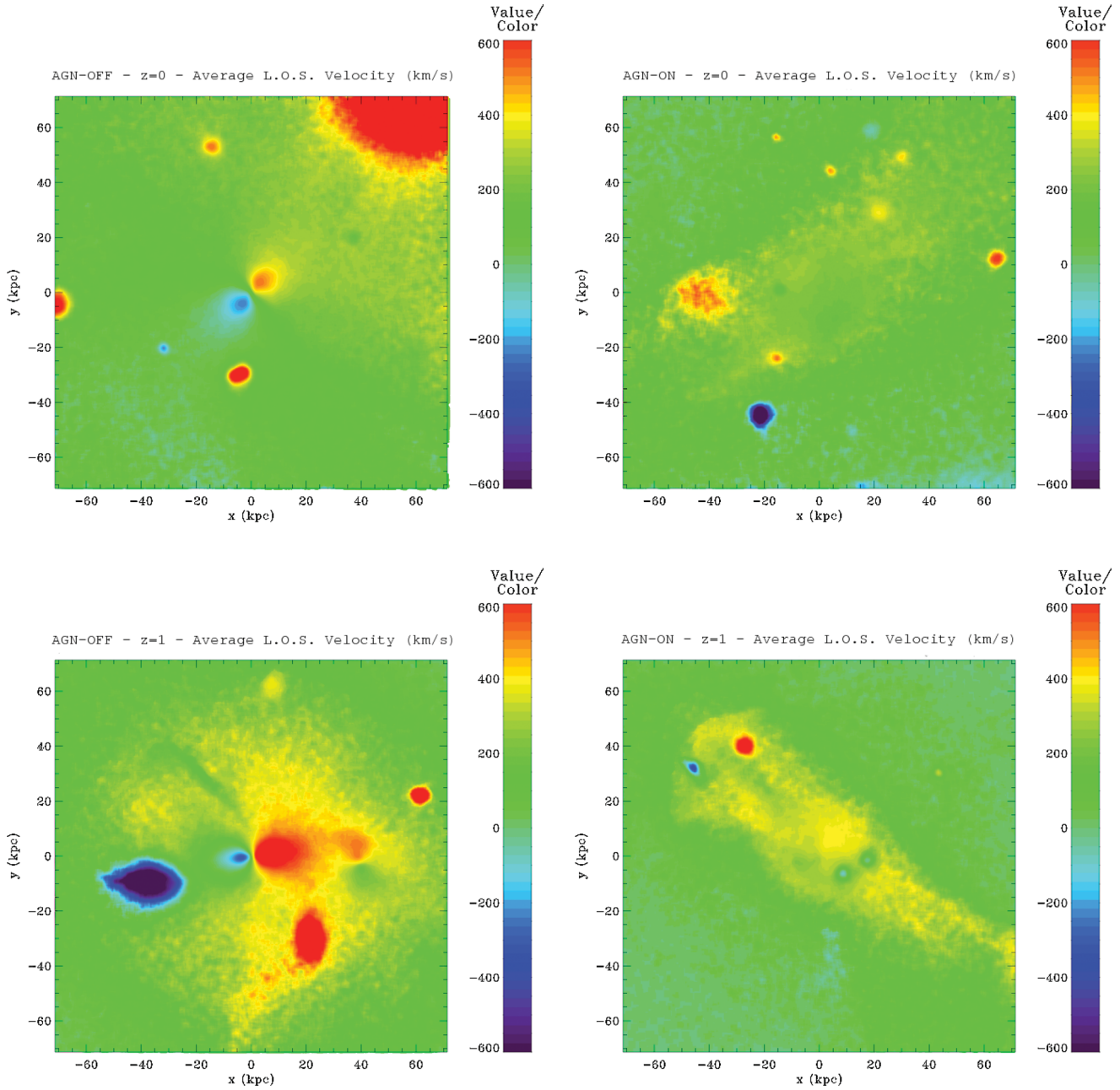

Figure 5. Average velocity along the line of sight. The projection is along the z-axis of the periodic box. Top left: $z = 0$, AGN-OFF. Top right: $z = 0$, AGN-ON. Bottom left: $z = 1$, AGN-OFF. Bottom right: $z = 1$, AGN-ON.

the kinematic properties of M87 have been measured down to ∼0.1 kpc (Emsellem et al. 2004), but our spatial resolution limit is much larger: our AGN-ON model is not able to reproduce the velocity dispersion profile observed in M87 for $R < 1$ kpc. However, when we consider the resolved region, $R > 1$ kpc, the velocity dispersion profile of our AGN-ON model and that of M87 (Emsellem et al. 2004; Murphy et al. 2011) are rather similar.

On the right-hand panel of Fig. 7 we show the stellar mass surface density profiles at $z = 0$ for our two BCGs. We find that these profiles can be fitted by Sérsic profiles for $R > 10$ kpc for the AGN-ON BCG (blue line, Sérsic index $n = 10$) and $R > 4$ kpc for the AGN-OFF BCG (red line, Sérsic index $n = 10$). We find that there is almost an order of magnitude difference between the stellar mass surface density of our two models. It is also interesting to compare the measured profiles with the Sérsic functions at $1 < R < 10$ kpc: in the AGN-OFF case we find that there is a mass excess with respect to the Sérsic function and in the AGN-ON case we find a mass deficiency. On the observational side, similar results were described by several authors (Kormendy 1999; Quillen, Bower & Stritzinger 2000; Laine et al. 2003; Trujillo et al. 2004; Lauer et al. 2005; Côté et al. 2007; Kormendy et al. 2009; Graham 2011). Kormendy et al. (2009) analyse the surface brightness profiles of elliptical and spheroidal galaxies in the Virgo cluster and show that it is possible to fit them with single light profiles to large radii. The fits are generally not satisfactory in the central regions; in particular, they find that most luminous elliptical galaxies have either light excesses or deficiencies at there centres. Light deficiencies are preferably found in the most luminous objects like NGC 4472 and M87 and the regions where

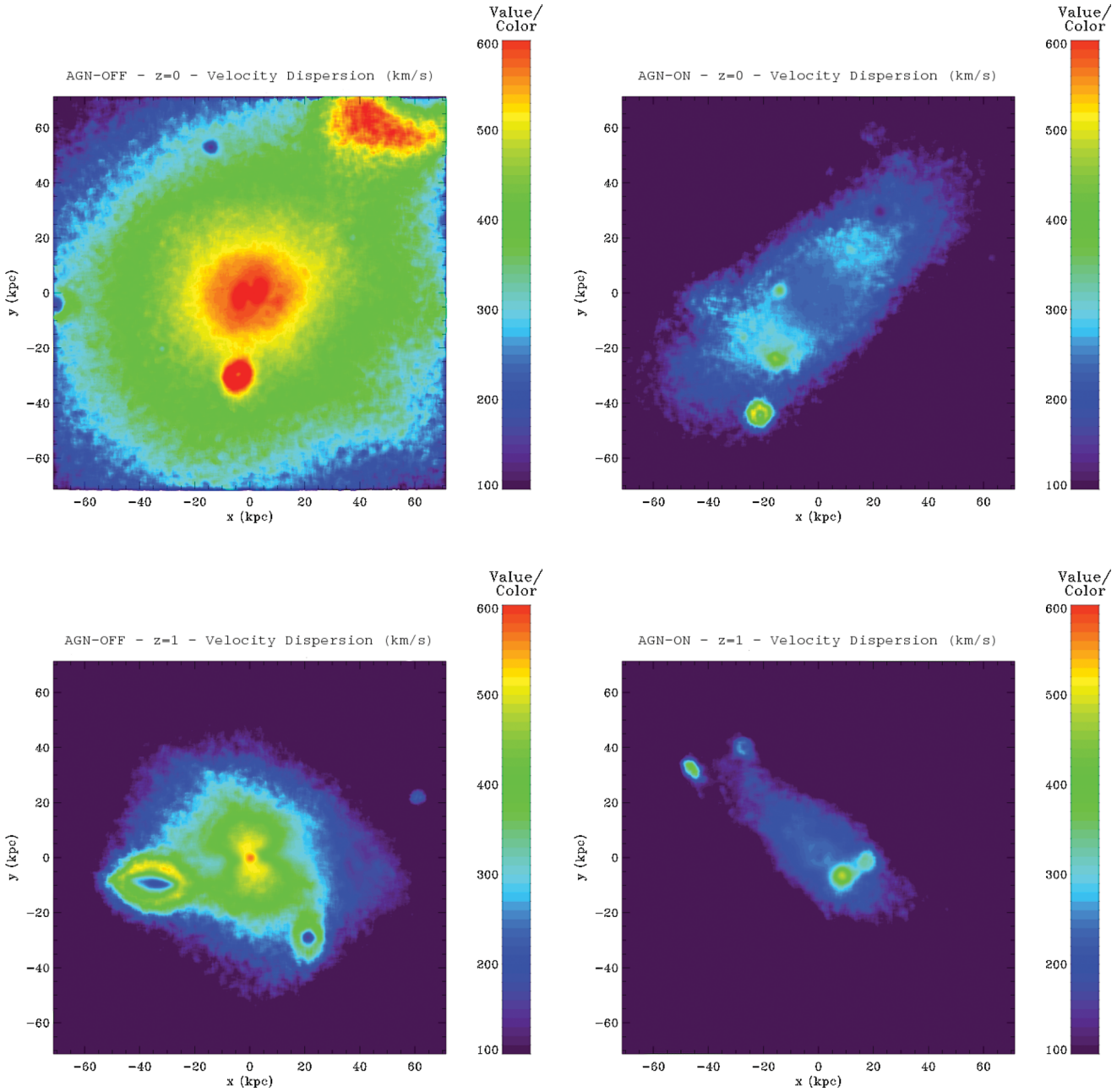

Figure 6. Velocity dispersion along the line of sight. The projection is along the z-axis of the periodic box. Top left: $z = 0$, AGN-OFF. Top right: $z = 0$, AGN-ON. Bottom left: $z = 1$, AGN-OFF. Bottom right: $z = 1$, AGN-ON.

they are found extend from the centre to a distance $\lesssim$10 kpc. If we assume that our surface density profiles can be mapped directly to surface brightness profiles, the observations of luminous galaxies are a much closer match to the AGN-ON simulation. In the next subsection we discuss the core formation process in more details.

3.5 Formation of the stellar core

The stellar surface density profile of the AGN-ON BCG within the inner 10 kpc has constant-density core. In the left-hand panel of Fig. 8 we show the time evolution of the stellar surface density profile of the AGN-ON BCG, from $z = 2$ to 0. From this plot we can see that early on the stars are centrally concentrated, but a significant core starts developing at redshift $z = 1$. The core seems to be in place by redshift $z = 0.6$, or about 3 Gyr, which is a cluster crossing time-scale, but about 100 crossing times at the half-light radius of 10 kpc. The core in the AGN-ON BCG does not form naturally; the AGN-OFF simulation has no such effect. Something has caused stars to move away from the inner region and this requires a significant amount of energy.

Naab et al. (2009) showed that repeated minor dry mergers lead to large increases in the size of massive elliptical galaxies and to decreases of the central stellar density concentration. The cores of accreted galaxies act as perturbers and modify the stellar mass distribution through dynamical friction. We do not see this effect in our AGN-OFF run because completely dry mergers are rare due to the large reservoirs of gas residing in galaxies. In the AGN-ON case a significant fraction of the gas is removed from galaxies and

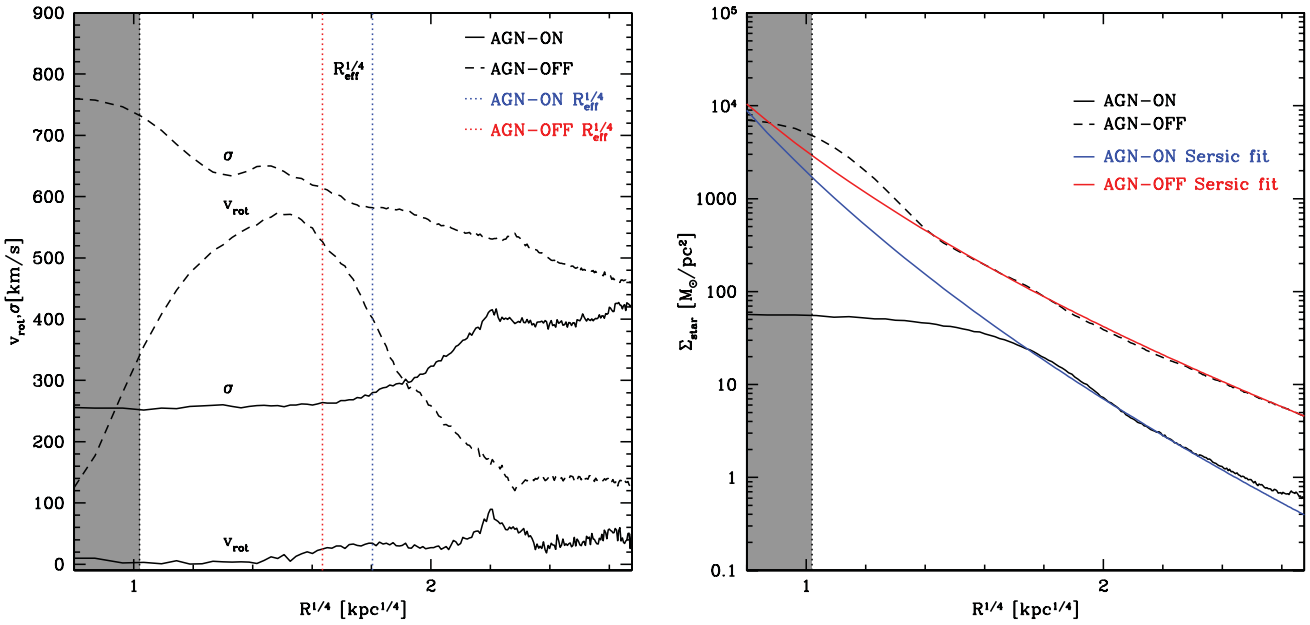

Figure 7. Left-hand panel: stellar velocity dispersion and rotational velocity of the BCG in our two models. The black solid lines are for the AGN-ON model and the black dashed lines are for the AGN-OFF model. The dotted lines indicate the effective radii of the AGN-ON (blue) and AGN-OFF (red) BCGs. Right-hand panel: stellar mass surface density profile of the BCG in our two models, compared with Sérsic profiles (see text for details). The black solid lines are for the AGN-ON model and the black dashed lines are for the AGN-OFF model. In both panels the grey shaded area shows the unresolved region of our simulations.

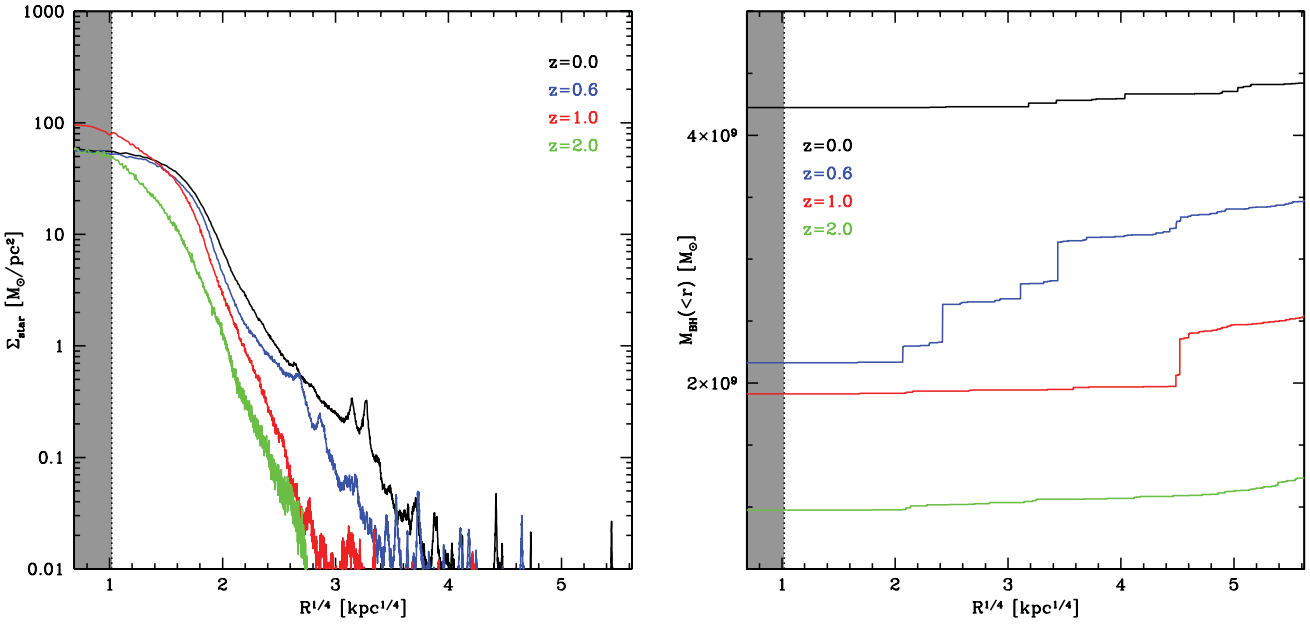

Figure 8. Secular evolution of the stellar surface density profile towards a cored profile (left-hand panel). The right-hand panel shows the cumulative SMBH mass, showing that the late time evolution is governed by a succession of dry SMBH mergers towards the central galaxy, while, at early time, the total mass in SMBH is still growing by gas accretion.

the mechanism proposed by Naab et al. (2009) can be efficient. As we will show in Section 3.6, we observe that the AGN-ON BCG is much more extended than the AGN-OFF BCG, in agreement with the Naab et al. (2009) picture, but it is challenging to produce an extended flat core like the one observed in our AGN-ON model only through repeated dry minor mergers. SMBHs and AGN feedback provide additional processes able to contribute to the core formation mechanism.

SMBH binaries are expected to form naturally in the hierarchy of mergers that lead to massive ellipticals and they provide several mechanisms that can produce cores. The most favoured model is *SMBH scouring* (Milosavljević & Merritt 2003). At the galaxy centres the black holes form binary pairs that decay as they transfer energy to stars via three-body encounters; thus they are able to eject stellar material from the central regions and form a core. Numerical experiments suggest that the cumulative effect of multiple SMBH

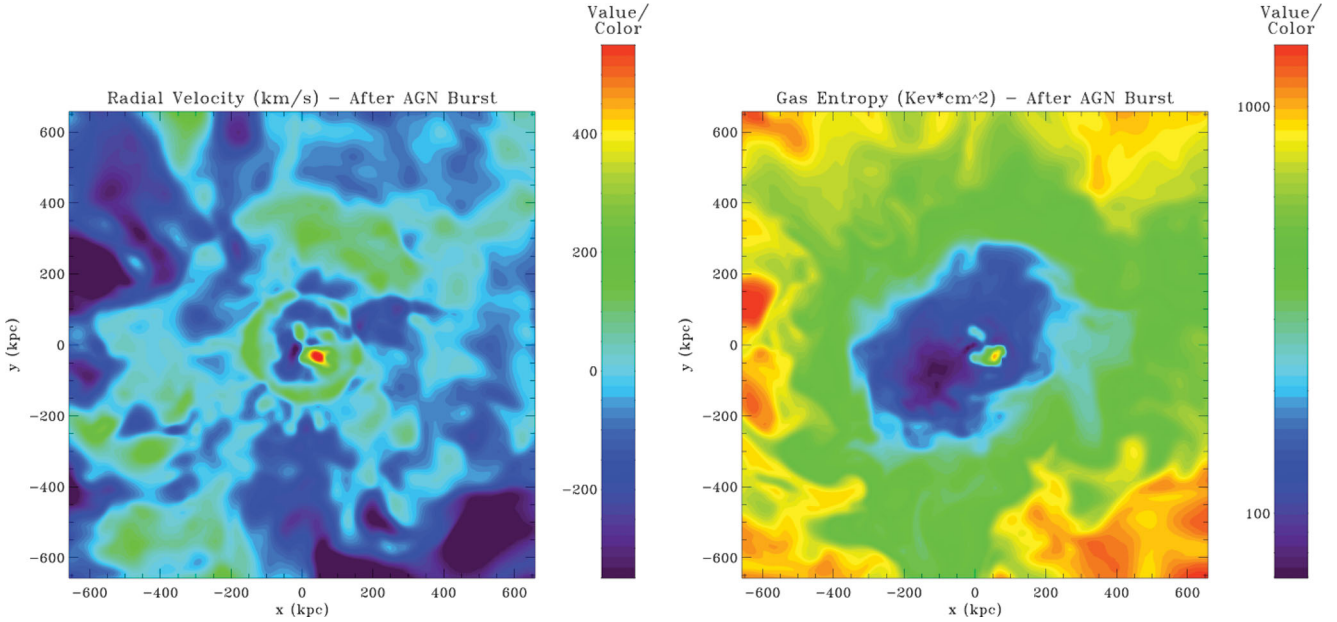

Figure 9. Left-hand panel: gas radial velocity map after an AGN burst in the AGN-ON simulation. Only the inner part of the cluster is shown. Positive values (green to red) of the radial velocity correspond to outflowing material, negative values (blue to violet) are associated to inflowing material. Right-hand panel: gas entropy map for the same region.

dry mergers is able to remove a stellar mass that is ∼2–4 times the final SMBH mass (Merritt, Mikkola & Szell 2007). This process is important from about 100 to 1 pc, so it is unresolved in our simulations which have 1 kpc force softening. At the softening length, the enclosed stellar mass is larger than the BH masses; therefore a binary BH system cannot form. However, there is an addition process that we do resolve: during the mergers the black holes would sink to the very central region due to dynamical friction. The numerical experiments presented in Goerdt et al. (2010) show that the energy transferred from the sinking SMBHs to stars contributes to the formation of cored profiles; the typical mass deficits are found to have a similar magnitude as the SMBH mass.

The right-hand panel of Fig. 8 shows the cumulative SMBH mass from the centre out to virial radius of the cluster at different output times. Each discontinuity in these profiles is associated to the presence of a SMBH. At early times the total mass in SMBHs is increasing mainly due to gas accretion, but at later times the growth is dominated by a succession of SMBH mergers. The mass of the central SMBH at $z = 0$ is $M_{\rm BH} = 4.2 \times 10^9\,{\rm M}_\odot$. The simulations of Goerdt et al. (2010) and Merritt et al. (2007) used idealized equilibrium models to study the effects of sinking massive binary objects. According to the model developed in Goerdt et al. (2010), a sinking SMBH of mass $M_{\rm BH} = 4.2 \times 10^9\,{\rm M}_\odot$ would produce a core of size $R_{\rm core} \sim 3$ kpc.

It should be stressed that these dynamical effects of sinking SMBHs act on all components of the mass distribution, although how stars, gas and dark matter respond can be quite different. Given this caveat, we note that the predictions for the mass deficit in such models is about one-third lower than the mass deficit within the inner 10 kpc of our AGN-ON BCG, $M_{\rm def} = 3.04 \times 10^{10}\,{\rm M}_\odot$, measured as the difference between the mass predicted by the Sérsic profile in Fig. 7 and the actual mass enclosed in the same region. However, recent *N*-body experiments performed by Kulkarni & Loeb (2011) showed that when multiple (three or more) SMBHs are present, the core formation process is much more efficient: mass deficits in this case can be more than five times the total SMBH mass. These results bring the mass deficit obtained in pure *N*-body simulations with perturbing SMBHs much closer to the mass deficit observed in our AGN-ON run.

Additional energy for the formation of the core can be provided by strong AGN-driven outflows at $z < 1$ that modify the local gravitational potential and may cause expansion of both the dark and stellar mass distribution. Similar processes have been observed in numerical cosmological simulations of dwarf galaxies in which gas outflows are generated by supernova feedback (Navarro, Eke & Frenk 1996; Governato et al. 2010). In the *N*-body simulations presented in Navarro et al. (1996), the mass outflows are simulated by growing and rapidly removing an idealized potential from the centre of an equilibrium realization of a dark matter halo; the effect is the formation of a core in the density profile. In this model the efficiency of the process is $\propto M_{\rm disc}^{1/2} R_{\rm disc}^{-1/2}$, where $M_{\rm disc}$ is the mass of the disc and $R_{\rm disc}$ is its scale radius. This model is substantially different from ours, since we have multiple epochs of AGN-driven gas outflows. However, these gravitational potential fluctuations should act in a similar way and could contribute to creating the large stellar cores we find.

The maps in Fig. 9 show the structure of such outflows in our AGN-ON simulation. We show the gas properties just after a strong AGN burst at $z \sim 0.1$: the map in the left-hand panel shows the radial velocity of gas with respect to the cluster centre (identified as the centre of the BCG), while the right-hand panel shows a map of the gas entropy $K = k_{\rm b} T / n_{\rm e}^{2/3}$. These plots show that in the outer regions of the cluster high-entropy gas is fastly moving towards the centre. This corresponds to hot intracluster medium cooling and flowing towards the cluster centre. On the contrary, the inner regions ($r \lesssim 400$ kpc) are characterized by convective motions pushing gas outwards at velocities ∼200 km s^{-1}, e.g. note the ring-like structure observed in the radial velocity map. Looking at the entropy map we see that gas within 400 kpc from the centre is typically a low-entropy material. Observing the regions very close

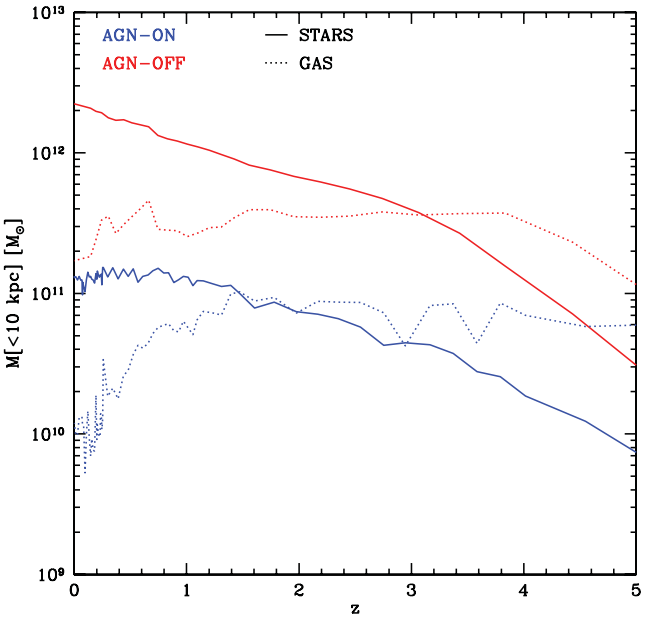

Figure 10. Time evolution of the total stellar and gas mass enclosed within 10 physical kpc.

to the cluster centre and the BCG, we can speculate on the origin of the convective motions observed at higher distances. Close to the BCG a significative fraction of the gas is falling towards the centre, but it is possible to observe an extended bubble of gas moving away from the centre at speed $\gtrsim$400 km s^{-1}. This bubble has particularly high entropy and corresponds to gas that has been heated by a strong AGN burst. This gas will be eventually pushed away from the central region and will mix with the hot intracluster medium. The net effect of AGN activity is that gas is continuously expelled from the cluster inner regions.

The plot in Fig. 10 highlights the effect of gas outflows in our simulations: we plot the stellar (solid line) and gas (dashed line) mass enclosed within 10 physical kpc as a function of redshift for both the AGN-ON (blue) and AGN-OFF (red) simulations. There is more than an order of magnitude difference between the central stellar/gas mass in the two simulations. The plot shows that in the AGN-OFF case gas continuously accretes on to the central region, while the stellar mass is constantly increasing due to star formation events; the sudden increase of the gas mass are associated with galaxy mergers. A different scenario emerges in the AGN-ON simulation: the central gas mass is roughly constant at $z \gtrsim 1$, due to the fact that AGN feedback is efficient in heating and pushing gas away. In this regime star formation is still proceeding but it is strongly quenched. At $z \lesssim 1$ AGN feedback in the central region becomes extremely efficient and $\sim 10^{11}$ M$_\odot$ of gas is expelled from the centre before $z = 0$. At $0 \lesssim z \lesssim 1$ the stellar mass inside the core is almost constant because there is very little star formation. The large gas outflows generate fluctuations in the gravitational potential that cause the ejection of stellar mass, possibly preventing the formation of a cusp in the surface density profile.

The efficiency of core formation through such mass outflows has not been studied before. Naively applying the Navarro et al. (1996) model under the assumption that $M_{\rm disc}$ equals the ejected gas mass and that $R_{\rm disc} = 10$ kpc, it is possible to predict the formation of a core of size $R_{\rm core} \sim 6$ kpc, which is close to the 10 kpc core observed in our simulations.

Finally, we note that the gas mass within the cluster core of the AGN-ON simulation slowly decreases over time. This slow decrease in gas mass will lead to an adiabatic expansion of the total mass distribution, which will also contribute to the formation of a central core. Furthermore, the cooling time of hot gas within the inner 30 kpc of the cluster centre is about 1 Gyr, thus we envisage that in its quiet mode the AGN can slowly eject the gas that rains down on to the centre from the inner cooling flow.

To further test the efficiency of these processes, extensive numerical tests should be performed using ad hoc high-resolution N-body simulations. We will go into further details about how these processes manifest themselves in galaxy clusters in a future paper (in preparation).

As mentioned in the previous section the size of the core in our AGN-ON BCG is slightly larger than what is expected for typical luminous elliptical galaxies. Also, the central surface brightness profiles of ellipticals in Virgo (Kormendy et al. 2009) are seldom as flat as the stellar profile we observe in our AGN-ON BCG. This may suggest that the model we adopt to describe AGN feedback is slightly too efficient in injecting energy in the gas and in removing mass from regions surrounding the SMBHs.

3.6 Masses, sizes and velocity dispersions

We now compare the global properties of the galaxies with the observational data of van der Wel et al. (2008). Their first sample is composed of $\gtrsim$17 000 early-type galaxies at redshifts $0.04 < z < 0.08$ taken from the SDSS data base and whose stellar masses, effective radii (recovered from SDSS g-band imaging) and average velocity dispersion within the effective radii are known. The second sample is composed of 57 cluster galaxies at redshifts $0.8 < z < 1.2$, also with known stellar masses, effective radii (recovered from z_{850}-band imaging) and average velocity dispersions. Some of the most massive early-type galaxies in these samples are BCGs. To make our comparison with observations more focused on BCGs, we also compare our simulated central galaxies to the four BCGs at $z < 0.09$ analysed by Brough et al. (2011).

For the two simulated BCGs we measured stellar masses, $M_{\rm star}$, half-mass radii, $R_{\rm eff}$,[1] and velocity dispersions within the half-mass radius, $\sigma_{\rm eff}$ at $z = 0$ and 1. The results are summarized in Table 2. The difference between the properties of our two BCGs is remarkable at $z = 0$ as well as at $z = 1$. We find the following.

(i) At $z = 1$ the AGN-OFF stellar mass is an order of magnitude larger than in the AGN-ON case. The difference is even larger at $z = 0$.

(ii) The core of the stellar distribution, quantified by $R_{\rm eff}$, is almost twice as extended in the AGN-ON case than in the AGN-OFF case, both at $z = 1$ and 0.

(iii) The average velocity dispersion within $R_{\rm eff}$ is a factor of $\sim$2 larger in the AGN-OFF case at $z = 0$ as well as at $z = 1$.

The results of Naab et al. (2009) imply that the properties of very massive early-type are determined by repeated dry minor mergers that lead to the increase of galaxy sizes and masses between $z = 1$ and 0. In our AGN-ON model a large fraction of the gas is expelled from galaxies due to AGN feedback, increasing the probability of dry mergers. This effect is completely lacking in the AGN-OFF

[1] We assume that the radius that encloses half the mass of stars is close to the half-light radii.

Table 2. Properties of the BCGs. Columns are as follows: (1) type of simulation; (2) redshift z; (3) stellar mass $M_{\rm star}$; (4) half-mass radius $R_{\rm eff}$; (5) velocity dispersion within $R_{\rm eff}$, $\sigma_{\rm eff}$; (6) ellipticity ϵ at $R_{\rm eff}$; (7) average v/σ within $R_{\rm eff}$.

Simulation	Redshift	$M_{\rm star}$ ($\rm M_\odot$)	$R_{\rm eff}$ (kpc)	$\sigma_{\rm eff}$ ($\rm km\,s^{-1}$)	ϵ	v/σ
AGN-ON	$z = 0$	2.243×10^{11}	10.286	292.96	[0.123, 0.155]	0.08
AGN-OFF	$z = 0$	3.484×10^{12}	6.858	652.83	[0.257, 0.498]	0.65
AGN-ON	$z = 1$	1.697×10^{11}	8.254	277.93	[0.201, 0.424]	0.16
AGN-OFF	$z = 1$	1.637×10^{12}	4.784	525.32	[0.120, 0.721]	0.82

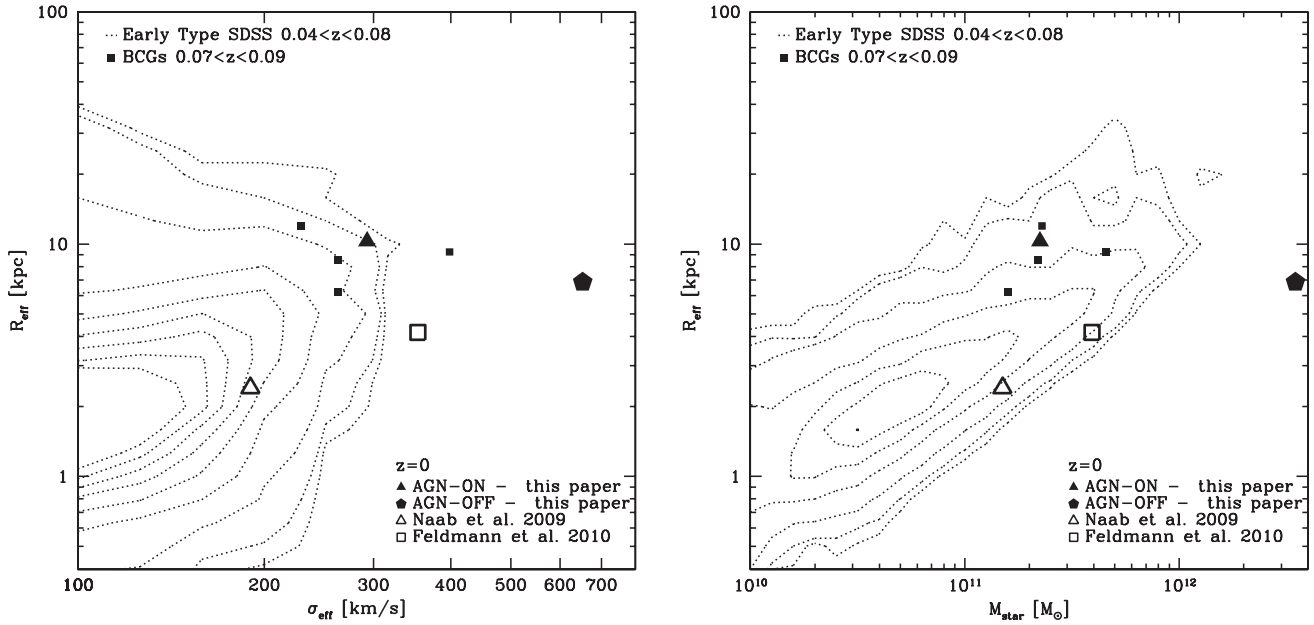

Figure 11. Velocity–size (left-hand panel) and mass–size (right-hand panel) relations of early-type galaxies at redshift $z = 0$ from Sloan data, compared to four early-type galaxies from different cosmological simulations. The black dotted lines are contours of the number of early-type galaxies per bin in the $0.04 < z < 0.08$ sample; going from outside-in we show contours for 5, 10, 30, 100, 200, 300, 400, 500, 600 galaxies per bin. Each bin has a size $\Delta\log(M_{\rm star}) = \Delta\log(R_{\rm eff}) = \Delta\log(\sigma_{\rm eff}) = 0.1$. The four BCGs analysed by Brough et al. (2011) are also shown as black filled squares.

run because much more gas is present in all galaxies. This may partially explain why the AGN-ON BCG is more extended than its AGN-OFF counterpart.

Fig. 11 shows the distribution of galaxies at low redshift in the ($\sigma_{\rm eff}$, $R_{\rm eff}$) plane (left) and in the ($M_{\rm star}$, $R_{\rm eff}$) plane (right). We compare the observations with our simulations and those of Naab et al. (2009) and Feldmann et al. (2010) (which do not include SMBHs nor AGN feedback). The simulation performed by Naab et al. (2009) reproduces quite well the properties of a typical early-type galaxy embedded in a Milky Way-sized halo at $z = 0$. The central galaxy in the group simulated by Feldmann et al. (2010) has a stellar mass and effective radius compatible with several observed early-type galaxies, but a velocity dispersion slightly larger than expected.

The AGN-OFF BCG of this paper is completely different from any observed low-redshift massive early-type galaxy in the SDSS sample. Its mass and velocity dispersion are larger than those of any observed early-type galaxy by a factor of $\sim$3 and 2, respectively. On the contrary, the properties of the AGN-ON BCG are quite consistent with those of observed galaxies. We point out that the properties of our AGN-ON BCG are also very similar to the four BCGs of Brough et al. (2011). These facts give strong observational support to galaxy formation models including AGN feedback.

To further test the effects of including the AGN we study the properties of the simulated galaxies at $z = 1$. Fig. 12 shows the distribution of the sample of cluster galaxies at $z \approx 1$ in the ($\sigma_{\rm eff}$, $R_{\rm eff}$) plane (left) and in the ($M_{\rm star}$, $R_{\rm eff}$) plane (right). For comparison, we also show also the results of Naab et al. (2009) and Feldmann et al. (2010), even if they do not refer to galaxies in clusters. Again, we find that the AGN-OFF BCG does not match the observations. The properties of the AGN-ON BCG at $z = 1$ are quite close to those of some of the most massive cluster galaxies in the sample, but the agreement is worse than at low redshift.

4 SUMMARY AND CONCLUSIONS

We simulated the formation of a Virgo-sized galaxy cluster to study the properties of the massive bright galaxy that assembled at its centre. We considered two different models: the first one includes standard galaxy formation recipes (gas cooling, star formation and supernova feedback) but no AGN feedback, whereas the second one also includes the effect of AGN feedback. Our results suggest that the effects of AGN feedback in clusters of galaxies is very important for the formation and evolution of the BCGs. Whereas Naab et al. (2009) and Feldmann et al. (2010) show that AGN feedback is not strictly required to reproduce the properties of massive early-type galaxies in the field and in groups, we provide evidence that AGN

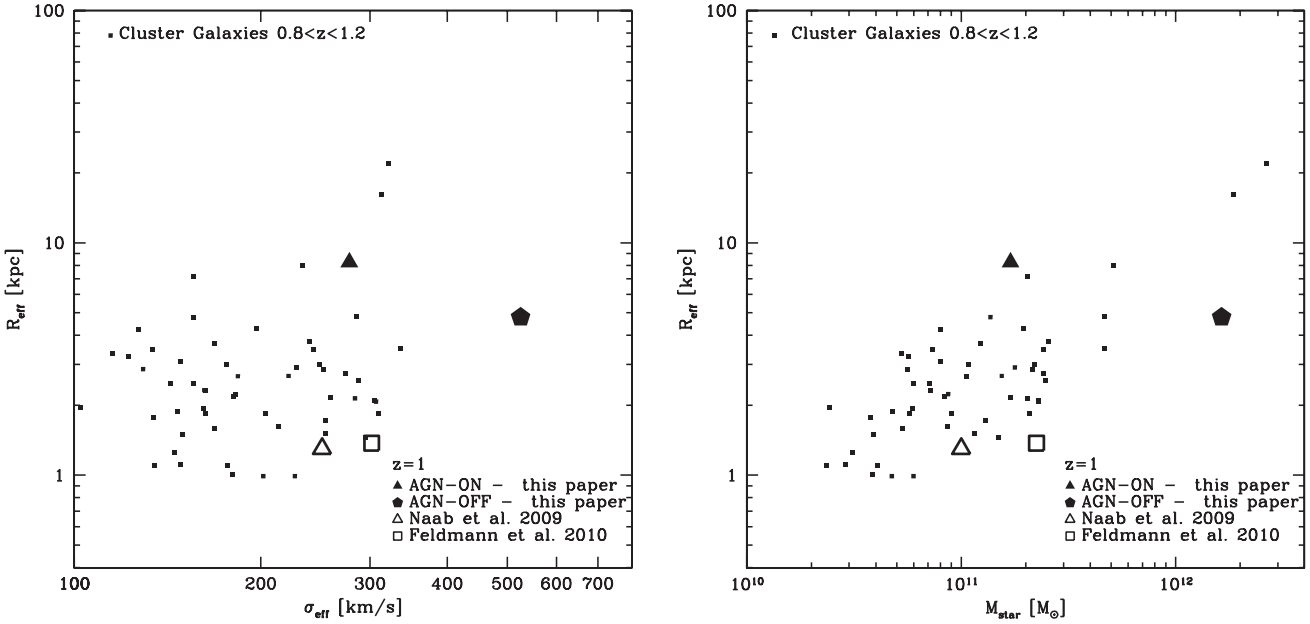

Figure 12. Velocity–size (left-hand panel) and mass–size (right-hand panel) relations of clusters elliptical galaxies at redshift $z = 1$ from van der Wel et al. (2008), compared to four early-type galaxies from different cosmological simulations.

feedback is needed to form realistic BCGs in clusters, i.e. in more massive haloes.

We compared the BCGs of our two simulations and we found substantial differences: when AGN feedback is neglected we obtain an elliptical galaxy whose properties (mass, size, kinematic structure and stellar density profile) are incompatible with observed elliptical galaxies at $z \sim 0$ and 1. It is an extremely massive and fastly rotating galaxy, with a stellar cusp in the centre. When AGN feedback is included the BCG appears to be completely different: it is 10 times less massive because star formation quenching is very efficient; it slowly rotates and its stellar surface density profile is cored in the inner 10 kpc.

AGN feedback results in a stellar-to-halo mass ratio is consistent with the prediction of abundance matching (Moster et al. 2010). A comparison with the massive early-type galaxies in the samples analysed by van der Wel et al. (2008) shows that the mass, the velocity dispersion and the effective radius are consistent with those of the most massive early-type galaxies observed in the SDSS at $z \sim 0$ and cluster galaxies at $z \sim 1$. We note that a slight decrease in the efficiency of AGN feedback would produce a slightly larger mass and a lower effective radius at $z = 1$, bringing our simulated galaxy into an even closer agreement with the observations.

The existence of the core in the stellar surface density distribution is in agreement with what is observed for the most luminous and massive galaxies in the Virgo cluster that show significant mass deficiencies in their central regions (Trujillo et al. 2004; Côté et al. 2007; Kormendy et al. 2009; Graham 2011). We have discussed several mechanisms that could contribute to the shaping of the final properties of the BCG and, especially, to the formation of its core: (I) a series of dry mergers that lead to SMBHs sinking to the halo centre via dynamical friction. This process can eject a large fraction of stars and dark matter from the central regions of the BCG (Milosavljević & Merritt 2003; Goerdt et al. 2010). (II) AGN feedback driven gas outflows can modify the gravitational potential in the regions close to SMBHs; these outflows are impulsive and the 'revirialization' of the inner material can lead to the formation of a core (Navarro et al. 1996). (III) The central hot gas slowly cools radiatively, falling on to the SMBH in a convective flow and is subsequently ejected impulsively. The slow loss of mass from the central region will result in the inner mass distribution expanding. The efficiency of each of these mechanisms will be explored using idealized numerical experiments in a subsequent study.

Observations show that low-mass early-type galaxies typically have cusps in their surface brightness profiles, while high-mass early-type galaxies preferably have centrally cored profiles (Trujillo et al. 2004; Côté et al. 2007; Kormendy et al. 2009). We find that neglecting the presence of SMBHs and AGN feedback produces a cusp, while including these effects produces a core. These considerations suggests that there may be a close connection between the mass dichotomy in early-type galaxies and the presence of SMBHs. In high-mass early-type galaxies the efficiency of the processes that lead to a core formation are expected to be higher than in lower mass early-type galaxies, thus lower mass galaxies may retain the cusps in the distribution of their stars.

ACKNOWLEDGMENTS

We thank our anonymous referee for helpful suggestions that greatly improved the quality of the paper. We also thank Lea Giordano for her suggestions about the topics discussed in this paper. We thank Robert Feldmann for providing us the group simulation data and Thorsten Naab for providing us the Milky Way-sized simulation data. The AMR simulations presented here were performed on the Cray XT-5 cluster at CSCS, Manno, Switzerland.

REFERENCES

Agertz O., Teyssier R., Moore B., 2011, MNRAS, 410, 1391
Aubert D., Pichon C., Colombi S., 2004, MNRAS, 352, 376
Bacon R. et al., 2001, MNRAS, 326, 23
Begelman M. C., 2004, in Ho L. C., ed., Coevolution of Black Holes and Galaxies. Cambridge Univ. Press, Cambridge, p. 374
Begelman M. C., Volonteri M., Rees M. J., 2006, MNRAS, 370, 289
Bertschinger E., 2001, ApJS, 137, 1

Birnboim Y., Dekel A., 2003, MNRAS, 345, 349
Booth C. M., Schaye J., 2009, MNRAS, 398, 53
Borgani S., Kravtsov A., 2009, preprint (arXiv:0906.4370)
Borgani S. et al., 2004, MNRAS, 348, 1078
Bromm V., Loeb A., 2003, ApJ, 596, 34
Brough S., Tran K., Sharp R. G., von der Linden A., Couch W. J., 2011, MNRAS, 414, L80
Brüggen M., Kaiser C. R., Churazov E., Enßlin T. A., 2002, MNRAS, 331, 545
Cappellari M. et al., 2007, MNRAS, 379, 418
Cattaneo A., Teyssier R., 2007, MNRAS, 376, 1547
Cattaneo A., Dekel A., Devriendt J., Guiderdoni B., Blaizot J., 2006, MNRAS, 370, 1651
Chandran B. D. G., Rasera Y., 2007, ApJ, 671, 1413
Ciotti L., Ostriker J. P., 1997, ApJ, 487, L105
Ciotti L., Ostriker J. P., 2001, ApJ, 551, 131
Côté P. et al., 2007, ApJ, 671, 1456
Devriendt J. et al., 2010, MNRAS, 403, L84
de Zeeuw P. T. et al., 2002, MNRAS, 329, 513
Dubois Y., Teyssier R., 2008, A&A, 477, 79
Dubois Y., Devriendt J., Slyz A., Teyssier R., 2011, preprint (arXiv:1109.1457)
Eisenstein D. J., Hu W., 1998, ApJ, 496, 605
Emsellem E. et al., 2004, MNRAS, 352, 721
Emsellem E. et al., 2007, MNRAS, 379, 401
Feldmann R., Carollo C. M., Mayer L., Renzini A., Lake G., Quinn T., Stinson G. S., Yepes G., 2010, ApJ, 709, 218
Fromang S., Hennebelle P., Teyssier R., 2006, A&A, 457, 371
Gaspari M., Melioli C., Brighenti F., D'Ercole A., 2011, MNRAS, 411, 349
Gebhardt K. et al., 2000, ApJ, 539, L13
Giodini S. et al., 2009, ApJ, 703, 982
Goerdt T., Moore B., Read J. I., Stadel J., 2010, ApJ, 725, 1707
Gonzalez A. H., Zaritsky D., Zabludoff A. I., 2007, ApJ, 666, 147
Governato F. et al., 2009, MNRAS, 398, 312
Governato F. et al., 2010, Nat, 463, 203
Graham A. W., 2011, preprint (arXiv:1108.0997)
Gültekin K. et al., 2009, ApJ, 698, 198
Haardt F., Madau P., 1996, ApJ, 461, 20
Hirschmann M., Naab T., Somerville R., Burkert A., Oser L., 2011, preprint (arXiv:1104.1626)
Iliev I. T., Shapiro P. R., McDonald P., Mellema G., Pen U.-L., 2008, MNRAS, 391, 63
Kormendy J., 1999, inMerritt D. R., Valluri M., Sellwood J. A., eds, ASP Conf. Ser. Vol. 182, The Central Structure of Elliptical Galaxies and the Stellar-Dynamical Search for Supermassive Black Holes. Astron. Soc. Pac., San Francisco, p. 124
Kormendy J., Fisher D. B., Cornell M. E., Bender R., 2009, ApJS, 182, 216
Krajnović D. et al., 2008, MNRAS, 390, 93
Kravtsov A. V., Nagai D., Vikhlinin A. A., 2005, ApJ, 625, 588
Krumholz M. R., McKee C. F., Klein R. I., 2004, ApJ, 611, 399
Kulkarni G., Loeb A., 2011, preprint (arXiv:1107.0517)
Laine S., van der Marel R. P., Lauer T. R., Postman M., O'Dea C. P., Owen F. N., 2003, AJ, 125, 478
Lauer T. R. et al., 2005, AJ, 129, 2138
Lin Y.-T., Mohr J. J., Stanford S. A., 2003, ApJ, 591, 749
Lucia G. D., Blaizot J., 2007, MNRAS, 375, 2
Madau P., Rees M. J., 2001, ApJ, 551, L27
Mayer L., Governato F., Kaufmann T., 2008, Advanced Sci. Lett., 1, 7
Merritt D., Mikkola S., Szell A., 2007, ApJ, 671, 53
Milosavljević M., Merritt D., 2003, ApJ, 596, 860
Moster B. P., Somerville R. S., Maulbetsch C., van den Bosch F. C., Macciò A. V., Naab T., Oser L., 2010, ApJ, 710, 903
Murphy J. D., Gebhardt K., Adams J. J., 2011, ApJ, 729, 129
Naab T., Johansson P. H., Ostriker J. P., Efstathiou G., 2007, ApJ, 658, 710
Naab T., Johansson P. H., Ostriker J. P., 2009, ApJ, 699, L178
Navarro J. F., Eke V. R., Frenk C. S., 1996, MNRAS, 283, L72
Oser L., Ostriker J. P., Naab T., Johansson P. H., Burkert A., 2010, ApJ, 725, 2312
Prunet S., Pichon C., Aubert D., Pogosyan D., Teyssier R., Gottloeber S., 2008, ApJS, 178, 179
Puchwein E., Sijacki D., Springel V., 2008, ApJ, 687, L53
Puchwein E., Springel V., Sijacki D., Dolag K., 2010, MNRAS, 406, 936
Quillen A. C., Bower G. A., Stritzinger M., 2000, ApJS, 128, 85
Rudick C. S., Mihos J. C., Harding P., Feldmeier J. J., Janowiecki S., Morrison H. L., 2010, ApJ, 720, 569
Sijacki D., Springel V., 2006, MNRAS, 366, 397
Sijacki D., Springel V., Matteo T. D., Hernquist L., 2007, MNRAS, 380, 877
Silk J., Rees M. J., 1998, A&A, 331, L1
Springel V., Matteo T. D., Hernquist L., 2005, MNRAS, 361, 776
Stinson G., Seth A., Katz N., Wadsley J., Governato F., Quinn T., 2006, MNRAS, 373, 1074
Sutherland R. S., Dopita M. A., 1993, ApJS, 88, 253
Tabor G., Binney J., 1993, MNRAS, 263, 323
Teyssier R., 2002, A&A, 385, 337
Teyssier R., Fromang S., Dormy E., 2006, J. Comput. Phys., 218, 44
Teyssier R., Moore B., Martizzi D., Dubois Y., Mayer L., 2011, MNRAS, 414, 195
Toro E. F., Spruce M., Speares W., 1994, Shock Waves, 4, 25
Trujillo I., Erwin P., Asensio Ramos A., Graham A. W., 2004, AJ, 127, 1917
Tweed D., Devriendt J., Blaizot J., Colombi S., Slyz A., 2009, A&A, 506, 647
van de Voort F., Schaye J., Booth C. M., Dalla Vecchia C., 2011, MNRAS, 415, 2782
van der Wel A., Holden B. P., Zirm A. W., Franx M., Rettura A., Illingworth G. D., Ford H. C., 2008, ApJ, 688, 48
Woosley S. E., Weaver T. A., 1995, ApJS, 101, 181

This paper has been typeset from a TEX/LATEX file prepared by the author.

Chapter 5

Third Publication - The effects of baryon physics, black holes and active galactic nucleus feedback on the mass distribution in clusters of galaxies

Published on MNRAS

Monthly Notices
of the
ROYAL ASTRONOMICAL SOCIETY

Mon. Not. R. Astron. Soc. **422,** 3081–3091 (2012) doi:10.1111/j.1365-2966.2012.20879.x

The effects of baryon physics, black holes and active galactic nucleus feedback on the mass distribution in clusters of galaxies

Davide Martizzi,[1]★ Romain Teyssier,[1,2] Ben Moore[1] and Tina Wentz[1]

[1]*Institute for Theoretical Physics, University of Zurich, CH-8057 Zürich, Switzerland*
[2]*CEA Saclay, DSM/IRFU/SAP, Bâtiment 709, F-91191 Gif-sur-Yvette, Cedex, France*

Accepted 2012 February 24. Received 2012 February 21; in original form 2011 December 12

ABSTRACT

The spatial distribution of matter in clusters of galaxies is mainly determined by the dominant dark matter component; however, physical processes involving baryonic matter are able to modify it significantly. We analyse a set of 500 pc resolution cosmological simulations of a cluster of galaxies with mass comparable to Virgo, performed with the AMR code RAMSES. We compare the mass density profiles of the dark, stellar and gaseous matter components of the cluster that result from different assumptions for the subgrid baryonic physics and galaxy formation processes. First, the prediction of a gravity-only *N*-body simulation is compared to that of a hydrodynamical simulation with standard galaxy formation recipes, and then all results are compared to a hydrodynamical simulation which includes thermal active galactic nucleus (AGN) feedback from supermassive black holes (SMBHs). We find the usual effects of overcooling and adiabatic contraction in the run with standard galaxy formation physics, but very different results are found when implementing SMBHs and AGN feedback. Star formation is strongly quenched, producing lower stellar densities throughout the cluster, and much less cold gas is available for star formation at low redshifts. At redshift $z = 0$ we find a flat density core of radius 10 kpc in both the dark and stellar matter density profiles. We speculate on the possible formation mechanisms able to produce such cores and we conclude that they can be produced through the coupling of different processes: (I) dynamical friction from the decay of black hole orbits during galaxy mergers; (II) AGN-driven gas outflows producing fluctuations of the gravitational potential causing the removal of collisionless matter from the central region of the cluster; (III) adiabatic expansion in response to the slow expulsion of gas from the central region of the cluster during the quiescent mode of AGN activity.

Key words: black hole physics – methods: numerical – galaxies: clusters: general – galaxies: formation – cosmology: theory – large-scale structure of Universe.

1 INTRODUCTION

Clusters of galaxies are the most massive virialized structures observed in the Universe and provide a wonderful laboratory to test astrophysical theories. In the Λ cold dark matter (ΛCDM) cosmological scenario, clusters are assembled via a hierarchy of mergers of less massive structures like galaxies and groups of galaxies. Many physical processes play a role during the formation of a cluster. When satellite galaxies are accreted into a cluster, their properties can be changed by tidal and ram pressure stripping, leading to the formation of a wide variety of galaxy morphologies. Furthermore, clusters are known to be dark matter dominated structures, with most of the baryonic matter residing in a hot diffuse X-ray emitting gaseous phase, the intracluster medium. The stellar mass is less significant and mainly contained in the massive central elliptical galaxy.

Since they are dominated by dark matter, this mass component determines the global properties of the mass distribution in the cluster. However, from the theoretical side, it is well known that baryonic processes can produce significant differences in the distribution of matter in collapsed structures with respect to models including only collisionless CDM. For example, baryons are known to condense the centre of dark matter haloes due to dissipative processes, producing adiabatic contraction of the total mass distribution (Gnedin et al. 2004). Several models including baryonic physics have been invoked to solve the so-called cusp/core problem in the ΛCDM cosmological framework, i.e. the discrepancy between the centrally cuspy dark matter profiles observed in dark matter haloes in numerical *N*-body simulations and the centrally cored dark matter profiles

★E-mail: martdav@physik.uzh.ch

inferred by observations in dwarf galaxies and low surface brightness galaxies (see the recent review by de Blok 2010, and references therein). The study of baryon physics induced modifications in the mass distribution in collapsed structures, and clusters of galaxies in particular, is still a field with many open issues.

This paper is dedicated to the study of the effects of baryonic processes on the mass distribution in clusters of galaxies. In particular, we use a set of cosmological hydrodynamical simulations performed using the AMR code RAMSES (Teyssier 2002) to study the effect of different models for baryons and galaxy formation physics on the mass density profile of a cluster of galaxies comparable to the Virgo cluster. This work can be considered as an extension of the analysis performed by Teyssier et al. (2011) on the same simulations, and is complementary to the analysis presented by Martizzi, Teyssier & Moore (2012). Here, we focus on the peculiar properties produced in the mass density profile when including supermassive black holes (SMBHs) and the related AGN feedback in the recipes for galaxy formation physics. We stress that AGN feedback was initially introduced to solve the so-called 'overcooling problem', namely the fact that too much stellar mass is produced in massive collapsed structure in hydrodynamical simulations with respect to what is observed in the real Universe (Borgani & Kravtsov 2009). The strong quenching of star formation produced by processes that couple AGN activity with the gas is expected to improve the match between simulations and observations (Tabor & Binney 1993; Ciotti & Ostriker 1997; Silk & Rees 1998). Strong evidence for the existence of AGN feedback is provided by observations of X-ray cavities and radio blobs in galaxy clusters, typically interpreted as buoyantly rising bubbles of high-entropy material injected in the central region of clusters by jets of relativistic particles. In this paper, we show that by including SMBH physics and AGN feedback it is possible to obtain interesting predictions on the modifications they can induce on the mass distribution in massive dark matter haloes.

The paper is organized as follows: the first section is dedicated to the numerical methods and the galaxy formation recipes adopted for our simulations; we show our main results and provide our interpretation in the second section; the last section is left for a short summary of our results and a discussion.

2 NUMERICAL METHODS

In this section, we describe the numerical techniques used to model the cluster we consider in this paper. We consider two cosmological hydrodynamical simulations presented in Teyssier et al. (2011) and Martizzi et al. (2012), plus a third cosmological simulation with only dark matter. For all the three runs we used the AMR code RAMSES (Teyssier 2002). The simulations were performed using the zoom-in technique which allows us to obtain the required effective resolution only in selected regions of the computational domain. For all the three simulations the computational domain is a cubic box of side 100 Mpc h^{-1}. For the dark matter only run (DMO, Tables 1 and 2) run we adopt a standard ΛCDM cosmology with parameters $\Omega_{\rm m} = 0.3$, $\Omega_\Lambda = 0.7$, $\Omega_{\rm b} = 0.0$, $\sigma_8 = 0.77$ and $H_0 = 70\ {\rm km\,s^{-1}\,Mpc^{-1}}$. For the two hydrodynamical runs (HYDRO runs in Tables 1 and 2) we adopt the same values for $\Omega_{\rm m}$, Ω_Λ, σ_8 and H_0, but we set $\Omega_{\rm b} = 0.045$. The initial conditions for the three simulations were computed using the Eisenstein & Hu (1998) transfer function and the GRAFIC package (Bertschinger 2001) in its parallel implementation MPGRAFIC (Prunet et al. 2008). To perform the zoom-in technique we adopted the following approach: first, we ran a low-resolution DMO simulation, and then we identified dark matter haloes at $z = 0$. From this halo catalogue we built a set of haloes whose virial masses lie in the range 10^{14} to $2 \times 10^{14}\,{\rm M}_\odot\,h^{-1}$. Finally, we identified the final halo based on its assembly history: the halo is already in place at $z = 1$; therefore, it can be considered as relaxed at $z = 0$. In particular the last major merger is observed at redshift $z \sim 1.3$. The final virial mass is $M_{\rm vir} \simeq 10^{14}\,{\rm M}_\odot$, while $M_{200c} = 1.04 \times 10^{14}\,{\rm M}_\odot$ or $M_{500c} = 7.80 \times 10^{13}\,{\rm M}_\odot$, where index c refers to the critical density. This halo has been resimulated at higher resolution, focusing the computational resources in the region of the computational domain where it forms.

Table 1. Cosmological parameters adopted in our simulations. The DMO label refers to the dark matter only run. The HYDRO label refers to the hydrodynamical runs.

Type	H_0 (km s^{-1} Mpc^{-1})	σ_8	Ω_Λ	$\Omega_{\rm m}$	$\Omega_{\rm b}$
	Cosmological parameters				
DMO	70	0.77	0.7	0.3	–
HYDRO	70	0.77	0.7	0.3	0.045

Table 2. Mass resolution for dark matter particles, gas cells and star particles and spatial resolution (in physical units) for our two sets of simulations.

Type	$m_{\rm cdm}$ ($10^6\,{\rm M}_\odot\,h^{-1}$)	$m_{\rm gas}$ ($10^6\,{\rm M}_\odot\,h^{-1}$)	m_* ($10^6\,{\rm M}_\odot\,h^{-1}$)	$\Delta x_{\rm min}$ (kpc h^{-1})
	Mass and spatial resolution			
DMO	9.6	n.a.	n.a.	0.38
HYDRO	8.2	1.4	0.3	0.38

In the DMO simulations the dark matter particle in the high-resolution region has a mass of $9.6 \times 10^6\,{\rm M}_\odot\,h^{-1}$. In the two hydrodynamical runs, the dark matter particle in the high-resolution region has a mass of $8.2 \times 10^6\,{\rm M}_\odot\,h^{-1}$, whereas the baryon resolution element has a mass of $1.4 \times 10^6\,{\rm M}_\odot\,h^{-1}$. Hydrodynamics is solved on an AMR grid that was initially refined to the same level of refinement as the particle grid (2048^3, level $\ell = 11$). During the runs, seven more levels of refinement were considered (level $\ell_{\rm max} = 18$). The refinement criterion we used allows spatial resolution to be roughly constant in physical units; the minimum cell physical size was always close to $\Delta x_{\rm min} = L/2^{\ell_{\rm max}} \simeq 500\,{\rm pc}\,h^{-1}$. The grid was dynamically refined using a quasi-Lagrangian strategy: when the dark matter or baryons mass in a cell reaches eight times the initial mass resolution, it is split into eight children cells.

In the HYDRO runs, gas dynamics is modelled using a second-order unsplit Godunov scheme (Teyssier 2002; Fromang, Hennebelle & Teyssier 2006; Teyssier, Fromang & Dormy 2006) based on the HLLC Riemann solver and the MinMod slope limiter (Toro, Spruce & Speares 1994). We assume a perfect gas equation of state with $\gamma = 5/3$. The HYDRO runs include standard subgrid models for gas cooling (accounting for H, He and metals; we use the Sutherland & Dopita 1993 cooling function), star formation (we adopt a star formation efficiency $\epsilon_* = 0.01$) and supernovae feedback (we adopt the 'delayed cooling' scheme; Stinson et al. 2006) and metal enrichment. In one of the two hydrodynamical simulations we also implement AGN feedback, using a modified version of the Booth & Schaye (2009) model. SMBHs are modelled as sink particles, following the prescriptions of Krumholz, McKee & Klein (2004), and they are allowed to merge. Gas accretion on to each SMBH is computed adopting a modified Bondi–Hoyle formula (Booth & Schaye 2009). A fraction of the accreted mass is

converted into thermal energy that is directly injected into the gas surrounding the black hole (BH). For practical purposes, in the rest of the paper we will refer to the run with AGN feedback as AGN-ON, and to the run without AGN feedback as AGN-OFF. Further details about the galaxy formation and AGN feedback recipes can be found in Martizzi et al. (2012) and Teyssier et al. (2011).

As discussed in Teyssier et al. (2011), the AGN feedback energy is effectively deposited in two different modes: the energetic and impulsive quasar mode (Eddington limited luminosity $\sim 5 \times 10^{46}\,\mathrm{erg\,s^{-1}}$) during cold gas accretion when the accretion rate is high, and the quiescent radio mode during hot gas accretion when the accretion rate is low (Bondi–Hoyle limited luminosity $\sim 5 \times 10^{41}\,\mathrm{erg\,s^{-1}}$). At $z \sim 0$ the central SMBH in the AGN-ON cluster accretes mass in radio mode at a rate $\sim 10^{-4}\,\mathrm{M_\odot\,yr^{-1}}$, producing a total luminosity of $9 \times 10^{40}\,\mathrm{erg\,s^{-1}}$, comparable to the X-ray luminosity of the AGN in M87 $L_{\mathrm{X},0.5-7\,\mathrm{keV}} \approx 7 \times 10^{40}\,\mathrm{erg\,s^{-1}}$ (Allen et al. 2006); the mechanical power of the jet of the AGN in M87 is much larger, $P \approx 3.3 \times 10^{43}\,\mathrm{erg\,s^{-1}}$. These considerations imply that the AGN in M87 lies in an intermediate state between the radio and the quasar modes of our model. Further indications that the activity of the central SMBH is not particularly atypical are provided by comparison of the accretion rates and star formation rates in the AGN-ON simulation with observational results at redshift $z \sim 0$. The mass accretion rate on to the SMBH is $\sim 10^{-4}\,\mathrm{M_\odot\,yr^{-1}}$ and the star formation rate within the inner few kpc from the cluster centre is $\sim 10^{-2}\,\mathrm{M_\odot\,yr^{-1}}$. These values are comparable with those recently measured by Diamond-Stanic & Rieke (2012) for type 1 Seyfert galaxies.

3 RESULTS

In this section, we show how SMBHs and AGN feedback are able to change dramatically the properties of the mass distribution in clusters of galaxies. We focus on 3D mass density profiles of the cluster, analysing separately the dark matter and stellar components, as well as the total mass distribution. The goal is to highlight differences between the profiles in the DMO, AGN-ON and AGN-OFF runs. The interpretation of our main results is provided in the next section.

3.1 Mass density profiles at redshift $z = 0$

Spherically averaged mass density profiles of the cluster at redshift $z = 0$ have been computed for all the simulations. A reliable identification of halo centres is required to compute density profiles. Halo centres and virial radii have been identified using the AdaptaHOP algorithm (Aubert, Pichon & Colombi 2004), in the version implemented and tested by Tweed et al. (2009), using the most massive substructure method (MSM) to identify haloes as well as their substructures. AdaptaHOP can be used to find the centres of groups of dark matter particles (i.e. 'haloes') as well as groups of star particles in the HYDRO runs (i.e. 'galaxies'). In the DMO run we directly use the centre of the dark matter halo, whereas in the AGN-ON and AGN-OFF runs we use the centre of the most massive group of star particles (i.e. the centre of the brightest cluster galaxy) since it traces better the minimum of the gravitational potential. To test that the latter choice does not lead to errors in the estimate of the profiles in the inner region of the cluster, we verified that picking the halo centre instead of the galaxy centre does not change the measured profiles.

Fig. 1 shows the dark matter and stellar mass density profiles at $z = 0$ for the AGN-ON (solid line) and AGN-OFF (dashed line) runs; in this plot we use physical units. In the left-hand panel the result of the DMO run (dotted line) is also plotted for comparison. All the profiles extend to the virial radius of the cluster. The three dark matter profiles look quite similar in the outer regions ($r \gtrsim 50\,\mathrm{kpc}$), while they are significantly different in the inner regions. The AGN-OFF profile is much more centrally peaked and concentrated than the DMO profile, a result that can be interpreted as a result of adiabatic contraction of dark matter haloes in response to the condensation of baryons at their centres (Gnedin et al. 2004; Teyssier et al. 2011); we test the quality of adiabatic contraction models in reproducing our results in Subsection 3.2. The AGN-ON profile is much different, with a very shallow inner slope. Within the inner 10 kpc we observe a dark matter core whose size is much larger than our spatial resolution limit (grey shaded area), whereas the AGN-OFF and DMO profiles seem to be consistent with cuspy dark matter profiles. Observational support to the results of our AGN-ON model comes from studies where gravitational lensing and dynamical data are combined to estimate the dark matter

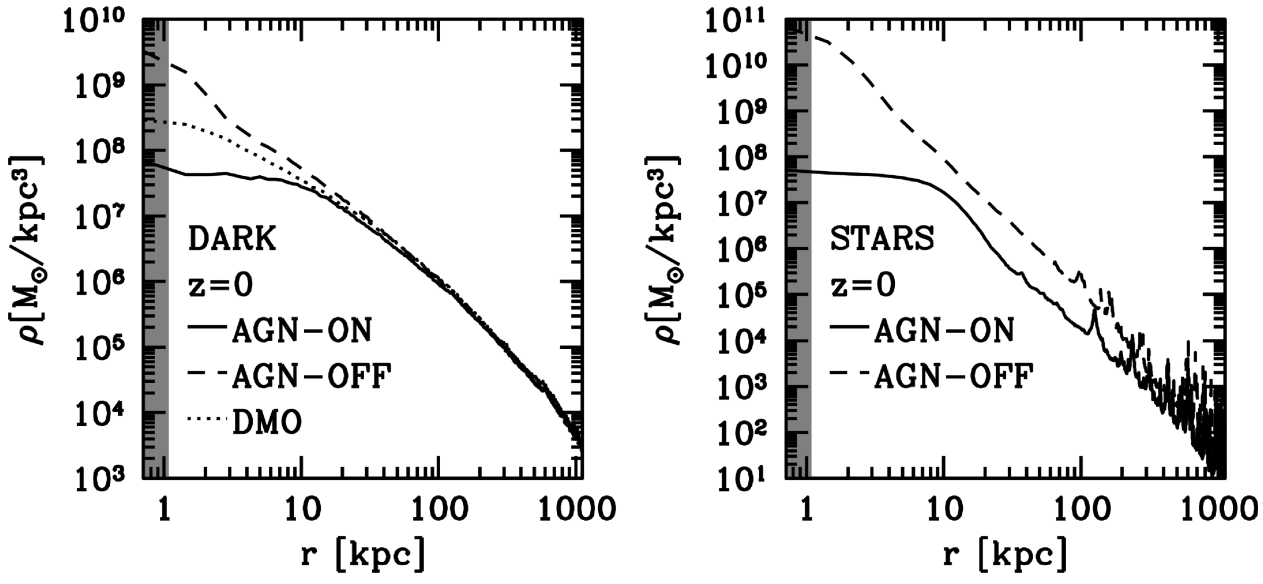

Figure 1. Mass density profiles at $z = 0$. Left: dark matter. Right: stars. In all panels the grey shaded area represents the spatial resolution.

profiles of clusters of galaxies (Sand et al. 2004, 2008; Newman et al. 2009, 2011; Richtler et al. 2011): these studies provide significative evidence of the existence of clusters of galaxies with dark matter profiles presenting cores or shallower inner slopes than in the Navarro–Frenk–White model.

Looking at the stellar mass density profiles, we see that significantly less stellar mass forms in the AGN-ON run with respect to the AGN-OFF run that is affected by overcooling. At $r > 50$ kpc the stellar mass density in the AGN-OFF run is $\sim$10 times bigger than in the AGN-ON run in all the radial bins, and a very significative difference can be observed between the two profiles within $\sim$10 kpc from the centre: the AGN-OFF density profile is increasing towards the centre, whereas the AGN-ON profile shows a flat core with a size comparable to that observed in the dark matter profile. It is interesting that cores in the stellar surface brightness profiles of very massive elliptical galaxies and cluster central galaxies have been observed by several authors (Kormendy 1999; Quillen, Bower & Stritzinger 2000; Laine et al. 2003; Trujillo et al. 2004; Lauer et al. 2005; Côté et al. 2007; Kormendy et al. 2009; Graham 2011) and they can be deprojected in cored 3D stellar density profiles (Terzić & Graham 2005).

In the AGN-OFF cluster the mass budget in the central region is strongly dominated by stellar mass: in the absence of AGN feedback the star formation process is very efficient in turning gas into stars; the large stellar mass in the central region of the AGN-OFF cluster has been assembled through cooling flows providing gaseous material to trigger intense star formation events and through the accretion of satellite galaxies on to the central galaxy. In contrast, the mass in the central regions of the AGN-ON cluster has comparable contributions from stars and dark matter: overcooling is prevented from happening by AGN feedback and star formation is strongly quenched.

3.2 Dark matter profiles at $z = 0$: testing the adiabatic contraction model

It is possible to estimate some of the effects of baryonic processes, SMBHs and AGN feedback using an approach similar to that used by observers when analysing the surface brightness profiles of galaxies. First, an analytical model is used to fit the profile, and then any significant deviation from the model is interpreted as a signature of physical processes. The same approach has been used to detect central light excesses/deficiencies with respect to a Sérsic fit to the surface brightness profiles of early-type galaxies (Kormendy et al. 2009; Graham 2011). In Martizzi et al. (2012) we also adopted this approach to discuss the properties of the stellar core observed in the stellar mass density profile in the AGN-ON run, showing that the Sérsic function can be used to fit the stellar mass surface density profile outside the cored region. Here, we use this criterion to analyse the dark matter profiles we measure in our simulations at $z = 0$.

We adopt the Einasto profile as our fiducial analytical model, since it has been shown to provide excellent fits to the dark matter profiles observed in cosmological N-body simulations (Merritt et al. 2005; Graham et al. 2006). We use the following parametrization:

$$\rho_{\rm Ein}(r) = \rho_{\rm e} \exp\left\{-d_n \left(\frac{r}{r_{\rm e}}\right)^{1/n} - 1\right\}, \quad (1)$$

where

$$d_n = 3n - 1/3 - 0.0079/n. \quad (2)$$

We use this analytical function to fit the dark matter profiles at $z = 0$, leaving $I_{\rm e}$, n and $r_{\rm e}$ as free parameters. Our fits are performed using the Levenberg–Marquardt non-linear least-squares fit algorithm (Press et al. 1992). The parameters we obtain after the fits are summarized in Table 3. In the DMO case we measure a concentration $c_{200} = R_{200\rm c}/R_{-2} = 5.88$, where R_{-2} is the radius at which the logarithmic slope of the dark matter profile is -2. This value is typical for haloes of mass $\sim 10^{14}\,{\rm M}_\odot$ (Reed, Koushiappas & Gao 2011).

The fits are compared to the measured profiles in Fig. 2. The Einasto profile provides a very good fit to the dark matter profile of our halo in the DMO run, despite the fact that it is typically used to fit the average profile in cosmological simulations whereas we analyse only one halo. Both in the AGN-ON and AGN-OFF we observe that the Einasto profile is a good fit for $r > 10$ kpc, while we observe significative deviations with respect to the fitting formula in the inner regions (see the bottom-right panel of Fig. 2). The presence of these features can be interpreted as a manifestation of processes that influence the formation of a standard distribution of dark matter in phase space; since these features are not observed in the gravity-only DMO run, we try to give them an explanation in terms of baryon physics.

Dark matter haloes are expected to respond adiabatically to the condensation of baryons at their centres (Gnedin et al. 2004; Teyssier et al. 2011). We compare the results of our hydrodynamical runs at $z = 0$ with the prediction of a simple adiabatic contraction model used by Abadi et al. (2010), and already adopted in Teyssier et al. (2011); details of this model can be found in Appendix A. We adiabatically contract the Einasto fit to the DMO profile assuming that the baryons are distributed in a constant surface density, truncated sphere of mass $m_{\rm d}$ and radius $r_{\rm d}$, despite the fact that the actual distribution is different. The values of $m_{\rm d}$ and $r_{\rm d}$ adopted in this paper are shown in Table 4. The result is plotted in Fig. 2 (blue lines): in both the AGN-ON and AGN-OFF cases the adiabatically contracted profiles match the Einasto fits quite well at all radii, but, like the fits, the model does not provide a satisfactory description of the measured profiles for $r < 10$ kpc. A mass excess with respect to the adiabatic contracted profile is detected in the AGN-OFF case.

Table 3. Best-fitting parameters $\rho_{\rm e}$, $r_{\rm e}$ and n for the Einasto profile at redshift $z = 0$. The value of the reduced chi-squared $\widetilde{\chi}^2$ (1386 d.o.f.) for $10 < r < 1000$ kpc is also reported. The values are reported for the DMO, AGN-ON and AGN-OFF simulations.

Simulation	$\rho_{\rm e}({\rm M}_\odot\,{\rm kpc}^{-3})$	$r_{\rm e}$(kpc)	n	$\widetilde{\chi}^2$
	Einasto profile fits – $z = 0$			
DMO	$1.43 \times 10^3 \pm 1.5 \times 10^2$	$1.60 \times 10^3 \pm 6 \times 10^1$	$5.93 \pm 1.2 \times 10^{-1}$	0.94
AGN-ON	$1.39 \times 10^3 \pm 1.1 \times 10^2$	$1.55 \times 10^3 \pm 5 \times 10^1$	$5.65 \pm 9 \times 10^{-2}$	0.97
AGN-OFF	$6.2 \times 10^2 \pm 9 \times 10^1$	$2.0 \times 10^3 \pm 1.1 \times 10^2$	$7.38 \pm 1.8 \times 10^{-1}$	2.21

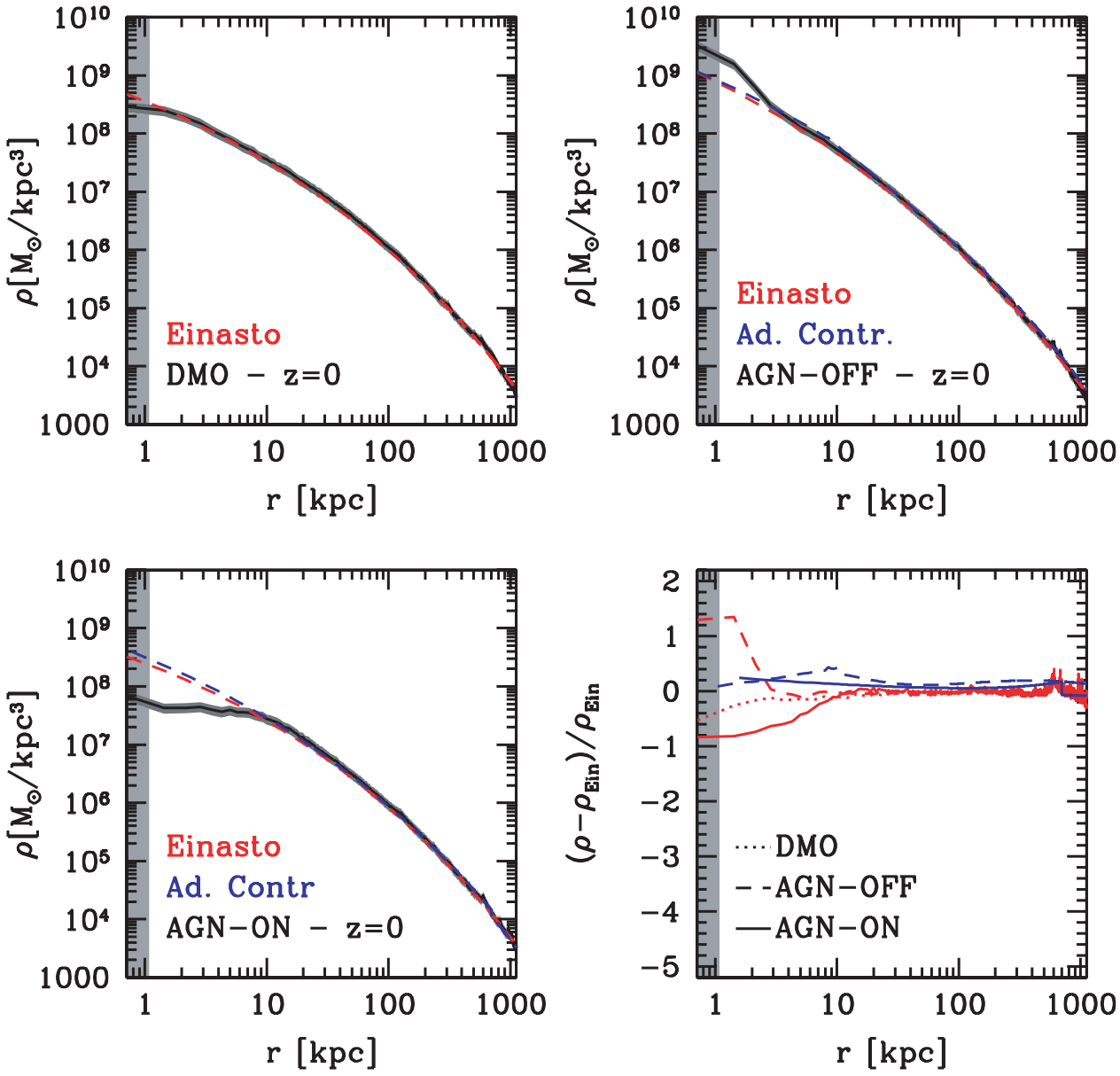

Figure 2. Comparison between the dark matter profiles measured at redshift $z = 0$ (black solid lines) and the Einasto fits (red dashed lines). The scatter due to Poisson noise in each radial bin is also represented as a dark-grey shaded area. The DMO Einasto fit is adiabatically contracted to get the two blue dashed profiles. Top-left panel: DMO run. Top-right panel: AGN-OFF run. Bottom-left panel: AGN-ON run. Bottom-right panel: relative difference between the measured profile and the Einasto fit as a function of radius (red lines); we use a dotted line for the DMO run, a dashed line for the AGN-OFF run and a solid line for the AGN-ON run; the blue lines show the residuals of the adiabatic contraction models with respect to the Einasto fits. In all panels the grey shaded area represents the spatial resolution.

Table 4. Parameters adopted for the adiabatic contraction model: truncated sphere mass $m_{\rm d}$ and radius $r_{\rm d}$.

Simulation	$m_{\rm d}$ ($M_\odot$)	$r_{\rm d}$ (kpc)
Adiabatic contraction model parameters		
AGN-ON	1.7×10^{13}	700
AGN-OFF	2.6×10^{11}	10

The adiabatic contraction model works reasonably well, especially at radii beyond a few kpc. In the interval $10 < r < 1000$ kpc we measure reduced chi-squared values for the adiabatic contraction models $\widetilde{\chi}^2 = 2.14$ for the AGN-OFF case and $\widetilde{\chi}^2 = 0.72$ for the AGN-ON case. These values are quite similar to what we obtain for the Einasto fits in the same radial range (Table 3).

In the AGN-ON run we find a mass deficiency with respect to the adiabatically contracted profile within 10 kpc from the centre; this mass deficiency is $M_{\rm def} = 5.7 \times 10^{10}\,M_\odot$. The fact that adiabatic contraction works for the outer regions of the cluster, but cannot predict the formation of the core, highlights the fact that additional processes play a role in shaping the properties of the mass distribution. Given the theoretical and computational limits of our phenomenological model for AGN feedback and the formation of SMBHs, and given that we limit our analysis to the evolution of one halo, these results provide evidence that SMBH physics is indeed relevant in shaping the properties of clusters of galaxies,

especially in the most overdense regions where SMBHs are expected to be found. We will discuss these topics in further detail in Subsection 3.4.

3.3 Evolution of the mass density profiles

The study of the evolution of the mass density profiles in our simulations can be used to shed more light on the mechanisms through which SMBHs and AGN feedback influence the mass distribution in clusters. To do so, we found the centres of the most massive progenitors of the cluster in each simulation, computed density profiles at redshifts $z = 1, 2, 3, 4, 5$ and then compared to the result at $z = 0$. All the profiles shown in this subsection are plotted in physical units.

First of all, we analyse the dark matter profile evolution in the DMO simulation (Fig. 3). In the outskirts of the cluster, the profiles change their slope; this transition marks the virial radius of the cluster. At redshift $z = 5$ the mass distribution in the halo is still quite different than at later times, with a shallower central slope and a radius $R_{200c} \approx 60$ kpc. At later times the inner part of the profiles ($r \lesssim 20$ kpc) reaches stability and evolution can be observed only in the outskirts where additional mass collapses into the halo; in fact, the high r tail of the profile is constantly extending towards bigger distances from the centre. At redshift $z = 0$ we measure that $R_{200c} \approx 1$ Mpc. This kind of evolution is a clear example of stable clustering.

In Fig. 4 we show the evolution of the dark and stellar mass density profiles in the AGN-OFF run. The effect of adiabatic contraction due to the condensation of baryonic mass at the centre of the cluster is already evident at redshift $z = 5$: the density within the inner 10 kpc is almost an order of magnitude larger than in the DMO case. Similarly to the DMO case, as the dark matter halo is assembled, the dark matter profile in the inner region appears to be stable from $z = 4$ to 0, while additional dark mass appears to be accreted at higher radii. The stellar mass profiles evolve maintaining its shape, but increasing in amplitude. New stars are constantly formed and a significant increase of the stellar mass can be observed between all the considered snapshots.

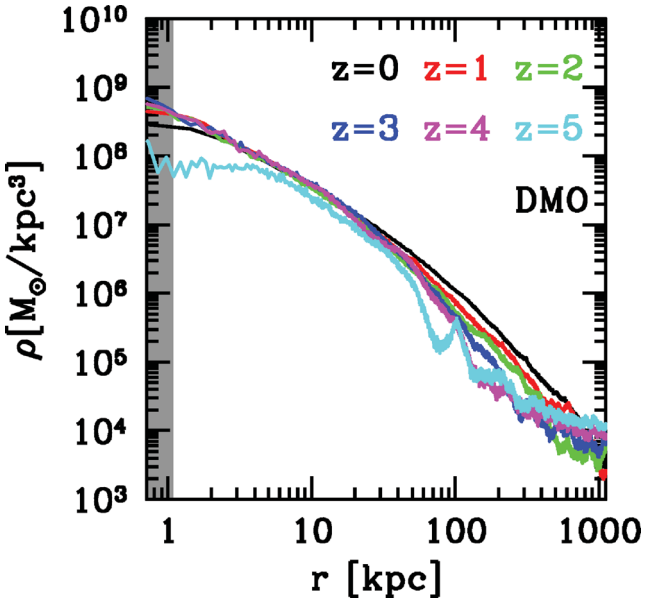

Figure 3. Evolution of the dark matter density profile in the DMO run from $z = 5$ to 0. The grey shaded area represents the spatial resolution.

Finally, Fig. 5 shows the same profiles for the AGN-ON run, highlighting some of the most interesting peculiarities of our model. The evolution of the dark matter profile in the outer regions of the cluster ($r \gtrsim 20$ kpc) is very similar to that observed in the DMO case, but the inner region is strikingly different. The effects of the processes leading to the formation of the core observed at $z = 0$ can be directly observed. At redshift $z = 5$ the dark matter profile appears to be contracted with respect to the DMO case, but much less than in the AGN-OFF case. Instead of maintaining the original slope, like in the AGN-OFF case, the inner part of the dark matter profiles becomes shallower with time, until a core is formed. A very similar behaviour is observed for the stellar mass density profile. While stellar mass is always increasing with time at radii $r \gtrsim 20$, the inner profile evolves in a very peculiar way: at redshift $z = 5$ the stellar profile is very cuspy, but it evolves becoming shallower and shallower, despite the fact that the total stellar mass within 10 kpc from the centre increases. Between $z = 1$ and 0 the stellar profile becomes almost completely flat for $r < 10$ kpc.

3.4 Formation of central cores in the density profile

The most evident peculiarity of the mass distribution in our AGN-ON simulation is the central core observed in the stellar and dark matter density profiles. From the plots (Fig. 5) in the previous subsection we see that the dark matter core forms more gradually than the stellar core. At $z > 1$ we see that the dark matter profile gradually evolves towards a cored configuration, while the stellar profile builds up maintaining its cuspy inner shape. The most interesting transition towards the formation of the two cores happens between redshifts $z = 1$ and 0: in this interval the dark matter profile becomes extremely flat, while the cusp at the centre of the stellar profile is completely erased. The fact that this behaviour is not observed in the AGN-OFF simulation suggests that the cores in the AGN-ON dark and stellar matter profiles do not form naturally, but they are generated through external processes influencing the dynamics of collisionless matter. The aim of this subsection is to elucidate the mechanisms that lead to core formation in our simulated cluster.

Several models have been proposed to produce cores in the density profile of a distribution of collisionless matter starting from a cuspy profile; these models were originally developed to explain the dark matter cores observed in gas-rich dwarf galaxies (de Blok 2010), but may be applied, in principle, to any distribution of collisionless matter. El-Zant, Shlosman & Hoffman (2001) showed that sufficiently massive gas clumps can disrupt cusps through dynamical friction; this is not observed in our AGN-ON run since gas clouds are easily disrupted by AGN feedback. El-Zant et al. (2004) showed that galaxies moving within the dark matter background and transferring their orbital energy to the dark matter via dynamical friction may contribute to the formation of cores. More recently, the very high resolution simulation of Naab, Johansson & Ostriker (2009) showed a similar effect: repeated minor dry mergers lead to decreases of the central stellar density concentration. This result has been confirmed by subsequent numerical experiments, like those presented by Laporte et al. (2012). The dense cores of accreted galaxies able to survive for a few crossing times modify the stellar mass distribution through dynamical friction. We emphasize that the same principle applies to the dark matter component, due to its collisionless nature. This effect is not observed in our AGN-OFF run because completely dry mergers are rare due to the high gas fractions in galaxies in this simulation. In the AGN-ON run, instead, a significant fraction of the gas is expelled from galaxies and the Naab et al. (2009) mechanism can be more efficient.

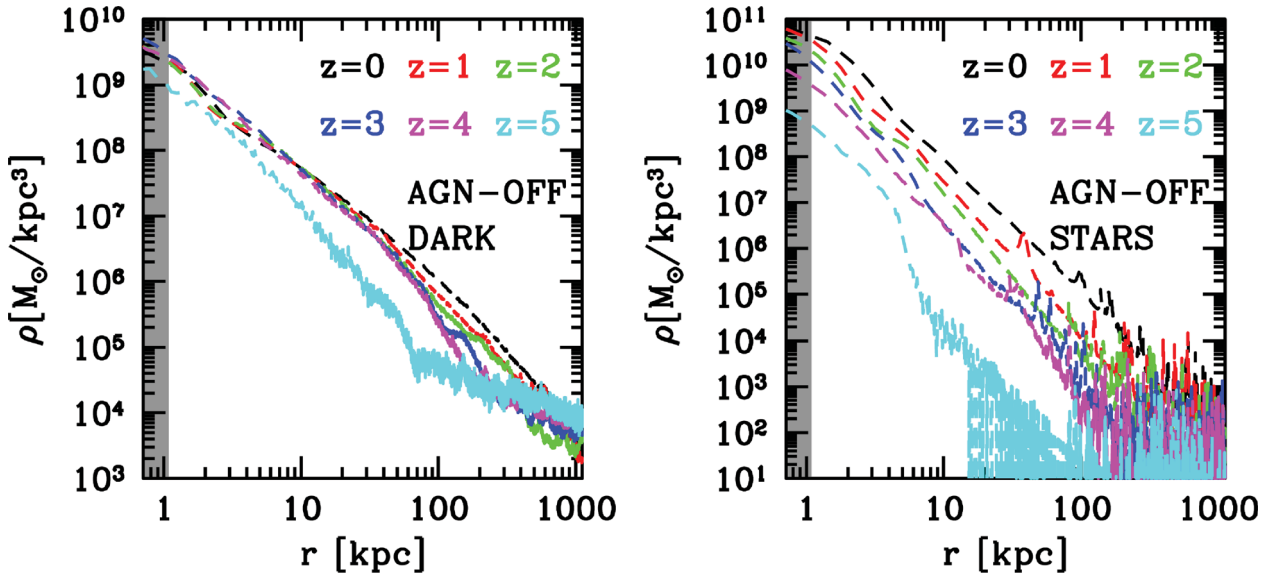

Figure 4. Evolution of the density profiles in the AGN-OFF run from $z = 5$ to 0. Left: dark matter. Right: stars. In all panels the grey shaded area represents the spatial resolution.

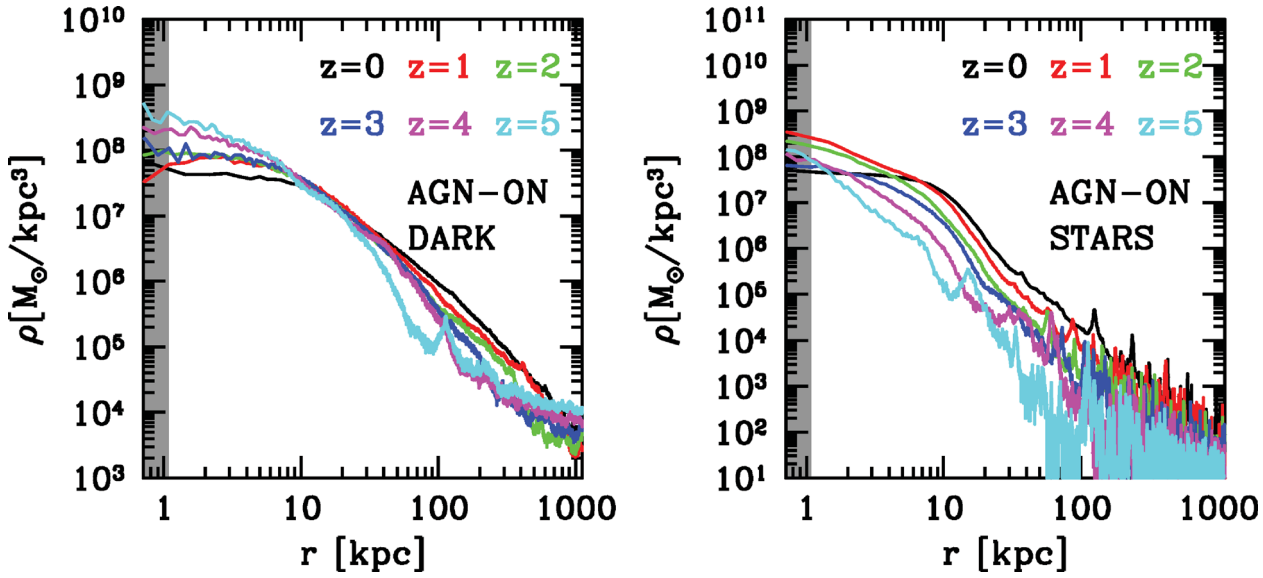

Figure 5. Evolution of the density profiles in the AGN-ON run from $z = 5$ to 0. Left: dark matter. Right: stars. In all panels the grey shaded area represents the spatial resolution.

Unfortunately, it seems to be challenging to produce an extended flat core like the one observed in our AGN-ON model only through repeated dry minor mergers.

Alternative mechanisms to produce cores in dark matter profiles involve purely gravitational processes related to SMBHs. In the context of a ΛCDM cosmology, where massive structures form through the hierarchical mergers of less massive structures, the formation of SMBH binaries is an expected result. At the centre of collapsed objects SMBHs form binary pairs whose orbits decay as they transfer their orbital energy to collisionless matter via three-body interactions: the result is that collisionless matter can be expelled from the central regions via the gravitational slingshot effect and a core is formed. This process is usually referred to as SMBH scouring (Milosavljević & Merritt 2003) and it is expected to remove approximately two to four times the mass of the SMBH formed after the binary completely decays (Merritt, Mikkola & Szell 2007). SMBH scouring is important on spatial scales from 100 to 1 pc; thus, it cannot be resolved in our simulations which has 1 kpc force softening. At the softening length the mass is completely dominated by dark matter and stars so that SMBH binaries cannot form.

Despite the fact that SMBH scouring is not resolved in our simulations, they are able to resolve another process able to produce cores, namely SMBHs sinking to the very central region due to dynamical friction during mergers. The efficiency of this process has been extensively studied by Goerdt et al. (2010) and their results show that the orbital energy transferred from the SMBHs to collisionless matter contributes to the formation of cores. The efficiency of this process is not as high as in the SMBH scouring, but

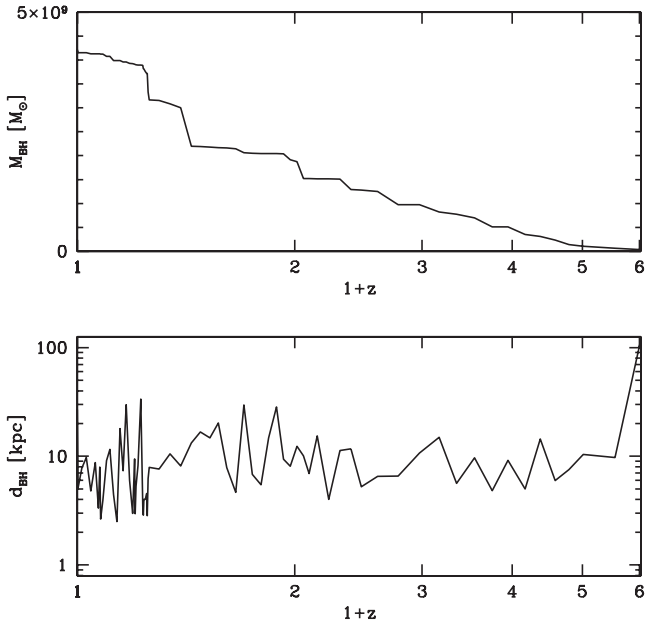

Figure 6. Top: evolution of the central SMBH observed at redshift $z = 0$. Bottom: evolution of the distance between the central SMBH observed at redshift $z = 0$ and its closest neighbour.

it is able to produce mass deficiencies comparable to the mass of the infalling SMBHs. In our AGN-ON simulation the mass of the central SMBH at $z = 0$ is $M_{\rm BH} = 4.2 \times 10^9\,{\rm M}_\odot$, so this process by itself is not able to explain the mass deficiencies we observe in the central regions of the cluster: $M_{\rm def}^{\rm dark} = 5.7 \times 10^{10}\,{\rm M}_\odot$ for dark matter and $M_{\rm def}^{\rm star} = 3.04 \times 10^{10}\,{\rm M}_\odot$ for stars, measured with respect to an Einasto fit and a Sérsic fit to the entire profile, respectively.

Recently, the pure N-body simulations performed by Kulkarni & Loeb (2012) showed that when multiple (two or more) SMBHs are present in a halo, the core formation process is much more efficient than during the inspiral of a single SMBH. Considering this enhanced core formation via dynamical friction it is possible to create mass deficits of more than five times the total SMBH mass. The top panel of Fig. 6 shows the mass growth of the central SMBH at the centre of the cluster at $z = 0$. The mass growth of this BH is very smooth for $z > 2$, but it proceeds mainly through major mergers (sudden jumps in the BH mass) at lower redshifts. The bottom panel of Fig. 6 shows the distance between the central SMBH and its closest neighbour as a function of redshift, denoted as $d_{\rm BH}$. Any sudden increase in the SMBH mass $M_{\rm BH}$ due to a BH merger in the top-panel plot can be detected as an increase in $d_{\rm BH}$, because after mergers the second neighbour becomes the first neighbour. The continuous variation of $d_{\rm BH}$ tells us that at any redshift BHs are moving in the halo and losing orbital energy because of dynamical friction. A significative number of major mergers of very massive BHs happen at $z < 1$. This fact suggests that the Kulkarni & Loeb (2012) mechanism is particularly efficient at redshifts $z < 1$.

SMBH infall is not the only process contributing to the formation of the core. In the AGN-ON simulation strong AGN-driven outflows are observed (Martizzi et al. 2012). AGN feedback greatly increases the local temperature and entropy of gas; then the high-entropy material is transported out of the central region of the cluster through convective motions. These outflows modify the local gravitational potential and may cause expansion of both the dark and stellar mass distribution. Similar processes have been observed in numerical simulations in which gas outflows generated by supernovae feedback are used to produce cores in the dark matter profiles of dwarf galaxies (Navarro, Eke & Frenk 1996; Gnedin & Zhao 2002; Read & Gilmore 2005; Governato et al. 2010; Pontzen & Governato 2011). In the simulations performed by Navarro et al. (1996), the mass outflows are simulated by growing and rapidly removing an idealized potential from the centre of an equilibrium realization of a dark matter halo, showing that the natural consequence is the formation of a core. The efficiency of this core formation process is $\propto M_{\rm disc}^{1/2} R_{\rm disc}^{-1/2}$, where $M_{\rm disc}$ is the mass of the disc and $R_{\rm disc}$ is its scale radius.

The calculations performed by Gnedin & Zhao (2002) show that this mechanism is extremely inefficient when a single supernova explosion is considered; however, Read & Gilmore (2005) showed that repeated explosions followed by gas outflows and subsequent infalls are able to account for the formation of dark matter cores. The recent numerical experiments performed by Governato et al. (2010) and Pontzen & Governato (2011) confirm the efficiency of this mechanism in a fully cosmological context. In particular, Pontzen & Governato (2011) suggest that gravitational potential fluctuations induced by supernovae-driven outflows happening on a time-scale shorter than the dynamical time cause the expansion of the dark matter distribution and the formation of a core. For this mechanism to be effective it is required to have gas outflows able to remove a significant fraction of the mass enclosed in the region where the core forms. Since we have multiple epochs of AGN-driven gas outflows, this mechanism is likely to be active also in our AGN-ON run. This is indeed the case: Fig. 7 shows that the gas mass fluctuations induced by AGN burst-driven outflows can be high fractions of the total mass in the central regions. Regions close to the central SMBH (radius $r < R = 2$–5 kpc) present extreme mass fluctuations on short time-scales. Within $r < R = 10$ kpc fluctuations become smaller, but can be as large as 10 per cent of the enclosed total mass. At higher distances from the centre the effect of these mass fluctuations is almost undetected. This means that potential fluctuations will be particularly strong only within the inner 10 kpc from the centre, that is the region where the core is observed. It is interesting to note that the amplitude of the mass fluctuations is

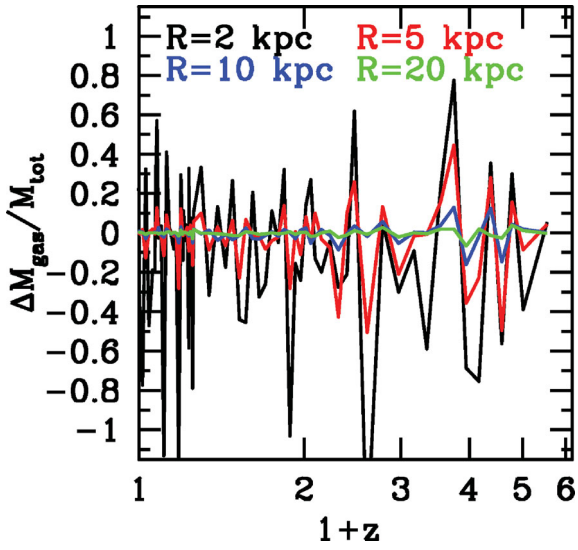

Figure 7. Variation of the gas mass enclosed in spheres of radius $R = 2$, 5, 10 and 20 physical kpc with respect to the total mass in the same region. The absolute value of the fluctuations can be larger than 1 because the variation of the gas mass is divided by the total mass after the outflow.

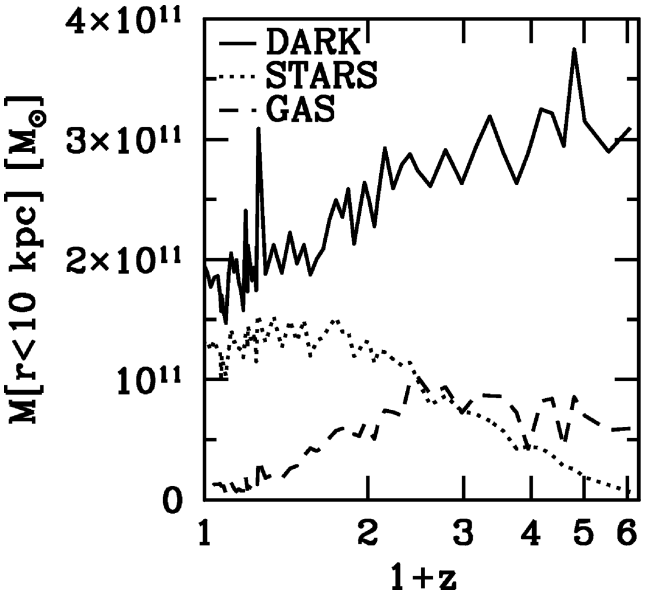

Figure 8. Time evolution of the total dark, stellar and gas mass enclosed within 10 physical kpc in the AGN-ON run.

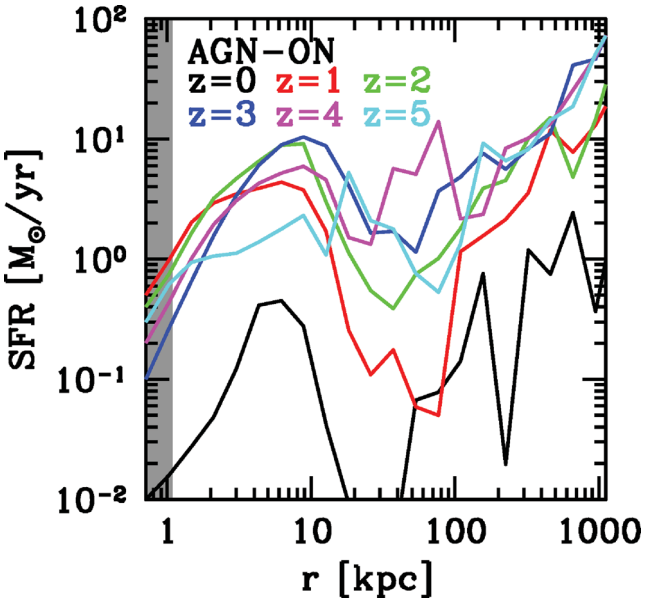

Figure 9. Average star formation rate in radial bins in the AGN-ON run. The grey shaded area represents the spatial resolution.

typically higher at $z > 1$; however, quite strong fluctuations are also observed at low redshift.

Before drawing our conclusions, we carefully analyse what happens in the central region of the cluster. Fig. 8 shows how the mass distribution in the central region of the cluster is influenced by the core formation mechanisms. We plot the evolution of the mass enclosed within 10 physical kpc for all the different components: dark matter (solid lines), stars (dotted lines) and gas (dashed lines). The core formation processes produce a decrease in the dark mass within 10 kpc from the centre from $\sim 3 \times 10^{11}\,\mathrm{M}_{\odot}$ at $z = 5$ to $\sim 2 \times 10^{11}\,\mathrm{M}_{\odot}$ at $z = 0$. The stellar mass in the centre increases with time only down to $z = 1$, staying approximately constant until $z = 0$. At high redshift the star formation rate in the central region is high and the concentration of the stellar mass distribution is boosted by star formation events (Fig. 9); at redshift $z < 1$ the star formation in the central galaxy is strongly quenched by AGN feedback (Fig. 9), so the concentration of the stellar distribution cannot be boosted by strong star formation events, thus letting the core formation processes be effective. At $z < 1$ when AGN feedback becomes very strong because of the presence of very massive BHs, a slow decrease in the gas mass in the centre is observed: a gas mass $\sim 10^{11}\,\mathrm{M}_{\odot}$ is slowly removed from the central region before $z = 0$. This slow decrease in gas mass is expected to produce an adiabatic expansion of the total mass distribution, which will also contribute to the formation of a central core. Furthermore, the cooling time of hot gas within the inner 30 kpc of the cluster centre is ~ 1 Gyr, suggesting that in its quiet mode the AGN can slowly eject the gas that rains down on to the centre from the inner cooling flow.

The general picture we find from our analysis seems to show that the interplay between dynamical processes connected to SMBHs and the effects of AGN feedback on the star formation and the gas spatial distribution may provide an explanation to what is observed in our simulations. The dark matter core starts forming at redshift $z = 4$–5 due to AGN burst-driven gas mass fluctuations on short time-scales. The process goes on with very high efficiency down to redshift $z = 1$. At redshift $z < 1$ the infall of very massive SMBHs contributing to the core formation process compensates for the smaller amplitude of the gas mass fluctuations. The final result is a flat dark matter core at redshift $z = 0$. The formation of the stellar core proceeds quite differently, with star formation compensating for the ejection of stellar material at $z > 1$, preventing the early formation of a core. At $z < 1$ the decrease in the star formation rate caused by AGN feedback finally allows the stellar core to form by redshift $z = 0$.

Given our conclusions, we must stress that a clearer picture on the core formation problem has still to be drawn. The problem needs to be studied within a larger class of haloes with different merger histories and masses, and idealized simulations are probably required to shed more light on the core formation process in clusters.

4 SUMMARY AND CONCLUSIONS

We used the results of a set of cosmological simulations to study the effect of baryons in massive dark matter haloes, focusing on phenomena involving SMBHs and AGN feedback. We use the zoom-in technique to simulate the formation of a galaxy cluster of mass comparable to Virgo at high spatial and mass resolution. In this work we analyse three different simulations: the first is a gravity-only run with no baryons (DMO), the second is a hydrodynamical run with standard galaxy formation physics (AGN-OFF), the third is a hydrodynamical run with standard galaxy formation physics plus SMBHs and AGN feedback (AGN-ON). We adopt a modified version of the Booth & Schaye (2009) model to implement thermal AGN feedback in the AGN-ON run. This model allows us to reproduce the self-regulated growth of BHs throughout the cosmic ages and it is tuned to reproduce the observed M_{BH}–σ relation.

Our analysis focuses on the evolution of the 3D mass density profiles of the cluster from redshift $z = 5$ to 0. We find a number of interesting differences between our models that highlight the importance of accounting for all the physical processes taking place during the formation and evolution of the most massive bound structures in the Universe. Our results can be summarized in the following points.

(i) At redshift $z = 0$ the dark matter density profiles of the three simulations are consistent with each other at distances $r > 10$ kpc from the centre, but they differ significantly in the central region. The DMO profile is consistent with a standard Einasto model. The AGN-OFF profile shows a mass excess with respect to an Einasto fit due to adiabatic contraction of the baryons at the centre of the cluster. The AGN-ON profile presents a flat core of radius 10 kpc, i.e. a mass deficiency with respect to an Einasto fit. The dark matter core forms gradually from $z = 5$ to 0. We stress that dark matter cores in dark matter profiles have been claimed to be observed in several clusters (Sand et al. 2004, 2008; Newman et al. 2009, 2011; Richtler et al. 2011).

(ii) The stellar density profile at $z = 0$ is also very different between the AGN-OFF and AGN-ON runs. The AGN-OFF profile is very peaked at the centre, while the AGN-ON profile has a core of the same size as that of the dark one. Unlike the dark core, the stellar one forms between $z = 1$ and 0. Note that cores in the surface brightness profiles of massive ellipticals and cluster central galaxies have been observed by several authors (Kormendy 1999; Quillen et al. 2000; Laine et al. 2003; Trujillo et al. 2004; Lauer et al. 2005; Côté et al. 2007; Kormendy et al. 2009; Graham 2011), so our model is not in disagreement with observations and it *predicts* the existence of dark matter cores associated with stellar cores in massive ellipticals. Furthermore, in the AGN-OFF run the stellar density is larger than that in the AGN-ON run at all radii. This is a clear effect of overcooling of gas leading to enhanced (and too efficient) star formation. In the AGN-ON run, AGN feedback strongly quenches star formation and the overcooling problem is avoided (Martizzi et al. 2012; Teyssier et al. 2011). The result is also that less cool gas is available at the centre of the AGN-ON cluster with respect to the AGN-OFF run: gas is heated by AGN feedback and carried away via convective motions and slow adiabatic expansion.

(iii) The core in the dark matter and stellar mass density profiles is a peculiar feature of our simulation that includes the physics associated with AGNs. In this paper, we suggest that the coupling of several mechanisms is responsible for their formation. First, SMBHs transfer part of their orbital energy to collisionless matter via dynamical friction during dry galaxy mergers (Goerdt et al. 2010), especially at redshift $z < 1$. Secondly, AGN-driven gas outflows modify the gravitational potential in regions close to SMBHs with resulting ejection of collisionless matter from the central region of the cluster; subsequent gas outflows followed by the central 're-virialization' of the central material are expected to produce cores (Pontzen & Governato 2011); due to the stronger AGN feedback at $z > 1$, this mechanism is more effective at high redshift, but preserves an important role at low redshift. Thirdly, the central hot gas slowly cools radiatively, falling on to the SMBHs in convective flows and is subsequently ejected impulsively; the slow loss of mass from the central region will produce an expansion of the inner mass distribution.

Despite assertions that AGN feedback can affect central cluster dynamics, in fact our results seem to be complementary to the those obtained by other authors for less massive dark matter haloes (Governato et al. 2010; Maccio' et al. 2012; Pontzen & Governato 2011). Related processes involving baryons seem to be active at the low and high mass end of the galaxy mass function, especially mechanisms involving gas outflows produced by feedback.

Given the fact that we perform the analysis on zoom simulations of one cluster, we need to stress that our result needs support from a suite of dedicated cosmological simulation aimed at exploring the effect of SMBHs, AGN feedback and baryon physics in general on the most massive clusters in the universe. Furthermore, a number of numerical experiments are also needed to explore in detail the core formation processes that have been considered in our discussion, with particular attention on their coupling. The role of baryon mass outflows in galaxy clusters has been recently studied by Ragone-Figueroa, Granato & Abadi (2012) using collisionless matter simulations where gas is modelled as a time varying external contribution to the gravitational potential; their results provide important support to ours. To conclude, we are convinced that our results are robust enough to assert that the implementation of AGN feedback and SMBHs in cosmological hydrodynamical simulations is an important ingredient for modelling massive clusters of galaxies.

ACKNOWLEDGMENT

The AMR simulations presented here were performed on the Cray XT-5 cluster at CSCS, Manno, Switzerland.

REFERENCES

Abadi M. G., Navarro J. F., Fardal M., Babul A., Steinmetz M., 2010, MNRAS, 407, 435
Allen S. W., Dunn R. J. H., Fabian A. C., Taylor G. B., Reynolds C. S., 2006, MNRAS, 372, 21
Aubert D., Pichon C., Colombi S., 2004, MNRAS, 352, 376
Bertschinger E., 2001, ApJS, 137, 1
Booth C. M., Schaye J., 2009, MNRAS, 398, 53
Borgani S., Kravtsov A., 2009, preprint (arXiv:0906.4307)
Ciotti L., Ostriker J. P., 1997, ApJ, 487, L105
Côté P. et al., 2007, ApJ, 671, 1456
de Blok W. J. G., 2010, Adv. Astron., 789293
Diamond-Stanic A. M., Rieke G. H., 2012, ApJ, 746, 168
Eisenstein D. J., Hu W., 1998, ApJ, 496, 605
El-Zant A., Shlosman I., Hoffman Y., 2001, ApJ, 560, 636
El-Zant A. A., Hoffman Y., Primack J., Combes F., Shlosman I., 2004, ApJ, 607, L75
Fromang S., Hennebelle P., Teyssier R., 2006, A&A, 457, 371
Gnedin O. Y., Zhao H., 2002, MNRAS, 333, 299
Gnedin O. Y., Kravtsov A. V., Klypin A. A., Nagai D., 2004, ApJ, 616, 16
Goerdt T., Moore B., Read J. I., Stadel J., 2010, ApJ, 725, 1707
Governato F. et al., 2010, Nat, 463, 203
Governato F. et al., 2010, Nat, 463, 203
Graham A. W., 2011, preprint (arXiv:1108.0997)
Graham A. W., Merritt D., Moore B., Diemand J., Terzić B., 2006, AJ, 132, 2701
Kormendy J., 1999, in Merritt D. R., Valluri M., Sellwood J. A., eds, ASP Conf. Ser. Vol. 182, The Central Structure of Elliptical Galaxies and the Stellar-Dynamical Search for Supermassive Black Holes. Astron. Soc. Pac., San Francisco, p. 124
Kormendy J., Fisher D. B., Cornell M. E., Bender R., 2009, ApJS, 182, 216
Krumholz M. R., McKee C. F., Klein R. I., 2004, ApJ, 611, 399
Kulkarni G., Loeb A., 2012, MNRAS, doi:10.1111/j.1365-2966.2012.20699.x
Laine S., van der Marel R. P., Lauer T. R., Postman M., O'Dea C. P., Owen F. N., 2003, AJ, 125, 478
Laporte C. F. P., White S. D. M., Naab T., Ruszkowski M., Springel V., 2012, preprint (arXiv:1202.2357)
Lauer T. R. et al., 2005, AJ, 129, 2138
Maccio' A. V., Stinson G., Brook C. B., Wadsley J., Couchman H. M. P., Shen S., Gibson B. K., Quinn T., 2012, ApJ, 744, L9
Martizzi D., Teyssier R., Moore B., 2012, MNRAS, 420, 2859
Merritt D., Navarro J. F., Ludlow A., Jenkins A., 2005, ApJ, 624, L85
Merritt D., Mikkola S., Szell A., 2007, ApJ, 671, 53
Milosavljević M., Merritt D., 2003, ApJ, 596, 860

Naab T., Johansson P. H., Ostriker J. P., 2009, ApJ, 699, L178
Navarro J. F., Eke V. R., Frenk C. S., 1996, MNRAS, 283, L72
Newman A. B., Treu T., Ellis R. S., Sand D. J., Richard J., Marshall P. J., Capak P., Miyazaki S., 2009, ApJ, 706, 1078
Newman A. B., Treu T., Ellis R. S., Sand D. J., 2011, ApJ, 728, L39
Pontzen A., Governato F., 2012, MNRAS, doi:10.1111/j.1365-2966.2012.20571.x
Press W. H., Teukolsky S. A., Vetterling W. T., Flannery B. P., 1992, Numerical Recipes in C. The Art of Scientific Computing. Cambridge Univ. Press, Cambridge
Prunet S., Pichon C., Aubert D., Pogosyan D., Teyssier R., Gottloeber S., 2008, ApJS, 178, 179
Quillen A. C., Bower G. A., Stritzinger M., 2000, ApJS, 128, 85
Ragone-Figueroa C., Granato G. L., Abadi M. G., 2012, preprint (arXiv:1202.1527)
Read J. I., Gilmore G., 2005, MNRAS, 356, 107
Reed D. S., Koushiappas S. M., Gao L., 2011, MNRAS, 415, 3177
Richtler T., Salinas R., Misgeld I., Hilker M., Hau G. K. T., Romanowsky A. J., Schuberth Y., Spolaor M., 2011, A&A, 531, A119
Sand D. J., Treu T., Smith G. P., Ellis R. S., 2004, ApJ, 604, 88
Sand D. J., Treu T., Ellis R. S., Smith G. P., Kneib J.-P., 2008, ApJ, 674, 711
Silk J., Rees M. J., 1998, A&A, 331, L1
Stinson G., Seth A., Katz N., Wadsley J., Governato F., Quinn T., 2006, MNRAS, 373, 1074
Sutherland R. S., Dopita M. A., 1993, ApJS, 88, 253
Tabor G., Binney J., 1993, MNRAS, 263, 323
Terzić B., Graham A. W., 2005, MNRAS, 362, 197
Teyssier R., 2002, A&A, 385, 337
Teyssier R., Fromang S., Dormy E., 2006, J. Comput. Phys., 218, 44
Teyssier R., Moore B., Martizzi D., Dubois Y., Mayer L., 2011, MNRAS, 414, 195
Toro E. F., Spruce M., Speares W., 1994, Shock Waves, 4, 25
Trujillo I., Erwin P., Asensio Ramos A., Graham A. W., 2004, AJ, 127, 1917
Tweed D., Devriendt J., Blaizot J., Colombi S., Slyz A., 2009, A&A, 506, 647

APPENDIX A: ADIABATIC CONTRACTION MODEL

The simplified model we adopt is based on that used in Teyssier et al. (2011). If one defines the initial radius of each dark matter shell as r_i, then an adiabatic contraction model is able to predict its value after contraction r_f. In our case we adopt the transformation

$$\frac{r_\mathrm{f}}{r_\mathrm{i}} = 1 + \alpha \left(\frac{M_\mathrm{i}}{M_\mathrm{f}} - 1 \right), \tag{A1}$$

where M_i and M_f are the cumulative mass distributions before and after contraction, respectively. The final cumulative mass distribution can be computed as

$$M_\mathrm{f} = M_\mathrm{dm}(r_\mathrm{f}) + M_\mathrm{bar}(r_\mathrm{f}) = f_\mathrm{dm} M_\mathrm{i}(r_\mathrm{i}) + M_\mathrm{bar}(r_\mathrm{f}), \tag{A2}$$

where $M_\mathrm{i}(r_\mathrm{i})$ is the initial mass distribution in the DMO case, $M_\mathrm{bar}(r_\mathrm{f})$ is the baryonic mass distribution and $M_\mathrm{dm}(r_\mathrm{f})$ is the adiabatically contracted dark matter distribution. The dark mass fraction is computed as $f_\mathrm{dm} = 1 - m_\mathrm{d}/M_{200}$. Our aim is to recover the contracted dark matter profile $M_\mathrm{dm}(r_\mathrm{f})$ given $M_\mathrm{i}(r_\mathrm{i})$ and $M_\mathrm{bar}(r_\mathrm{f})$. We assume that the $M_\mathrm{i}(r_\mathrm{i})$ can be described by the fit to the Einasto profile we obtain for the DMO run at redshift $z = 0$:

$$M_\mathrm{i}(r_\mathrm{i}) = 4\pi \int_0^{r_\mathrm{i}} r^2 \rho_\mathrm{Ein}(r)\, \mathrm{d}r. \tag{A3}$$

The baryonic mass distribution is modelled as a constant surface density sphere with size r_d and mass m_d:

$$M_\mathrm{bar}(r_\mathrm{f}) = \begin{cases} m_\mathrm{d} \left(\frac{r_\mathrm{f}}{r_\mathrm{d}} \right)^2 & \text{if } r < r_\mathrm{d} \\ m_\mathrm{d} & \text{if } r \geq r_\mathrm{d}. \end{cases}$$

We obtain the r_f value associated with each r_i solving numerically equation (A1), and naturally obtain the adiabatically contracted dark matter profile $M_\mathrm{dm}(r_\mathrm{f})$ using equation (A2). Finally, we estimate the dark matter density profile after contraction as

$$\rho_\mathrm{dm}(r) = \frac{1}{4\pi r^2} \frac{\mathrm{d}M_\mathrm{dm}(r)}{\mathrm{d}r}. \tag{A4}$$

This paper has been typeset from a TEX/LATEX file prepared by the author.

Chapter 6

Fourth Publication - Cusp-core transformations induced by AGN feedback in the progenitors of cluster galaxies

Published on MNRAS

Monthly Notices of the ROYAL ASTRONOMICAL SOCIETY

MNRAS Advance Access published May 9, 2013

MNRAS (2013)

doi:10.1093/mnras/stt297

Cusp–core transformations induced by AGN feedback in the progenitors of cluster galaxies

Davide Martizzi,[1]⋆ Romain Teyssier[1,2] and Ben Moore[1]

[1]*Institute for Theoretical Physics, University of Zurich, CH-8057 Zürich, Switzerland*
[2]*CEA Saclay, DSM/IRFU/SAP, Bâtiment 709, F-91191 Gif-sur-Yvette Cedex, France*

Accepted 2013 February 15. Received 2013 February 11; in original form 2012 November 12

ABSTRACT

In a recent study, we used cosmological simulations to show that active galactic nuclei (AGN) feedback on the gas distribution in clusters of galaxies can be important in determining the spatial distribution of stars and dark matter in the central regions of these systems. The hierarchical assembly of dark matter, baryons and black holes obscures the physical mechanism behind the restructuring process. Here, we use idealized simulations to follow the response of a massive dark matter halo as we feed the central black hole with a controlled supply of cold gas. This removes most of the complexity taking place in the cosmological simulations that may have biased our previous study. We confirm our previous results: gas heated and expelled from the central regions of the halo by AGN feedback can return after cooling; repeated cycles generate gravitational potential fluctuations responsible for irreversible modifications of the dark matter mass profile. The main result is the expulsion of large amounts of baryons and dark matter from the central regions of the halo. According to the work presented here, outflow-induced fluctuations represent the only mechanism able to efficiently create dark matter cores in clusters of galaxies.

Key words: black hole physics – methods: numerical– galaxies: clusters: general – galaxies: formation – cosmology: theory – large-scale structure of Universe.

1 INTRODUCTION

In the concordance cosmological scenario, the large-scale structure of the universe is globally determined by the dominant mass component, dark matter. The situation is different within highly non-linear regions, where the baryons dominate. Gas cooling, star formation, feedback processes and dynamical interactions between different mass components can modify the spatial distributions of all components. For example, dark matter haloes are known to globally respond to the condensation of baryonic matter in their central regions via dissipative processes. This increases the central mass density through adiabatic contraction, and causes the halo to become rounder. More recent studies of baryonic processes have focused on the effects of supernovae feedback in galaxies (Governato et al. 2010; Maccio' et al. 2011; Teyssier et al. 2013); however, there are fewer studies of the effects of AGN feedback on massive galaxies.

Clusters of galaxies provide a wealth of opportunities to test the validity of the current paradigm for cosmic structure formation. Analysing the details of the spatial distribution of the different components of a cluster, as predicted by theory, and comparing them to those measured (or inferred) from observations allows us to test our current understanding of high-mass galaxy formation.

In this paper, we focus on the role of active galactic nucleus (AGN) feedback in shaping the mass distribution of clusters of galaxies. The main motivation for this work comes from recent observational constraints of cluster mass profiles using gravitational lensing: Sand et al. (2004), Sand et al. (2008), Newman et al. (2009, 2011, 2012), Richtler et al. (2011). These report mass density profiles whose central slopes, measured within the inner ≈5 kpc, are much shallower than the universally adopted NFW profile. On a slightly smaller scale, within 1–2 kpc from the centre, very shallow slopes in the stellar surface brightness profiles of massive elliptical and cD galaxies have been observed (Kormendy 1999; Quillen, Bower & Stritzinger 2000; Laine et al. 2003; Trujillo et al. 2004; Lauer et al. 2005; Côté et al. 2007; Kormendy et al. 2009; Graham 2011). The combination of these two observational facts suggests a possible connection between the mechanisms that produce shallow density slopes in the dark matter distribution and in the stellar distribution. For example, both the dark matter and stellar components can respond similarly to dynamical perturbations since they behave like collisionless fluids.

The formation of cores with a shallow central density profile is currently a challenge for the concordance cosmological scenario. Dissipationless collapse and hierarchical merging always gives rise

⋆E-mail: martdav@physik.uzh.ch

to cuspy central density profiles. Alternative dark matter candidates, including self-interactive dark matter, seem to provide a viable mechanism to form dark matter cores (Rocha et al. 2013; Vogelsberger, Zavala & Loeb 2012). In addition, Laporte et al. (2012) showed that dynamical heating obtained through a long series of dry mergers can produce density cores in galaxy clusters, even in the context of the standard cosmological scenario. Similar results are discussed in Del Popolo (2009) and Del Popolo (2012). However, there is growing theoretical consensus that processes related to baryonic physics may play a dominant role in the formation of dark matter cores (Mashchenko, Couchman & Wadsley 2006; Mashchenko, Wadsley & Couchman 2008; Peirani, Kay & Silk 2008; Duffy et al. 2010; Governato et al. 2010; Maccio' et al. 2011; Pontzen & Governato 2012; Ragone-Figueroa, Granato & Abadi 2012; Teyssier et al. 2013). Of particular interest is Pontzen & Governato (2012), who use an analytical model to study the dynamical effects of potential fluctuations. According to this scenario, in low-mass haloes the energy injected by supernovae explosions is sufficient to erase dark matter cusps via the generation of repeated impulsive gas outflows responsible for rapid potential fluctuations (Peñarrubia et al. 2012). In galaxy clusters, supernovae feedback does not provide enough energy to unbind the gas; however, AGN feedback is expected to be strong enough to generate repeated gas outflows in their central regions.

In a recent study (Martizzi et al. 2012b), we used high-resolution cosmological hydrodynamical simulations including AGN feedback to show that it is possible to produce clusters with similar properties as indicated by these observations. We argued that at least three processes could contribute to creating shallow density profiles: (i) supermassive black holes (SMBHs) can transfer part of their orbital energy to collisionless matter via dynamical friction during mergers; part of the collisionless matter is expelled from the central regions (i.e. Goerdt et al. 2010); (ii) AGN-driven gas outflows modify the gravitational potential close to SMBHs; ejection of collisionless matter from the central region of the cluster is produced if the potential fluctuations happen on a time-scale smaller than, or resonant with, the dynamical time. To be effective, this mechanism requires many subsequent potential fluctuations (Navarro, Eke & Frenk 1996; Gnedin & Zhao 2002; Read & Gilmore 2005; Pontzen & Governato 2012); (iii) slow loss of gas mass from the central regions of a cluster can produce an expansion of the inner mass distribution; this slow loss of gas can be obtained as an effect of AGN heating.

Our previous results indicated that process (ii) was the dominant contribution to the shallowing of our central dark matter and stellar cusps. Very similar results were also found by Duffy et al. (2010) using the OWLS suite of cosmological simulations. Related mechanisms have been found to be active in lower mass haloes (Governato et al. 2010; Maccio' et al. 2011; Pontzen & Governato 2012; Teyssier et al. 2013). Unfortunately, the complexity of hierarchical structure formation makes it difficult to disentangle the efficiency of this mechanism. To obtain a clearer understanding, we will use simpler, idealized simulations, that remove these ambiguities in order to provide a better insight into the core creation process.

In a recent paper, Ragone-Figueroa et al. (2012) study the role of baryonic mass outflows in galaxy clusters, using collisionless matter simulations where gas is modelled as a time varying external potential. In this paper, we choose a similar approach, but we choose to perform full *N*-body+hydrodynamical simulations of an isolated dark matter halo, including gas cooling and AGN feedback from a single central SMBH. AGN heating can produce the impulsive expulsion of a large quantity of gas from the central regions of a cluster. The result of this is a fast varying central gravitational potential without the dynamical effects of hierarchical mergers of galaxies and their black holes.

The paper is organized as follows: the first section is dedicated to the numerical methods we adopted for our simulations; the second section gives our main results; in the last section, we discuss and provide a short summary.

2 THE SIMULATIONS

We use the adaptive mesh refinement code RAMSES (Teyssier 2002) to perform simulations that follow the evolution of the mass distribution of an isolated dark matter halo in presence of a gaseous component. The simulations differ in the way initial conditions for the gas are set, as explained in Section 2.1. The gas dynamics is modelled using a second-order unsplit Godunov scheme (Teyssier 2002; Fromang, Hennebelle & Teyssier 2006; Teyssier, Fromang & Dormy 2006) based on the HLLC Riemann solver and the MinMod slope limiter (Toro, Spruce & Speares 1994). We assume a perfect gas equation of state with $\gamma = 5/3$. We sample the dark matter distribution with 10^6 particles of mass $m_{\rm dark} = 1.78 \times 10^7$ M$_\odot$. In all simulations, gas represents 17 per cent of the total mass in the halo; the gas mass resolution element is $m_{\rm gas} = 3.79 \times 10^6$ M$_\odot$. The minimum cell size is $\Delta x_{\rm min} = 0.18$ kpc. The AMR grid was dynamically refined using a quasi-Lagrangian strategy: when the dark matter or baryons mass in a cell reaches eight times the mass resolution, it is split into eight children cells.

Gas is allowed to cool: we use the Sutherland & Dopita 1993 cooling function to account for H, He and metal cooling. We include AGN feedback, using the same implementation we adopted in Teyssier et al. (2011), Martizzi, Teyssier & Moore (2012a) and Martizzi et al. (2012b), a modified version of the Booth & Schaye (2009) model. SMBHs are modelled as sink particles, following Krumholz, McKee & Klein (2004). The gas accretion on to SMBHs is computed using a modified Bondi–Hoyle formula (Booth & Schaye 2009; Dubois et al. 2012). A fraction of the accreted mass is converted into thermal energy that is directly injected into the gas surrounding the black hole. Despite its simplicity, when properly tuned, the model reproduces basic features of AGN feedback (as it is thought to work), in particular the existence of two feedback modes: the impulsive 'quasar mode' during cold gas accretion, when the accretion rate is high, and the quiescent 'radio mode' during hot gas accretion, when the accretion rate is low. In this picture, the effect of 'radio mode' feedback is to prevent hot gas from cooling, while the effect of 'quasar mode' feedback is to eject gas from galaxies, violently suppressing star formation.

2.1 Initial conditions

The initial conditions for dark matter are scaled-up versions of those adopted by Teyssier et al. (2013). The dark matter distribution follows the NFW density profile. We chose a concentration parameter $c = 10$ and a circular velocity $V_{200} = 350$ km s^{-1}, corresponding to a virial mass $M_{200} = 1.42 \times 10^{13}$ M$_\odot$ and a virial radius $R_{200} = 500$ kpc. We truncate the halo at 1.13 Mpc, so that the total enclosed mass is $M_{\rm halo} = 1.78 \times 10^{13}$ M$_\odot$. Progenitors of haloes of mass $\sim 10^{14}$ M$_\odot$ identified at redshift $z = 0$ have a typical mass of a few 10^{13} M$_\odot$ at redshift $z \gtrsim 2$. This means that our simulations are particularly suited for comparing with the early evolution of clusters of galaxies. We choose the initial velocity field of the particles in a way that equilibrium can be maintained and such that the system

has spin parameter $\lambda = 0$ (no rotation). This choice has been made to avoid dealing with the details of gas accretion on to SMBHs in a clumpy disc (Bournaud et al. 2012) and it allows us to study test cases in which a high gas accretion efficiency is reached.

In all simulations a gaseous halo is embedded in the dark matter halo. The gas density ρ, pressure P and temperature T follow specific profiles:

$$\rho(x) = \rho_0 \left[\frac{\ln(1+x)}{x}\right]^{\frac{1}{\Gamma-1}} \quad (1)$$

$$P(x) = 4\pi G \rho_0 \rho_s r_s^2 \frac{\Gamma-1}{\Gamma} \left[\frac{\ln(1+x)}{x}\right]^{\frac{\Gamma}{\Gamma-1}} \quad (2)$$

$$T(x) = T_0 \frac{\ln(1+x)}{x}, \quad (3)$$

where r_s is the NFW scale radius, ρ_s is the dark matter density at r_s and $x = r/r_s$. We set the central temperature T_0 according to

$$\frac{k_B T_0}{\mu m_p} = 4\pi G \rho_s r_s^2 \frac{\Gamma-1}{\Gamma}. \quad (4)$$

Note that our choice implies that $P \propto \rho^\Gamma$. The effective polytropic index Γ is set according to

$$\Gamma = 1 + \frac{(1+x_{eq})\ln(1+x_{eq}) - x_{eq}}{(1+3x_{eq})\ln(1+x_{eq})}, \quad (5)$$

where $x_{eq} = \sqrt{5}c$. See Komatsu & Seljak (2001) for a similar, but slightly more complex model. With our choice of parameters, the gas density profile follows the slope of the NFW profile for $x \geq x_{eq}$ and tends to a constant value ρ_0 for $x \ll x_{eq}$.The central density ρ_0 is set requiring the gaseous halo mass fraction to be $f_{gas} = 0.15$. The metallicity of the gaseous halo is set to $Z = 10^{-2} Z_\odot$. The stability of the initial conditions was confirmed by running adiabatic simulations (no gas cooling).

Within the halo, we place 10 spherical gas clumps of equal mass, $M_{cl} = 2.1 \times 10^{10}$ M$_\odot$ and radius $R_{cl} = 10$ kpc. We set the temperature of the gas in the clumps to be a few 10^4 K; its metallicity is set to $Z = Z_\odot$. Each clump is given an initial velocity of magnitude $V_{cl} = V_{200}$ directed towards the halo centre. The aim of these clumps is to roughly mimic the cold gas reservoirs provided by infalling galaxies into a cluster. We have chosen radial orbits to be able to efficiently provide gas to the central regions of the halo; such a choice allows us to study the maximum effect gas dynamics can have on the dark matter distribution.

Our simulations differ in the initial geometrical distribution of the clumps. In one simulation, the distance of the clouds from the centre is in the range 200 kpc $\lesssim r \lesssim$ 1 Mpc; in this case, the clouds are far from the centre and reach it slowly, we labelled this simulation as SLOW. In the second simulation, the distance of the clouds from the centre is in the range 50 $\lesssim r \lesssim$ 250 kpc; since the clouds are close to the centre and reach it faster, we labelled this simulation as FAST. We also consider a third run in which the clumps distribution is the same as the SLOW case, but no AGN feedback is considered; this run has been labelled as AGNOFF.

Finally, as additional test cases, we run two simulations which only include the dark matter and smooth gaseous haloes. The first one includes AGN feedback and is labelled as SMOOTH AGNON, the second one does not include AGN feedback and is labelled as SMOOTH NOAGN. In these two runs, the halo metallicity is set to a higher value $Z = 0.2\,Z_\odot$. These latter two simulations allow us to study the effects of a cooling flow, rather than clumpy accretion.

In the FAST, SLOW and SMOOTH AGNON simulations, we place a SMBH of mass $M_{BH} = 10^9$ M$_\odot$ at the centre of the halo. This choice for the black hole mass roughly matches the value measured at redshift $z \approx 2$ for the central SMBH in the cosmological simulation analysed in Martizzi et al. (2012b) and agrees with the expected mass from the $M_{BH}-\sigma$ relation (Tremaine et al. 2002).

3 RESULTS

We run our simulations for 3.5 Gyr. For comparison, the dynamical time in the central region of the halo ($r < 5$ kpc), which depends on the density and radius, is of the order of 10^8 yr. As shown by the top-left panel of Fig. 1, 3.5 Gyr is sufficient time to see convergence in the effects of dark matter removal from the central regions of the halo. The black continuous line shows the initial mass profile in both simulations. After 1–2 Gyr a significant amount of mass has been ejected from the region $r < 5$ kpc in both the FAST (red line) and SLOW (green line) simulations.

The convergence to a central inner core occurs in both simulations with AGN feedback. In contrast, the AGNOFF simulation (blue line) is completely different: as the clumps fall to the central region of the cluster and as the gaseous halo cools, the dark matter halo contracts as a response to gas condensation and as a result the central density increases.

Some differences can be observed when considering the evolution of the mass of the central SMBH as a function of time t in our models (top-right panel of Fig. 1). As expected, in the FAST simulation the SMBH starts growing much earlier. The final black hole masses are $M_{BH} = 2.28 \times 10^9$ and 2.86×10^9 M$_\odot$ for the FAST and SLOW simulations, respectively. In the FAST simulation, the gas clumps feed the SMBH earlier, triggering a phase of rapid mass growth ($t <$ 1.5 Gyr) followed by a phase of intense AGN feedback. This is then responsible for the subsequent slowing down of mass accretion on to the SMBH. In the SLOW simulation, the gas clumps start feeding the SMBH later, so the early evolution of its mass is mild ($t <$ 1.8 Gyr); at later times a large quantity of gas becomes available to accrete on to the SMBH, triggering a very rapid mass growth in the time interval $1.8 < t < 2.1$ Gyr; this phase is also followed by intense AGN activity which slows down the SMBH mass growth.

The bottom panels of Fig. 1 show the evolution of the gas and dark mass enclosed within 5 kpc from the halo centre as a function of time. This is useful for understanding the effect of AGN feedback in the central region. The passages of the gas clumps close to the centre during the early evolution can be detected as peaks in the enclosed gas mass ($t < 0.7$ Gyr for FAST and $t < 1.4$ Gyr for SLOW). Before the central SMBH becomes massive enough to unbind the gas provided by the clumps, a large quantity of mass is accumulated in the central region. This produces a contraction of the total mass distribution that can be observed in this plot as a steep increase in the gas and dark mass within 5 kpc.

The striking effect we observe is that this contraction is completely erased as soon as the AGN activity becomes violent enough to unbind the gas. After the first passage of the clumps through the centre, the high-metallicity material mixes with the low-metallicity gas in the halo. By this time, a large reservoir of cooling gas is available. This gas is feeding the SMBH but is also influenced by its feedback. AGN heating results in the ejection of gas from this region. The ejected gas eventually cools down and begins infalling again. The accretion–ejection cycle happens on a time-scale that is always comparable to the dynamical time in the considered region. Fluctuations of the dark matter mass enclosed in this region follow the fluctuations in the

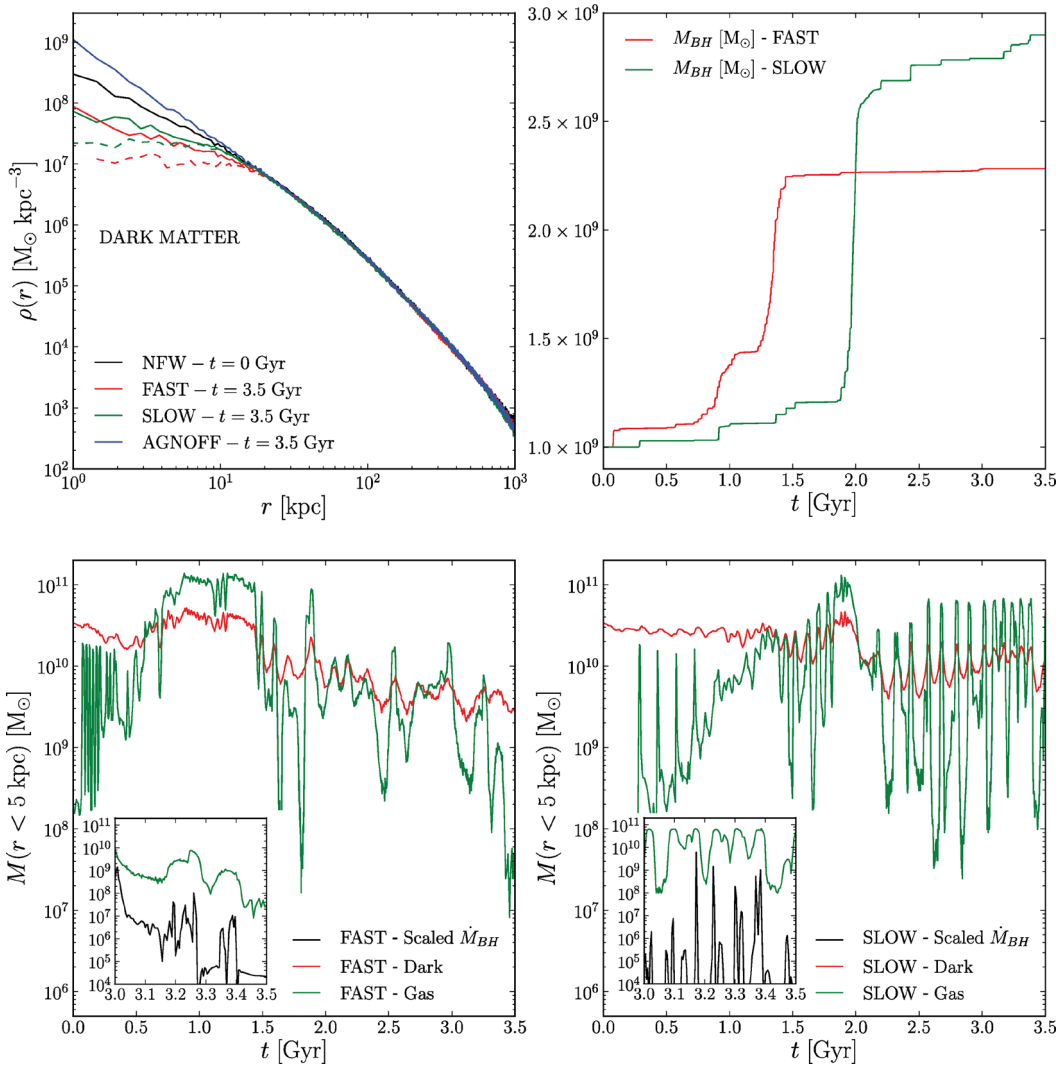

Figure 1. Top left: dark matter density profiles at different times and for different simulations. After 3.5 Gyr a large amount of mass has been removed from the central region in the FAST and SLOW simulations. The AGNOFF simulation shows signs of adiabatic contraction, with a large accumulation of mass in the central region. The solid lines are obtained when the peak of the dark matter distribution is chosen as a centre, whilst the dashed lines are obtained when the SMBH is chosen as the centre. Top right: SMBH mass evolution in the FAST and SLOW simulations. The mass evolves differently in the two runs, but the qualitative evolution through bursts of Eddington-limited gas accretion is the same. Bottom panels: evolution of the dark (red line) and gaseous (green line) mass within 5 kpc from the cluster centre in the FAST (left) and SLOW (right) simulations. After 2 Gyr, a large amount of dark matter is removed from the central region. The inset panels show a zoomed view of the evolution of the gas mass within 5 kpc, which correlates with the evolution of the accretion rate. As soon as gas is pushed away from the SMBH by AGN feedback the accretion rate drops.

gas mass. The result of subsequent accretion–ejection cycles is the irreversible ejection of $\sim 2 \times 10^{10}$ M$_\odot$ from $r < 5$ kpc, which is roughly 60 per cent of the dark mass initially enclosed in this region.

There are interesting differences in the properties of the accretion–ejection cycles in the two simulations: they are longer and more irregular in the FAST case, but they appear to be quasi-periodic in the SLOW case. This difference is possibly due to the fact that for $t > 2$ Gyr, the SMBH in the SLOW simulation can provide a more efficient feedback due to its larger mass.

The inset panels in Fig. 1 show the correlation between the accretion rate on to the SMBH and the amount of gas in the centre. Whenever gas mass in the centre is removed, the accretion rate suddenly decreases. To check whether this is a real effect or just a product of the black hole oscillating within a perturbed potential or within a harmonic core, we compare the distance of the SMBH from the dark matter centre as a function of time to the evolution of the gas mass within 5 kpc during the same time interval (Fig. 2). This plot is made using the SLOW simulation and a similar result is found in the FAST case. There is no obvious correlation between these quantities, implying that the adopted centring technique is not biasing our results. Furthermore, the mass of the dark matter particles is $\gtrsim$50–100 times smaller than the mass of the SMBH and for most of the time gas dominates the potential in the central region of the halo. We can therefore exclude spurious two-body interactions from driving the black hole motions.

Fig. 3 shows a time sequence of images of the gas distribution over an interval of 100 Myr. This spans the period in which the SMBH dramatically lowers the central gas density. The left-hand panels show four projected gas density maps at four different times, before, during and after an intense AGN activity burst. The SMBH is located at the centre of each map. The right-hand panel of the same figure shows the evolution of the gas mass within 5 kpc (green) from

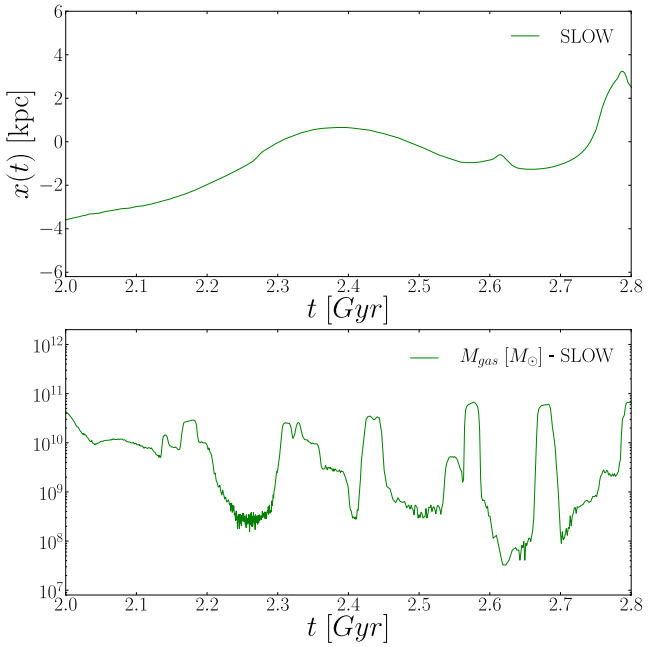

Figure 2. Top panel: distance of the SMBH from the centre of the dark matter distribution as a function of time. Bottom: gas mass within 5 kpc as a function of time. The SMBH is chosen as the centre. This plot shows that the decrease in the gas mass poorly correlates with the black hole motions. Therefore, the decrease in gas mass is not a consequence of the SMBH moving to lower density regions but rather due to AGN feedback.

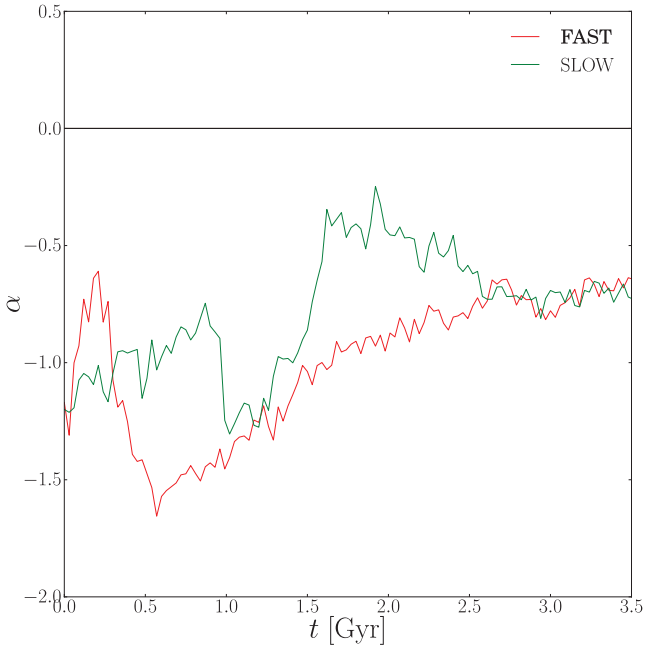

Figure 4. Evolution of the central slope of the dark matter profile as a function of time when the dark matter density peak is chosen as a centre.

the SMBH and the rescaled gas accretion rate (black). The times of the above four snapshots in the maps are labelled as numbers in the right-hand panel. We can clearly see that a large amount of gas is available for accretion in snapshot 1 and this is observed in the right-hand plot as large values of the accretion rate and enclosed gas mass within 5 kpc. In snapshots 2 and 3, AGN feedback blows gas away from the central region and the accretion rate decreases. Finally, in snapshot 4, we see gas returning to the centre and beginning to accrete again on to the SMBH.

In Fig. 4, we plot $\alpha = \mathrm{d}\log(\rho)/\mathrm{d}\log(r)$, the central slope of the dark matter density profiles as a function of time. We fit a power law to the density profiles in the region $0.4 < r < 8$ kpc. The dark

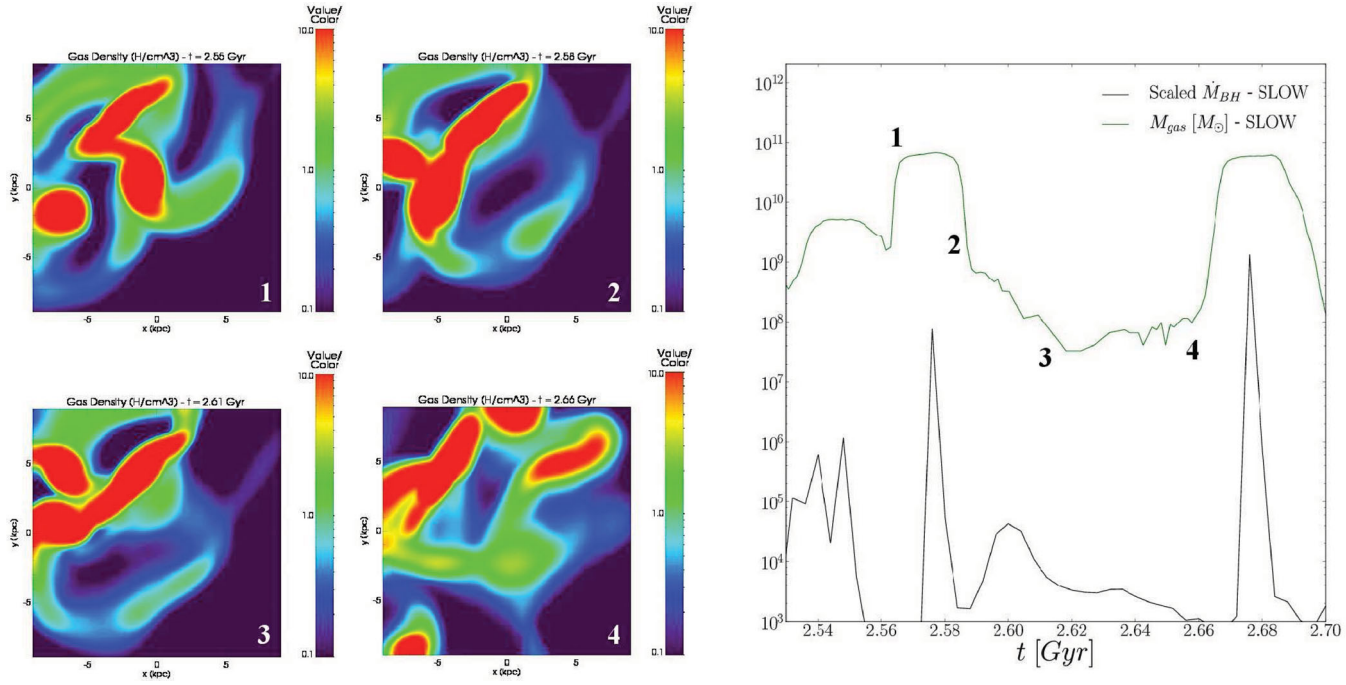

Figure 3. Projected density maps are shown for four snapshots over an accretion event followed by strong feedback. The SMBH is located at the centre of each map. This time sequence illustrates how AGN activity is able to excavate a hole in the gas density that is replenished on a time-scale of $\sim 10^8$ Gyr. The right-hand panel shows the evolution of the gas mass within 5 kpc from the SMBH together with the gas accretion rate (rescaled).

matter peak location has been measured using a shrinking spheres algorithm. A slope of $\alpha = -0.7$ is found if we choose the dark matter peak as the centre. As it is well known, inferred density profiles are sensitive to the choice of centre: assuming that the black hole is located exactly at the centre of the cluster may lead to slightly different estimates of the central slope. This fact has to be considered as an important caveat for observationally inferred density profiles.

Both the FAST and SLOW simulations converge to the same final density profiles and their evolution over time is qualitatively similar. Initially, the clumps transfer their energy to dark matter via dynamical friction; the result of this energy transfer is an initial shallowing of the slope of the dark matter profile. This process has been shown to be efficient by e.g. El-Zant et al. (2004). Recently, Laporte et al. (2012) showed that dynamical heating caused by dry mergers in a cosmological context can lead to a similar effect. However, in our simulations as gas in the halo cools, this adiabatically contracts the dark matter and steepens the central profile, reversing the initial flattening. This period continues until the black hole has grown massive enough to halt the accretion process. The steepest slopes are obtained at $t \sim 0.6$ and $t \sim 1.2$ Gyr in the FAST and SLOW simulations, respectively, as expected from the difference between the clump arrival times in the two runs.

As soon as AGN feedback becomes strong enough to unbind large quantities of gas, the accretion-ejection cycles start to be efficient in expelling dark matter from the central region with the final result of producing shallower density slopes. For $0.6 < t < 3.5$ Gyr, the value of α in the FAST simulation increases with time. In contrast, in the SLOW case, α only increases in the interval $1.2 < t < 1.7$ Gyr, and then remains approximately stable for $t > 1.7$ Gyr. This difference is caused by the different SMBH mass evolution observed in the two runs which makes AGN feedback operate in different modes, as already observed in Fig. 1. Despite these differences, the final state of the system is very similar in both the FAST and SLOW cases, demonstrating that once AGN feedback is properly triggered and repeated accretion–ejection cycles are produced, the final configuration of the system is weakly dependent on the initial conditions.

3.1 Experiments with smooth gas distributions

To understand the importance of clumpy accretion, we also carried out simulations using a smooth halo without infalling gas clouds. These simulations showed that it is not possible to trigger heating–ejection cycles when low metallicity ($Z \sim 0.01\,Z_\odot$) is adopted: the cooling time is so long that the gas cannot cool efficiently. AGN feedback stays active in its weak radio mode, which provides enough energy to maintain equilibrium and the original gas distribution hardly evolves. The situation is different if a higher metallicity is taken for the gas.

Fig. 5 shows the results we obtain choosing $Z = 0.2\,Z_\odot$ in the SMOOTH AGNON and SMOOTH AGNOFF simulations. For this choice of gas metallicity, the cooling time is comparable to that of the FAST and SLOW simulations after the gas in the clumps mixed with the gaseous halo. In the SMOOTH AGNOFF case, gas cools fast enough to produce contraction of the dark matter profile and steepening of the central cusp after 3.5 Gyr. When AGN feedback is turned on, there is a slight flattening of the initial central cusp after 3.5 Gyr, and within ∼3 kpc from the centre. The right-hand panel of Fig. 5 shows how the mass enclosed within 5 kpc evolves in the SMOOTH AGNON run. Gas infall characterizes the first 1.5 Gyr of evolution until AGN activity becomes strong enough to prevent further infall. Since dark matter still dominates the central regions of the halo, no significant variation of the enclosed dark matter mass is observed as a response to gas motions. By $t = 2$ Gyr, the black hole is massive enough to trigger some weak heating–ejection cycles.

These results need to be carefully interpreted. The region affected by the AGN in these 'cooling flow' simulations, is close to our resolution limit. Our adopted halo properties are chosen to correspond to a high-redshift cluster progenitor, rather than a massive cooling flow cluster. The metallicity for the above simulation, that shows a mild evolution, is therefore rather high.

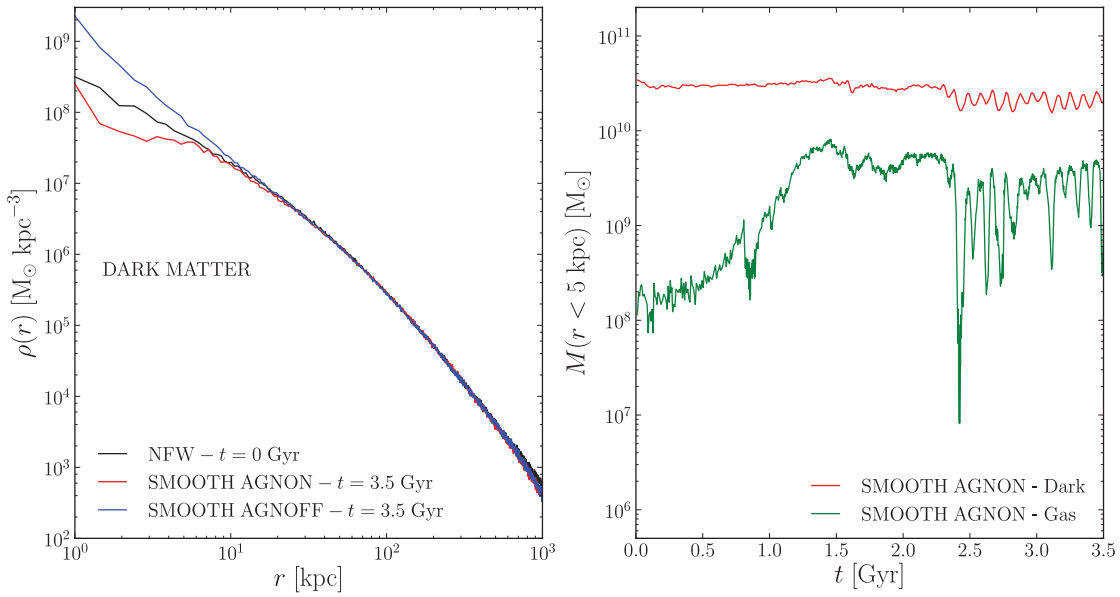

Figure 5. Left: dark matter density profiles at different ages and for the SMOOTH AGNOFF and SMOOTH AGNON simulations which do not include gas clumps. The peak of the dark matter distribution is chosen as a centre. In the AGNOFF case, we observe the effects of adiabatic contraction. In the AGNON case, the effect of the heating–ejection mechanism is very weak compared to the case with clumps. Right: evolution of the dark (red line) and gaseous (green line) mass within 5 kpc from the cluster centre in the SMOOTH AGNON simulation.

4 SUMMARY

We analysed the results of *N*-body hydrodynamical simulations of a dark matter halo of mass $M_{200} = 1.42 \times 10^{13}$ M$_\odot$ in the presence of gas cooling and AGN feedback. Our initial conditions are chosen to represent the early evolution of the mass distribution in cluster-sized haloes. Progenitors of haloes of mass $\sim 10^{14}$ M$_\odot$ identified at redshift $z = 0$ have a typical mass of a few 10^{13} M$_\odot$ at redshift $z \gtrsim 2$. A low-metallicity gaseous halo is embedded in the dark matter distributions and we provide additional fuel for the central SMBH by letting 10 high-metallicity cold gas clumps fall into the central region. In all our runs, we consider radiative gas cooling. In two of our runs, we also set a SMBH at the centre of the halo and we implement AGN feedback following a modification of the Booth & Schaye (2009) already adopted by Teyssier et al. (2011).

The aim of this work was to further investigate and confirm the results of the cosmological hydrodynamical simulations of Martizzi et al. (2012b), in which the central distribution of stars and dark matter within a cD galaxy were modified through violent gas motions induced by AGN feedback. These results are similar to those obtained by other authors using supernovae feedback in low-mass dark matter haloes (Governato et al. 2010; Maccio' et al. 2011; Pontzen & Governato 2012; Teyssier et al. 2013).

There are limitations to our study. The resolution of our simulations is ~ 0.5 kpc which could be improved in the future. Furthermore, compared to the observational data, our simulations overpredict the size of the regions in which the shallowing of dark matter mass profiles is measured. The simple AGN feedback model we adopt is probably too efficient in unbinding baryons from the central regions of haloes. Given these considerations, our results should be considered as a demonstration of the maximum effect that AGN feedback can have on the mass distribution in haloes hosting galaxy clusters.

Given these caveats, we can summarize our results as follows.

(i) In the absence of AGN feedback, the gas clumps fall into the central region of the halo and mix with the rest of the gas. Given that the clumps provide high-metallicity material, the result is a decrease of the cooling time in the central regions of the halo. Radiative cooling leads to the condensation of gas at the halo centre. The dark matter halo responds to the gas condensation via adiabatic contraction, increasing the central density.

(ii) In the presence of AGN feedback, after 1–2 Gyr, we find a reduction in the dark matter density in the central regions of the halo. Roughly 60 per cent of the dark mass within 5 kpc from the centre is moved to larger radii. The result is a mass distribution characterized by a dark matter density profile with a density slope in the region $r \lesssim 5-10$ kpc significantly shallower than that of the initial NFW model.

(iii) The only process responsible for the dark mass depletion in the central regions of the halo is related to AGN feedback and the resulting gas dynamics. After the gas clumps fall into the central region of the halo and mix with halo gas, we observe cycles of fast accretion on to the SMBH, followed by AGN feedback activity that blows gas away. The expelled gas cools and falls back into the central region of the halo. The whole cycle happens on a timescale comparable to the dynamical time. Repeated episodes generate a series of gravitational potential fluctuations that influence the total mass distribution in an irreversible way (Pontzen & Governato 2012).

(iv) If we use a smooth gas distribution without infalling gas clumps, we are not able to trigger the mechanism we just described unless we assume high-gas metallicity (shorter cooling time). The observed effect on the dark matter profile is then rather small. High central gas densities that arise from infall emerges as a key element to produce cusp–core transformations. At high redshift this may be triggered through mergers, gas stripping and fuelling from cold streams.

Recent observational work (Sand et al. 2004, 2008; Newman et al. 2009, 2011, 2012; Richtler et al. 2011) shows that cluster with shallow central dark matter density profiles may have been observed. Furthermore, very massive elliptical galaxies are observed to have surface brightness profiles with shallow central slopes (Kormendy 1999; Quillen et al. 2000; Laine et al. 2003; Trujillo et al. 2004; Lauer et al. 2005; Côté et al. 2007; Kormendy et al. 2009; Graham 2011).

The two phenomena might be related, given that dark matter and stars can both be influenced by the same physical processes. Indeed, a strong prediction from our past simulations is that the sizes of the central cores in the dark matter and the stars are similar (Martizzi et al. 2012b). Additional observational evidence would be important to clarify this claim and to reveal possible correlations between AGN activity, stellar and dark matter cores and the global properties of clusters and the intracluster medium.

ACKNOWLEDGEMENTS

We thank our referee for many suggestions that improved the quality of our paper. The simulations were performed on the Schrödinger cluster at the University of Zürich.

REFERENCES

Booth C. M., Schaye J., 2009, MNRAS, 398, 53
Bournaud F. et al., 2012, ApJ, 757, 81
Côté P. et al., 2007, ApJ, 671, 1456
Del Popolo A., 2009, ApJ, 698, 2093
Del Popolo A., 2012, MNRAS, 424, 38
Dubois Y., Devriendt J., Slyz A., Teyssier R., 2012, MNRAS, 420, 2662
Duffy A. R., Schaye J., Kay S. T., Dalla Vecchia C., Battye R. A., Booth C. M., 2010, MNRAS, 405, 2161
El-Zant A. A., Hoffman Y., Primack J., Combes F., Shlosman I., 2004, ApJ, 607, L75
Fromang S., Hennebelle P., Teyssier R., 2006, A&A, 457, 371
Gnedin O. Y., Zhao H., 2002, MNRAS, 333, 299
Goerdt T., Moore B., Read J. I., Stadel J., 2010, ApJ, 725, 1707
Governato F. et al., 2010, Nat, 463, 203
Graham A. W., 2011, preprint (arXiv:1108.0997)
Komatsu E., Seljak U., 2001, MNRAS, 327, 1353
Kormendy J., 1999, in Merritt D. R., Valluri M., Sellwood J. A., eds, ASP Conf. Ser. Vol. 182, The Central Structure of Elliptical Galaxies and the Stellar-Dynamical Search for Supermassive Black Holes. Astron. Soc. Pac., San Francisco, p. 124
Kormendy J., Fisher D. B., Cornell M. E., Bender R., 2009, ApJS, 182, 216
Krumholz M. R., McKee C. F., Klein R. I., 2004, ApJ, 611, 399
Laine S., van der Marel R. P., Lauer T. R., Postman M., O'Dea C. P., Owen F. N., 2003, AJ, 125, 478
Laporte C. F. P., White S. D. M., Naab T., Ruszkowski M., Springel V., 2012, MNRAS, 424, 747
Lauer T. R. et al., 2005, AJ, 129, 2138
Maccio' A. V., Stinson G., Brook C. B., Wadsley J., Couchman H. M. P., Shen S., Gibson B. K., Quinn T., 2011, ApJ, 744, L9
Martizzi D., Teyssier R., Moore B., 2012a, MNRAS, 420, 2859
Martizzi D., Teyssier R., Moore B., Wentz T., 2012b, MNRAS, 422, 3081
Mashchenko S., Couchman H. M. P., Wadsley J., 2006, Nat, 442, 539
Mashchenko S., Wadsley J., Couchman H. M. P., 2008, Sci, 319, 174

Navarro J. F., Eke V. R., Frenk C. S., 1996, MNRAS, 283, L72
Newman A. B., Treu T., Ellis R. S., Sand D. J., Richard J., Marshall P. J., Capak P., Miyazaki S., 2009, ApJ, 706, 1078
Newman A. B., Treu T., Ellis R. S., Sand D. J., 2011, ApJ, 728, L39
Newman A. B., Treu T., Ellis R. S., Sand D. J., Nipoti C., Richard J., Jullo E., 2012, 765, 24
Peirani S., Kay S., Silk J., 2008, A&A, 479, 123
Peñarrubia J., Pontzen A., Walker M. G., Koposov S. E., 2012, ApJ, 759, L42
Pontzen A., Governato F., 2012, MNRAS, 421, 3464
Quillen A. C., Bower G. A., Stritzinger M., 2000, ApJS, 128, 85
Ragone-Figueroa C., Granato G. L., Abadi M. G., 2012, 423, 3243
Read J. I., Gilmore G., 2005, MNRAS, 356, 107
Richtler T., Salinas R., Misgeld I., Hilker M., Hau G. K. T., Romanowsky A. J., Schuberth Y., Spolaor M., 2011, A&A, 531, A119
Rocha M., Peter A. H. G., Bullock J. S., Kaplinghat M., Garrison-Kimmel S., Onorbe J., Moustakas L. A., 2013, MNRAS, 430, 81
Sand D. J., Treu T., Smith G. P., Ellis R. S., 2004, ApJ, 604, 88
Sand D. J., Treu T., Ellis R. S., Smith G. P., Kneib J.-P., 2008, ApJ, 674, 711
Sutherland R. S., Dopita M. A., 1993, ApJS, 88, 253
Teyssier R., 2002, A&A, 385, 337
Teyssier R., Fromang S., Dormy E., 2006, J. Comput. Phys., 218, 44
Teyssier R., Moore B., Martizzi D., Dubois Y., Mayer L., 2011, MNRAS, 414, 195
Teyssier R., Pontzen A., Dubois Y., Read J., 2013, MNRAS, 429, 3068
Toro E. F., Spruce M., Speares W., 1994, Shock Waves, 4, 25
Tremaine S. et al., 2002, ApJ, 574, 740
Trujillo I., Erwin P., Asensio Ramos A., Graham A. W., 2004, AJ, 127, 1917
Vogelsberger M., Zavala J., Loeb A., 2012, MNRAS, 423, 3740

This paper has been typeset from a TEX/LATEX file prepared by the author.

Chapter 7

The effect of AGN on the mass function of galaxy clusters

The dark matter halo mass function is an extremely important quantity that will be measured to high precision by ongoing and next generation surveys. It is therefore crucial to determine which are the theoretical uncertainties that need to be taken into account when comparing the observed halo mass function to the predictions of theoretical cosmological models and numerical simulations. In this paper we study the effect of baryonic processes on the halo mass function in the galaxy cluster mass range using a catalogue of 153 high resolution cosmological hydrodynamical simulations performed with the AMR code RAMSES. We use the results of our simulations within a simple analytical model to gauge the effects of baryon physics on the halo mass function. We find that neglect of AGN feedback leads to a significant boost in the cluster mass function similar to that reported by other authors. However, including AGN feedback not only gives rise to systems that are similar to observed galaxy clusters, but they also reverse the global baryonic effects on the clusters. The resulting mass function is closer to the unmodified dark matter halo mass function but still contains a mass dependent bias at the 5–10% level. We then explore how these effects bias measurements of the cosmological parameters, such as σ_8 and $\Omega_{\rm m}$. For current cluster surveys baryonic effects are within the noise for current survey volumes, but forthcoming and planned large surveys will be biased at the percent level by these processes. These results have significant implications for the correct comparison of theoretical models with halo counts in present and next generation SZ, X-ray and multi-wavelength surveys. The predictions for the halo mass function including baryonic effects need to be carefully studied with larger and improved simulations. However, simulations of full cosmological boxes with the resolution we achieve and including AGN feedback are still

computationally challenging.

7.1 Introduction

In the hierarchical structure formation scenario, the abundance of dark matter halos within a representative volume of the universe is characterized by the halo mass function. Since the statistical properties of the cosmic density field are related to the underlying cosmological model, the halo mass function contains great deal of information about the cosmological parameters of our Universe. In particular, within the standard Λ cold dark matter cosmological scenario, dark matter halos form from initial density peaks via gravitational instability. The resulting halo mass function is directly related to the statistical properties of the primordial density field. Early studies suggested that the halo mass function can be expressed as a universal function of $\sigma(M)$, the rms value of the density perturbations at a particular mass scale M (Press & Schechter, 1974; Efstathiou et al., 1988; Sheth & Tormen, 1999; Sheth et al., 2001).

Cosmological N-body simulations have been extensively used to calibrate the halo mass function and to test whether this quantity is universal and how accurately it can be determined (Audit et al., 1997; Sheth et al., 2001; Jenkins et al., 2001; Reed et al., 2003; Springel, 2005; Warren et al., 2006; Reed et al., 2007; Tinker et al., 2008; Crocce et al., 2010; Reed et al., 2013). These studies demonstrated that the mass function measured in cosmological N-body simulations deviates from universality at the 10% level. Despite the importance of precise calibrations of the halo mass function and the ability to make accurate theoretical predictions, there is another issue that needs to be considered when studying the halo mass function: the effect of baryons on halo masses. This issue might be extremely relevant for the comparison of observationally determined halo mass functions and the prediction of cosmological simulations. In fact, present and next generation surveys such as Euclid, the Dark Energy Survey or eROSITA, are expected to measure halo masses and the halo mass function with an unprecedented percent level precision.

The effect of baryonic processes on the power spectrum and on the weak gravitational lensing shear signal has been studied in detail (White, 2004; Zhan & Knox, 2004; Jing et al., 2006; Rudd et al., 2008; Guillet et al., 2010; van Daalen et al., 2011; Semboloni et al., 2011; Reddick et al., 2013). A series of recent papers (Stanek et al., 2009; Cui et al., 2012; Balaguera-Antolinez & Porciani, 2013) attempts to assess the importance of baryonic processes in shaping the properties of the halo mass function. The simulations performed

by Stanek et al. (2009) and Cui et al. (2012) show a significant increase of halo counts in the galaxy cluster mass range in the cases in which cooling and star formation are considered. This is caused by the condensation of baryons at the centres of dark matter halos which leads to the contraction of the matter distribution and an enhancement of their masses. However, none of the simulations used by these authors include AGN feedback, which is expected to be an important process in shaping the properties of galaxy clusters, especially of their mass distribution (Duffy et al., 2010; Teyssier et al., 2011; Martizzi et al., 2012). In this paper, we carry out a large suite of simulations that follow the formation of galaxy clusters over a range of masses. These are fully cosmological hydrodynamical simulations performed with the RAMSES code. The aim of this study is to explicitly study the impact of AGN feedback on halo masses and the effects of baryonic processes on the halo mass function at redshift $z = 0$ and the subsequent biases this introduces in recovering the underlying cosmological parameters.

The paper is organized as follows. In Section 2, we describe the numerical simulations. In Section 3, we describe the analytical formalism we adopt to compute the effect of baryons on the halo mass function. In Section 4, we discuss the measurements we perform on the simulations that will be used as an input for the analytical formalism. In Section 5, we show our predictions on the halo mass function. In Section 6, we test the impact of our predictions on the estimate of cosmological parameters. In Section 7, we summarize and discuss our results.

7.2 The simulations

We performed a set of 153 cosmological resimulations with the RAMSES code (Teyssier, 2002). We assume the standard ΛCDM cosmological scenario with matter density parameter $\Omega_{\rm m} = 0.272$, cosmological constant density parameter $\Omega_\Lambda = 0.728$, baryonic matter density parameter $\Omega_{\rm b} = 0.045$, power spectrum normalization $\sigma_8 = 0.809$, primordial power spectrum index $n_{\rm s} = 0.963$ and Hubble constant $H_0 = 70.4$ km/s/Mpc. The cosmological parameters are summarized in Table 7.1. The initial conditions for our simulations were computed using the Eisenstein & Hu (1998) transfer function and the GRAFIC++ code developed by Doug Potter (http://sourceforge.net/projects/grafic/) which is based on the original GRAFIC code (Bertschinger, 2001). We first ran a dark matter only simulation with particle mass $m_{\rm cdm} = 1.55 \times 10^9$ $\mathrm{M}_\odot$/h and box size 144 Mpc/h. The initial level of refinement is $\ell = 9$ (512^3), but 7 more levels of refinement were carried out during the runs (maximum level $\ell_{\rm max} = 16$).

Cosmological parameters

Type	H_0 [km s^{-1}Mpc^{-1}]	σ_8	n_s	Ω_Λ	Ω_m	Ω_b
DMO	70.4	0.809	0.963	0.728	0.272	-
HYDRO	70.4	0.809	0.963	0.728	0.272	0.045

Table 7.1: Cosmological parameters adopted in our simulations. The DMO label refers to the dark matter only run. The HYDRO label refers to the hydrodynamical runs.

From this cubic cosmological volume we identified dark matter halos with the AdaptaHOP algorithm (Aubert et al., 2004), using the version implemented and tested by Tweed et al. (2009). From the list of identified halos we selected a subsample of 51 halos whose *total* masses are $M_{\rm tot} > 10^{14}$ M$_\odot$ and whose neighbouring halos do not have masses larger than $M/2$ within a spherical region of five times their virial radius. This choice allowed us to extract high resolution initial conditions to perform re-simulations of these 51 halos. Each halo was re-simulated three times: the first time considering only dark matter, the second and the third time including baryons, but using different physical prescriptions for feedback. Our results are based on these 153 simulations which constitute our cluster catalog. We label the dark matter only simulation as DMO and the hydrodynamical simulations as HYDRO.

In the 51 DMO simulations the dark matter particle mass is $m_{\rm cdm} = 1.94 \times 10^8$ M$_\odot$/h. In the HYDRO runs the dark matter particle mass is $m_{\rm cdm} = 1.62 \times 10^8$ M$_\odot$/h, while the baryon resolution element has a mass of $m_{\rm gas} = 3.22 \times 10^7$ M$_\odot$. In all our simulations we set the maximum refinement level to $\ell = 17$ which corresponds to a minimum cell size $\Delta x_{\rm min} = L/2^{\ell_{\rm max}} \simeq 1.07$ kpc/h. The grid was dynamically refined using a quasi-Lagrangian approach: when the dark matter or baryonic mass in a cell reaches 8 times the initial mass resolution, it is split into 8 children cells. The mass and spatial resolution of our simulations is summarized in Table 7.2

In the HYDRO runs, gas dynamics is modeled using a second-order unsplit Godunov scheme (Teyssier, 2002; Teyssier et al., 2006; Fromang et al., 2006) based on the HLLC Riemann solver and the MinMod slope limiter (Toro et al., 1994). We assume a perfect gas equation of state (EOS) with polytropic index $\gamma = 5/3$. All the HYDRO runs include subgrid models for gas cooling which account for H, He and metals and that use the Sutherland & Dopita 1993 cooling function. We directly follow star formation and supernovae feedback ("delayed cooling" scheme, Stinson et al. 2006) and metal

Mass and spatial resolution

Type	$m_{\rm cdm}$ [10^8 $M_\odot$/h]	$m_{\rm gas}$ [10^7 $M_\odot$/h]	$\Delta x_{\rm min}$ [kpc/h]
DMO cube	15.5	n.a.	2.14
DMO clusters	1.94	n.a.	1.07
HYDRO clusters	1.62	3.22	1.07

Table 7.2: Mass resolution for dark matter particles, gas cells and star particles, and spatial resolution (in physical units) for our simulations.

enrichment. In 51 of the HYDRO simulations we also implement AGN feedback, using a modified version of the Booth & Schaye (2009) model in which supermassive black holes (SMBHs) are modeled as sink particles and AGN feedback is provided in form of thermal energy injected in a sphere surrounding each SMBH. We label these simulations as AGN-ON. The other 51 HYDRO simulations do not include AGN feedback. We label these simulations as AGN-OFF.

As we showed in Martizzi et al. (2012), after implementing the physical effects of AGN feedback we were able to obtain galaxy clusters with correct stellar masses and kinematics. There are a number of unconstrained free parameters in these simulations, for example, the efficiency of the AGN feedback and star formation process. A careful study of the tuning of AGN feedback models implemented in the RAMSES code has been performed by Dubois et al. (2012). In our case, the tuning has been performed re-simulating one of the halos in our catalog (the less massive one) several times while varying the star formation efficiency ϵ_* and the size of the region where the AGN feedback energy is injected. We found that the model that best reproduces the $M_{\rm BH} - \sigma$ relation and the central galaxy masses has star formation efficiency $\epsilon_* = 0.03$ and size of the AGN feedback injection region equal to twice the cell size. For the AGN-OFF simulations we adopt $\epsilon_* = 0.01$, which is close to the lower limit of the observed star formation efficiencies. Despite this low value, Agertz et al. (2011) produced realistic "Milky Way" candidates assuming $\epsilon_* = 0.01$, however we expect very different results in galaxy clusters because the AGN-OFF simulations are affected by gas overcooling.

Figure 7.1 shows the abundance matching predictions (Moster et al., 2010) for the relation between halo mass and stellar fraction associated to the central galaxy in the clusters, compared to our results. The stellar mass of the central galaxies has been measured as in Martizzi et al. (2012). Our choice of parameters for the AGN-ON simulations produces results in good

agreement with the data. It is worth commenting on the presence of the two outliers in the AGN-ON case: these two objects are highly unrelaxed clusters. In one cluster the BCG is still interacting with a close companion. In the other cluster the BCG is interacting with two companions. It is likely that taking into account the mass in the companions might improve the agreement with the abundance matching prediction. We believe that the selection criterion we adopt to identify the halos used in this study does not bias the following results. As all the unrelaxed clusters, these two outliers were excluded from the analysis concerning the mass function.

7.3 Effect of baryonic processes on the halo mass function

From a theoretical perspective, the easiest way to define the mass of a dark matter halo is to use spherical overdensities. We can define the average density within a given radius as:

$$\Delta = \frac{3M(r)}{4\pi r^3} \tag{7.1}$$

where r is the distance from the centre of the halo and $M(r)$ is the spherically averaged enclosed mass profile of the halo. Conventional definitions of the halo mass can be obtained by requiring Δ to be a multiple of the critical density ρ_c. For example, by requiring $\Delta = 500\rho_c$ we define the M_{500} halo mass. In this paper we are interested in studying the effect of baryonic processes related to hydrodynamics and galaxy formation on halo masses, and subsequently on the halo mass function. To do so we adopt a very simple analytical formalism, very similar to the one used by Balaguera-Antolinez & Porciani (2013).

Cosmological hydrodynamical simulations have been used to show that phenomena related to galaxy formation can strongly influence the internal mass distribution of dark matter halos. Baryon condensation at the centre of halos tends to increase the concentration of the total mass distribution (Gnedin et al., 2004), whereas feedback processes tend to act in the opposite direction by decreasing the concentration through dynamical processes related to the strong winds feedback can drive (Governato et al., 2010; Duffy et al., 2010; Macciò et al., 2012; Pontzen & Governato, 2012; Martizzi et al., 2012; Teyssier et al., 2013). It has been shown that the effects of baryons are not limited to changes in the inner density profile, but to global properties such as their mass, e.g. by Stanek et al. (2009) and Cui et al. (2012) and

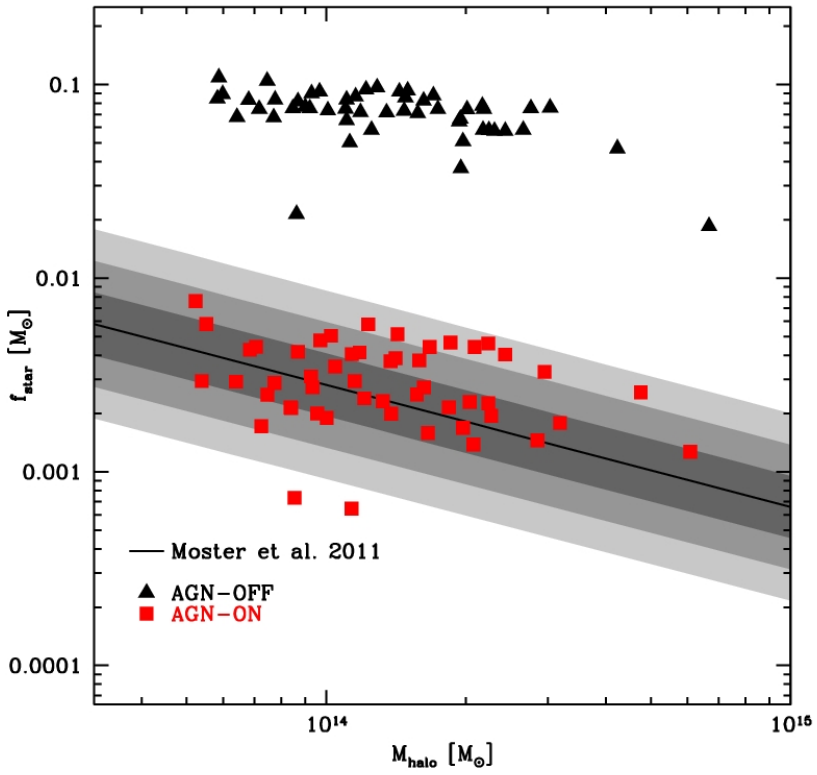

Figure 7.1: Halo mass vs. stellar fraction associated to the central galaxy of each of our simulated clusters (ratio between galaxy stellar mass and total mass of the halo). Coloured points represent the results from the AGN-ON (red) and AGN-OFF (black) re-simulations. The black solid line represents the average relation from Moster et al. (2010) with its 1, 2 and 3 σ scatter (shaded areas).

shape, e.g. Kazantzidis et al. (2004). All of these effects can have important consequences for the halo mass function.

The analytical formalism we adopt is very simple and relies on some approximations that we outline here. We will focus on M_{500} halo masses, but the formalism can be easily adapted to any definition of the halo mass. We have verified that the results we obtain are qualitatively similar in the case in which M_{200} is used. We find that the adoption of M_{500} is more robust because the definition of halo masses is weakly influenced by the presence of structures at the outskirts of the halo. If baryonic effects are important then if we measure $M_{500}^{\rm DMO}$, the mass of a halo in a cosmological dark matter only simulation, the mass measured in a cosmological hydrodynamical simulation will be different, $M_{500}^{\rm HYD} \neq M_{500}^{\rm DMO}$. $M_{500}^{\rm HYD}$ is the sum of the baryonic and non-baryonic mass. We assume the baryon fraction within R_{500} to be a function of halo mass:

$$f_{\rm b,500} = f_{\rm b,500}(M_{500}^{\rm HYD}) \tag{7.2}$$

which implies that $f_{\rm b,500}$ is generally different from the cosmological baryon fraction $f_{\rm c}$. In this paper, we adopt a very simple power-law scaling of the baryon fraction with mass:

$$f_{\rm b,500}(M_{500}^{\rm HYD}) = A \left(\frac{M_{500}^{\rm HYD}}{10^{14}{\rm M}_{\odot}} \right)^{B}. \tag{7.3}$$

This choice is convenient since the parameters A and B can be easily measured from simulations as well as from observational data.

Similar formulae have been used to fit observational data, e.g. by Lin et al. (2003) and Giodini et al. (2009). This has been shown to be appropriate in the range of massive groups and clusters, however significant deviations from a power-law formula have been reported for very massive clusters (Leauthaud et al., 2012; Lin et al., 2012; Laganá et al., 2013). In the mass range we consider in this paper a power-law, like the one in Equation 7.2, should correctly capture the scaling of the baryon fractions with halo masses.

The effect of baryonic processes on the halo mass is modeled as a relation between $M_{500}^{\rm HYD}$ and $M_{500}^{\rm DMO}$. To obtain such a relation, Balaguera-Antolinez & Porciani (2013) assume that the dark matter halo mass is the same, with or without the presence of baryons. In this paper, we generalize this assumption to take account of the dynamical effect of baryons. Large concentrations of baryonic material at the centre of dark matter halos are expected to generate a contraction of the mass distribution and change the amount of dark matter present in the halos. We parametrize this effect by assuming:

$$M_{dark}^{\rm DMO} = \frac{1}{\alpha_c} M_{dark}^{\rm HYD}. \tag{7.4}$$

Here, we have introduced the parameter α_c to account for the fact that the presence of baryons in the halo can induce a steepening of the density distribution within the halo and possibly boost the mass within the virial radius. In the DMO case all the mass is modeled as collisionless dark matter, but we assume that a fraction f_c is associated to baryons. Therefore, in the DMO case we assume a dark matter mass $M_{\rm dark}^{\rm DMO} = (1 - f_{\rm c})M_{500}^{\rm DMO}$, whereas in the HYDRO case we assume $M_{\rm dark}^{\rm HYD} = (1 - f_{\rm b,500}(M_{500}^{\rm HYD}))M_{500}^{\rm HYD}$. This allows us to write Equation 7.4 as follows:

$$M_{500}^{\rm DMO}(M_{500}^{\rm HYD}) = \frac{1}{\alpha_c}\frac{1 - f_{\rm b,500}(M_{500}^{\rm HYD})}{1 - f_{\rm c}}M_{500}^{\rm HYD}. \tag{7.5}$$

We find that the α_c parameter is quite important for the correct determination of the relation $M_{500}^{\rm DMO}(M_{500}^{\rm HYD})$ and that we cannot simply assume $\alpha_c = 1$, i.e. we cannot assume that the dark matter mass is the same in the HYDRO and the DMO case as in Balaguera-Antolinez & Porciani (2013).

In the simplistic case in which the relation between baryon fraction and mass is exact, i.e. when the intrinsic scatter is assumed to be zero, it is straightforward to compute the effect of baryonic processes on the halo mass function. Let us label the mass function affected by baryonic processes as $n(M_{500}^{\rm HYD})$ and the standard mass function measured in dark matter only simulations as $n_0(M_{500}^{\rm HYD})$. Then, if $f_{\rm b,500}(M_{500}^{\rm HYD})$, we have that

$$n(M_{500}^{\rm HYD}) = n_0\left[M_{500}^{\rm DMO}(M_{500}^{\rm HYD})\right]\frac{dM_{500}^{\rm DMO}}{dM_{500}^{\rm HYD}}. \tag{7.6}$$

Equation 7.6 can be easily derived by the normalization condition:

$$\int n_0(M_{500}^{\rm DMO})dM_{500}^{\rm DMO} = \int n(M_{500}^{\rm HYD})dM_{500}^{\rm HYD}.$$

In the most general case, the relation between baryon fraction and halo mass is not a precise relation due to noise and variance, i.e. it is characterized by an average relation such as the one in Equation 7.2 and by a scatter about the mean. This fact means that, an $M_{500}^{\rm HYD}$ value is associated to an $M_{500}^{\rm DMO}$ value via a stochastic process. This process is characterized by $P(M_{500}^{\rm HYD}|M_{500}^{\rm DMO})$, the conditional probability density which gives the distribution of the total cluster mass for a given $M_{500}^{\rm DMO}$. In the general case, $n(M_{500}^{\rm HYD})$ has to be computed as

$$n(M_{500}^{\rm HYD}) = \int_0^{+\infty} n_0(M_{500}^{\rm DMO})P(M_{500}^{\rm HYD}|M_{500}^{\rm DMO})dM_{500}^{\rm DMO}. \tag{7.7}$$

In their discussion, Balaguera-Antolinez & Porciani (2013) argue that the conditional probability function is very well approximated by a log-normal distribution and we make the same assumption here:

$$P(M_{500}^{\rm HYD}|M_{500}^{\rm DMO}) = \frac{1}{\sqrt{2\pi\sigma^2}}\frac{1}{M_{500}^{\rm HYD}}\exp\left[-\frac{(\ln M_{500}^{\rm HYD}-\mu)^2}{2\sigma^2}\right], \tag{7.8}$$

where the parameters μ and σ are defined as

$$\mu = \ln\langle M_{500}^{\rm HYD}|M_{500}^{\rm DMO}\rangle - \frac{\sigma^2}{2},$$

$$\sigma^2 = \ln\left(1+\frac{\sigma_{\rm HYD}^2}{\langle M_{500}^{\rm HYD}|M_{500}^{\rm DMO}\rangle^2}\right),$$

where $\langle M_{500}^{\rm HYD}|M_{500}^{\rm DMO}\rangle$ is the average expected value of $M_{500}^{\rm HYD}$ given $M_{500}^{\rm DMO}$, and $\sigma_{\rm HYD}^2$ is the scatter about $\langle M_{500}^{\rm HYD}|M_{500}^{\rm DMO}\rangle$. The parameters μ and σ can be easily determined from the results of our simulations. Balaguera-Antolinez & Porciani (2013) argue that the log-normal approximation works very well when the log-scatter is a weak function of halo mass. We find that the scatter does not show significant variations in the mass range we are considering, therefore we group all halos in a single bin to compute a unique value for σ^2. In the AGN-ON case we find $\sigma_{\rm HYD}/\langle M_{500}^{\rm HYD}|M_{500}^{\rm DMO}\rangle = 0.046$, whereas in the AGN-OFF case we find $\sigma_{\rm HYD}/\langle M_{500}^{\rm HYD}|M_{500}^{\rm DMO}\rangle = 0.065$.

7.4 Baryon fractions and halo masses

The key elements to compute the effect of baryonic processes on the halo mass function using the formalism described in the previous section are a reliable measure of the $f_{\rm b,500}(M_{500}^{\rm HYD})$ relation and of its scatter, and a model for the conditional probability function $P(M_{500}^{\rm HYD}|M_{500}^{\rm DMO})$. It is important to note that the halos considered in this paper are less massive than the ones currently used for cosmological analysis, e.g. using all sky ROSAT samples.

We measured halo masses and baryon fractions of all the halos in our cluster catalog and fitted the data using Equation 7.2 to obtain an estimate of the average scaling relation $f_{\rm b,500}(M_{500}^{\rm HYD})$ and of its scatter. All halo masses are estimated using the spherically averaged overdensity definition of Equation 7.1. We then follow the formalism described in the previous section to calculate the expected halo mass functions from the three different simulations. In the following analysis we only consider relaxed clusters in order to avoid biases in the mass measurements that arise from unrelaxed systems. The relaxed clusters are identified through a morphological selection

Parameters of the baryon fraction scaling relation

Type	A	B	$\tilde{\chi}^2$
AGN-ON	0.1633 ± 0.0012	0.052 ± 0.016	0.56
AGN-OFF	0.2038 ± 0.0014	-0.0039 ± 0.014	0.37

Table 7.3: Fits to the baryon fraction scaling and mass model defined in Equation 7.3. The reduced chi-squared value $\tilde{\chi}^2$ for the fits is also reported.

based on mock X-ray emissivity maps. We identify the relaxed clusters by finding those that exhibit a unique emissivity peak within 100 kpc from their center. The selection reduces our cluster sample to 25 relaxed halos. We show the fitting parameters in Table 7.3, which have been obtained using a standard χ^2 algorithm. The reduced chi-squared value $\tilde{\chi}^2$ for our fits are reported in Table 7.3. Such values have been obtained by weighting each term of the χ^2 by the square of the inverse of 10% of the data point value.

The scaling of the baryon fraction with cluster mass has been measured in observed clusters by several groups (Lin et al., 2003; Gonzalez et al., 2007; Giodini et al., 2009; Andreon, 2010; Leauthaud et al., 2012; Lin et al., 2012). The debate on which technique provides the best estimate of the baryon fraction scaling with halo mass is still ongoing (weak and strong gravitational lensing, X-ray masses obtained assuming hydrostatic equilibrium, constraints from stellar kinematics, etc.). In this paper, we adopt the fits to the data provided by Lin et al. (2003) and Giodini et al. (2009), which are provided in the form of power laws similar to that in Equation 7.3.

Figure 7.2 shows a comparison of the baryon fractions measured within our virialised cluster sample at redshift $z = 0$ with the observational results by Lin et al. (2003) and Giodini et al. (2009) (re-normalized to fit our choice of cosmological parameters). As expected the AGN-OFF simulations show baryon fractions in excess of the observational results, an effect related to the overcooling of gas in simulations which do not include AGN feedback. The tension between observations and simulations is partially relaxed when the AGN-ON case is considered. There is a marginal agreement between the AGN-ON results and the data by Lin et al. (2003), whereas our baryon fractions are far in excess of those measured by Giodini et al. (2009). In the AGN-ON case, the power law normalization we find is very similar to that found by Lin et al. (2003), however their slope is steeper. The normalization found by Giodini et al. (2009) is lower than in our AGN-ON case, and our slope is shallower. However, since the difference between the observed relations is large, it is not clear if our fits to the simulated data are discrepant

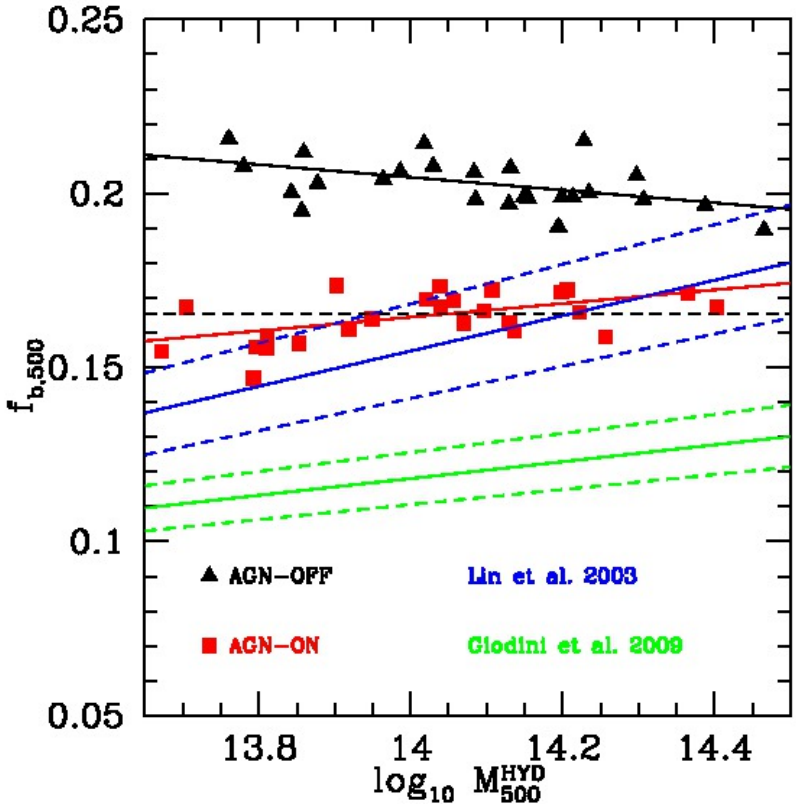

Figure 7.2: Baryon fraction scaling as a function of halo mass at redshift $z = 0$. Coloured points represent the results from the AGN-ON (red) and AGN-OFF (black) re-simulations. The red and black solid lines represent power-law fits to the simulations. The blue solid line represents the average relation measured by Lin et al. (2003), whereas the green solid line represents the average relation measured by Giodini et al. (2009). 1-σ error bars for the observational results are shown as dashed lines. The black dashed line represents the cosmological baryon fraction.

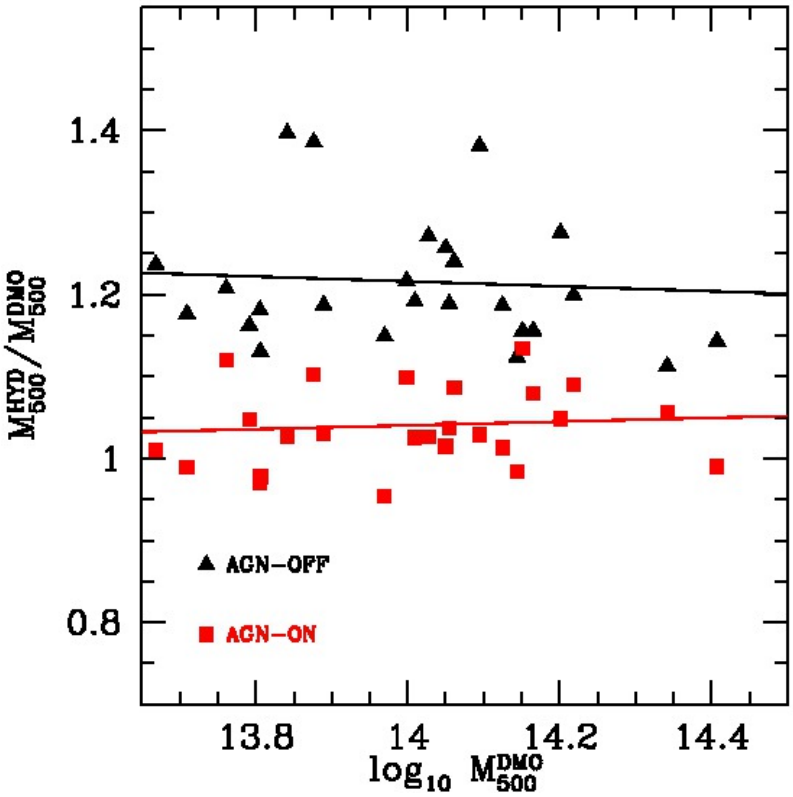

Figure 7.3: Ratio $M_{500}^{\rm HYD}/M_{500}^{\rm DMO}$ as a function of $M_{500}^{\rm DMO}$. Coloured points represent the results from the AGN-ON (red) and AGN-OFF (black) re-simulations. The red and black solid lines represent fits to the results of our simulations. This plot shows the effect of baryonic processes on the mass of the dark matter halos in our sample.

with the real universe.

The discussion in Section 7.3 argues that the baryon fraction scaling with mass determines the effects of baryonic processes on the halo mass function. The data shown in Figure 7.2 are relevant to this. In particular, the masses of individual halos are influenced by the nature of the physical processes involved in galaxy formation (Stanek et al., 2009; Cui et al., 2012). This is indeed what we find by analysing our cluster sample, as we show in Figure 7.3 in which we plot the ratio $M_{500}^{\rm HYD}/M_{500}^{\rm DMO}$ as a function of $M_{500}^{\rm DMO}$. This plot demonstrates by how much the masses of the halos in the HYDRO simulations deviate from those measured for the same halos in the DMO runs. We find that in simulations which do not include AGN feedback the halo masses

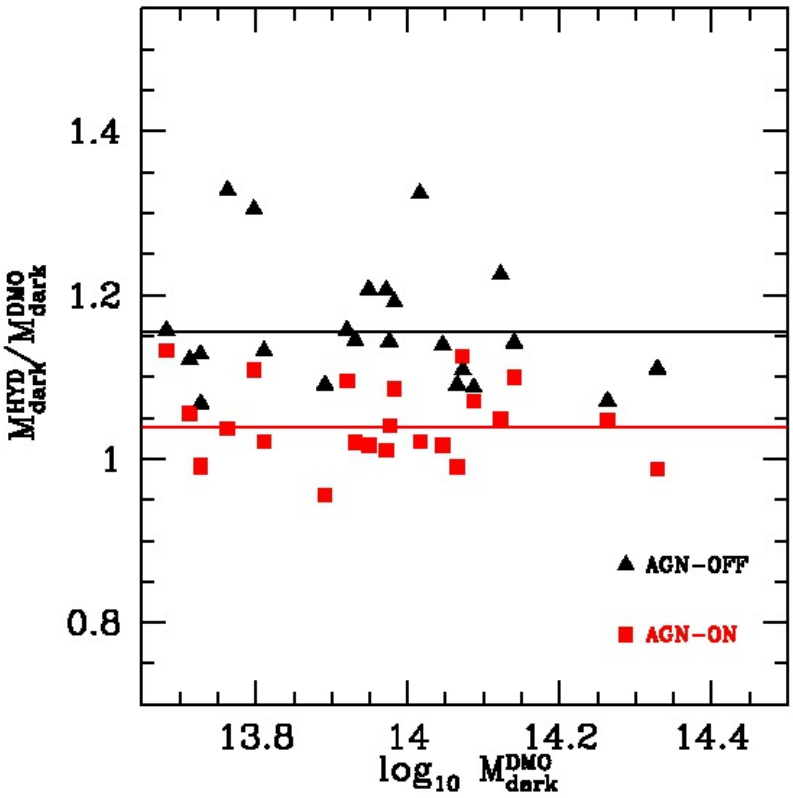

Figure 7.4: $M^{\rm DMO}_{\rm dark}$ vs. ratio $M^{\rm HYDRO}_{\rm dark}/M^{\rm DMO}_{\rm dark}$. Coloured points represent the results from the AGN-ON (red) and AGN-OFF (black) re-simulations. The red and black solid lines represent fits to the results of our analytical model, i.e. the α_c value.

are boosted to values that can be more than 20% higher than the corresponding DMO value. Previous results obtained with the RAMSES code show that this effect is caused by the contraction of the total mass distribution due to the high concentration of baryons at the centre of the halo (Martizzi et al., 2012). Including AGN feedback acts in the opposite direction, preventing the formation of high concentrations of baryonic mass at the centre of the halo. The net effect is that the halos in the AGN-ON runs have masses that are very similar to the ones measured in the DMO case, although a significant scatter appears to be present in the $M_{500}^{\rm HYD}/M_{500}^{\rm DMO}$ scaling relation. The red and black solid lines in Figure 7.3 show the results of our fit to the data using the model of Equation 7.5.

The importance of the contraction parameter α_c can be appreciated in Figure 7.4 where we plot the ratio $M_{dark}^{\rm HYD}/M_{dark}^{\rm DMO}$ as a function of $M_{dark}^{\rm DMO}$. This plot demonstrates that the slope in the relation observed in Figure 7.3 is set by the variation of the baryon fractions with halo mass. The ratio of dark matter masses $M_{dark}^{\rm HYD}/M_{dark}^{\rm DMO}$ is approximately constant with halo mass in both the AGN-ON and AGN-OFF cases, but it shows a large scatter. The α_c model successfully fits the results observed in our simulations. These results have two important implications: (I) contraction of dark matter induced by baryons has a relevant effect and can be observed only in high resolution simulations; (II) the contraction effect on halo masses can be described by a simple model.

We have explicitly tested the validity of the adiabatic contraction theory (Gnedin et al., 2004) to explain the α_c values we measure in our simulations. We adopt the adiabatic contraction model we already used in Teyssier et al. (2011) and Martizzi et al. (2012), but we assume that all the baryons are concentrated at the centre of the halo. The adiabatic contraction model predicts $\alpha_c = 1.050$ in the AGN-ON case and $\alpha_c = 1.102$ in the AGN-OFF case. Both values are in good agreement with the results of our simulations, but the AGN-ON halos are slightly under-contracted with respect to the predictions of the adiabatic contraction model, while the AGN-OFF halos are slightly over-contracted.

7.5 The halo mass function

In the following, we assume that the halo mass function in dark matter only simulations is described by the Tinker et al. (2008) formula. The masses used in the Tinker et al. (2008) formula are defined in terms of ρ_m the average matter density. To match our mass definitions with those of Tinker et al. (2008) we use the relation $500\rho_c = 500\rho_m/\Omega_{\rm m} = 1838.23\rho_m$. We use the

analytical formalism described above and the measurements performed on our re-simulations to calculate the effect of baryons on the halo mass function.

The comparison between the different results is summarized in Figure 7.5. We only show the mass range in which the baryon fraction scaling has been measured in our simulations. Figure 7.5 clearly shows how the boost in halo masses observed in the AGN-OFF runs influences the halo mass function by increasing the number of halos in the high mass bins. The scatter in the baryon scaling relation has been taken into account by considering the values reported at the end of Section 3 and assuming Equation 7.8 to be valid. The effect of the scatter of the baryon scaling relation boosts the number counts even more. As already discussed, AGN feedback acts in a way that partially suppresses the boost in halo masses observed in AGN-OFF simulations. The net effect is that the prediction for the halo mass function in the AGN-ON case is closer to the dark matter only case. Furthermore, the effect of scatter in the baryon fraction scaling relation is also boosting the number of counts in the AGN-ON case. This boost is simply due to the scatter which populates higher mass bins with lower mass clusters.

There is a small caveat in this determination of the scatter calculated by comparing the same clusters simulated as dark matter only and then with baryons. Some of this scatter will arise from the numerical effects associated with different simulations of a weakly chaotic system. As an extreme example, different simulation codes that start with the same initial conditions will end up with slightly different final masses for the same object. However, we expect that most of the scatter is physical and arises from the different formation history once baryons are included. For example, cooling and star-formation makes accreting halos denser and able to survive deeper into the potential and taking mass further in. We confirmed that there is a correlation between the mass increase and the stellar mass fraction of the clusters. However, to truly isolate these effects, a large number of clusters with very similar masses should be simulated.

With the aim of having a more quantitative estimate of how much the mass functions predicted for the HYDRO simulations differ from the dark matter only case, we plot the relative deviation $n/n_0 - 1$ as a function of halo mass in Figure 7.6. We also show the expected Poisson error bars on the halo mass function from a survey of volume 0.5 $h^{-3}\mathrm{Gpc}^3$ as a grey shaded area in Figure 7.6.This volume is comparable to the volume of currently available galaxy cluster surveys that have been used to obtain cosmological constraints. For instance, the MaxBCG cluster catalogue (Koester et al., 2007) covers a volume of $\sim 0.17\ h^{-3}\mathrm{Gpc}^3$ whereas the REFLEX II catalogue (Balaguera-Antolínez et al., 2011) probes a volume of $\sim 2\ h^{-3}\mathrm{Gpc}^3$. However, such a volume is quite small compared to the one that will be probed by future

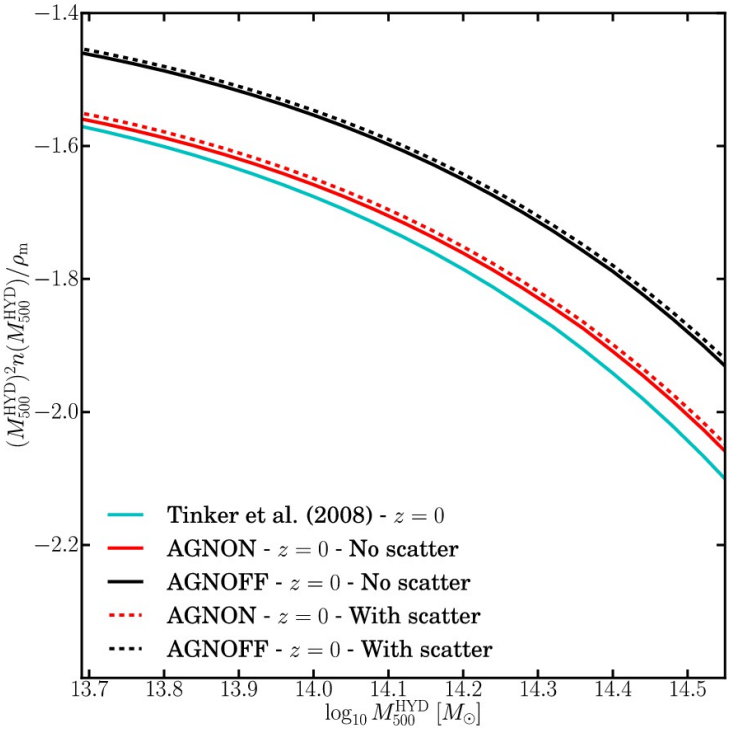

Figure 7.5: The halo mass functions inferred by our model. The cyan solid line is the Tinker et al. (2008) model for the halo mass function in dark matter only simulation. The red and black lines represent the predictions of our model in the AGN-ON and AGN-OFF cases: for the solid lines we assume an exact scaling of the baryon fractions, for the dashed lines we take into account the measured scatter.

surveys, e.g. eROSITA, with a covered sky-fraction of 0.658 and redshift limit to be 2.0, will have a survey volume larger than 400 Gpc^3. For Euclid the survey volume is expected to be even larger. For this reason the error bars shown in Figure 7.6 are much larger than the Poisson noise contribution to the expected uncertainty in the determination of the mass function from future surveys. For larger surveys the Poisson error bars will be much smaller.

The meaning of the error bars in Figure 7.6 is worth discussing in more detail. We are making predictions for the halo mass function, which requires halo counts in a given volume. Cosmological constraints from completed and ongoing surveys are limited by mass calibration and redshift evolution systematics (e.g. Vikhlinin et al. (2009)), therefore Poisson error bars we consider for the smaller volume represent a very idealized case. With larger volumes and better mass calibration, more halos will be counted and with the sensitivity of the future missions, like eROSITA, about 100000 clusters are expected. As already discussed, this means that the Poisson error bars will be much smaller than for smaller surveys that are currently ongoing. However, we argue that the binning of cluster counts is likely to be relevant: if a larger number of bins in mass and redshift is chosen, the Poisson errors in each bin will be larger but more data points are obtained. Ideally, one should optimize for number of bins as increasing the data points infinitely will results into larger error bars and no constraints can be obtained. If an optimization of the number of bins such that the errors introduced by redshift and mass calculations are negligible as compared to the Poisson error, then cosmological constraints are gained by the number of data points.

Firstly, we note that the predictions of the AGN-OFF model are well outside the Poisson error bars. In the case in which the scatter in the baryon fraction scaling is explicitly accounted for, the AGN-OFF mass function shows a 30-50% deviation from the dark matter only prediction of Tinker et al. (2008). If the AGN-OFF model provided the best match to reality, this would imply serious problems for the direct comparison between measured halo mass functions and the results of dark matter only simulations: baryons would need to be explicitly and carefully accounted for when comparing measurements with simulations. However, we already know that the AGN-OFF model is not a good description of observed clusters because it predicts baryon fractions and galaxy masses that are too large.

The AGN-ON model better matches observations, and the predictions we obtain for the halo mass function are close to the dark matter only case. However, we see that the AGN-ON mass function can still be distinguished from the dark matter only model assuming the Poisson error bars of a very large survey. This result is confirmed also when the scatter in the baryon fraction scaling relation is accounted for. If the results of our simulations are

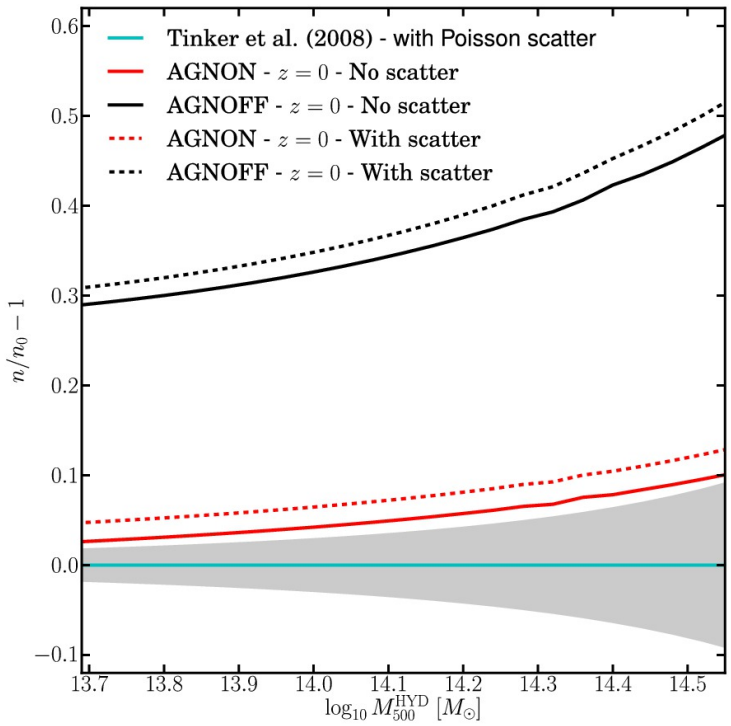

Figure 7.6: Relative deviation of our predictions from the Tinker et al. (2008) model for the halo mass function in dark matter only simulations. The shaded area represents Poisson scatter for a survey of volume 0.5 h^{-3}Gpc^3. The red and black lines represent the predictions of our model in the AGN-ON and AGN-OFF cases: for the solid lines we assume an exact baryon fraction scaling, for the dashed lines we take into account the measured scatter.

reliable this is a particularly important prediction, since it implies that mass functions directly measured from dark matter only simulations need to be corrected to account for the effect of baryons when comparing to observations. As we discussed above, the main effect of baryons on the halo mass function can be taken into account (e.g. by using Equations 7.4 to 7.7) once the scaling of baryon fractions with mass is known and once a simple analytical model is adopted to account for adiabatic contraction of the dark matter distribution.

7.6 Impact on the estimate of cosmological parameters

In the previous section we showed that including baryonic effects caused the halo mass function to differ from that found in dark matter only simulations. In this section we demonstrate that significant biases can be introduced into the estimation of cosmological parameters when baryon effects are not accounted for.

We adopt the COSMOMC (Lewis & Bridle, 2002) MCMC algorithm to infer $\Omega_{\rm m}$ and σ_8 whilst assuming a flat universe. In our analysis, we only allowed four parameters to vary: $\Omega_{\rm m}$, $\Omega_{\rm b}$, h and σ_8. We apply the algorithm to our mass function data using a standard Tinker et al. (2008) model to fit the data. We assume Poisson noise to compute the error bars for the resulting halo mass function. The Poisson noise is generated assuming a survey of volume 0.5 $h^{-3}{\rm Gpc}^3$, however in full sky surveys the volumes are larger than this leading to smaller error bars and tighter constraints on the cosmological parameters. To demonstrate that, we also generate Poisson noise for a larger survey of volume 500 $h^{-3}{\rm Gpc}^3$, comparable to eROSITA and Euclid. We stress that Poisson error bars represent an idealized case, however we do not consider this fact important for the significance of our results, as already discussed in the previous section.

First, we run the MCMC algorithm on the Tinker et al. (2008) model for our fiducial cosmology with the aim of obtaining likelihoods for the cosmological parameters. These likelihoods are our fiducial values, because they represent the result we would get if we apply a halo mass function model that does not account for baryonic effects. Our simulations show that the halo mass function is influenced by baryonic effects, so if we naively applied the Tinker et al. (2008) model to the real halo mass function we would obtain likelihoods that are biased with respect to the fiducial ones. The existence of this bias is explicitly demonstrated in Figure 7.7, which shows contour plots

representing the likelihood as a function of different cosmological parameters. The top panel is for a survey of volume 0.5 h^{-3}Gpc^3, the bottom panel is for a survey of volume 500 h^{-3}Gpc^3. The fiducial likelihoods are compared to the likelihoods obtained applying the MCMC algorithm to our AGN-ON model.

In the smaller volume, we find a bias in the $\Omega_{\rm m}$ and σ_8 parameters, at the 0.4% and 1.7% level respectively. In the larger, volume we find a bias in the $\Omega_{\rm m}$ and σ_8 parameters, at the 7% and 1.5% level respectively. In the bottom panel, the constraints are tighter than in the top panel (due to a larger volume), so the shift is noticeable. Because the case with baryons has a slightly higher mass function, Poisson bars are smaller and hence the constraints are also tighter. This is similar as case presented in the top panel, but the volume is smaller and hence the Poisson bars are larger, so the difference is not easily noticeable. Given the high degeneracy between the $\Omega_{\rm m}$ and σ_8 parameters the overall bias is higher, up to few %. This bias will be more significant if tighter constraints are obtained from full sky surveys, as shown in the bottom panel of Figure 7.7, and if the constraints coming from the halo mass function are combined with those obtained from other probes (CMB, SN-Ia, BAO). If sub-percent accuracy cosmology is the aim of the next generation observational campaign, baryonic effects clearly need to be taken into account.

In the bottom panel, the constraints are tighter than in the top panel (due to larger volume), so the shift is well noticeable. Also because the case with baryons has slightly higher mass function, Poisson bars are smaller and hence the constraints are also tighter. However, similar is the case for the top panel, but the volume is smaller and hence the Poisson bars are larger, so the difference is not easily noticeable.

7.7 Summary and Conclusions

We identified 51 isolated dark matter halos in a cosmological dark matter only simulation and re-simulated them at higher resolution using different prescriptions for galaxy formation. The *total* halo masses are 10^{14} M$_\odot$ $< M_{\rm tot} < 10^{15}$ M$_\odot$, therefore they host massive groups and clusters of galaxies. In the AGN-OFF model we implement standard galaxy formation recipes, including supernovae feedback. In the AGN-ON model we also include AGN feedback as in Booth & Schaye (2009). We measured the masses and baryon fractions of the halos in the catalog and we used our formalism to compute how the halo mass function changes under the effect of baryons. We adopted the Tinker et al. (2008) mass function as our fiducial analytical model for

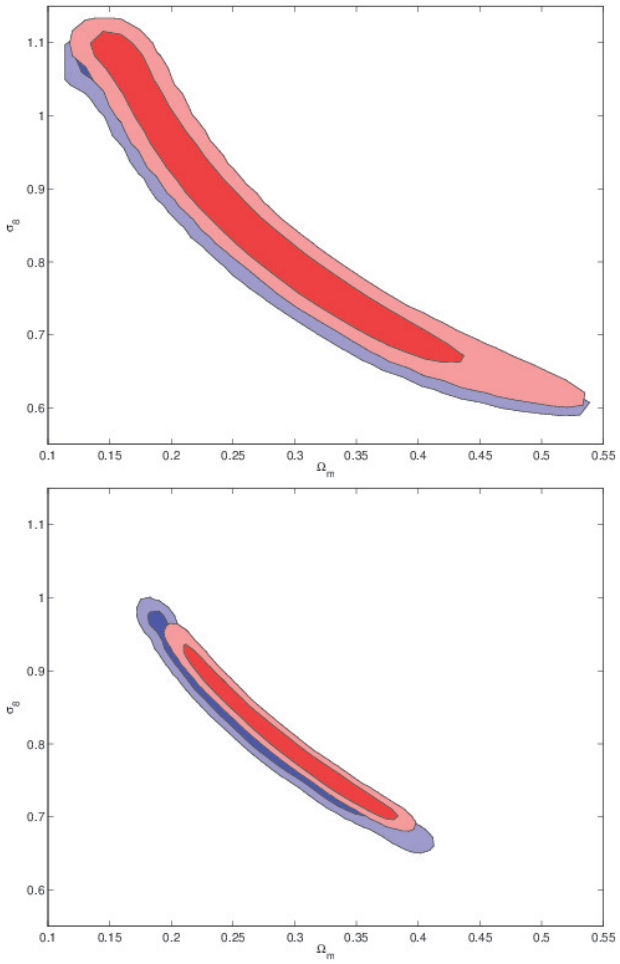

Figure 7.7: Contour plots representing the likelihood as a function of $\Omega_{\rm m}$ and σ_8. The inner and outer contours are 1σ and 2σ away from the peak, respectively. The blue contours represent the likelihood for our fiducial cosmology (Table 1). The red contours represent the likelihood in the case in which baryonic effects on the halo mass function are not considered. The top panel represents the case for a survey of volume 0.5 h^{-3}Gpc^3. The bottom panel represents the case for a survey of volume 500 h^{-3}Gpc^3.

the halo mass function measured in dark matter only simulations. We then used a simple analytical formalism to compute the effect of baryons on the dark matter halo mass function at redshift $z = 0$ and we applied it to obtain predictions from cosmological hydrodynamical simulations.

Our findings can be summarized in a few points:

- The AGN-ON model provides better fits to the observations. The masses of the central galaxies in the clusters are in agreement with the values expected from abundance matching (Moster et al., 2010; Moster et al., 2013). The scaling of baryon fractions with halo mass is in relatively good agreement with the results published by Lin et al. (2003), but in excess with respect to the values measured by Giodini et al. (2009). The AGN-OFF model produces central galaxies that are too massive and baryon fractions that are too high compared to the observational results. Therefore, the AGN-ON model produces more realistic results with respect to the case without AGN feedback.

- In the AGN-OFF case halo masses can be $> 20\%$ larger than in the dark matter only runs. This is an effect of the condensation of baryonic mass at the centre of the dark matter halos, which also boosts the concentration of the total mass distribution (Martizzi et al., 2012). AGN feedback acts in the opposite direction, preventing large condensations of baryonic mass at the centre of dark matter halos. The halo masses in the AGN-ON runs are very close to those measured in the dark matter only case.

- Halo counts in the sampled mass range are boosted by $\sim 30 - 50\%$ in the AGN-OFF case. In the more realistic AGN-ON case we found that the halo mass function for massive groups and clusters is still not consistent with the halo mass function measured in dark matter only simulations. The halo mass function in the AGN-ON case is boosted by 5-10 %. This fact implies that mass functions measured in dark matter only simulations may not be accurate enough to be directly compared to observational results.

- Neglecting baryonic effects on the halo mass function leads to biases at the % level in the estimate of cosmological parameters like $\Omega_{\rm m}$ and σ_8. If we assume a survey volume of 0.5 $h^{-3}{\rm Gpc}^3$, comparable to present the one of current surveys, we find a relevant bias in the $\Omega_{\rm m}$ and σ_8 parameters, at the 0.4% and 1.7% level, respectively.

- Modeling of the baryonic effects on the halo mass function requires to explicitly account for the contraction of the dark matter distribution

under the effect of baryons. We propose an extension of the model used by Balaguera-Antolinez & Porciani (2013), which uses the baryon fraction scaling with halo mass, parameterises the response of dark matter to baryonic condensations at the halo centres and predicts the effect of baryons on halo masses.

There are a few caveats that should be discussed. First of all, we measured properties only for a limited number of halos. The bias between the pure dark matter halo mass function and that found with a treatment of hydrodynamics, star-formation, supernovae and AGN feedback, may be present at the few percent level. To improve these estimates we need more statistics and a more detailed exploration of the parameter space. The best approach would be to consider a full cosmological box instead of several re-simulations. However, simulations of full cosmological boxes with the resolution we achieve and including AGN feedback are still computationally challenging. This might serve as a partial justification for the adoption of the semi-analytical approach we follow in this paper. The predictions for the halo mass function including baryonic effects need to be carefully studied with larger and improved simulations, since these effects will then be relevant.

Furthermore, our analytical model to correct the mass function for baryonic effects has two limitations: firstly, the baryon fraction scaling and its scatter needs to be known; secondly, a simplified model which accounts for adiabatic contraction needs to be adopted. The former limitation could be overcome using accurate observations of the baryon fraction scaling. The latter limitation represents an intrinsic theoretical issue - the adiabatic contraction theory is only an approximation to account for the response of the mass distribution to large baryon condensations. Our results seem to confirm that such an approximation is reasonable, since the features of the halos in our numerical simulations are well captured by a simple adiabatic contraction model. We also point out that alternative techniques that take into account the effect of baryons on the halo mass function are being developed by other authors (see e.g. Cusworth et al. (2013)).

Finally, we want to stress that our results have significant implications for the correct comparison of halo counts in present and next generation SZ (e.g. Planck, South Pole Telescope, Atacama Cosmology Telescope), X-ray (e.g. Chandra, XMM-Newton, Suzaku, eROSITA) and multi-wavelength surveys (e.g. Dark Energy Survey, Euclid): the effects of baryons influence the halo mass function at the cluster scale at a level $\sim 10\%$ or less, which is larger than the level of accuracy that next generation surveys should achieve. At the galaxy cluster scale, the proper modeling of baryon physics is still likely to be an issue for what concerns the comparison between the mass

function measured from observations and the one measured in simulations. For current cluster surveys baryonic effects are within the noise for current survey volumes. Recent constraints placed on cosmological parameters using cluster surveys (e.g. ROSAT (Balaguera-Antolínez et al., 2011; Rapetti et al., 2013), SDSS (Zu et al., 2012; Mana et al., 2013), ACT (Hasselfield et al., 2013), SPT (Reichardt et al., 2013; Benson et al., 2013), PLANCK (Planck Collaboration et al., 2013)) are not expected to be strongly influenced by baryonic effects, but forthcoming and planned large surveys will be biased at the % level by these processes.

Bibliography

Andreon S., 2010, MNRAS, 407, 263

Aubert D., Pichon C., Colombi S., 2004, MNRAS, 352, 376

Audit E., Teyssier R., Alimi J.-M., 1997, A&A, 325, 439

Balaguera-Antolinez A., Porciani C., 2013, , 4, 22

Balaguera-Antolínez A., Sánchez A. G., Böhringer H., Collins C., Guzzo L., Phleps S., 2011, MNRAS, 413, 386

Benson B. A., de Haan T., Dudley J. P., Reichardt C. L., Aird K. A., Andersson K., Armstrong R., Ashby M. L. N., Bautz M., Bayliss M., Bazin G., Bleem L. E., Brodwin M., Carlstrom J. E., Chang C. L. e. a., 2013, ApJ, 763, 147

Bertschinger E., 2001, The Astrophysical Journal Supplement Series, 137, 1

Booth C. M., Schaye J., 2009, Monthly Notices of the Royal Astronomical Society, 398, 53

Crocce M., Fosalba P., Castander F. J., Gaztañaga E., 2010, MNRAS, 403, 1353

Cui W., Borgani S., Dolag K., Murante G., Tornatore L., 2012, MNRAS, 423, 2279

Cusworth S. J., Kay S. T., Battye R. A., Thomas P. A., 2013, ArXiv e-prints

Dubois Y., Devriendt J., Slyz A., Teyssier R., 2012, MNRAS, 420, 2662

Duffy A. R., Schaye J., Kay S. T., Dalla Vecchia C., Battye R. A., Booth C. M., 2010, MNRAS, 405, 2161

Efstathiou G., Frenk C. S., White S. D. M., Davis M., 1988, MNRAS, 235, 715

Eisenstein D. J., Hu W., 1998, Astrophysical Journal v.496, 496, 605

Fromang S., Hennebelle P., Teyssier R., 2006, Astronomy and Astrophysics, 457, 371

Giodini S., Pierini D., Finoguenov A., Pratt G. W., Boehringer H., Leauthaud A., Guzzo L., Aussel H., Bolzonella M., the COSMOS Collaboration 2009, The Astrophysical Journal, 703, 982

Gnedin O. Y., Kravtsov A. V., Klypin A. A., Nagai D., 2004, The Astrophysical Journal, 616, 16

Gonzalez A. H., Zaritsky D., Zabludoff A. I., 2007, The Astrophysical Journal, 666, 147

Governato F., Brook C., Mayer L., Brooks A., Rhee G., Wadsley J., Jonsson P., Willman B., Stinson G., Quinn T., Madau P., 2010, Nature, 463, 203

Guillet T., Teyssier R., Colombi S., 2010, MNRAS, 405, 525

Hasselfield M., Hilton M., Marriage T. A., Addison G. E., Barrientos L. F., Battaglia N., Battistelli E. S., Bond J. R., Crichton D. e. a., 2013, , 7, 8

Jenkins A., Frenk C. S., White S. D. M., Colberg J. M., Cole S., Evrard A. E., Couchman H. M. P., Yoshida N., 2001, MNRAS, 321, 372

Jing Y. P., Zhang P., Lin W. P., Gao L., Springel V., 2006, ApJ, 640, L119

Kazantzidis S., Kravtsov A. V., Zentner A. R., Allgood B., Nagai D., Moore B., 2004, ApJ, 611, L73

Koester B. P., McKay T. A., Annis J., Wechsler R. H., Evrard A., Bleem L., Becker M., Johnston D., Sheldon E., Nichol R., Miller C., Scranton R. e. a., 2007, ApJ, 660, 239

Laganá T. F., Martinet N., Durret F., Lima Neto G. B., Maughan B., Zhang Y.-Y., 2013, A&A, 555, A66

Leauthaud A., George M. R., Behroozi P. S., Bundy K., Tinker J., Wechsler R. H., Conroy C., Finoguenov A., Tanaka M., 2012, ApJ, 746, 95

Lewis A., Bridle S., 2002, Phys. Rev. D, 66, 103511

Lin Y.-T., Mohr J. J., Stanford S. A., 2003, The Astrophysical Journal, 591, 749

Lin Y.-T., Stanford S. A., Eisenhardt P. R. M., Vikhlinin A., Maughan B. J., Kravtsov A., 2012, ApJ, 745, L3

Macciò A. V., Stinson G., Brook C. B., Wadsley J., Couchman H. M. P., Shen S., Gibson B. K., Quinn T., 2012, ApJ, 744, L9

Mana A., Giannantonio T., Weller J., Hoyle B., Hütsi G., Sartoris B., 2013, MNRAS, 434, 684

Martizzi D., Teyssier R., Moore B., 2012, MNRAS, 420, 2859

Martizzi D., Teyssier R., Moore B., Wentz T., 2012, MNRAS, 422, 3081

Moster B. P., Naab T., White S. D. M., 2013, MNRAS, 428, 3121

Moster B. P., Somerville R. S., Maulbetsch C., van den Bosch F. C., Macciò A. V., Naab T., Oser L., 2010, The Astrophysical Journal, 710, 903

Planck Collaboration Ade P. A. R., Aghanim N., Armitage-Caplan C., Arnaud M., Ashdown M., Atrio-Barandela F., Aumont J., Baccigalupi C., Banday A. J. e. a., 2013, ArXiv e-prints

Pontzen A., Governato F., 2012, MNRAS, 421, 3464

Press W. H., Schechter P., 1974, ApJ, 187, 425

Rapetti D., Blake C., Allen S. W., Mantz A., Parkinson D., Beutler F., 2013, MNRAS, 432, 973

Reddick R., Tinker J., Wechsler R., Lu Y., 2013, ArXiv e-prints

Reed D., Gardner J., Quinn T., Stadel J., Fardal M., Lake G., Governato F., 2003, MNRAS, 346, 565

Reed D. S., Bower R., Frenk C. S., Jenkins A., Theuns T., 2007, MNRAS, 374, 2

Reed D. S., Smith R. E., Potter D., Schneider A., Stadel J., Moore B., 2013, MNRAS, 431, 1866

Reichardt C. L., Stalder B., Bleem L. E., Montroy T. E., Aird K. A., Andersson K., Armstrong R., Ashby M. L. N., Bautz M., Bayliss M., Bazin G., Benson B. A., Brodwin M., Carlstrom J. E. e. a., 2013, ApJ, 763, 127

Rudd D. H., Zentner A. R., Kravtsov A. V., 2008, ApJ, 672, 19

Semboloni E., Hoekstra H., Schaye J., van Daalen M. P., McCarthy I. G., 2011, MNRAS, 417, 2020

Sheth R. K., Mo H. J., Tormen G., 2001, MNRAS, 323, 1

Sheth R. K., Tormen G., 1999, MNRAS, 308, 119

Springel V., 2005, MNRAS, 364, 1105

Stanek R., Rudd D., Evrard A. E., 2009, MNRAS, 394, L11

Stinson G., Seth A., Katz N., Wadsley J., Governato F., Quinn T., 2006, Monthly Notices of the Royal Astronomical Society, 373, 1074

Sutherland R. S., Dopita M. A., 1993, ApJS, 88, 253

Teyssier R., 2002, Astronomy and Astrophysics, 385, 337

Teyssier R., Fromang S., Dormy E., 2006, Journal of Computational Physics, 218, 44

Teyssier R., Moore B., Martizzi D., Dubois Y., Mayer L., 2011, MNRAS, 414, 195

Teyssier R., Pontzen A., Dubois Y., Read J. I., 2013, MNRAS, 429, 3068

Tinker J., Kravtsov A. V., Klypin A., Abazajian K., Warren M., Yepes G., Gottlöber S., Holz D. E., 2008, ApJ, 688, 709

Toro E. F., Spruce M., Speares W., 1994, Shock Waves, 4, 25

Tweed D., Devriendt J., Blaizot J., Colombi S., Slyz A., 2009, A&A, 506, 647

van Daalen M. P., Schaye J., Booth C. M., Dalla Vecchia C., 2011, MNRAS, 415, 3649

Vikhlinin A., Burenin R. A., Ebeling H., Forman W. R., Hornstrup A., Jones C., Kravtsov A. V., Murray S. S., Nagai D., Quintana H., Voevodkin A., 2009, ApJ, 692, 1033

Warren M. S., Abazajian K., Holz D. E., Teodoro L., 2006, ApJ, 646, 881

White M., 2004, Astroparticle Physics, 22, 211

Zhan H., Knox L., 2004, ApJ, 616, L75

Zu Y., Weinberg D. H., Rozo E., Sheldon E. S., Tinker J. L., Becker M. R., 2012, ArXiv e-prints

Conclusions and future perspectives

This Thesis discusses several issues related to the formation and evolution of galaxy clusters in a cosmological context. The main focus of this work is to characterize the relevance of the non-gravitational heating process known as AGN feedback in structure formation and evolution. Galaxy clusters and groups are the objects where AGN feedback is expected to be more relevant, therefore they represent the ideal class of astrophysical objects to test the AGN feedback paradigm. Given the complexity of the problem, numerical methods have been adopted. We performed many adaptive mesh refinement hydrodynamical simulations of galaxy clusters in isolation and in a full cosmological framework, then we analysed them to draw our conclusions. The results of this Thesis can be summarized in a few points:

- Simulations which do not include AGN feedback are not able to reproduce the mass distribution observed in real galaxy clusters. When AGN feedback is considered, the properties of simulated clusters are very similar to the ones measured in real objects.

- Simulations which do not include AGN feedback produce brightest cluster galaxies that are too massive with respect to the observed ones and that have unrealistic kinematic properties. AGN feedback is a very promising mechanism to quench star formation and modify the dynamical structure of central galaxies. In simulations that include AGN feedback, we observe brightest central galaxies that are very similar to the ones observed in the real universe.

- AGN feedback is an extremely violent heating source. Thermal energy can be easily converted in kinetic energy at the centre of galaxy clusters. This generally generates repeated outflows which influence the dynamical properties of the system. The net effect is a reduction of the concentration of the total mass profile with respect to the case of simulations which do not include AGN feedback.

- In extreme cases, the effect described in the previous point is able to generate constant density cores at the centre of clusters. Our simulations predict that cores of similar size are produced in the dark matter density distribution and in the stellar mass density distribution.

- The mass of dark matter halos is influenced by baryonic processes. In simulations without AGN feedback, halo masses are boosted with respect to the masses measured in dark matter only simulations. If AGN feedback is included, this boost is reduced. In the latter case, the halo mass function is found to be very similar to the one measured in dark matter only simulations.

Despite the relevance of the results presented in this Thesis, further studies on the effect of AGN feedback on structure formation are needed. First of all, it is extremely important to characterize this effect considering a statistically significant catalog of simulated objects with different histories and structural properties. Second, AGN feedback is implemented in cosmological simulations using very simple phenomenological sub-grid models. Efforts are being made to explore the parameter space of these sub-grid models and to construct new models that are less dependent on the numerical resolution of simulations. Improvements in sub-grid models might be extremely important for the correct reproduction of the small scale properties of collapsed structures, especially in galaxy groups where AGN feedback is expected to be extremely efficient. Finally, the cosmological implications of the inclusion of AGN feedback in cosmological simulations still need to be explored: the effect of AGN feedback on the mass distribution within halos might be extremely relevant for accurate theoretical predictions on the power spectrum, which will be measured to very high accuracy from the data provided by next generation surveys.

Finally, it is worth mentioning that interesting improvements can be made in making AGN feedback models for cosmological simulations more realistic. Distinguishing explicitly between the radio and quasar modes of AGN feedback is one of the main aims. Radiative feedback is one of the most favored candidates as a model for quasar mode feedback, while the effect of non-thermal pressure from cosmic rays accelerated at magneto-hydrodynamical shocks is a viable candidate to account for the radio mode. Furthermore, radiative feedback for stars is a mechanism that is not always included in numerical cosmological simulations and it might be also extremely relevant.